A Calibrated Dual-Port Acoustic Vector Network Analyzer

A thesis

submitted in partial fulfilment

of the requirements for the Degree

of

Doctor of Philosophy

at

The University of Waikato

by

M.S.G MacDonell

THE UNIVERSITY OF
WAIKATO
Te Whare Wānanga o Waikato

2022

Abstract

The Vector Network Analyzer (VNA) is a workhorse in electrical engineering, and has been refined over the last fifty years to offer many advantages. This technology is continually expanding and branching into other fields including optics. This thesis presents the design and calibration of an Acoustic Vector Network Analyzer (AVNA), which represents further adaptation of this technology into other engineering fields. This goal requires several developments; a repeatable acoustic waveguide flange/joint, a calibration method(s), calibration standards, and calibration verification.

The hardware that has been developed is used as an accessory to an existing commercial VNA mainframe (Agilent-4395A) and a retrofitted test-set (HP87511A) that now hosts connectivity for our "measurement heads" containing the acoustic directional couplers. Directional couplers are the fundamental technology that allows for Vector Network Analysis, the acoustic variant has an operational range of a little more than an octave and sufficient directionality for calibration. The coupler is a branch waveguide coupler and to enable reliable and repeatable connection has been equipped with a flange system. This flange system has alignment pins and O-rings to ensure proper sealing and repeatability. Several materials were used with additive manufacturing techniques to create couplers and waveguide sections, each with its own advantages. Titanium (Ti64) offered the best usability and reliability, while plastic offered better repeatability.

Calibration was a major advance in the VNA and one that popularized the instrument. The calibration's performance is limited by the repeatability of flanged joints. This is because several measurements are required to produce a linear system of equations, therefore this system contains within it the variation of the flange joints.

Developing a calibration method is the crux in realizing the aim of an Acoustic VNA. This thesis presents a set of five measurements and two competing algorithms that can be used to implement calibration. The analytical and numerical methods presented both have distinct advantages and disadvantages. The five measurements are performed with proposed calibration standards. A "Thru", "Reflect" and "Match" standard are required. The

"Match" standard is provided by a sliding load, the sliding load has been previously used as part of an acoustic calibration. To verify the operation of the calibrated instrument verification measurement was performed using a passive, asymmetrical, reciprocal device (PARD).

Acknowledgements

I would like to thank the following; Dr. Jonathan Scott (University of Waikato) and Dr. Marcus Wilson (University of Waikato) for their support, and guidance as my research supervisors. Peter Higgins in the university workshop for his assistance building waveguide hardware. Keshav Basnet for his contributions in the lab measuring repeatability and performing calibrations. My fiancèe Holly Armit for her tolerance of my erratic study schedule, and for the sacrifices she has made to support this achievement. My parents, Scott and Vicki MacDonell who have supported many young men in their academic pursuits. Thank-you on behalf of all of us. Hiroshi Romanes and Vance Farrow for their company on late nights in the lab. I'd also like to thank those people in the research office for their assistance in dealing with scholarship/funding issues and disputes. Namely; Brittney Duffy, Carol Robinson, and Stephen Turner. I would also like to acknowledge the Science for Technological Innovation (SfTI) challenge, one of the New Zealand Ministry of Business, Innovation, and Employment (MBIE) science challenges for funding this research. Lastly, Akira the Don, for the countless hours of meaningwave. It feels like it works.

Contents

Declaration of Originality

The work contained in this thesis is my own except where otherwise acknowledged. All of the CAD (Computer-Aided Design) is my work, including; schematics, PCB layouts, SolidWorks models and shop drawings. All measurements were performed by either myself or with the assistance of Keshav Basnet. Waveguide hardware was either 3D printed or built in the university workshop by Peter Higgins. The waveguide flange system, with its torque and bolt order requirements, is my design. Devising the use of the 16-term error model, design of the standards and the software implementation of the calibration analytically and numerically was my work. The design of the Passive Asymmetrical Reciprocal Device (PARD) is my adaptation of previous work by Jonathan Scott. It should be stated that the use of a PARD as a verification standard was not anticipated at the outset of this research. The PARD is a necessary substitution for a planned but never delivered verification standard. This planned standard was to be delivered under a Ministry of Business, Innovation, and Employment (MBIE) subcontract. The verification standard was to be some structure whose S-parameters were to be anticipated by Computational Fluid Dynamics (CFD). This structure would have then been measured, the agreement of measurement and simulation would constitute the verification standard.

Chapter 1

Introduction

1.1 Research Motivation & Scope

This research aims to construct a dual-port Acoustic Vector network analyser (VNA). This is motivated by the developments of VNA technology in the electromagnetic domain. The speed and traceable nature of modern VNA measurements in particular could be advantageous to the acoustic domain. VNA literature in the electromagnetic domain spans 50+ years, and there is potential to adapt much of it to an analogous instrument in the acoustic domain [1, 2]. This goal requires several developments; a repeatable acoustic waveguide joint, a calibration method(s), calibration standards, and calibration verification.

1.1.1 Current Acoustic Test & Measurement

Absorbing materials play an important role in architectural acoustics, the design of recording studios, listening rooms, and automobiles [3–6]. The reverberation time of a room is a very important acoustic quantity of concern to both architects and musicians. The growth and decay of the reverberant sound field in a room depends on the absorbing properties of the materials used. Knowledge of acoustic properties like the absorption coefficient and transmission-loss coefficient is necessary for the manufacturing of new materials, products or in

architecture where strict acoustic standards apply [7].

To know the acoustic properties of a material, it needs to be measured. These measurements will either be performed by a technician in the context of their work or, they may rely on those provided by a manufacturer. Manufacturer quoted parameters should be of typical measured performance.

1.1.2 The Impedance Tube

Acoustic impedance Z is used to describe the transmission of acoustic energy in acoustic materials and systems. The acoustic impedance is defined as

$$Z = \frac{p}{u} \tag{1.1}$$

where p is pressure and u is is the volume velocity. The acoustic reflection coefficient from one material to another is

$$\Gamma_{12} = \frac{Z_2 - Z_1}{Z_2 + Z_1} \tag{1.2}$$

where Z_1 and Z_2 are the acoustic impedance values of material one and material two respectively.

Acoustic impedance can be measured with a number of methods, these methods can be categorised by their use of either plane or spherical waves.

Methods that use spherical waves often use anechoic chambers or reverberation rooms with microphone arrays. These methods are useful with objects that are anisotropic because their response is dependent on geometry and orientation [8–11]. These methods are difficult to calibrate or perform repeatably due to environmental variables [11, 12].

Methods that use plane waves deploy a waveguide to create the plane wave, this waveguide is referred to as an "impedance tube". Samples are tested within the impedance tube, this offers advantages such as smaller material sample size, cost savings due to not needing a large anechoic chamber, reduced lab footprint, and increased repeatability and calibration. Impedance tube

methods fall into several sub categories, impedance divider methods [13–15], traversing microphone methods [15–17] and fixed microphone methods [10,18–20], the fixed microphone method(s) most commonly uses two microphones [3, 5,8,11], three and four microphone versions also exist [21–27] as well as systems using two impedance tubes to create 2-port measurement systems [25].

The impedance divider method has a maximum operating frequency of 100 Hz, has a low signal to noise ratio and cannot measure high impedance loads [11]. Traversing microphone methods are time consuming, can be laborious, require large tubes for low frequency and the microphones obstruct the sound field creating errors [11]. Fixed microphone methods rely on calculation, rather than direct measurement of the standing-wave-ratio (SWR) to determine reflection coefficient. This results in a quicker measurement [28,29], but these calculations can break down at half wavelength intervals as the matrices become ill conditioned [12] and the attenuation of the impedance tube needs to be accounted for [30]. Calibration methods have also been developed for some fixed microphone methods using "shorts" and "offset-shorts" [3, 22], and number and position of microphones can be fined tuned to increase accuracy [31, 32].

Shorts are ideally a perfect reflection placed on the end of the impedance tube, offset-shorts are the same except for an extra length of waveguide that shifts the short from the reference plane that changes their measured phase. These and other calibration standards will be explored in greater detail in Section 2 of Chapter 3.

1.1.3 Vector Network Analysis

A vector network analyzer (VNA) is a scientific instrument that measures network parameters, typically of electrical networks. Network analyzers commonly measure s–parameters but other network parameters such as y-parameters, z-parameters, and h-parameters can also be measured. Network analyzers are often used to characterize two-port networks, including devices like amplifiers

and filters, but an arbitrary number of ports is also possible.

VNA technology followed from slotted line measurements and the initial advantage of early VNAs like the HP8410 over the slotted line was that they allowed broadband swept measurements [2]. The transition from slotted line to VNA measurements followed the development of directional couplers. Directional couplers were developed through the 40's and 50's for use in telecommunications [33, 34]. Directional couplers are used as power dividers and can separate forward and reverse signals. These two properties are the fundamental mechanisms used by VNAs to perform measurements. As VNA technology matured the accuracy, dynamic range, and bandwidth improved greatly [1, 2]. Today VNAs are in widespread use with applications in every frequency band from 1 Hz into THz [35, 36].

The potential advantages of an Acoustic Vector Network Analyser (AVNA) over the impedance tube are; speed, accuracy, precision and traceability. These advantages are the primary motivation for an AVNA.

"In the early days of microwave development, the slotted line was the main measurement tool when reflection coefficient phase was needed. The slotted line allowed the magnitude and location of voltage minima and maxima to be found, so network parameters could be calculated. The process was indirect and time consuming." [2].

1.2 Thesis Outline

1. Chapter 2: A literature review which covers the history of electromagnetic VNAs in detail. Including S-parameters, error-models, the Smith chart, sliding loads, calibration and verification.

2. Chapter 3: Presents the acoustic analyser hardware, directional couplers, flanges, standards, and repeatability. The initial hardware development was published in ENZcon conference proceedings [37] and the development of the flanges and repeatability measurements were published in

IEEE I2MTC conference proceedings [38].

3. Chapter 4: Presents the selected calibration scheme is proposed, the two approaches are presented and compared with measurements of the proposed standards. These results were published in AES NY147 conference proceedings [39]

4. Chapter 5: Presents the development and measurement of the Passive Asymmetrical Reciprocal Device (PARD) as a partial verification standard. These results were published in the Journal of the Audio Engineering Society [40]

5. Chapter 6: Presents the conclusions and a summary of future work.

Chapter 2

Review: Vector Network Analysis

In this chapter, a brief history of VNA technology is presented. The directional coupler is then introduced and its operation in one and two-port systems. Scattering parameters are then introduced along with the Smith chart, and their advantages in the context of Vector Network Analysis. Finally, error models, flow graphs, their matrix representations are introduced before discussing calibration and verification.

2.1 A Brief History of Vector Network Analysis

When discussing the history of VNA technology it is important to start with the slotted line. The slotted line allowed for the measurement of the SWR (standing wave ratio) that resulted from an impedance mismatch. In this way, the slotted line is the radiofrequency (RF) equivalent of the impedance tube. The slotted line was used to measure many RF devices, including "power splitters", the measurements of which eventually became the basis for directional couplers. Directional couplers then enabled more advanced measurement. Directional couplers are covered in detail in section 2.2.

Using the properties of directional couplers, Rantec and Wiltron introduced various Phase/Gain/amplitude meters/receivers in the 1950s that covered the microwave frequency range. About this time s-parameters and the Smith chart were proposed as a design tool for microwave circuit design and engineering [1]. The impedance tube for acoustics was also developed shortly after this. Brüel and Kjær even suggested the use of the Smith chart for plotting acoustic reflection and transmission coefficients [41].

The Wiltron 310 introduced in 1965 was one of the first fully-fledged VNAs with a Smith chart display, and almost immediately after this error correction was proposed [42]. Hewlett Packard introduced the HP8410 analyser in 1967 and over the next 20 years, it was refined into the HP8510.

By the middle of the 1980s, the SOLT (Short, Open, Load, Thru) and TRL (Thru, Reflect, Line) calibrations had been proposed. And at this time the HP 8510 was introduced to the market as the first instrument with inbuilt error correction. The inbuilt error correction and digital signal processing made the HP8510 was a major milestone in creating VNA's that were more affordable and greatly improved usability [1].

By the 1990s VNA capability had been extended into the world of optics [43,44] and 'on-wafer' (Silicon wafer) measurement [45,46] with the added development of LR(R)M calibration techniques [47,48]. The further improvement of the TRL and development of TR(R)M (Thru, Reflect, (Reflect-Match), Match) calibration method greatly improved calibration accuracy at this time and with fewer physical standards than SOLT. Until this time error models were mostly used in a simplified form, either 8 or 12 error terms. Error models now had to be extended up to the full 16 error terms to account for all the possible systematic errors in 'on-wafer' measurement. Combined these improvements allowed for the world-changing and rapid growth of communication technologies in the coming decades.

"The Vector Network Analyzer (VNA) simplifies the network measurement process tremendously. It provides a direct reading of both magnitude

and phase, and has become a very basic tool in almost any microwave laboratory" [2].

2.2 Directional Couplers

A Directional Coupler is a 4-port network in which portions of the forward and reverse travelling waves on a transmission line are separately coupled to two of the ports [49]. Figure 2.1 shows a symbolic directional coupler. The coupled port receives a portion (typically in the order of 1 %) of the forward wave power that arrives at the input. The isolated port receives the same portion of the reverse wave power which is reflected at the output port. Examples of electromagnetic directional couplers can be seen if Figures 2.2 and 2.3, these are typical examples of coaxial ported and waveguide ported directional couplers respectively.

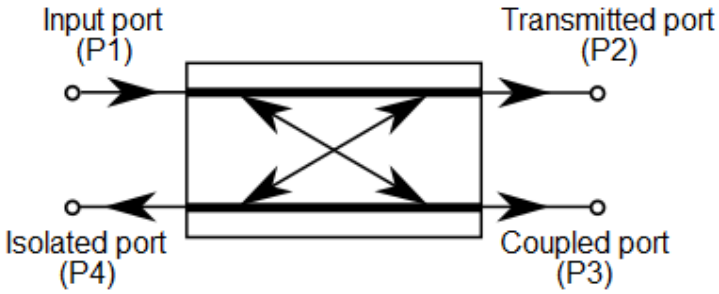

Figure 2.1: A symbolic Directional Coupler with labeled ports.

The directionality of a directional coupler is a measure of the isolation between the coupled and isolated ports i.e how much unwanted forward power arrives at the isolated port. Calibrations are used to measure and remove the error in a directional coupler, such as input signal present at the isolated port. A calibration algorithm will normally have some minimum directionality to work correctly. Typically a directionality of ≈ 8 dB is sufficient for calibration but higher values will perform better [49].

A directional coupler can be used to measure the reflection coefficient Γ. In a one-port network, the ratio of incident and reflected voltages (or currents)

Figure 2.2: An example of a 10 dB 1.7-–2.2 GHz directional coupler with N-type coaxial connections. Ports from left to right: input, coupled, isolated (terminated internally), and the transmitted port. Image credit:Vonvon CC BY-SA 3.0

is the reflection coefficient Γ, and in an electrical network is defined as:

$$\Gamma = \frac{V^-}{V^+}$$

where V^- and V^+ are the complex amplitudes of the reflected and incident wave respectively. Γ is related to impedance by the following relationship:

$$\Gamma = \frac{Z_L - Z_0}{Z_L + Z_0}$$

where, Z_L and Z_0, are the impedance of the load and source respectively. Since the reflected power is $|\Gamma|^2$ and the transmitted/absorbed power from the port is $1 - |\Gamma|^2$, the reflection coefficient Γ is also the scattering parameter S_{11} on one port.

The reflection coefficient Γ could be calculated by first using a slotted line to obtain the standing wave ratio (SWR) and the location of the first minima relative to the load. This is a multi-step process that requires manual adjustments for each frequency of interest [50, 51].

The reflection coefficient Γ can also be measured with a directional coupler. Since a directional coupler separates the forward and reflected waves, the

Figure 2.3: An example of a 10 dB, V-band (50–75 GHz), directional coupler with waveguide connections. Ports from left to right: Output, coupled, isolated (terminated internally), and input. This is a multi-hole type coupler. These are made with a series of holes along the length of waveguide with $\lambda/4$ separation, λ is typically the center frequency of the couplers usable range. Image: https://quinstar.com/shop/waveguides-related-products/couplers/directional-couplers/

magnitude and relative phase are immediately measured. Such a measurement system is shown in Figure 2.4. The ratio of 'coupled' and 'isolated' ports yields the reflection coefficient. This apparatus then does not require any adjustment with frequency, it, therefore, allows for swept frequency measurements. In this type of measurement, error arises from the port isolation. The port isolation is a measure of the amount of power that is present on the coupled port, that in an ideal coupler would be at the isolated port and vise-versa [52].

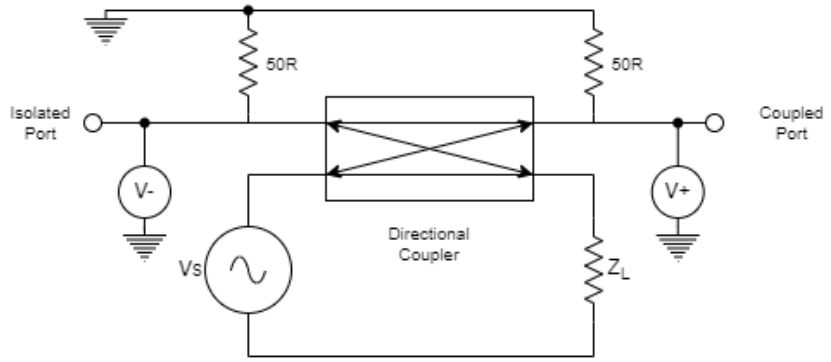

Figure 2.4: A simple one-port measurement system. 'one-port' systems measure an impedance function $Z = V/I$. The coupled and isolated ports are normally "matched" in coax systems, $50\,\Omega$ in this case, but, $75\,\Omega$ is also common in coax systems. The ratio of V^+ measured at the coupled port and V^- measured at the isolated port yields Γ and Z can then be calculated.

Directional couplers can be built in a variety of ways, the most common types are the coupled transmission line, branch-line, and multi-hole types. The waveguide directional coupler in Figure 2.3 is a multi-hole type coupler. A multi-hole coupler is made with holes spaced $\lambda/4$ of the mid-band frequency along the waveguide, this type of coupler relies on thin walls between sections of the waveguide. A branch-line coupler is similar to a multi-hole coupler in a sense. Branch-line couplers are the most relevant to this project since the acoustic coupler is of this type.

2.2.1 Branch-line Directional Couplers

A typical electromagnetic branch-line coupler is made up of two parallel transmission lines that are physically connected by several smaller transmission lines which are called branch lines. These so-called branch lines are typically $\lambda/4$ long and spaced at $\lambda/4$ where λ is the mid-band frequency. This structure can be created in coaxial cables and waveguides. A synthesis procedure for a symmetrical branch-line directional coupler is described by Levy and Lind in their 1968 paper 'Synthesis of Symmetrical Branch-Guide Directional Couplers' [53]. This procedure allows for the branch lines in a waveguide to be tuned, by changing lengths and spacing achieving 'Butterworth characteristics and almost exact Chebyshev equal-ripple characteristics' over bandwidths greater than an octave. These results led to the development of an acoustic branch-line directional coupler by Lagasse [54].

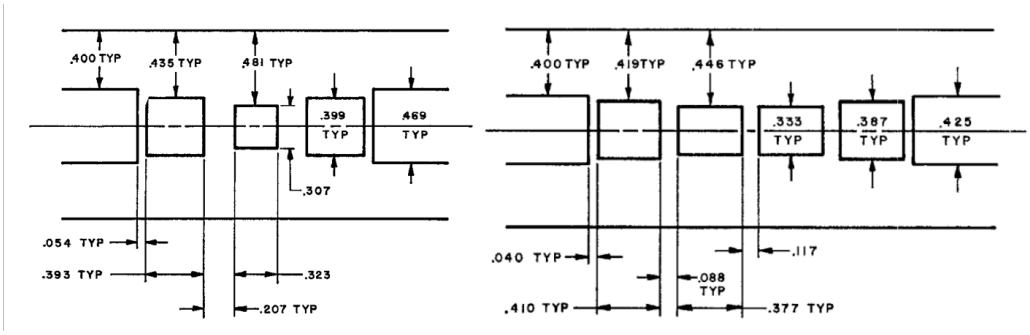

Figure 2.5: A 4-branch 6 dB Butterworth branch-line directional coupler (Left). A 5-branch 8 dB Chebyshev branch-line directional coupler (Right). Figure 10 and Figure 14 from [53] respectively. The structure shown is situated between two parallel sections of waveguide, the ends of which are the ports.

2.2.2 Acoustic Branch-line Directional Couplers

Any acoustic directional coupler has to have sufficiently stiff walls to closely approximate the Neumann sound hard boundary condition condition. At a sound hard boundary the impedance $Z_{boundary}$ approaches infinity since the sound velocity is $v = 0$. The sound hard boundary condition is therefore a

special case of an impedance boundary condition. Practically this requires the coupler itself to have thick walls which are "a non-negligible fraction of the wavelength" [54]. In their synthesis paper, Levy and Lind only consider transverse electromagnetic mode propagation (TEM), which is a reasonable assumption in the electromagnetic domain. In the acoustic case, longitudinal wave propagation means that waveguide discontinuity introduces higher-order nodes and significant reactance [54]. Lagasse built on the synthesis method with experiment to determine the general form of a branch-line acoustic directional coupler as seen in Figure 2.6 which is very similar to the Butterworth and Chebyshev synthesised couplers from [53] which can be seen in Figure 2.5.

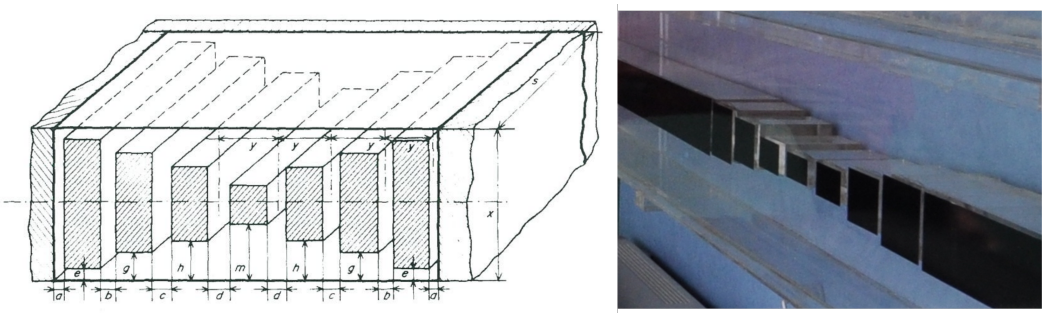

Figure 2.6: The general form of the acoustic branch-line structure that results in a directional coupler as described by Lagasse [54] (Left) and a physical implementation of the structure in acrylic (right). The branch-line structures shown sit between to parallel sections of waveguide. The 4 ports of the directional coupler are the openings at either end of these waveguide sections.

Lagasse designed an acoustic directional coupler with a 30 mm square waveguide and directivity better than 30 dB over an operational bandwidth of 2250–4250 Hz [54].

A version of the Lagasse design was built by K.Pennington and has been used as an acoustic impedance meter [55]. Pennington's coupler used a 60 mm square waveguide with a designed frequency range of 1–2 kHz and a usable range of 800–2,200 Hz. This design was scaled down by a factor of ten so that what was previously 1–2 kHz became 10–20 kHz [56]. Pennington's coupler branch-line structure can be seen in Figure 2.7 and a 3D model of the scaled branch-line structure can be seen in Figure 2.8.

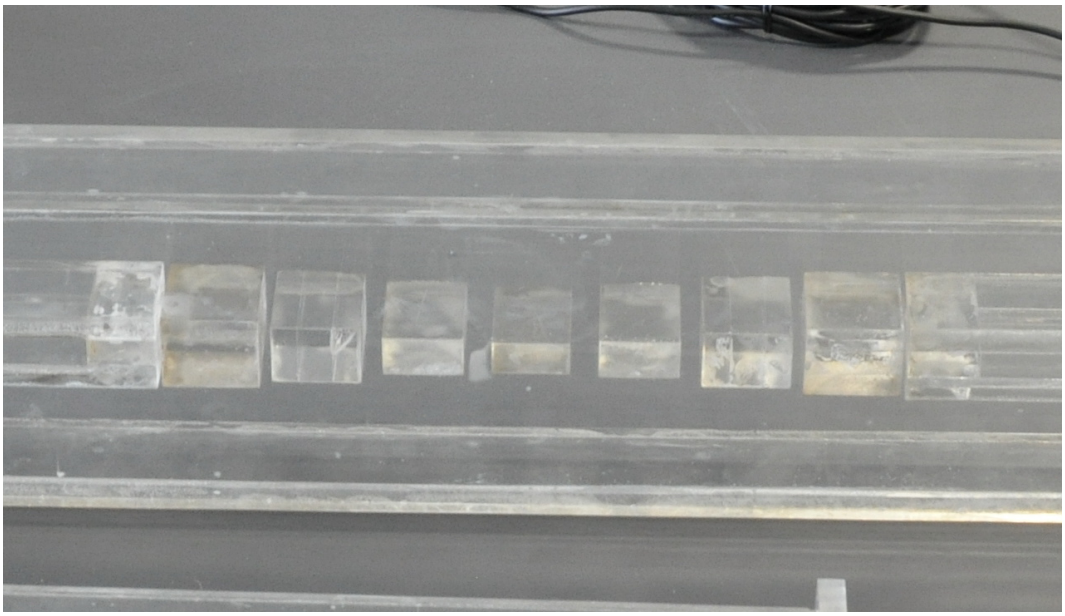

Figure 2.7: An 8-branch acoustic branch-line directional coupler as built by Pennington. The coupler is built out of acrylic sheet which shows the directional structure inside. Acrylic is easily bonded to form the structure and is sufficiently hard and rigid to approximate the boundary conditions.

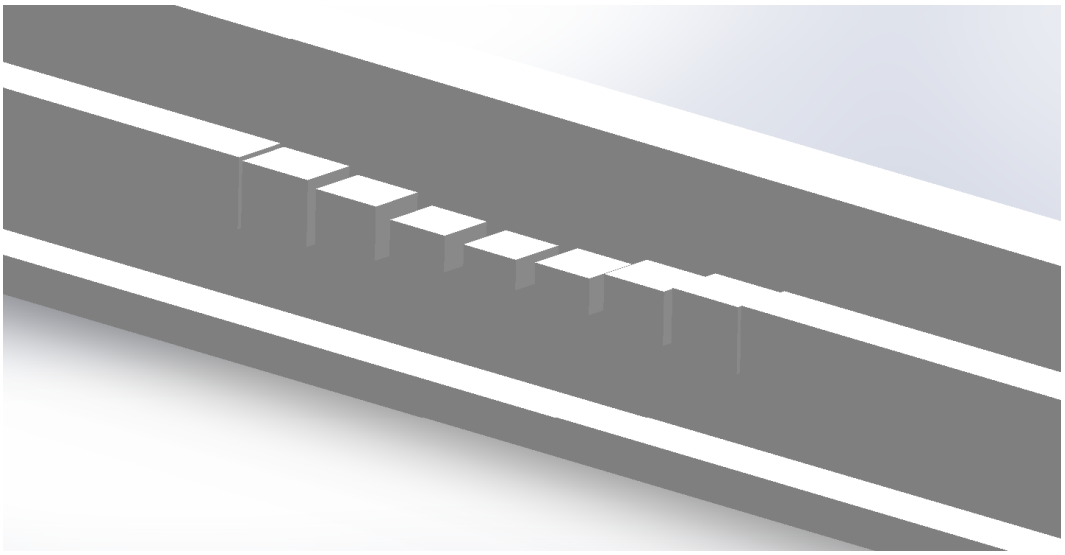

Figure 2.8: SolidWorks model for an 8-branch acoustic branch-line directional coupler scaled from Pennington's design to operate over a 10–20 kHz range.

2.3 S-parameters

Scattering parameters or S-parameters are used predominantly in radio frequency (RF) measurements because they are easier to measure than impedance directly at higher frequencies (>100 MHz) and when displayed on a Smith chart offer an easy to interpret visualisation of the system or Device Under Test (DUT). Measurement of the S-parameters for a DUT (with a two-port system) yields a set of four complex numbers that is a representation of the change in magnitude and phase of a test signal, these four numbers are S_{11}, S_{21}, S_{12}, and S_{22} which are the reflection and transmission coefficients measured from each port. This means that the S-parameters are related to impedance and offer an indirect measure of the DUT impedance.

In a multi-port network, there is a set of reflection and transmission coefficients for each port. A simple two-port measurement for some DUT is shown in Figure 2.9. In the case of such a two-port network, the reflection coefficients for each port can be measured in the same manner as in the one-port case. However, the transmission is now measured and the attenuation and phase change between ports can be calculated. This can be done because the second directional coupler again separates the travelling waves. The ratio of the "coupled" port of both directional couplers is the transmission coefficient.

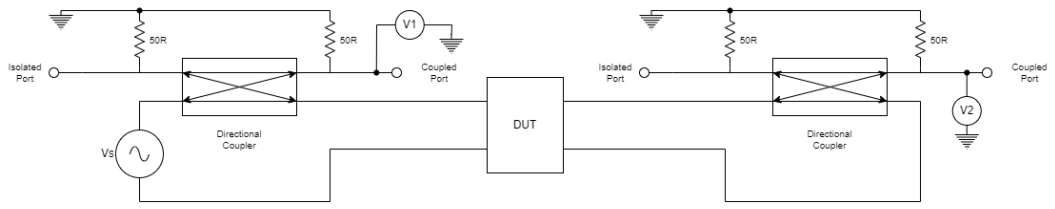

Figure 2.9: A simple two-port measurement system, showing the measurement of S_{21}. Two-port systems measure a transfer function $V2/V1$ or equivalently $I2/I1$. The voltage source is switched from one port to the other to effectively measure S_{11} and S_{21} and then S_{22} and S_{12}

The incident (a_i) and reflected (b_i) "power waves"[1] are

$$a_i = \frac{1}{2}k_i(V_i + Z_i I_i)$$

$$b_i = \frac{1}{2}k_i(V_i + Z_i{}^* I_i)$$

$$k_i = \sqrt{\Re Z_i}^{-1}$$

where i is the port number and $Z_i{}^*$ is the complex conjugate of Z_i, the impedance for port i [57].

The vectors $\mathbf{a}$ and $\mathbf{b}$ are then related by

$$\mathbf{b} = \mathbf{S}\mathbf{a}$$

or

$$\begin{bmatrix} b_1 \\ b_2 \end{bmatrix} = \begin{bmatrix} S_{11} & S_{12} \\ S_{21} & S_{22} \end{bmatrix} \begin{bmatrix} a_1 \\ a_2 \end{bmatrix}$$

Expanding the matrices into equations gives:

$$b_1 = S_{11}a_1 + S_{12}a_2$$

and

$$b_2 = S_{21}a_1 + S_{22}a_2$$

These are the relationships between the reflected and incident power waves in terms of the network's S-parameters, S_{11}, S_{21}, S_{12} and S_{22}. S_{11} and S_{22} are the reflection coefficients on port one and two respectively. S_{21} is the transmission coefficient to port two from port one, while S_{12} is the transmission coefficient to port one from port two.

[1] K. Kurokawa, proposed the use of "power waves" which contain both voltage and current terms to separate power flow into forward and reverse traveling components [57].

2.4 Smith Charts

The Smith chart is a graph-based method of visualising results and simplifying the complex mathematics (variables of the form $x + jy$) used to describe microwave components [58]. Computers now solve the problems the Smith chart was designed to solve but it remains a valuable tool. The Smith chart's graphical representation is used still in instrumentation and design-automation applications. These displays provide a quickly interpretable picture of the effect of changing a microwave network which allows for real time "tweaking" of a network to meet desired parameters.

The Smith chart is a special type of 2-D graph, similarly polar, semi-log and log-log scales are special 2-D graphs. The Smith chart is a bilinear transform which is a conformal mapping, meaning it preserves angles. Typically, the Smith chart is used to relate reflection coefficients to complex source, line, and load impedances. The Smith chart resides in the complex plane of reflection coefficient Γ [58,59]. Figure 2.10 shows the smith chart in its full context in the complex plane, with circles of constant (normalised) resistance shown in green and circles of constant (normalised) reactance in black. The outermost circle of the Smith chart corresponds to a reflection coefficient Γ of magnitude 1, and the centre point to magnitude 0. Because reflection-coefficient magnitudes must be 1 or less, regions outside this circle have no significance for passive physical systems. This is a great compression of information that allows us to visualize the entire space of realizable impedance values.

In Figure 2.10 lines representing a constant imaginary part of the impedances, Z_i are represented by circles centred along the blue vertical line. Real impedance components Z_r are represented by circles centred along the line Γ_r and tangent to the line $\Gamma_r = 1$. Those segments lying in the top half of the complex-impedance plane represent inductance and those lying in the bottom half represent capacitance.

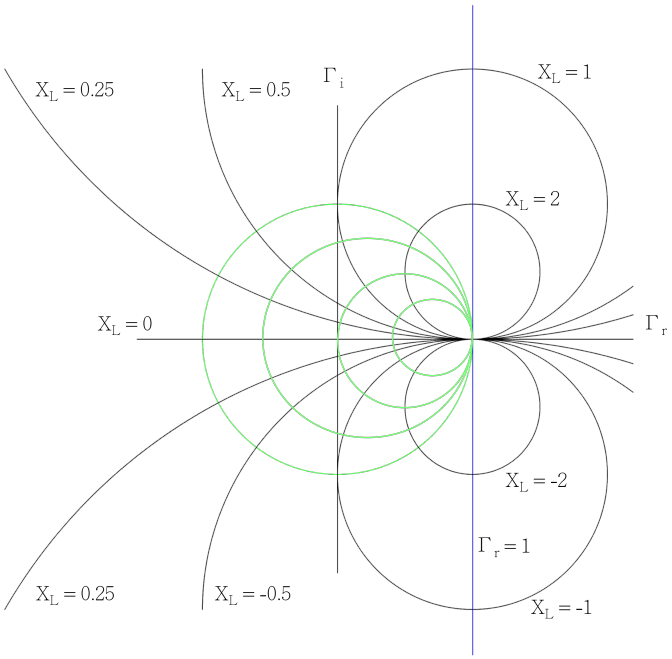

Figure 2.10: The Smith Chart in its full context of the complex reflection coefficient plane. This a reproduction from [58]. Circles of constant (normalised) resistance are shown in green and circles of constant (normalised) reactance are shown in black.

2.5 System Error Models, Flow Graphs and Calibration Techniques

2.5.1 Error Models

There are three types of measurement errors [60]:

1. Systematic errors
2. Random errors
3. Drift errors

Systematic errors are caused by imperfections in the test equipment, test setup, out of spec parts and even from sources outside of the measurement system. If these errors do not vary over time, they can be characterized through calibration and mathematically removed during the measurement process. The

Smith Chart

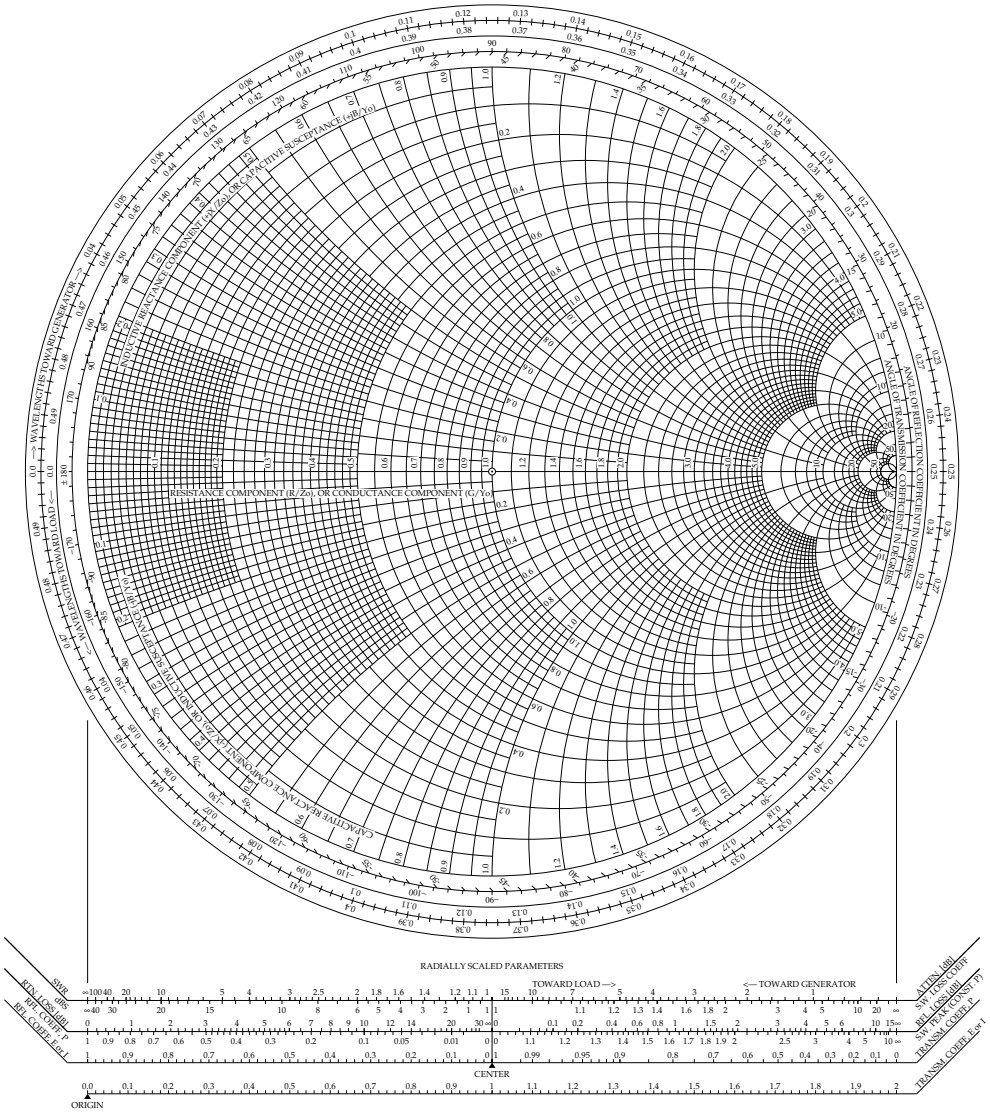

Figure 2.11: The Smith Chart as used for manual plotting, as is common for teaching. It is available readily in this form online. In this form impedances and admittances are normalised. There are three scales around this version of the smith chart, used to determine distances (in terms of λ) to and from the load/generator and the reflection/transmission coefficient phase. The scales at the bottom of the chart are used to determine VSWR, amplitudes of reflection/transmission coefficients, return loss, etc.

extent to which this is possible depends on the chosen calibration method and the initial performance of the hardware, set-up, and testing environment.

Systematic errors encountered in network measurements are usually related to signal leakage, signal reflections, and frequency response. These errors are caused by signal leakage from the system and around the DUT, impedance mismatches, and frequency response errors can be caused by reflection and transmission tracking within the test set receivers. These errors mostly arise from imperfections and design compromises in the directional coupler.

Random errors vary randomly as a function of time. Thermal noise is a typical source but also "shot" and "flicker" noise can be sources depending on application and at very high frequency (THz) and low temperatures quantum effects can also be significant sources [61, 62]. Since random errors are not predictable, they cannot be removed by calibration.

Drift errors occur when a test systems performance is changed after calibration is performed. They are primarily caused by temperature variation in RF systems. These drift errors can be removed by additional calibration. The rate of drift determines how frequently additional calibrations are needed [60]. With the proposed acoustic VNA relative humidity will be an important source of drift due to its impact on the speed of sound.

In the calibration process, a set of measurements is required to produce the set of equations required to solve for each term in the error model. These measurements are of known standards and are connected in such a way that the measurement is highly repeatable, or in other words, very highly precise. Without this repeatability, the calibration process would itself contribute a not-insignificant amount of error. As a result of this, as more measurements are required to solve the terms of the error model, higher mechanical tolerances in joints and connections can also be required.

To calibrate a traditional VNA there are several options available depending on bandwidth, technology (Wafer, coaxial cable, waveguide etc) and expected system leakage/performance of the Device Under Test (DUT). The error models for VNAs are typically described as either a matrix or signal flow graph and named simply after the number of error coefficients (terms) the

method solves for:

1. 16-term
2. 12-term
3. 8-term

2.5.2 Signal Flow Graphs

A signal flow graph (SFG) is a diagram used to represent the flow of energy in a Network. Flow graphs were developed by borrowing from graph theory [63,64]. Flow graphs then borrow the nomenclature from graph theory and are formed of nodes (points) connected by edges (lines). For example, a two-port DUT has four nodes and four edges. The edges for the DUT correspond to the S-parameters S_{11}, S_{21}, S_{12}, and S_{22}.

The relationship between these S-parameters and incident and reflected power waves is

$$\mathbf{b} = \mathbf{Sa}$$

where **a** and **b** are vectors whose elements are the incident and reflected waves respectively. The elements of vectors **a** and **b** are then the nodes of the flow graph.

Signal flow graphs are used to describe DUTs and VNA systems because they graphically detail the relationships between signals which would otherwise be described by (potentially large) matrices. Because of their ability to represent simply a network/system, it is useful to consider error models using flow graphs.

2.5.3 16 Term Error Model

If all possible sources of systemic error for a VNA are included the flow graph for the system becomes Figure 2.13.

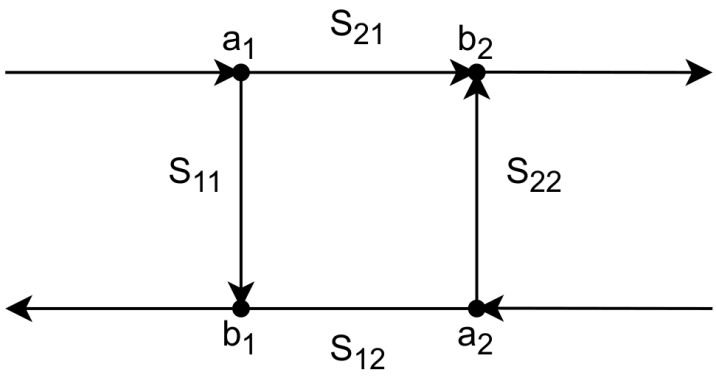

Figure 2.12: The signal flow graph for a two port DUT. The edges (S_{nm}) connect nodes (a_i, b_i) such that the S-parameters relate the incident and reflected power waves to one another.

Nodes a_0 and b_0 are the connections at port one and a_3 and b_3 are the connections at port two. The flow graph is broken into two parts, often called the forward and reverse error adapters or the X and Y error adapters. The error adapters contain the error terms which are labelled in the same manner as S-parameters. For example, e_{10} is the error that arises from attenuating the signal arriving at node a_1 from a_0.

The error terms if known can therefore be used to relate the measured values of a_0, b_0, a_3, and b_3 to the actual values of the DUT b_1, a_1, a_2 and b_2.

Both ports of the VNA have errors resulting from directivity, port matching, and transmission/reflection tracking. These are the main sources of error in a VNA system, shown in solid edges. Further errors arise from "leakage" or isolation, which is energy that is directly coupled from one port to another bypassing the DUT, these errors are shown as dashed edges. The resulting flow graph can also be expressed as a matrix equation, once the error terms are determined, the equation can be solved enabling error correction.

The error terms are as follows:

e_{00}, e_{33} : Directivity

e_{11}, e_{22} : Port Match

e_{10}, e_{23} : Transmission Tracking

e_{01}, e_{32} : Reflection Tracking

e_{30}, e_{03} : Primary Leakage

e_{02}, e_{31}, e_{13}, e_{20}, e_{21}, e_{12} : Secondary Leakage

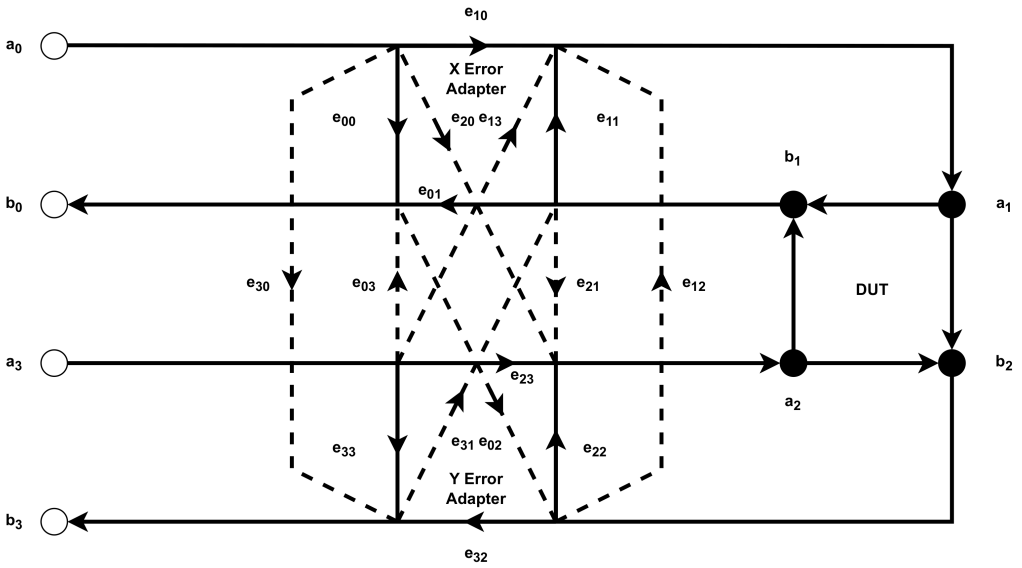

Figure 2.13: A flow graph of the 16 term error model

The complete network from 2.13 then can be expressed as a matrix E [65–67].

$$E \equiv \begin{bmatrix} E_1 & E_2 \\ E_3 & E_4 \end{bmatrix} = \left[\begin{array}{cc:cc} e_{00} & e_{03} & e_{01} & e_{02} \\ e_{30} & e_{33} & e_{31} & e_{32} \\ \hdashline e_{10} & e_{13} & e_{11} & e_{12} \\ e_{20} & e_{23} & e_{21} & e_{22} \end{array}\right] \tag{2.1}$$

The relationship between the measured S-parameters S_m and the actual S-parameters S_a is:

$$\begin{bmatrix} b_0 \\ b_3 \end{bmatrix} = S_m \begin{bmatrix} a_0 \\ a_3 \end{bmatrix}, \; S_m = \begin{bmatrix} S_{11m} & S_{12m} \\ S_{21m} & S_{22m} \end{bmatrix} \tag{2.2}$$

$$\begin{bmatrix} a_1 \\ a_2 \end{bmatrix} = S_a \begin{bmatrix} b_1 \\ b_2 \end{bmatrix}, \; S_a = \begin{bmatrix} S_{11a} & S_{12a} \\ S_{21a} & S_{22a} \end{bmatrix} \tag{2.3}$$

$$S_m = E_1 + E_2 S_a (I - E_4 S_a)^{-1} E_3 \tag{2.4}$$

where I is the unit matrix. Solving for S_a yields

$$S_a = [E_3 (S_m - E_1)^{-1} E_2 + E_4]^{-1}. \tag{2.5}$$

The 16-term is used in applications like on-wafer measurement and where the assumption of negligible leakage is not possible. The 16-term model is the primary error model explored in this thesis because it is expected that the acoustic analyser will be a 'leaky' system. All of the aforementioned error models have a matrix representation that relates the 'raw' S-parameters to 'calibrated' S-parameters, otherwise called the 'measured' and 'actual' S-parameters.

2.5.4 12 Term Error Model

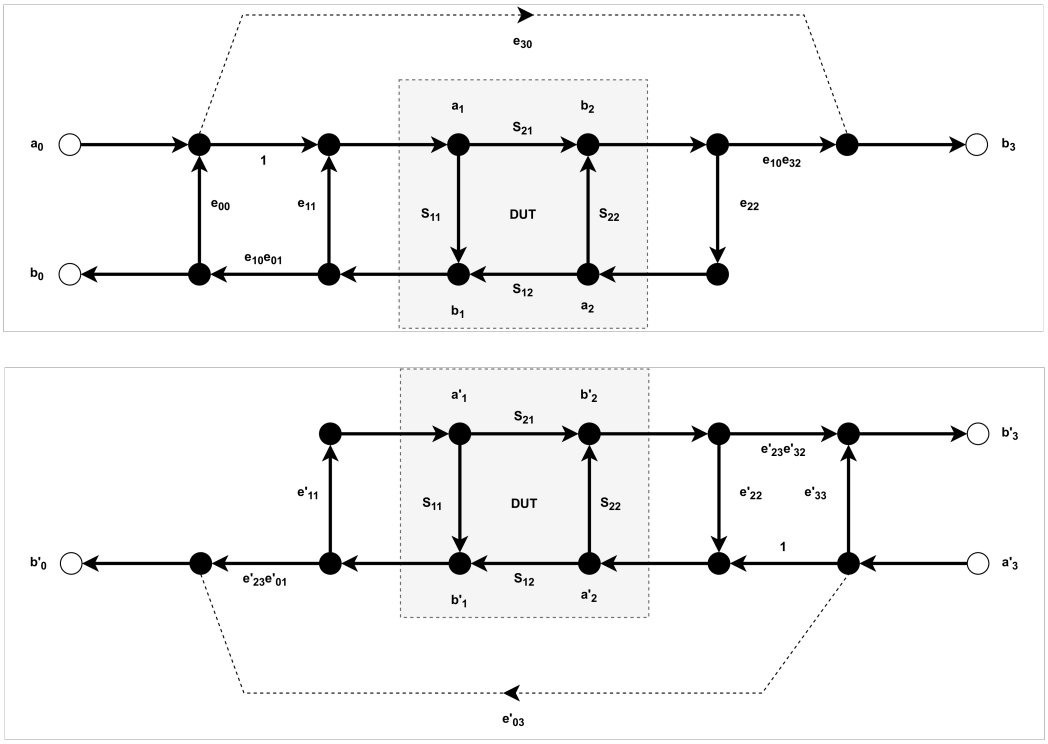

Figure 2.14: The forward (top) and reverse (bottom) signal flow graphs for the 12 term model.

The 12-term model was one of the first error models created and is often used where the two primary isolation/leakage terms cannot be treated as being negligible [65, 66]. The 12-term model is broken into two parts, a forward model and a reverse model. The forward model represents the system for measurements of S_{11} and S_{21} and the reverse model represents the system for measurements of S_{12} and S_{22}.

A common method of solving the 12-term error model is the SOLT calibration method [65] which is as follows. The relationship between the measured and actual S-parameters for the forward model is:

$$\Delta_S = S_{11}S_{22} - S_{21}S_{12} \tag{2.6}$$

$$S_{11M} = \frac{b_0}{a_0} = e_{00} + (e_{10}e_{01})\frac{S_{11} - e_{22}\Delta_S}{1 - e_{11}S_{11} - e_{22}S_{22} + e_{11}e_{22}\Delta_S} \tag{2.7}$$

$$S_{21M} = \frac{b_3}{a_0} = e_{30} + (e_{10}e_{32})\frac{S_{21}}{1 - e_{11}S_{11} - e_{22}S_{22} + e_{11}e_{22}\Delta_S} \tag{2.8}$$

The relationship between the measured and actual S-parameters for the reverse model is:

$$S_{22M} = \frac{b'_3}{a'_3} = e'_{33} + (e'_{23}e'_{32})\frac{S_{22} - e'_{11}\Delta_S}{1 - e'_{11}S_{11} - e'_{22}S_{22} + e'_{11}e'_{22}\Delta_S} \tag{2.9}$$

$$S_{12M} = \frac{b'_0}{a'_3} = e'_{03} + (e'_{23}e'_{01})\frac{S_{12}}{1 - e'_{11}S_{11} - e'_{22}S_{22} + e'_{11}e'_{22}\Delta_S} \tag{2.10}$$

The 12 error terms can be determined by using three known one-port standards and a thru connection. The three known standards produce the following set of independent equations

$$e_{00} + S_{11a1}\Delta_e + e_{11}S_{11a1}S_{11m1} - S_{11m1} = 0 \tag{2.11}$$

$$e_{00} + S_{11a2}\Delta_e + e_{11}S_{11a2}S_{11m2} - S_{11m2} = 0 \tag{2.12}$$

$$e_{00} + S_{11a3}\Delta_e + e_{11}S_{11a3}S_{11m3} - S_{11m3} = 0 \tag{2.13}$$

where $\Delta_e = e_{00}e_{11} - (e_{10}e_{01})$

which can be can be solved for e_{00}, e_{11}, and $e_{10}e_{01}$.

With matched loads on both ports, the isolation term is measured directly.

$$S_{21m} = e_{30} \tag{2.14}$$

The Thru connection reduces equation 2.7 to

$$S_{11m} = \frac{b_0}{a_0} = e_{00} + (e_{10}e_{01})\frac{e_{22}}{1 - e_{11}e_{22}} \tag{2.15}$$

and equation 2.8 becomes

$$S_{21m} = \frac{b_3}{a_0} = e_{30} + (e_{10}e_{32})\frac{1}{1 - e_{11}e_{22}} \tag{2.16}$$

which can be solved for e_{22} and $e_{10}e_{32}$. These are the 6 error terms of the forward model, the same procedure can be followed for the reverse model.

2.5.5 8 Term Error Model

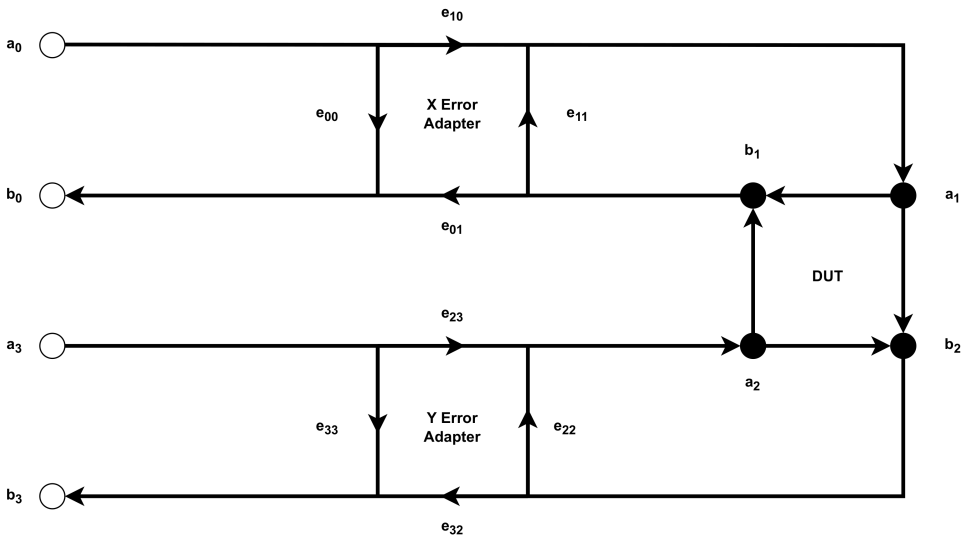

Figure 2.15: A flow graph of the 8 term error model

Figure 2.15 shows the flow graph for the 8-term model. The flow graph shows all of the non-leakage energy paths between the two ports of the analyser.

Removing the leakage error terms, the 8-term error model can also be expressed as a matrix E [66]

$$\begin{bmatrix} b_0 \\ b_3 \\ b_1 \\ b_2 \end{bmatrix} = E \begin{bmatrix} a_0 \\ a_3 \\ a_1 \\ a_2 \end{bmatrix} \tag{2.17}$$

$$E \equiv \begin{bmatrix} E_1 & E_2 \\ E_3 & E_4 \end{bmatrix} = \left[\begin{array}{cc:cc} e_{00} & 0 & e_{01} & 0 \\ 0 & e_{33} & 0 & e_{32} \\ \hdashline e_{10} & 0 & e_{11} & 0 \\ 0 & e_{23} & 0 & e_{22} \end{array}\right]. \tag{2.18}$$

The relationship between the measured S-parameters S_m and the actual S-parameters S_a is:

$$\begin{bmatrix} b_0 \\ b_3 \end{bmatrix} = S_m \begin{bmatrix} a_0 \\ a_3 \end{bmatrix}, \; S_m = \begin{bmatrix} S_{11m} & S_{12m} \\ S_{21m} & S_{22m} \end{bmatrix} \tag{2.19}$$

$$\begin{bmatrix} a_1 \\ a_2 \end{bmatrix} = S_a \begin{bmatrix} b_1 \\ b_2 \end{bmatrix}, \; S_a = \begin{bmatrix} S_{11a} & S_{12a} \\ S_{21a} & S_{22a} \end{bmatrix} \tag{2.20}$$

$$S_m = E_1 + E_2 S_a (I - E_4 S_a)^{-1} E_3 \tag{2.21}$$

Where I is the unit matrix. Solving for S_a yields

$$S_a = [E_3 (S_m - E_1)^{-1} E_2 + E_4]^{-1} \tag{2.22}$$

Equation 4.13 is the result that is used to de-embed the actual S-parameters from the measured S-parameters.

The 8-term model is commonly used. It achieves this simplified model by assuming that isolation/leakage terms are zero. The 8-term model can make this assumption and still be effective in many applications because leakage is often negligibly small. In applications where the primary leakage is potentially an issue, it can be added to the model with an additional measurement of matched ports.

2.5.6 Calibration Techniques and Standards

The error models that have been introduced can usually be solved for the error terms in several ways. The reason for this is that there are sets of "knowns" or standards that can be measured to produce the required information to then solve for the error terms. This wasn't always the case, in the early development of VNA technology there were only a few accurately known standards and even making these was a large hurdle to overcome.

These "knowns" were initially created by making things that are often assumed to be ideal, as ideal as possible. A good example is a short circuit, an ideal short circuit produces a perfect reflection that is 180° out of phase with the incident signal. These were initially made with large lumps of very

conductive materials like silver [68]. Another example is the Line, a "known" transmission line. A transmission line is ideally lossless and has a phase change related to its length. These could be made by taking precise lengths of waveguide lined with silver to produce as close to lossless transmission lines with a "known" phase change [68].

Typically there are several sets of standards that can be measured to solve the error model. The selection process for the standards for a calibration algorithm has to consider what is physically possible and what is required to achieve a solution mathematically.

Measurement of any one standard produces a set of four equations. To solve an error model, you need independent equations equal to the number of error coefficients. The sets of equations produced by standards are not necessarily independent, however. For example, a popular solution for the 8-term error model is TRM (Thru, Reflect, Match), this overall produces a set of twelve equations. This makes the matrix overdetermined. If we ignore or simply do not measure the information that is duplicated we can solve for the error coefficients analytically. Another approach may be to use numerical methods. An overdetermined matrix lends itself to being solved numerically via methods like Single Value Decomposition (SVD) [65–67, 69, 70].

2.5.7 The Sliding Load & Circle Fitting Method

The sliding load has been used and is of particular interest to this research. A sliding load is used to separate the magnitude of any residual reflection due to the imperfections of a practical load. The magnitude of any fixed reflection from the actual load is assumed not to change with the position of the absorber. The reflection from the load can be separated from other reflections in the system by sliding the load and using the resulting phase change. In the electromagnetic case, the magnitude of the reflection from the load does not change with position, but the phase does. In the acoustic case, some attenuation of the reflection is expected with increased distance to the

absorber.

The magnitudes of the system reflection and the load are added vectorially, as the phase of the load magnitude changes the resulting vector changes. As the load element is moved, its reflection vector rotates in a circle about the system reflection vector [71]. A perfect system would have no reflection vector, and therefore the centre of the circle produced by measurements of an imperfect sliding load would be the centre of the Smith chart. Practically, the offset of the circle centre from the centre of the Smith chart reveals the system reflection vector. An example of a coaxial sliding load can be seen in Figure 2.16.

Figure 2.16: An example of a sliding load from Agilent technologies, 00915–60004 2.4 mm sliding load. Image credit: A13ean. This file is licensed under the Creative Commons Attribution-Share Alike 3.0 Unported license. https://creativecommons.org/licenses/by-sa/3.0/deed.en

2.5.8 The Acoustic Sliding Load

The acoustic sliding load was used by Pennington to create a calibrated acoustic reflectometer [11, 55]. An absorber material was selected using empirical measurements of several absorbent foams shaped into a wedge. The selected foam wedge was then placed in a length of impedance tube for it to slide along. Ideally, the sliding load is assumed to stay constant as the foam wedge is moved down the impedance tube and only the phase changes. In this ideal case the acoustic sliding load results in the same circle produced in the RF case. Practically, their is also attenuation from the required transmission line. The attenuation of the transmission line reduces the reflection coefficient of the load and transforms the circle into a spiral [11]. Pennington used a sliding short to exaggerate the spiral effect, enabling the measurement of the attenu-

ation from the impedance tube at different displacements. It was found that the Taubin numerical circle fit method was a good approximation to the spiral produced by a sliding acoustic load [11,72]. The Taubin method was developed to estimate planar curves, surfaces and non-planar space curves. The method estimates and then minimises the mean square distance from the fitted curve to the data points [72]. The Taubin method provides a good performance circle fit when compared against other methods [73].

2.5.9 Calibration Verification

Calibrations of VNAs are usually verified by measurements of verification standards, these standards are characterized and traceable. Typically, users calibrate their VNA, measure the S-parameters of the verification standard and then they compare their measurements to traceable measurements of the same standard. Users can also compare their measurement uncertainties with those of traceable measurements. The traceable measurements are usually performed by instrument manufacturers or standards institute [74,75]. The typical source of traceability for VNA measurements is an impedance standard, but some techniques also use the reciprocity of a device as well as the impedance standard [76]. A passive, asymmetrical, reciprocal device (PARD) was used to optimize Short, Open, Line, Thru (SOLT) calibrations for the 12-term error model [76]. The same principles can be adapted to build an acoustic PARD which can partly verify the calibration of the AVNA.

An asymmetrical, reciprocal device has the following characteristics: $S_{12} = S_{21}$ and $S_{11} \neq S_{22}$ [76]. If such an asymmetrical device's orientation is reversed and it is then measured again, swapped-around S-parameters S'_{11}, S'_{12}, S'_{21}, and S'_{22} are obtained. Then if $S'_{11} = S_{22}$, $S'_{22} = S_{11}$, $S'_{12} = S_{21}$, and $S'_{21} = S_{12}$ the calibration has successfully accounted for the error adapters on both ports. An acoustic asymmetrical device was made by folding some light gauge sheet metal into a "V" shape and filling the "V" shape with foam. Sides were added that extend past the "V" shape. This is so that it can be placed in the waveguide

and rest on the bottom surface. This structure was created using a guess and check method and when placed in the waveguide provide the characteristics of a PARD since it is passive, asymmetrical due to the “V” structure and is reciprocal since it can be flipped and measured in both orientations.

Chapter 3

Hardware Design & Implementation

In this chapter, directional couplers, their construction, operation, and the performance of the flange design is presented. The remaining hardware including power supplies, amplifiers and modifications to an existing VNA test set are also presented.

Figure 3.1 shows an Agilent performance VNA (Often shortened to PNA) system with external "heads" which contain external hardware like couplers, amplifiers, receivers etc. The bandwidth of the "heads" is normally limited by that of the waveguide hardware internal to the "head". "Heads" are commonly used in conjunction with analysers that have broadband capability, this particular analyser has a range of 10 MHz–67 GHz. The implemented acoustic analyser is similar to this configuration in that it has external heads, amplifiers etc. A block diagram of the acoustic vector network analyser is shown in figure 3.2.

3.1 Acoustic Waveguide Hardware

The acoustic waveguide hardware for this research is divided into two target bands. The first band is 1–2 kHz, and the second is 10–20 kHz, these bandwidths were chosen because there was already some existing directional coupler

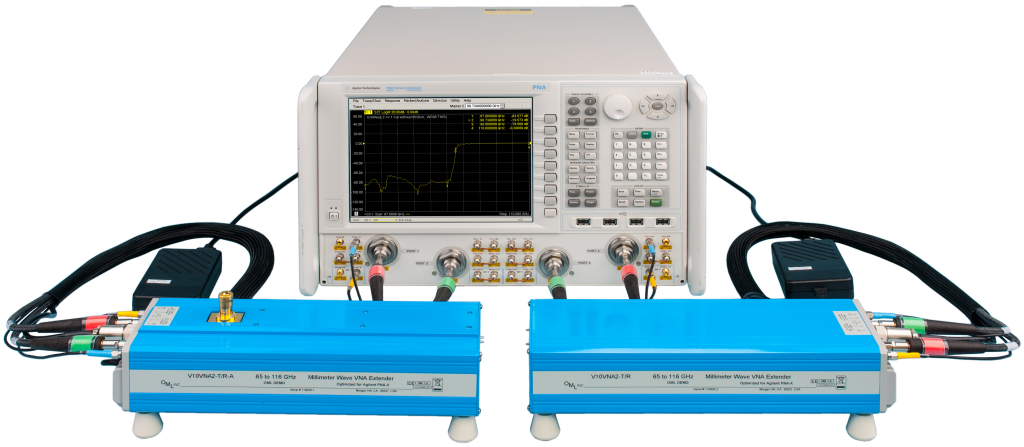

Figure 3.1: An example of a VNA with coupler heads. The heads are the blue boxes, these contain external hardware like couplers, amplifiers, etc. Outboard heads like these are used frequently to interface an analyser with waveguide or 'on-wafer' probing systems.

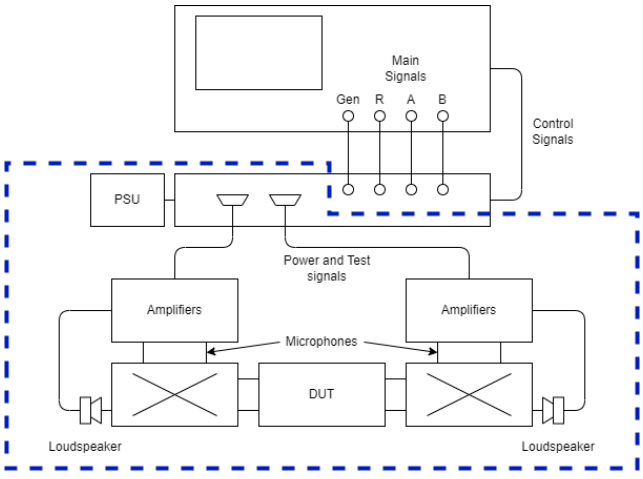

Figure 3.2: A block diagram for the acoustic vector network analyser, including, analyser (HP4395A), test-set (modified HP87511A), power supply unit (PSU), amplifiers, analyser connections, couplers, and device under test (DUT). Each block inside of the blue dashed line was developed/built for this research.

hardware in these sizes. In both bandwidths, there are directional couplers, calibration standards and waveguides. All of the waveguide hardware needs to be able to be connected and disconnected to function as part of the network analyser. Connections in electronics at low frequency are often paid little attention, but at high frequency and in waveguide systems in particular these connections are critical to the repeatability, precision and reliability of equipment.

Microwave waveguide is typically machined from brass and has a rectangular cross-section and mounting flanges for each port. There are several standards for microwave flange construction and testing such as IEC 60154-1:2016, and IEC 60154-2:2016 [77, 78]. The EIA and IEC standards can be seen in Figure 3.3, a mechanical drawing for a commercially available WR-22 can be seen in Figure 3.4.

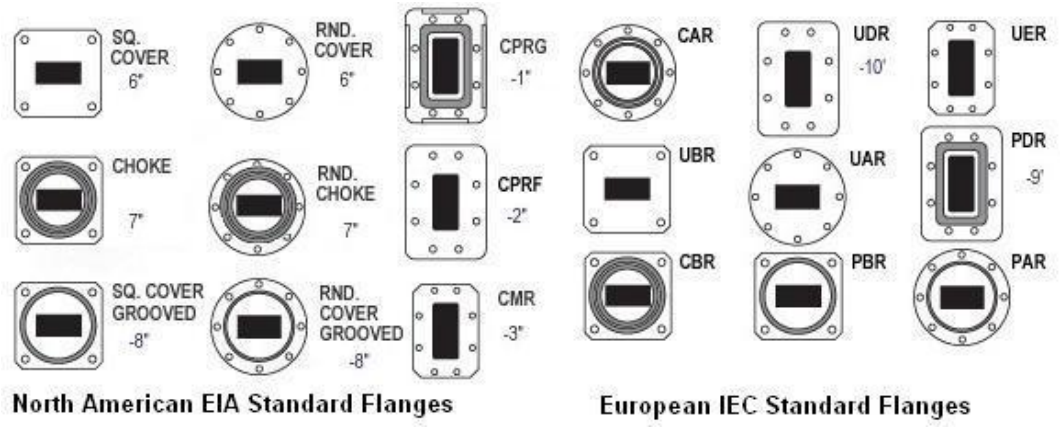

Figure 3.3: EIA and IEC standard Microwave Waveguide flanges. Choke flanges are shown, made with a "gap" (quarter-wave transformer) and "ditch" (resonant short-circuit stub). Choke flanges are intended to mate with a cover/gasket flange to reduce arcing while not obstructing surface currents in RF waveguide applications. Choke flanges were not considered for acoustic applications. https://www.microwave-link.com/microwave/microwave-waveguide-flange/

Microwave waveguide is often pressurised stopping the ingress of dust and moisture. For these applications, the waveguide needs to seal, as such O-rings can feature in microwave waveguide flange systems [79]. Another common

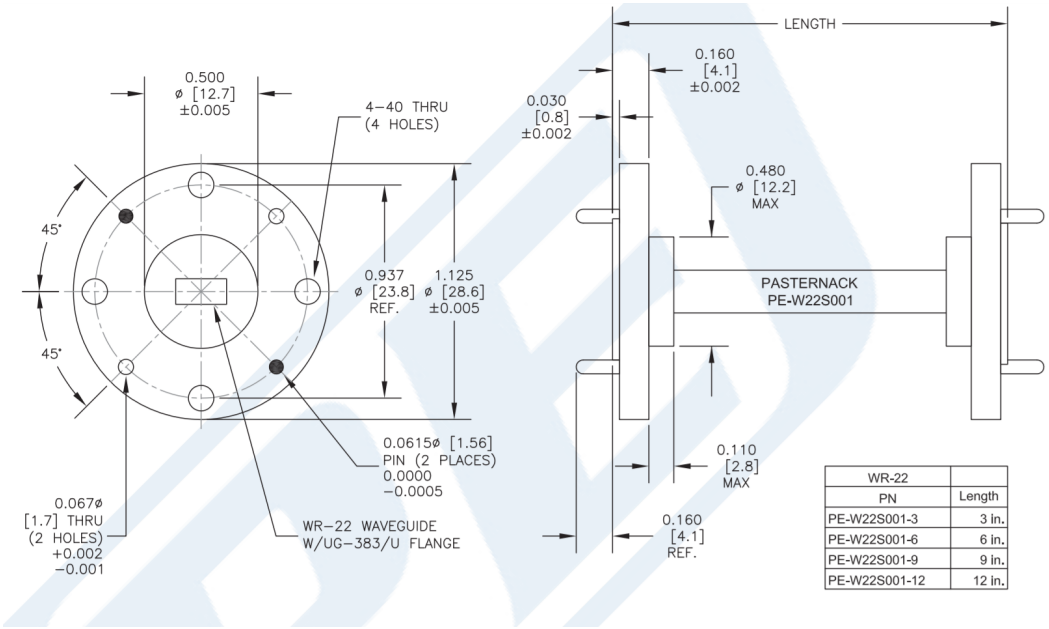

Figure 3.4: WR-22 mechanical specifications taken from the datasheet for a pasternack PE-W22S001-12. Dimmensions are in inches and [mm]. https://www.pasternack.com/wr-22-straight-waveguide-section-ug-383-33-50-ghz-pe-w22s001-12-p.aspx

feature of microwave waveguide is alignment pins that allow for the precision mating of any two flanges and specific bolt tightening patterns with specific torque requirements [80–84]. These alignment pins feature in Figure 3.4.

When a standard is connected for measurement, any variation in the connection will result in uncertainty that in turn can add to the uncertainty in the calibration. The repeatability of the waveguide connections then is critical to the performance of any vector network analyser. Previous acoustic couplers [55] feature a set of 4 threaded holes for the connection of DUT/standards with an option for a gasket. A new flange system was developed, borrowing from microwave waveguide systems to include alignment pins, specific bolt patterns and torque requirements for repeatable and precise connections.

By borrowing from these standard microwave waveguide features, the flanges for the acoustic coupler were developed with experiment and consultation with the university workshop. Since leakage has been identified as an issue with acoustic systems, the O-ring feature was adapted to the acoustic waveguide to prevent signal leakage. But also, there is no reason that you could not use the

analyser at varying pressures or with another gas/liquid. The alignment pins increase the ease of assembly by preventing lateral offsets between the flange faces during assembly. Because of the materials used and forces involved the 10–20 kHz flange system also features a U-shaped washer to distribute the fastening force across the whole flange. Figures 3.5 and 3.6 show the final designs for the small (10–20 kHz) and large (1–2 kHz) waveguide systems respectively.

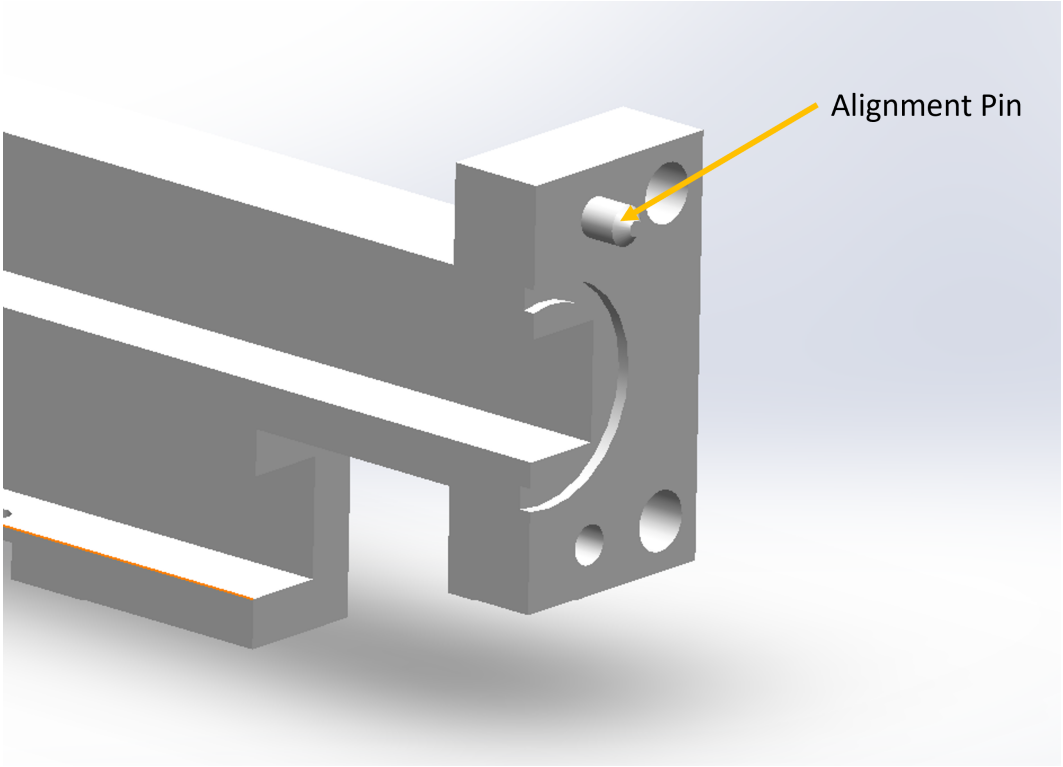

Figure 3.5: A cross-section of the flange designed for the scaled and 3D printed directional couplers. This flange features an O-ring groove and alignment pins.

The performance of the acoustic waveguide flanges is studied using statistical methods. This is done by taking several measurements of the same DUT and disconnecting the DUT in between each measurement. It is then possible to determine the standard deviation in these measurements and then use this value as an indicator of the repeatability of the joint.

Before measuring the repeatability of the joint it is important to establish a baseline for the rest of the system. This is done by collecting several measurements of a Thru without disconnecting the couplers. This reveals the standard deviation expected between sweeps in a best-case scenario where the

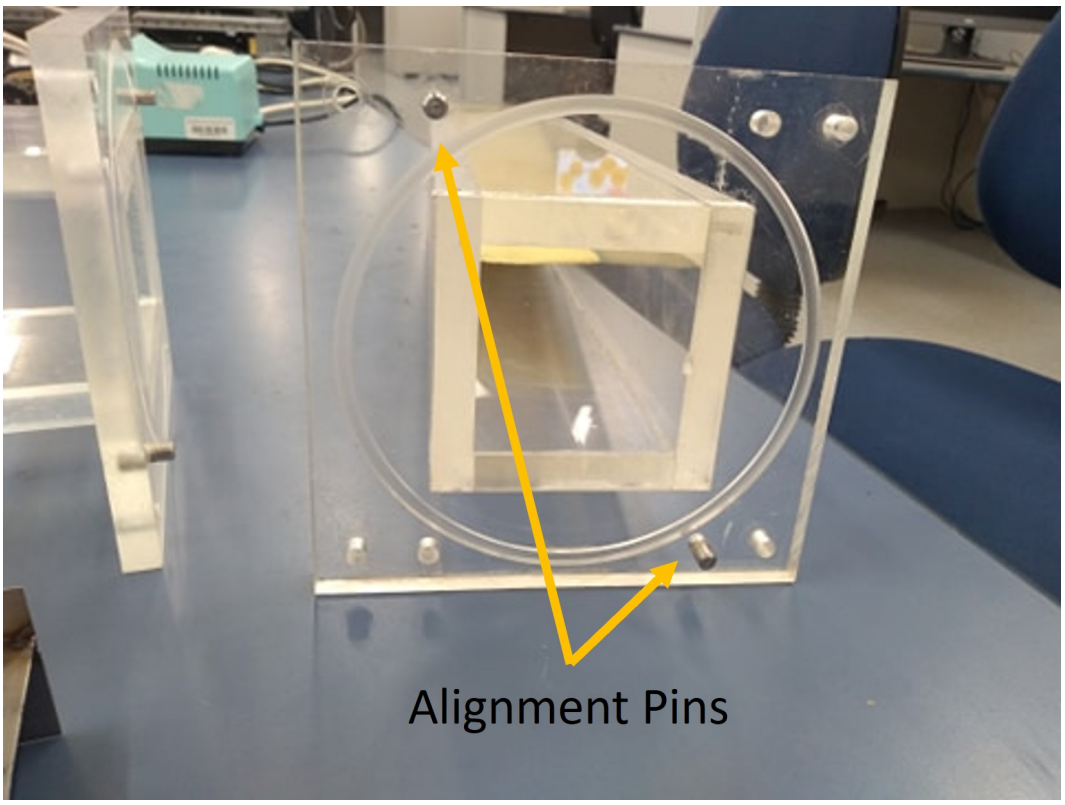

Figure 3.6: An example of the larger acoustic waveguide with flanges and alignment pins visible.

apparatus remains fixed. This also indicates the random noise in the system.

Standard deviation (s) is defined as $s = \sqrt{\frac{1}{N-1}\sum_{i=1}^{N}(x_i - \overline{x})^2}$ and retains the same units as the input sample data. Standard deviation is closely related to variance (s^2) and is defined as $s^2 = \dfrac{\Sigma(x_i - \overline{x})^2}{n-1}$.

A pair of the 10–20 kHz couplers were fabricated using a resin 3D printer [56]. These couplers were used to assess the designed flange system. Figure 3.7 shows the results of two sweeps of a static Thru, Figure 3.8 shows the standard deviation for the full set of measurements with a static DUT. With this baseline now established it is possible to assess the performance of the flange system. Figure 3.9 shows the repeatability that was obtained with the repeated connection of the 3D printed resin guide. This suggests that an overall average uncertainty of about 0.2 dB is to be expected across most measurements. The standard deviation at some frequencies is increased to approximately 0.4 dB, which is much larger than the uncertainty from the baseline Thru measure-

ments.

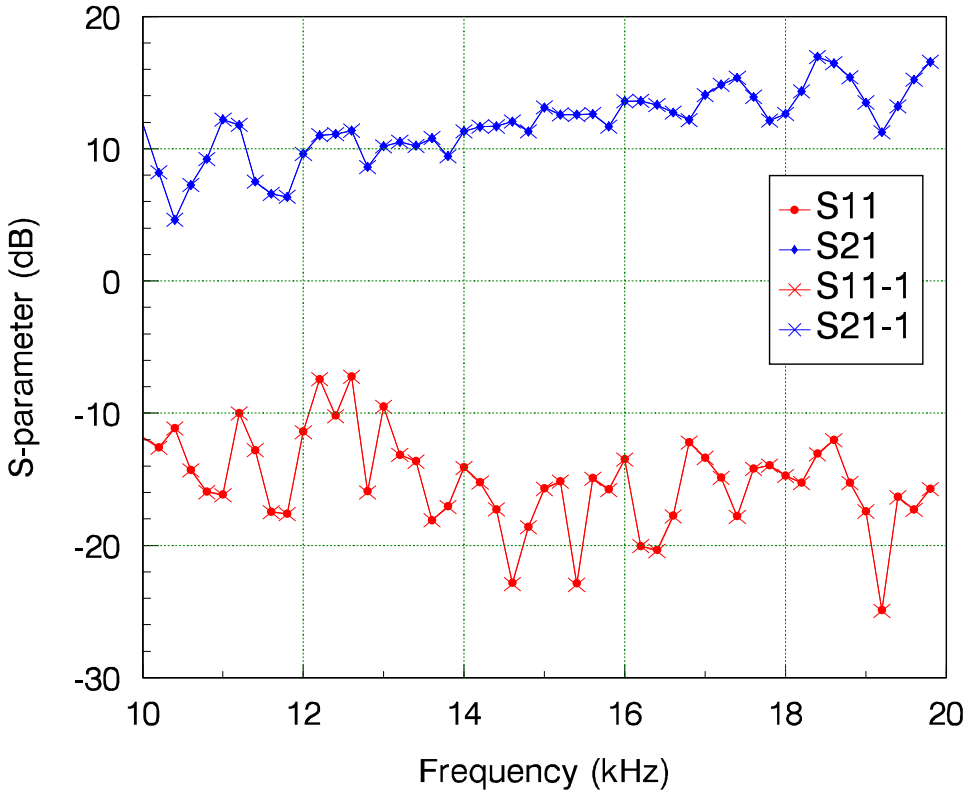

Figure 3.7: Raw magnitude (dB) data from a two measurements (a sub-set of the ten total measurements) of S_{11} and S_{21} for a static THRU. The flanges were resin, the joints fitted with O-rings and U-shaped washers to distribute force. Bolt torque was 0.5 N m.

To demonstrate bolt order is important a set of measurements with variable bolt order were performed. Figure 3.10 shows the raw data for S_{21} for a set of measurements performed where the flanges are assembled with a random bolt order. The variation in the raw data is immediately obvious and there is no need to plot the standard deviation. Clearly assembly procedure including bolt fastening order matters.

To select a bolt fastening order, a sample of ten measurements was taken in the 1–2 kHz waveguide system for each tested bolt pattern. The patterns were, rotational (clockwise), a zig-zag pattern (top bolts, followed by bottom bolts) or a “Star” Pattern (one corner, then its opposite corner, then the other

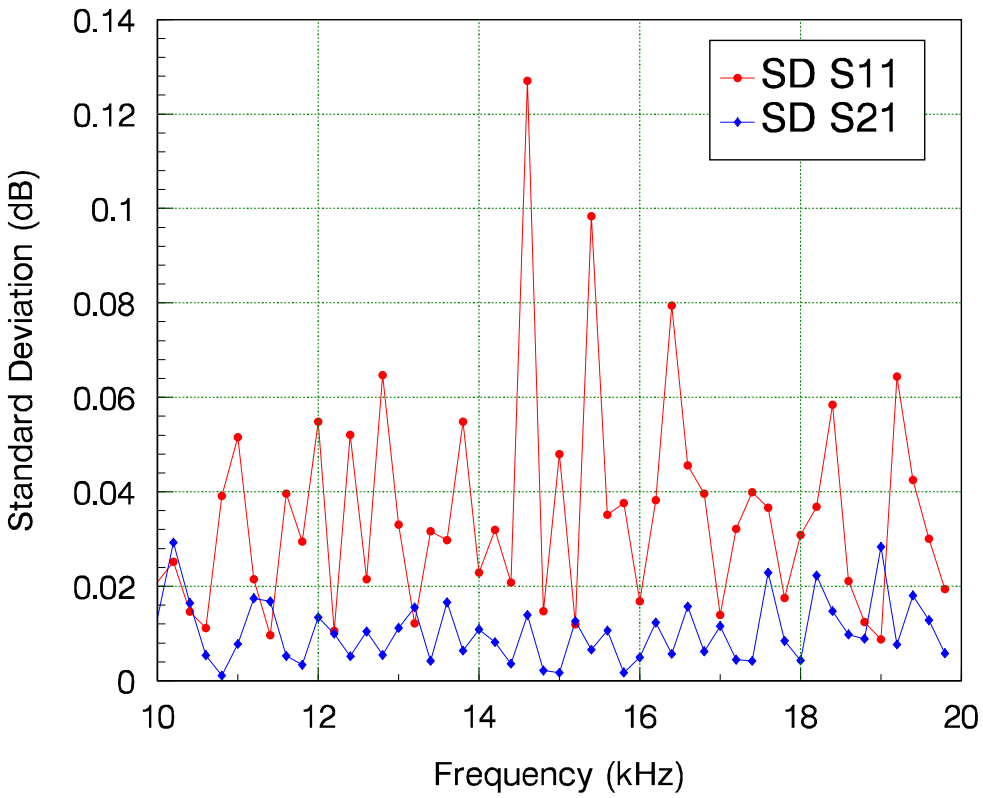

Figure 3.8: Standard Deviation (dB) for ten measurements of S_{11} and S_{21} for a static THRU. The flanges were resin, the joints fitted with O-rings and U-shaped washers to distribute force. Bolt torque was 0.5 N m.

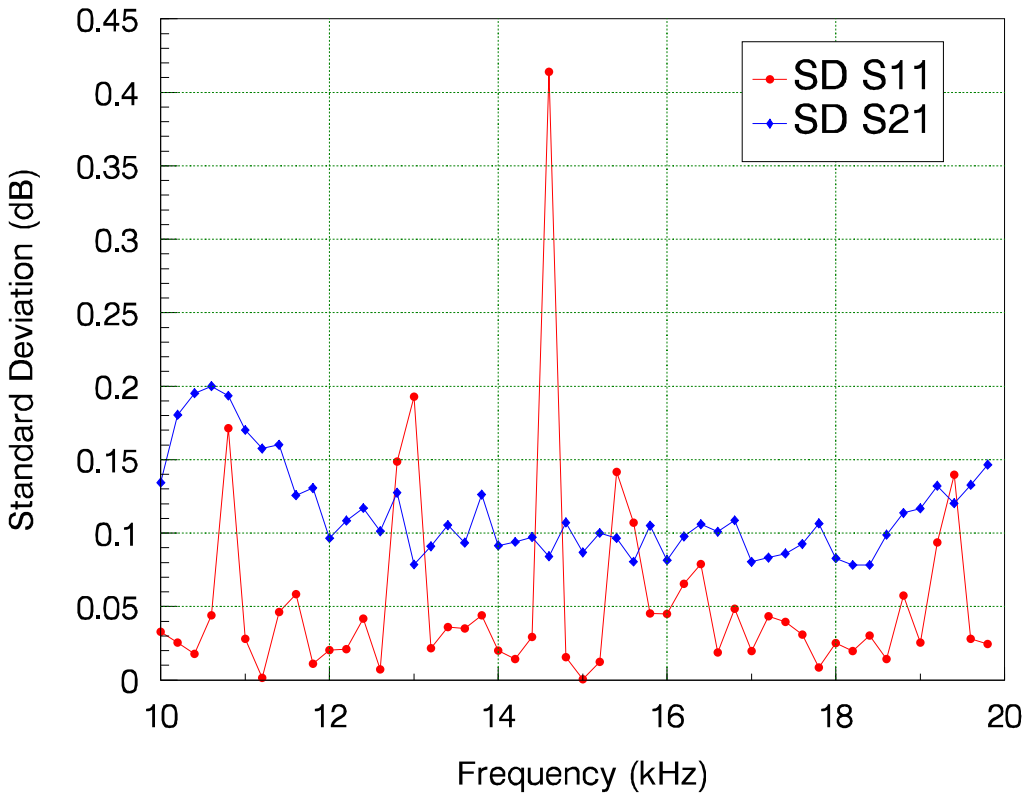

Figure 3.9: Standard Deviation (dB) for ten measurements of S_{11} and S_{21} obtained at each measurement frequency when the joint was disassembled and reassembled. The flanges were resin, the joints fitted with O-rings and U-shaped washers to distribute force. Bolt fastening order was consistent and bolt torque was 0.5 N m.

corners). The results from this experiment can be seen in Figure 3.11, these results showed that a "star" pattern as shown in Figure 3.12 was the optimal bolt order for fastening the flanges together.

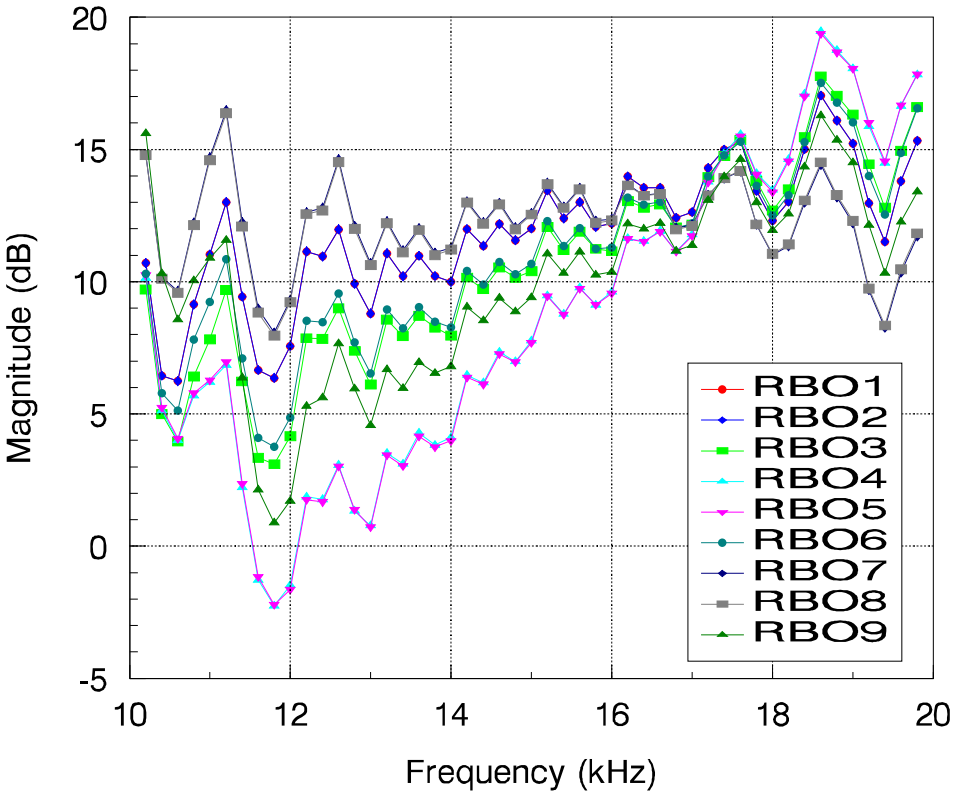

Figure 3.10: Magnitude of raw S_{21} measured on multiple instances of disassembly and reassembly with variable bolt order in the resin flanges. Traces are labelled RBO (Random Bolt Order) and then numbered sequentially. There is a large variance between the raw data for each measurement which clearly demonstrates that bolt order is important to the repeatability of the flange.

The 1–2 kHz waveguide structures were made from acrylic sheet, that is machined and assembled with adhesive. These large couplers and waveguide flanges performed reliably and with sufficient repeatability without any further iteration. Figure 3.11 shows the standard deviation for the large flanges with three different assembly patterns. Using the recommended pattern reduces the standard deviation below 0.16 dB for all frequencies.

The reliability of the 3D printed waveguide was a problem that was encountered early on while assessing flange repeatability. The original resin prints

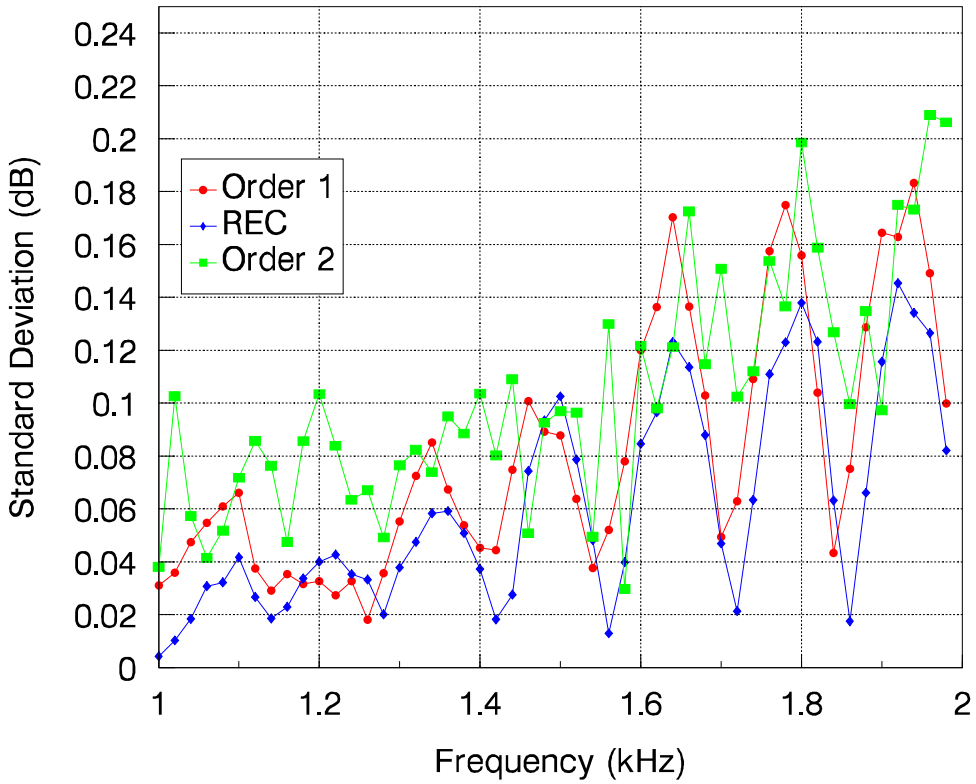

Figure 3.11: The standard deviation for each of the bolt assembly orders. REC corresponds to the recommended "Star" pattern.

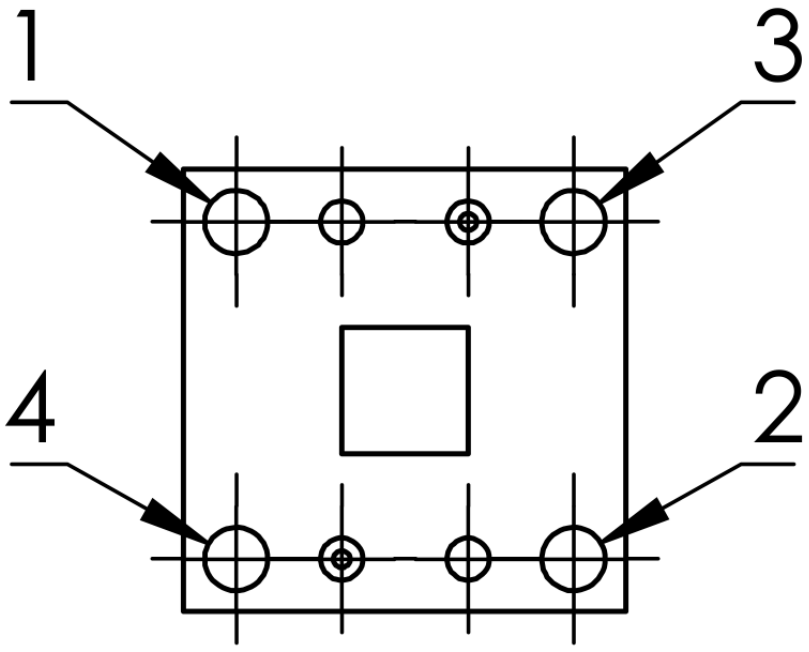

Figure 3.12: Suggested bolt order for assembly of flange joints.

were prone to brittle failure after a few dozen connections. After these failures, two other materials were selected and used in an additive manufacturing process to create new parts. U-shaped washers were also developed to distribute the force from the bolts across the flange. The U-shaped washers slightly increased the reliability of the resin parts. Figure 3.13 shows an example of the kind of failure that was typical in the 3D printed resin waveguide structures.

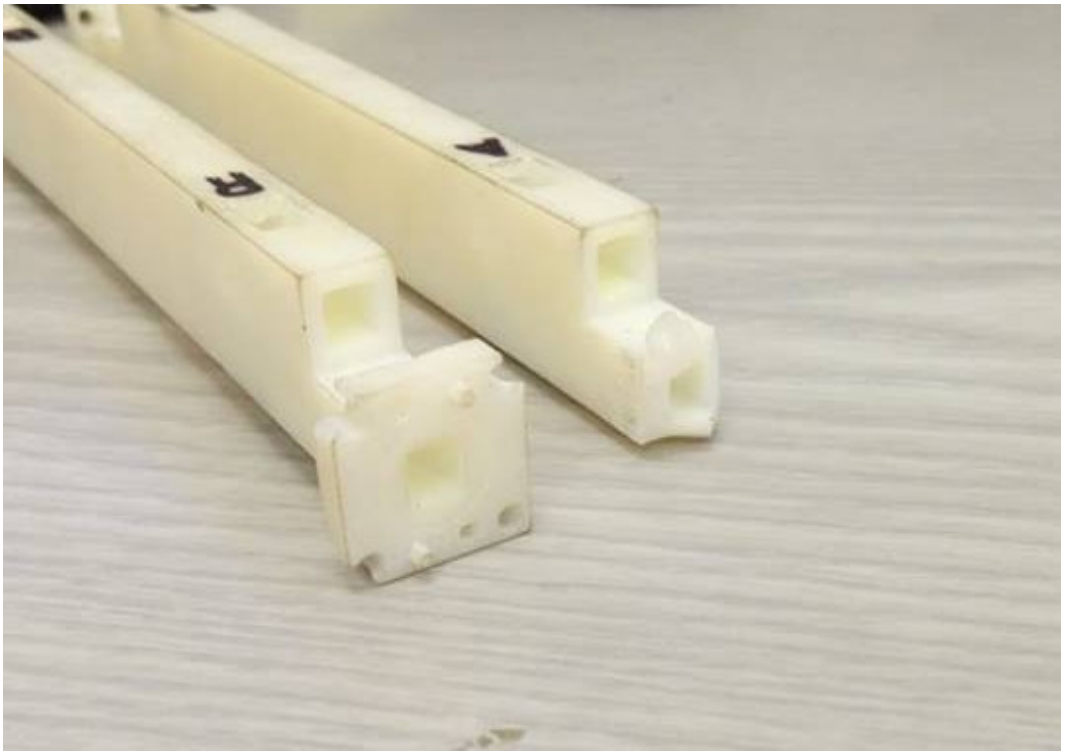

Figure 3.13: Examples of broken flanges from repeated use. Left: without U-shaped washers. Right: with U-shaped washers. The U-shaped washer effectively spread load from the fasteners and mitigated the kind of damage caused on the left hand example. However, repeated use of the U-shaped washers caused failure at the join between waveguide and flange.

Another two sets of directional couplers were 3D printed in transparent plastic, and Titanium (Ti64). The plastic parts were made using a multi-jet process with a softer material less prone to brittle failure. The titanium parts were made by a process called laser sintering, Titanium is sufficiently hard and strong that it has not yet failed, even without the use of U-shaped washers.

The reliability of these two manufacturing techniques was tested by repeated assembly and disassembly at the rated flange bolt torque. In addition

to the standard plastic flange, a set of reinforcing steel washers in a U-shape were used to spread the force across the plastic flange and 'sandwich' the joint. This increased the reliability of the plastic flange significantly but ultimately after months of experimentation and use they also failed. The 'sandwich' construction over time squashed and deformed the plastic and weakened the connection to the rest of the transmission line. The 90°angle between the flange and transmission line walls acted as a stress concentration. This could be mitigated by introducing a fillet to the flange design. The plastic couplers also warped along their length, which will have also distorted the branch-line structure of the directional coupler. Figures 3.14 and 3.15 show the assembled flanges with U-shaped washers. Figure 3.16 shows the warping along the length of the transmission line made from transparent plastic.

The titanium joints showed the best reliability of the waveguide structures made using an additive manufacturing process. Unfortunately, the repeatability of the titanium joints was worse than both the resin and plastic waveguide which were almost indistinguishable from one another. Figure 3.18 shows the data for a titanium (Ti) joint. This reduced repeatability is attributed to the dimensional accuracy of the titanium parts. The flanges as-sintered had a slight convexity and a rough surface finish. The combination of these two factors means that two flanges are less able to seat and seal properly and repeatably. The repeatability could be improved by surface grinding the flanges flat and then adding the alignment pins to the flange by another process. An electrical discharge machining (EDM) wire cutting process could also be explored. The convexity of the flanges and surface finish can be seen in Figure 3.19. The light passing under the straight edge shows the convexity while the pitting in the surface from the laser sintering process is seen on the flange. Figure 3.21 shows a feeler gauge between two titanium flanges and shows that the resulting gap at the edges from the convexity is 0.254 mm.

Unlike the large 60 mm, 1–2 kHz couplers developed by Pennington, the 10–20 kHz waveguide at 6 mm is much smaller than the diaphragm of almost all

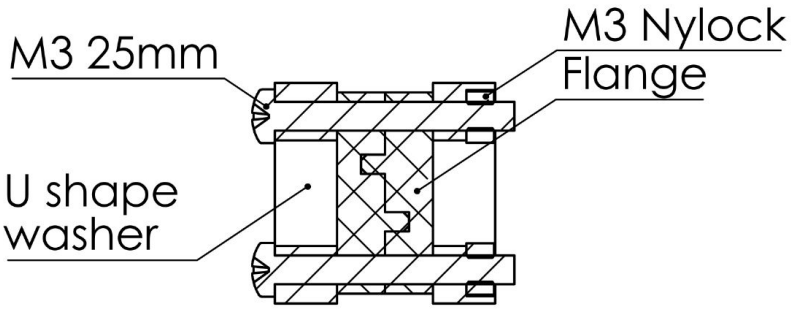

Figure 3.14: Cross section diagram of two mated flanges held by bolts passing through mild steel washers. Nylon locking nuts are used with stainless steel M3 bolts.

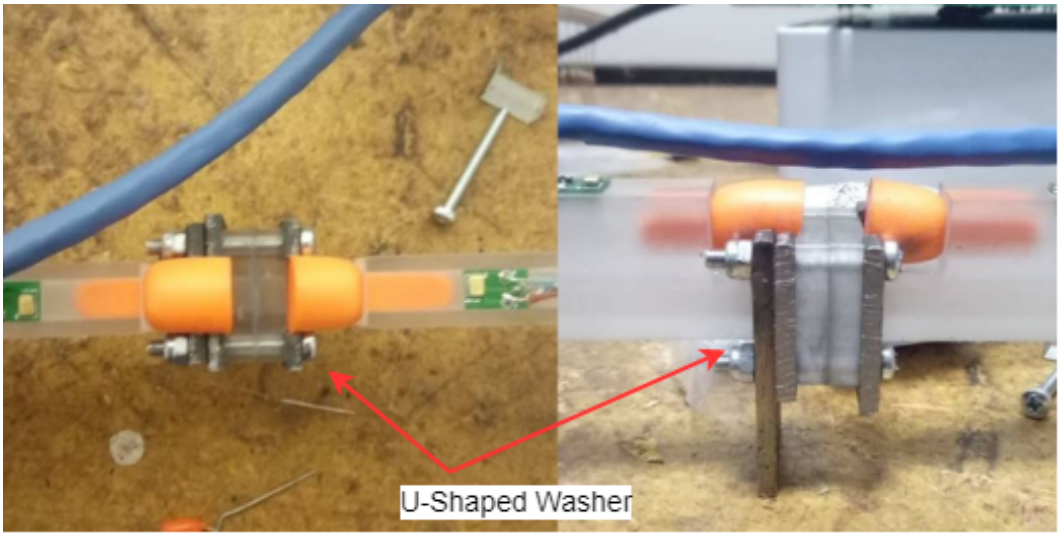

Figure 3.15: Actual flange assembly. Left: Top down view, Right: Profile view. The mild steel U-shape washers have been labelled.

Figure 3.16: The warping (in the plane of the image) of the length of the directional coupler is visible. Two red straight lines have been added to help show the warping.

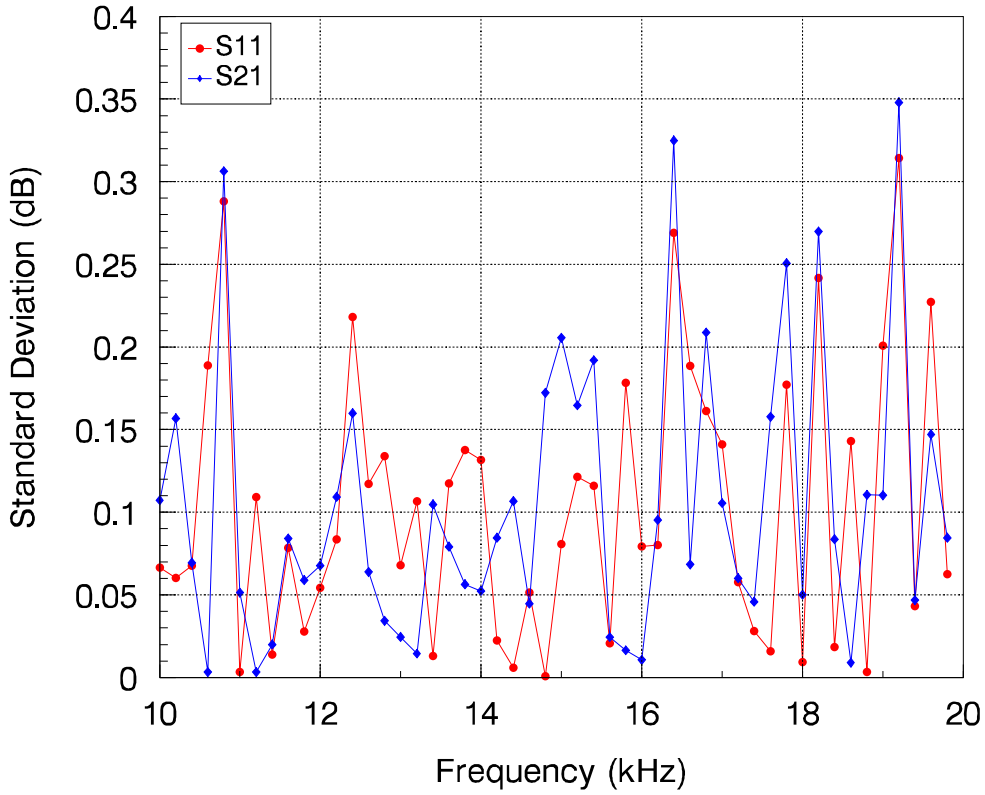

Figure 3.17: Standard Deviation of raw S_{11} and S_{21} obtained at each measurement frequency ten times. The flanges were Ti, the joints fitted with O-rings. Bolt torque was 0.5 N m, and the bolt order was random.

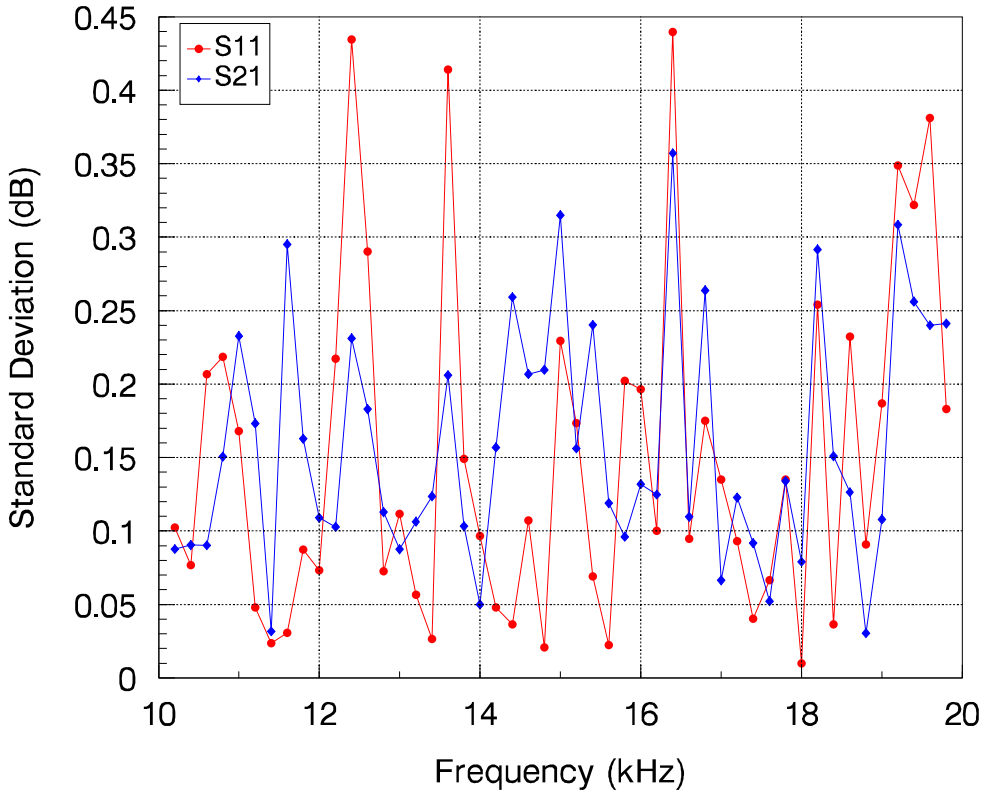

Figure 3.18: Standard Deviation of raw S_{11} and S_{21} obtained at each measurement frequency when the joint was disassembled and reassembled ten times. The flanges were Ti, the joints fitted with O-rings. Bolt torque was 0.5 N m, and the bolt order was random.

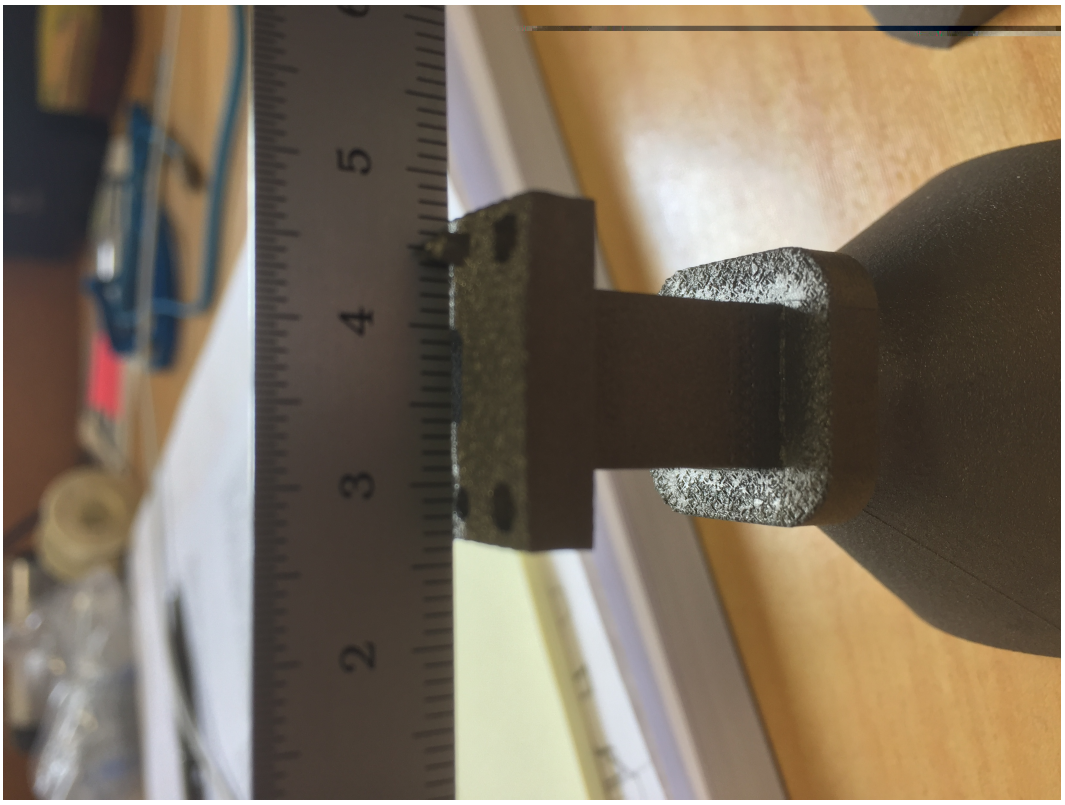

Figure 3.19: The surface finish for the Ti parts.

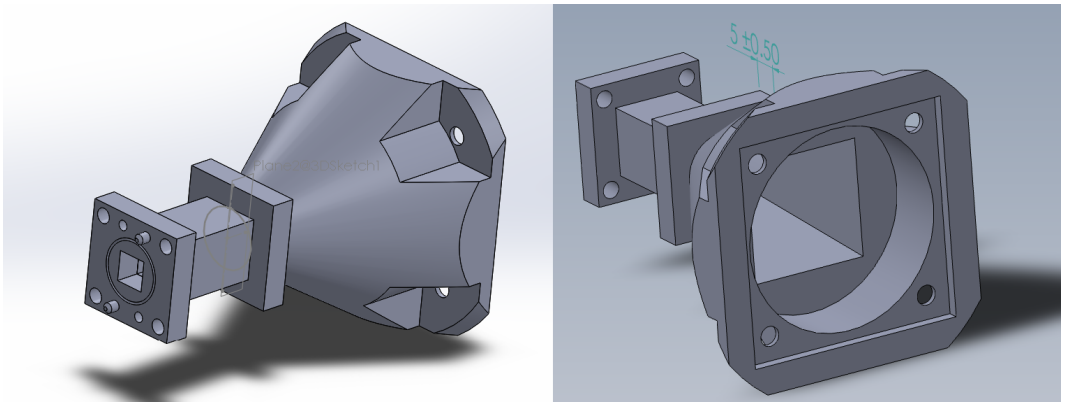

Figure 3.20: A 3D CAD model of the horn required for mounting the loudspeaker to the 10–20 kHz waveguide. The horn is square, 21 mm at its opening and 6 mm at its join to the transmission line. The selected loudspeaker is fitted into the round opening before the horn.

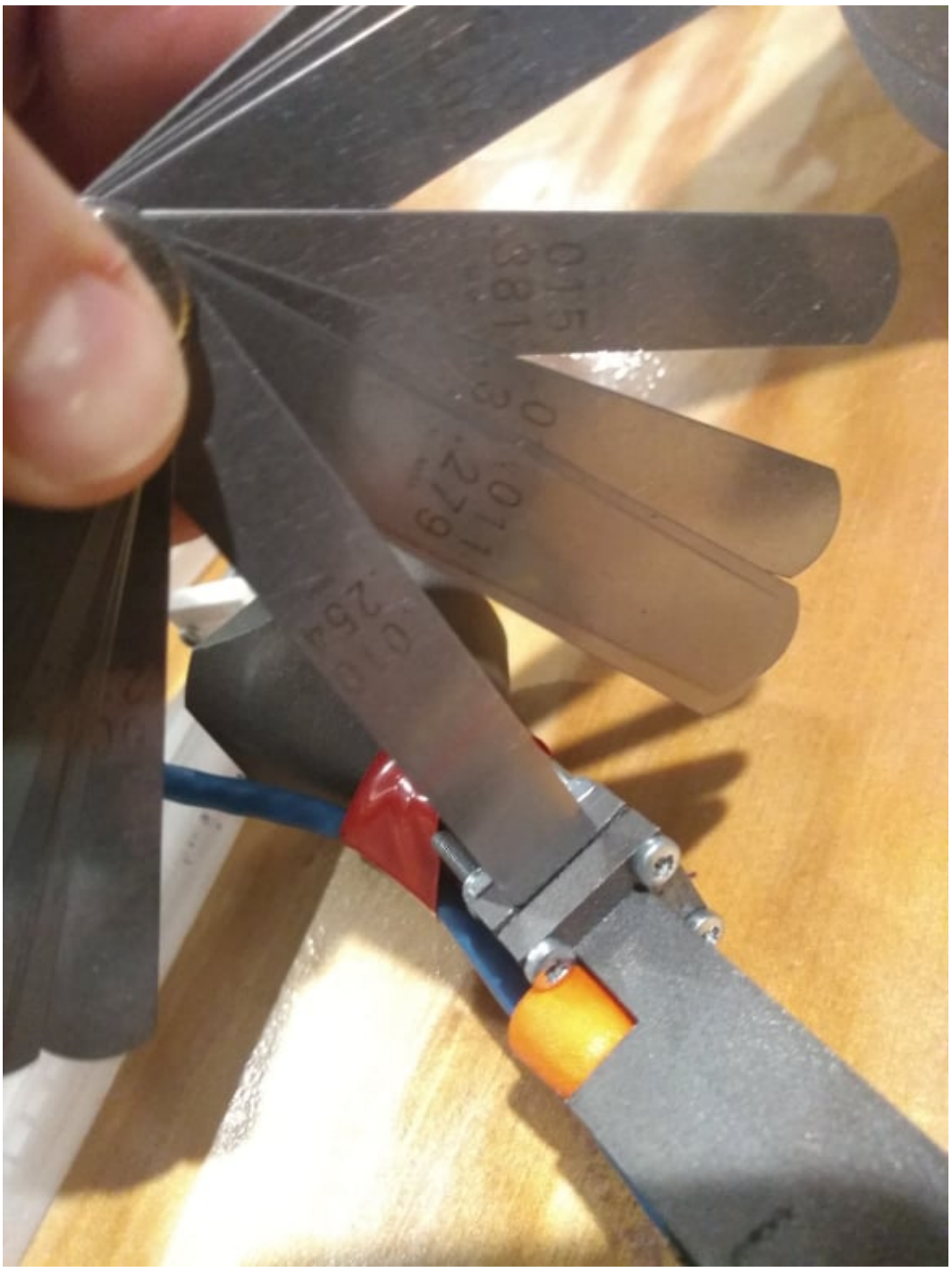

Figure 3.21: An imperial (Thou/mm) feeler gauge inserted between two 3D printed titanium (Ti64) flanges bolted up to their rated torque. The gap is approx 10 Thou or 0.254 mm.

commercially available loudspeakers designed for the bandwidth. To connect such a loudspeaker to the coupler a section of horn-like waveguide was also designed. Three sets of this horn waveguide section were made to match the waveguide materials tested. The 3D model for the horn waveguide can be seen in Figure 3.20, the titanium version is shown figure 3.19. The Dayton audio ND20FB-4 is a 4 Ω tweeter with a usable frequency range of 3,500–25,000 Hz, this range makes it suitable for the 10,000–20,000 Hz coupler set. Its rear mount design makes it ideal for mounting to the coupler via a horn waveguide.

3.2 Acoustic Standards

Commercial vector network analysers often have a calibration kit like the one pictured in figure 3.22. These commercially produced standards must be manufactured with very high precision and tolerances so that any customer can be confident that their results are reproducible in other laboratories around the world.

To achieve a commercial Acoustic VNA the acoustic standards also need to be produced with very high precision and tolerances. A full set of standards that make up the 1–2 kHz acoustic calibration kit can be seen in figure 3.23. A "Line", or "Thru" of non-zero length was also built, since it is of known length it is possible to know the phase change through its length for each frequency making it a potential acoustic standard.

Figure 3.22: An Agilent 85056A 2.4 mm VNA calibration kit including sliding loads and calibration data.

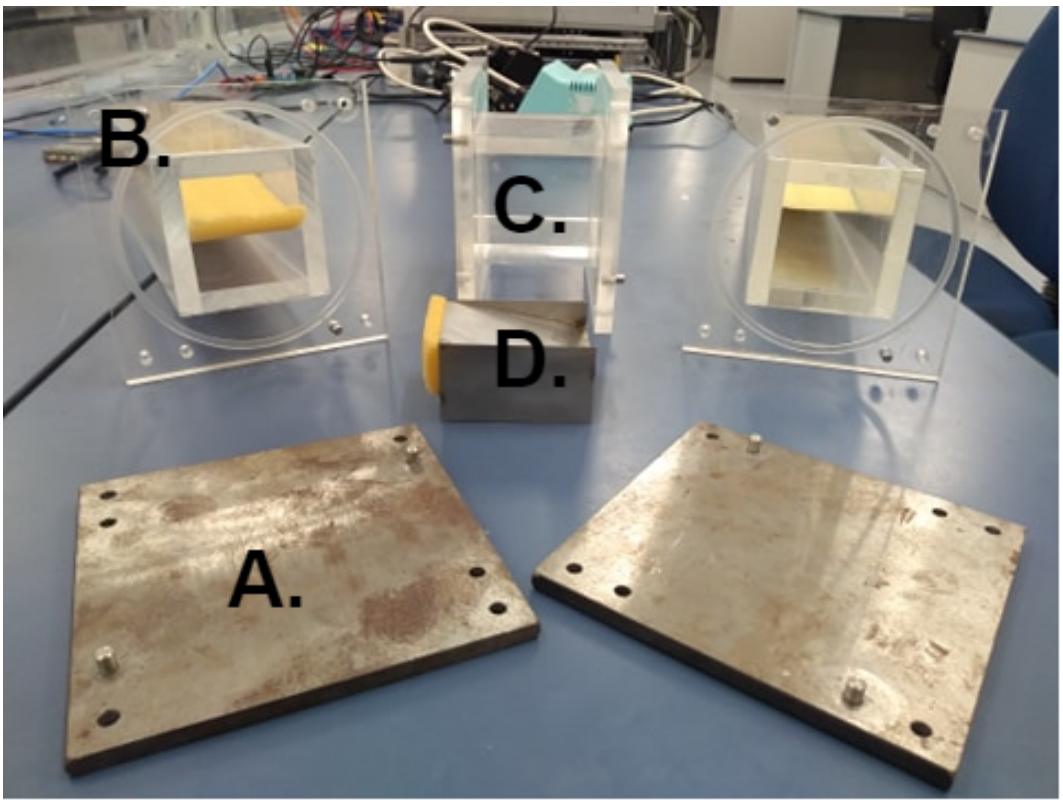

Figure 3.23: A full set of acoustic standards and the verification PARD. Large Reflect standards (Labelled A.) made from 5 mm mild steel plate, front left and right. Large Match standards (Labelled B.) are made from open-cell foam in a section of waveguide, rear left and right. A Line standard (Labelled C.) made with a known length of waveguide, rear center. The PARD (Labelled D.) is shown directly in front of the Line standard.

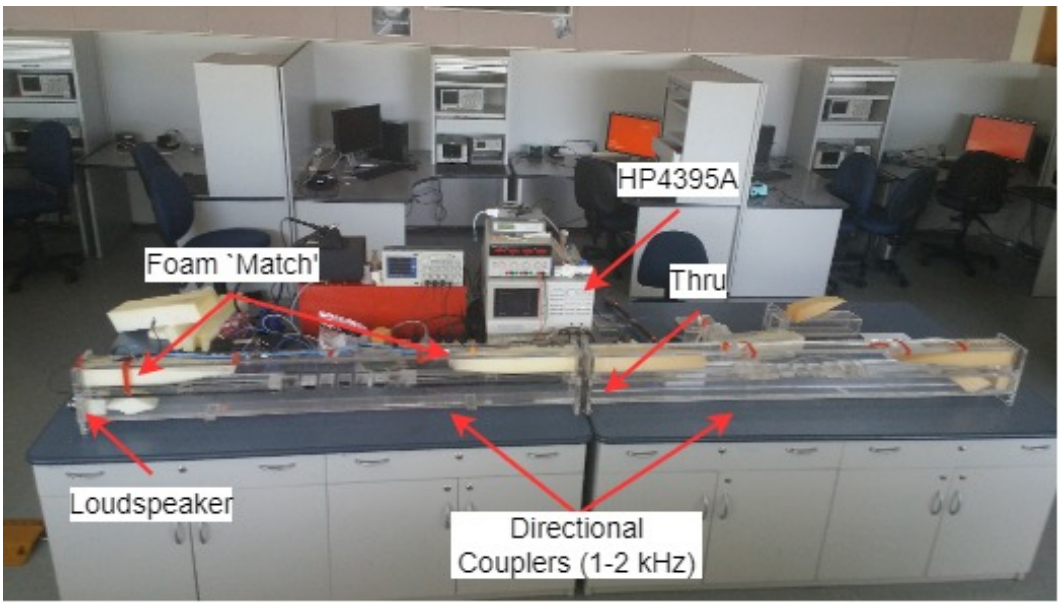

Figure 3.24: Preliminary AVNA set-up with the 1–2 kHz couplers. The internal foam loads are visible in each coupler.

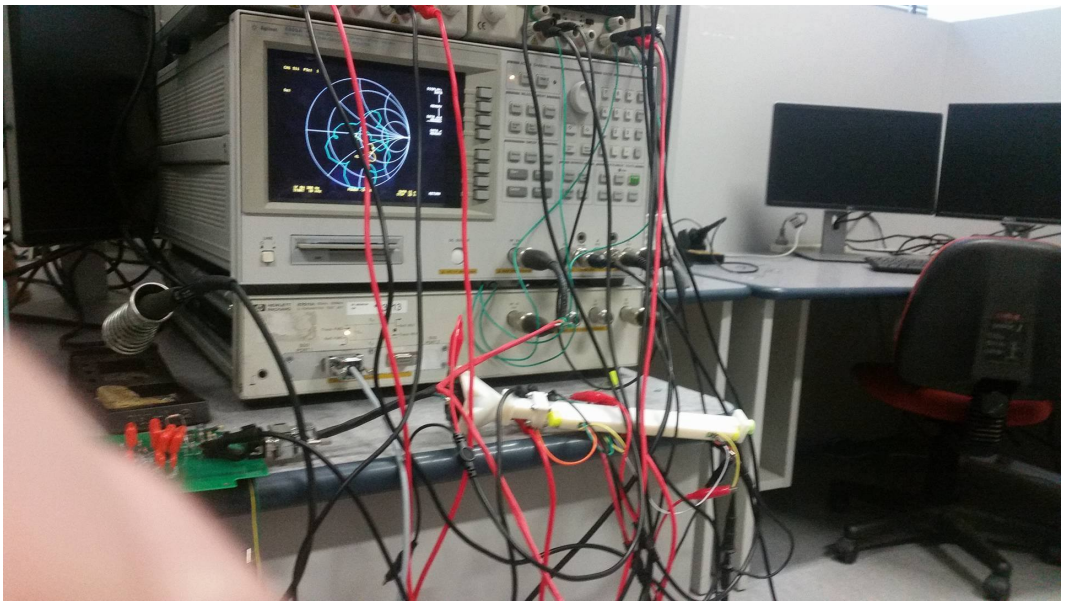

Figure 3.25: Preliminary AVNA set-up with the 10–20 kHz couplers and standards.

To verify that the proposed standards function as intended some initial test setups were created. The results of these tests and the final acoustic standard designs are presented here.

Figure 3.25 shows the AVNA set-up for preliminary measurements with the 10–20 kHz couplers. The equipment is powered by bench power supplies. The

Tektronix MSO 4054 oscilloscope was used to check levels, monitor operation, and ensure there was no system failure during measurement. By using the data-to-memory and math functions, traces can be shown for multiple S_{11} measurements on the instrument display. Figures 3.26 and 3.27 capture the key results. Figure 3.26 shows the result of measuring an "OPEN", verifying that it is not a viable acoustic "Reflect" standard. Figure 3.27 shows an early measurement showing that the "Reflect" standard is achievable with a metal plate, shown in the blue trace. The yellow trace has the port terminated with a load in the form of an earplug. Earplugs were found to perform well in previous research on acoustic directional couplers [56]. With appropriate dwell time and port extension, the Smith chart has been made to display sensible uncalibrated results. In this case, the coupler is nearly 200 mm in total length so a port extension was made to approximately 200–300 μs, corresponding to approximately 70–100 mm. For the 1–2 kHz couplers the port extensions will need to be in the order of milliseconds corresponding to the relative change in electrical length.

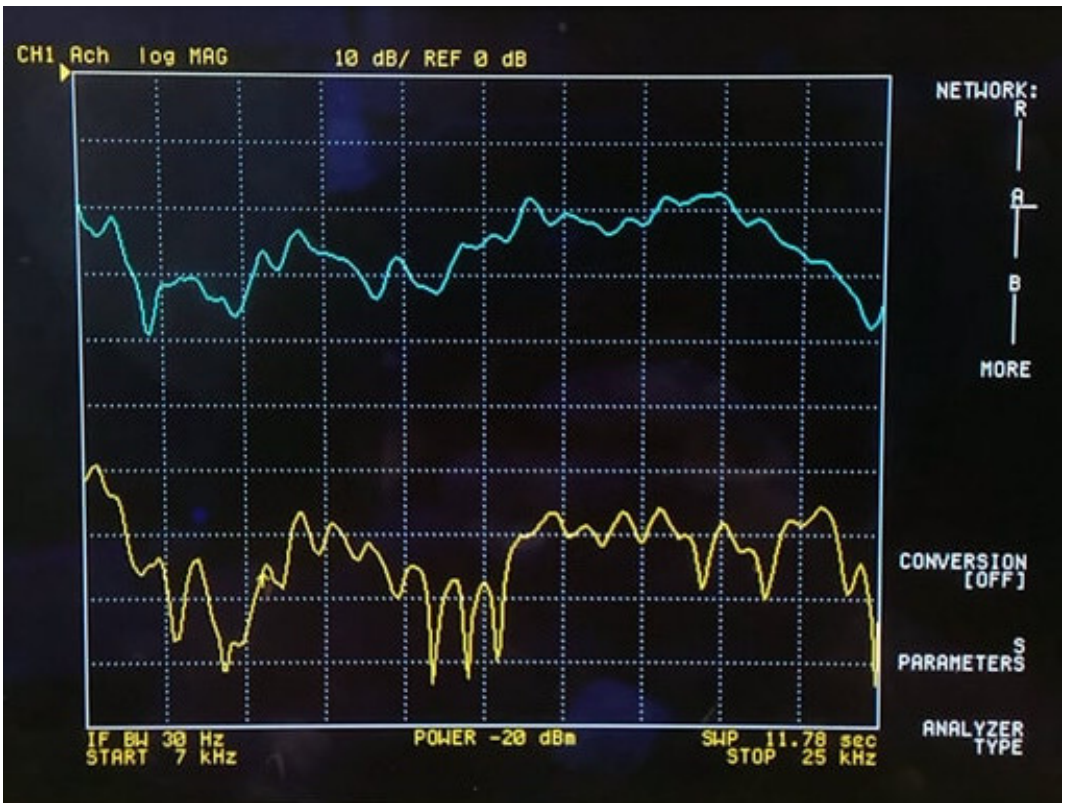

Figure 3.26: Magnitude measurements of an 'open', the blue trace is the "R" signal to the analyser and the yellow trace is the "A" signal to the analyser, as expected the R signal is much larger than the A signal, this is because most of the energy leaves the coupler rather than being reflected back to the "A" microphone

Figure 3.27: Both S_{11} traces for the metal reflect and the load as displayed on the HP4395A screen. The smith chart shows amplitude information as a ratio of the source power (therefore always ≤ 1) as the distance from the center, position indicates phase, the arcs from the outside of the circle to the far right are lines of constant phase.

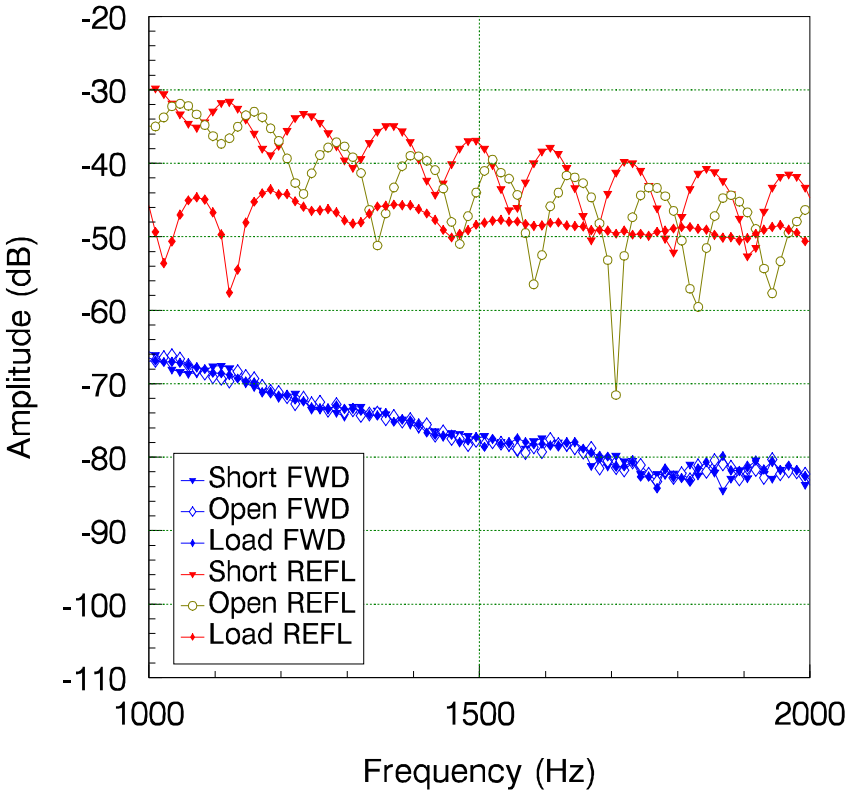

Figure 3.28: Measurements of the "R" and "A" signals for a Short, Open and Load in the 1-2 kHz couplers. S_{11} for each potential standard is as expected, the 'Short' reflects more energy than an 'Open' and the 'Load' reflects the least amount of energy.

To perform preliminary measurements with the 1–2 kHz couplers, the test system used by Pennington was adapted to the VNA. The Behringer ECM8000 microphones and an AudioBox recording interface were used. The AudioBox1818VSL has eight microphone pre-amplifiers [85]. Using the AudioBox1818VSL as an amplifier for microphone signals, uncalibrated S_{11} measurements were made. Figure 3.28 shows magnitude measurements for S_{11} with an 'Open', 'Short' and 'Load'.

The reflects for each waveguide size are made from metal. The 1–2 kHz reflect it is machined from 5 mm mild-steel plate and mild steel rod pieces are inserted into the plate as the alignment pins. The 10–20 kHz reflect is laser sintered in titanium and has a nominal thickness of 5 mm. Figure 3.29 shows

the ‘Reflect’ standard made from mild steel plate and rod. Figure 3.30 shows the ‘Reflect’ laser sintered in titanium, and the 3D model.

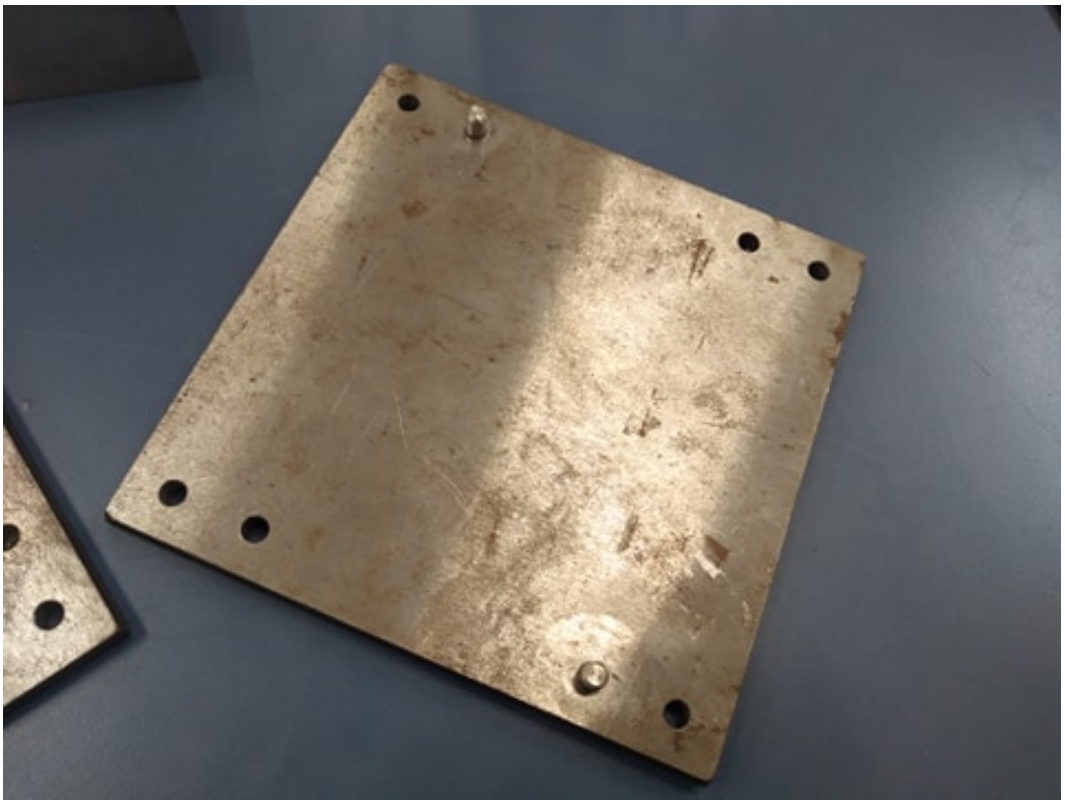

Figure 3.29: 1–2 kHz Reflect standard made from 5 mm mild steel plate and rod.

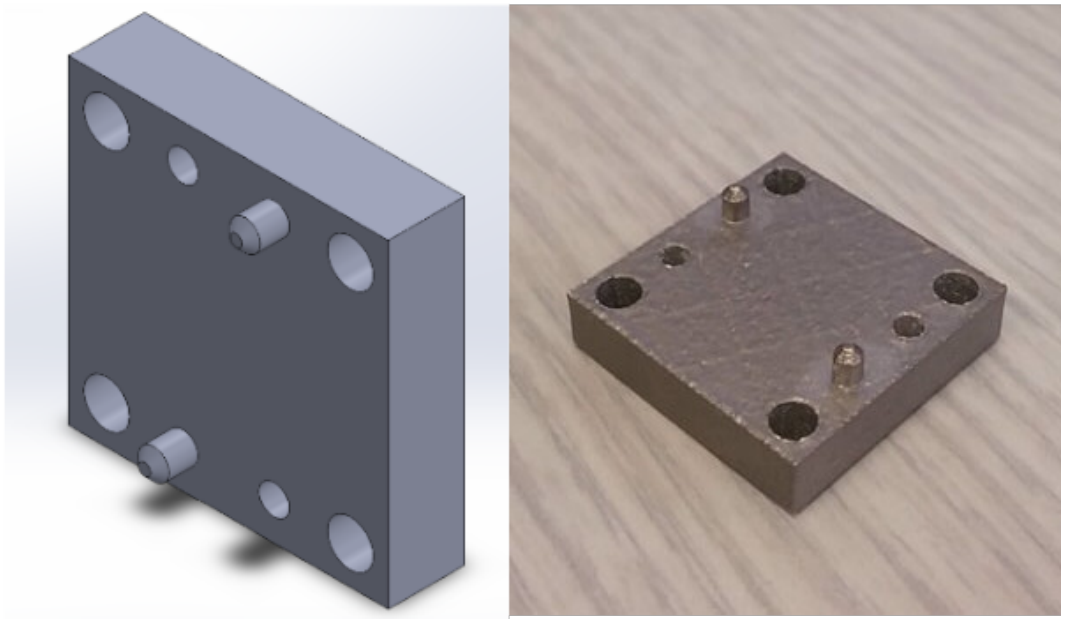

Figure 3.30: Left: 3D model of the 10-20 kHz Reflect standard. Right: Laser sintered 10-20 kHz Ti64 Reflect standard.

A section of acrylic 1–2 kHz waveguide is used to house a foam load, the foam load slides along this waveguide section as the "Match" standard, the foam section is easily moved by hand. Figure 3.31 shows the foam load in the waveguide section as used for the sliding load "Match" standard. Similarly, a section of 3D printed 10–20 kHz waveguide is used to slide a section of earplug as the "Match" standard. The earplug section is cut to size and glued to the end of a rod so it is not lost inside the waveguide. Figure 3.32 shows the 3D model for the section of waveguide used as the sliding load "Match" standard.

A full set of mechanical drawings is included in Appendix D.

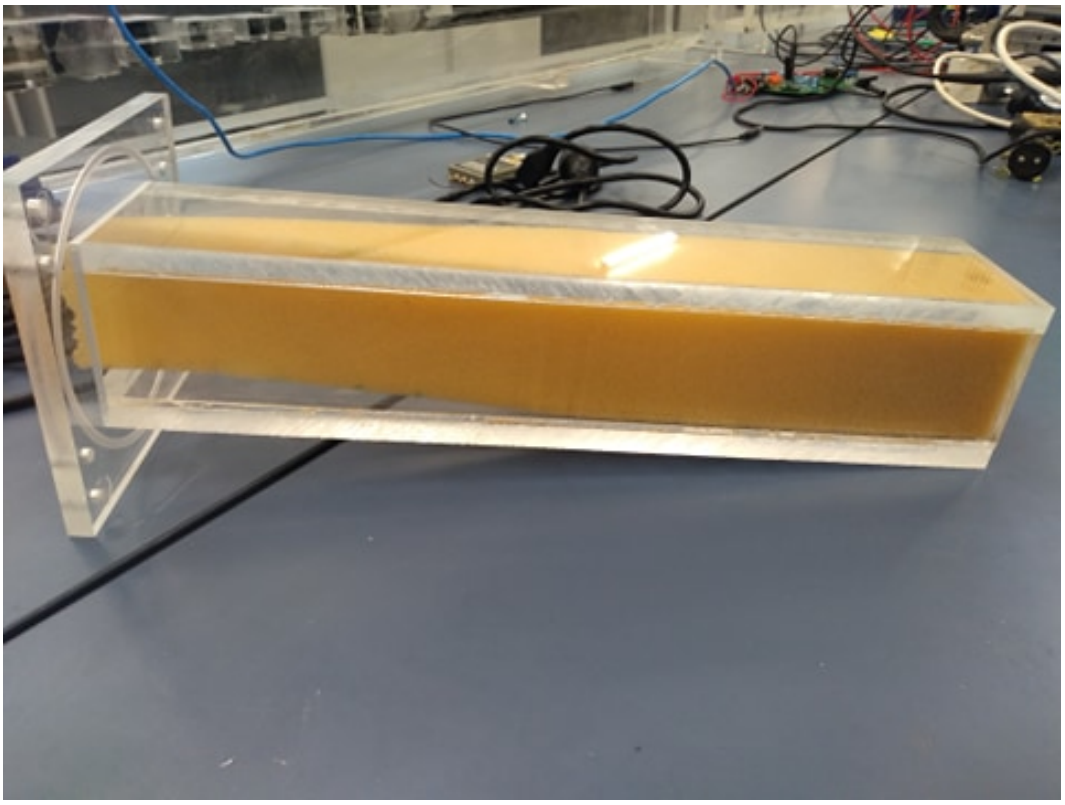

Figure 3.31: foam load in the section of waveguide as used for the sliding load "Match" standard

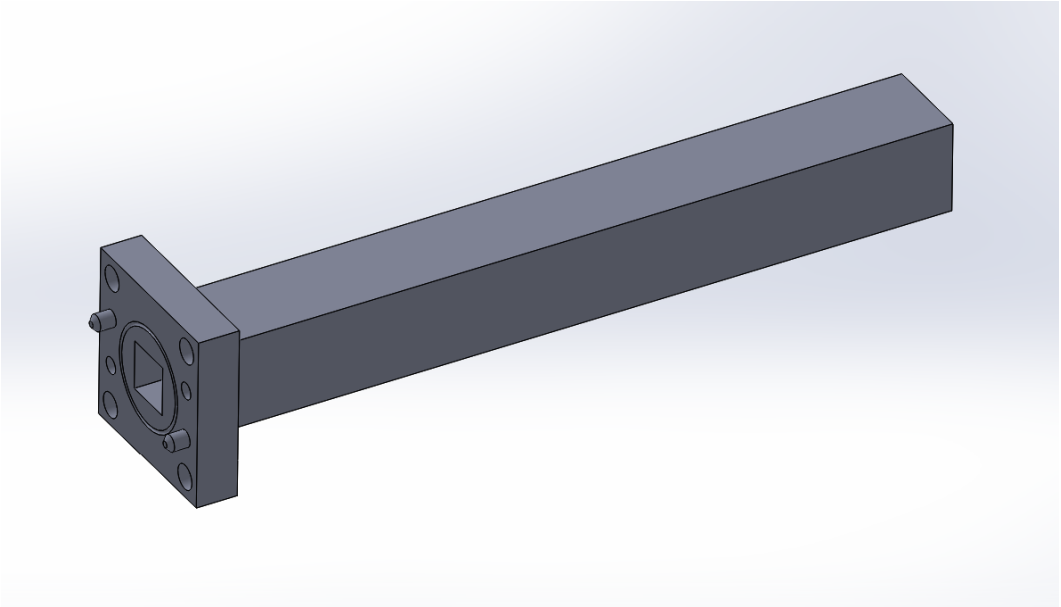

Figure 3.32: 3D model for the section of waveguide used as the sliding load "Match" standard.

3.3 Electronics Hardware

The electronics hardware is comprised of amplifiers, loudspeakers, microphones, cabling, and a "test-set".

A modified Agilent 87511A test set was created to adapt the acoustic directional couplers to the HP4395A. The 87511A test set was dismantled, the directional couplers were removed and the test set was refitted with D-sub connections for the connection of outboard acoustic couplers. An additional relay was required to switch the 'R' signal from one "coupled" microphone to the other. A power supply was added to the test set, this connects to mains via a toroidal transformer and powers the new external PCBs. The centre-tapped toroidal transformer output is rectified with a simple bridge rectifier to DC. The power supply has three output voltage rails: +15 V, -15 V and +2.5 V, each voltage rail is regulated with a linear regulator.

The amplifiers on the external amplifier PCB are to drive the loudspeaker and amplify the microphone signals specifically to interface with the 50 Ω input ports on the HP4395A. There are three amplifiers, one to drive a loud-

speaker and another two as microphone receivers per amplifier PCB. Each of the amplifiers is based around a NE5534 operational amplifier (op-amp), The NE5534 was chosen because of its very low noise, low distortion, and high slew rate. The loudspeaker driver output stage is a class AB amplifier using BD139 and BD140 transistors, it is non-inverting and has a gain of 11. The microphone receivers are non-inverting with a gain of 11. Each amplifier uses the ± 15 V rails. This board passes the $+2.5$ V rail to the micro-electromechanical systems (MEMS) microphones. There are two MEMS microphones per directional coupler. The MEMS microphones are used with both the 1–2 kHz and 10–20 kHz for this new analyser.

Microphones are also required to detect the sound pressure in the directional coupler at the coupled and decoupled ports. Microphones are available as micro-electromechanical systems (MEMS) and these are typically used in small portable devices such as cell phones. Because of their size, they are suitable for usage in the 6 mm waveguide, integral microphone mounting is provided in the 3D printed couplers by a square slot for the MEMS microphone printed circuit board (PCB). The microphones used are the MP23AB02B which covers the full audible frequency range but becomes more responsive at frequencies above 15,000 Hz, its characteristics above 20,000 Hz are not specified. These microphones are designed to be surface mounted to a PCB, with a PCB through-hole for sound to pass through to the sensor.

The PCBs for this research were designed using EAGLE CAD from AutoDesk. Microphone frequency response and a full set of PCB layouts and schematics are included in Appendix A.

The connections from the refitted test-set to the amplifier PCBs and then onto the coupler need to be reliable physically and in terms of signal integrity. The test-set houses two DB9 plugs on the front panel to connect to the amplifier PCBs and four N-type panel mount coaxial connectors to connect the 'GEN', 'R', 'A', and, 'B' signals to the analyser.

Chapter 4

Acoustic Calibration Method & Implementation

In this chapter, the error model for the Acoustic VNA, selected standards for the calibration algorithm, and matrix representations and their solutions are presented. A full derivation of the solutions will be available in the appendices. The selected calibration algorithm and comparison of the numerical and analytical approaches were presented as part of an AES conference paper [39].

4.1 Calibration Method

The 16-term error model has been selected as the error model for the AVNA, this is because the potential leakage of acoustic energy has been identified as an issue. In order to create a calibration method, there needs to be some known standards or measurements that can be used to satisfy the equations and solve for the error matrix. In the acoustic domain, we might have knowledge of the following standards.

- "Thru"

  A zero-length Line or "Thru" is provided by directly coupling the two ports of the analyser by their flanges and provides no attenuation or phase change.

- Line

  A Line is less accurately known but its attenuation and phase change are related to its length. The attenuation is due to the "lossy" nature of air as a medium.

- Reflect/Short

  A Reflect is provided by the interface between air and very hard/stiff materials.

- Match/Load

  A Match is provided by the sliding load method. The sliding load produces a number of points on the Smith chart, circles are then fitted to these results by the Taubin method [11, 72] and the circle center reveals the position of an ideal load.

- Open

  An Open is provided by not attaching anything to a port. Open standards are useful in coaxial systems, but in waveguide systems, including acoustic waveguide they do not provide a suitable standard.

The 16-term error model typically requires four measurements, these measurements would each produce a set of four independent equations to solve for the error matrix. However, there are only three potential acoustic standards that are sufficiently well known to be used confidently. They are the "Thru", Match, and Reflect. Fortunately, there exists a method to solve the 16-term error model using just these three standards.

TRRM was selected as the calibration method because it met our requirements of solving the 16-term error model and is achievable with the available standards. Using TRRM in order to solve for the 16 term model, five measurements are required. A Thru, Match-Match, Reflect-Reflect, Match-Reflect and Reflect-Match. These measurements produce five sets of "measured" S-parameter matrices that have a corresponding known "actual" or ideal S-parameter matrix.

The ideal matrices are:

$$\text{Thru:} \quad A = \begin{bmatrix} 0 & T \\ T & 0 \end{bmatrix}$$

$$\text{Match-Match:} \quad B = \begin{bmatrix} 0 & 0 \\ 0 & 0 \end{bmatrix}$$

$$\text{Reflect-Reflect:} \quad C = \begin{bmatrix} \Gamma & 0 \\ 0 & \Gamma \end{bmatrix}$$

$$\text{Reflect-Match:} \quad D = \begin{bmatrix} \Gamma & 0 \\ 0 & 0 \end{bmatrix}$$

$$\text{Match-Reflect:} \quad E = \begin{bmatrix} 0 & 0 \\ 0 & \Gamma \end{bmatrix}$$

For a Line, $T = e^{-\gamma l}$. where l is the length and γ is the complex propagation constant. For a Thru where the length is zero, $T = 1$.

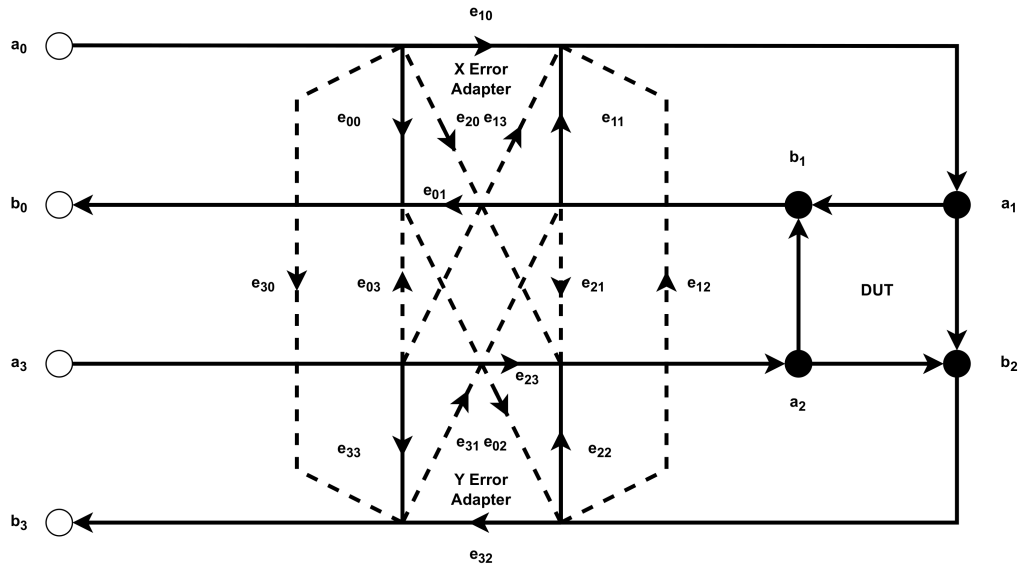

Figure 4.1: A flow graph of the 16 term error model. Reproduced from Chapter 2.

As discussed previously the 16 term error model shown in figure 4.1 yields the following matrix representation.

$$\begin{bmatrix} b_0 \\ b_3 \\ b_1 \\ b_2 \end{bmatrix} = E \begin{bmatrix} a_0 \\ a_3 \\ a_1 \\ a_2 \end{bmatrix} \tag{4.1}$$

$$E \equiv \begin{bmatrix} E_1 & E_2 \\ E_3 & E_4 \end{bmatrix} = \left[\begin{array}{cc:cc} e_{00} & e_{03} & e_{01} & e_{02} \\ e_{30} & e_{33} & e_{31} & e_{32} \\ \hdashline e_{10} & e_{13} & e_{11} & e_{12} \\ e_{20} & e_{23} & e_{21} & e_{22} \end{array}\right] \tag{4.2}$$

S_m and S_a are defined as

$$\begin{bmatrix} b_0 \\ b_3 \end{bmatrix} = S_m \begin{bmatrix} a_0 \\ a_3 \end{bmatrix}, \; S_m = \begin{bmatrix} S_{11m} & S_{12m} \\ S_{21m} & S_{22m} \end{bmatrix} \tag{4.3}$$

$$\begin{bmatrix} a_1 \\ a_2 \end{bmatrix} = S_a \begin{bmatrix} b_1 \\ b_2 \end{bmatrix}, \; S_a = \begin{bmatrix} S_{11a} & S_{12a} \\ S_{21a} & S_{22a} \end{bmatrix} \tag{4.4}$$

$$S_m = E_1 + E_2 S_a (I - E_4 S_a)^{-1} E_3 \tag{4.5}$$

Where I is the unit matrix. Solving for S_a yields

$$S_a = [E_3 (S_m - E_1)^{-1} E_2 + E_4]^{-1} \tag{4.6}$$

Equation 4.6 is a high-order polynomial and difficult to solve directly, cascading T parameters are used to reduce the complexity of solving the problem [86].

The E and T matrices are related by the following:

$$E = \begin{bmatrix} T_2 T_4^{-1} & T_1 - T_2 T_4^{-1} T_3 \\ T_4^{-1} & -T_4^{-1} T_3 \end{bmatrix} \tag{4.7}$$

$$T = \begin{bmatrix} E_2 E_1 E_3^{-1} E_4 & E_1 E_3^{-1} \\ E_3^{-1} E_4 & E_3^{-1} \end{bmatrix} \tag{4.8}$$

Substituting the T matrix into the system yields:

$$\begin{bmatrix} b_0 \\ b_3 \\ a_0 \\ a_3 \end{bmatrix} = T \begin{bmatrix} a_1 \\ a_2 \\ b_1 \\ b_2 \end{bmatrix} \tag{4.9}$$

$$T \equiv \begin{bmatrix} T_1 & T_2 \\ T_3 & T_4 \end{bmatrix} = \left[\begin{array}{cc:cc} t_0 & t_1 & t_2 & t_3 \\ t_4 & t_5 & t_6 & t_7 \\ \hdashline t_8 & t_9 & t_{10} & t_{11} \\ t_{12} & t_{13} & t_{14} & t_{15} \end{array}\right] \tag{4.10}$$

Using the T parameters and the definitions of S_m and S_a the following can be derived

$$S_m = (T_1 S_a + T_2)(T_3 S_a + T_4)^{-1} \tag{4.11}$$

$$T_1 S_a + T_2 - S_m T_3 S_a - S_m T_4 = 0 \tag{4.12}$$

$$S_a = (T_1 - S_m T_3)^{-1}(S_m T_4 - T_2) \tag{4.13}$$

Equation (4.12) forms the basis of calibration and can be arranged into the form of $\mathbf{A}T = 0$ and produces a set of four linear equations in terms of the 16 T-parameters t_n. Equation (4.13) allows for de-embedding of the DUT.

Equation (4.12) can be written in the form of

$$A\vec{T} = 0$$

as:

$$\begin{pmatrix} S_{a11} & S_{a21} & 0 & 0 & 1 & 0 & 0 & 0 & -S_{m11}S_{a11} & -S_{m11}S_{a21} & -S_{m12}S_{a11} & -S_{m12}S_{a21} & -S_{m11} & 0 & -S_{m12} & 0 \\ S_{a12} & S_{a22} & 0 & 0 & 0 & 1 & 0 & 0 & -S_{m11}S_{a12} & -S_{m11}S_{a22} & -S_{m12}S_{a12} & -S_{m12}S_{a22} & 0 & -S_{m11} & 0 & -S_{m12} \\ 0 & 0 & S_{a11} & S_{a21} & 0 & 0 & 1 & 0 & -S_{m21}S_{a11} & -S_{m21}S_{a21} & -S_{m22}S_{a11} & -S_{m22}S_{a21} & -S_{m21} & 0 & -S_{m22} & 0 \\ 0 & 0 & S_{a12} & S_{a22} & 0 & 0 & 0 & 1 & -S_{m21}S_{a12} & -S_{m21}S_{a22} & -S_{m22}S_{a12} & -S_{m22}S_{a22} & 0 & -S_{m21} & 0 & -S_{m22} \end{pmatrix} \begin{pmatrix} t_0 \\ t_1 \\ \vdots \\ t_{15} \end{pmatrix} = 0$$

This representation is useful because it is easier to see how to arrive at the

full system of equations. When each matrix A is combined, there is sufficient information to solve for the column vector $\vec{T}$. For each of the measurements a set of four equations is generated. For the Thru standard $A\vec{T} = 0$ becomes:

$$\begin{pmatrix} A_{11} & A_{21} & 0 & 0 & 1 & 0 & 0 & 0 & -M_{a11}A_{11} & -M_{a11}A_{21} & -M_{a12}A_{11} & -M_{a12}A_{21} & -M_{a11} & 0 & -M_{a12} & 0 \\ A_{12} & A_{22} & 0 & 0 & 0 & 1 & 0 & 0 & -M_{a11}A_{12} & -M_{a11}A_{22} & -M_{a12}A_{12} & -M_{a12}A_{22} & 0 & -M_{a11} & 0 & -M_{a12} \\ 0 & 0 & A_{11} & A_{21} & 0 & 0 & 1 & 0 & -M_{a21}A_{11} & -M_{a21}A_{21} & -M_{a22}A_{11} & -M_{a22}A_{21} & -M_{a21} & 0 & -M_{a22} & 0 \\ 0 & 0 & A_{12} & A_{22} & 0 & 0 & 0 & 1 & -M_{a21}A_{12} & -M_{a21}A_{22} & -M_{a22}A_{12} & -M_{a22}A_{22} & 0 & -M_{a21} & 0 & -M_{a22} \end{pmatrix} \begin{pmatrix} t_0 \\ t_1 \\ \vdots \\ t_{15} \end{pmatrix} = 0$$

where M_a and A are the measured and ideal values of the Thru standard respectively. Then for the remaining standards: The Match standard with ideal matrix B and measured values M_b becomes:

$$\begin{pmatrix} B_{11} & B_{21} & 0 & 0 & 1 & 0 & 0 & 0 & -M_{b11}B_{11} & -M_{b11}B_{21} & -M_{b12}B_{11} & -M_{b12}B_{21} & -M_{b11} & 0 & -M_{b12} & 0 \\ B_{12} & B_{22} & 0 & 0 & 0 & 1 & 0 & 0 & -M_{b11}B_{12} & -M_{b11}B_{22} & -M_{b12}B_{12} & -M_{b12}B_{22} & 0 & -M_{b11} & 0 & -M_{b12} \\ 0 & 0 & B_{11} & B_{21} & 0 & 0 & 1 & 0 & -M_{b21}B_{11} & -M_{b21}B_{21} & -M_{b22}B_{11} & -M_{b22}B_{21} & -M_{b21} & 0 & -M_{b22} & 0 \\ 0 & 0 & B_{12} & B_{22} & 0 & 0 & 0 & 1 & -M_{b21}B_{12} & -M_{b21}B_{22} & -M_{b22}B_{12} & -M_{b22}B_{22} & 0 & -M_{b21} & 0 & -M_{b22} \end{pmatrix} \begin{pmatrix} t_0 \\ t_1 \\ \vdots \\ t_{15} \end{pmatrix} = 0$$

The Reflect standard with ideal matrix C and measured values M_c becomes:

$$\begin{pmatrix} C_{11} & C_{21} & 0 & 0 & 1 & 0 & 0 & 0 & -M_{c11}C_{11} & -M_{c11}C_{21} & -M_{c12}C_{11} & -M_{c12}C_{21} & -M_{c11} & 0 & -M_{c12} & 0 \\ C_{12} & C_{22} & 0 & 0 & 0 & 1 & 0 & 0 & -M_{c11}C_{12} & -M_{c11}C_{22} & -M_{c12}C_{12} & -M_{c12}C_{22} & 0 & -M_{c11} & 0 & -M_{c12} \\ 0 & 0 & C_{11} & C_{21} & 0 & 0 & 1 & 0 & -M_{c21}C_{11} & -M_{c21}C_{21} & -M_{c22}C_{11} & -M_{c22}C_{21} & -M_{c21} & 0 & -M_{c22} & 0 \\ 0 & 0 & C_{12} & C_{22} & 0 & 0 & 0 & 1 & -M_{c21}C_{12} & -M_{c21}C_{22} & -M_{c22}C_{12} & -M_{c22}C_{22} & 0 & -M_{c21} & 0 & -M_{c22} \end{pmatrix} \begin{pmatrix} t_0 \\ t_1 \\ \vdots \\ t_{15} \end{pmatrix} = 0$$

The Reflect-Match standard with ideal matrix D and measured values M_d becomes:

$$\begin{pmatrix} D_{11} & D_{21} & 0 & 0 & 1 & 0 & 0 & 0 & -M_{d11}D_{11} & -M_{d11}D_{21} & -M_{d12}D_{11} & -M_{d12}D_{21} & -M_{d11} & 0 & -M_{d12} & 0 \\ D_{12} & D_{22} & 0 & 0 & 0 & 1 & 0 & 0 & -M_{d11}D_{12} & -M_{d11}D_{22} & -M_{d12}D_{12} & -M_{d12}D_{22} & 0 & -M_{d11} & 0 & -M_{d12} \\ 0 & 0 & D_{11} & D_{21} & 0 & 0 & 1 & 0 & -M_{d21}D_{11} & -M_{d21}D_{21} & -M_{d22}D_{11} & -M_{d22}D_{21} & -M_{d21} & 0 & -M_{d22} & 0 \\ 0 & 0 & D_{12} & D_{22} & 0 & 0 & 0 & 1 & -M_{d21}D_{12} & -M_{d21}D_{22} & -M_{d22}D_{12} & -M_{d22}D_{22} & 0 & -M_{d21} & 0 & -M_{d22} \end{pmatrix} \begin{pmatrix} t_0 \\ t_1 \\ \vdots \\ t_{15} \end{pmatrix} = 0$$

The Match-Reflect standard with ideal matrix E and measured values M_e becomes:

$$\begin{pmatrix} E_{11} & E_{21} & 0 & 0 & 1 & 0 & 0 & 0 & -M_{e11}E_{11} & -M_{e11}E_{21} & -M_{e12}E_{11} & -M_{e12}E_{21} & -M_{e11} & 0 & -M_{e12} & 0 \\ E_{12} & E_{22} & 0 & 0 & 0 & 1 & 0 & 0 & -M_{e11}E_{12} & -M_{e11}E_{22} & -M_{e12}E_{12} & -M_{e12}E_{22} & 0 & -M_{e11} & 0 & -M_{e12} \\ 0 & 0 & E_{11} & E_{21} & 0 & 0 & 1 & 0 & -M_{e21}E_{11} & -M_{e21}E_{21} & -M_{e22}E_{11} & -M_{e22}E_{21} & -M_{e21} & 0 & -M_{e22} & 0 \\ 0 & 0 & E_{12} & E_{22} & 0 & 0 & 0 & 1 & -M_{e21}E_{12} & -M_{e21}E_{22} & -M_{e22}E_{12} & -M_{e22}E_{22} & 0 & -M_{e21} & 0 & -M_{e22} \end{pmatrix} \begin{pmatrix} t_0 \\ t_1 \\ \vdots \\ t_{15} \end{pmatrix} = 0$$

When these sets of equations are combined, they form the the matrix:

$$\begin{pmatrix}
A_{11} & A_{21} & 0 & 0 & 1 & 0 & 0 & 0 & -M_{a11}A_{11} & -M_{a11}A_{21} & -M_{a12}A_{11} & -M_{a12}A_{21} & -M_{a11} & 0 & -M_{a12} & 0 \\
A_{12} & A_{22} & 0 & 0 & 0 & 1 & 0 & 0 & -M_{a11}A_{12} & -M_{a11}A_{22} & -M_{a12}A_{12} & -M_{a12}A_{22} & 0 & -M_{a11} & 0 & -M_{a12} \\
0 & 0 & A_{11} & A_{21} & 0 & 0 & 1 & 0 & -M_{a21}A_{11} & -M_{a21}A_{21} & -M_{a22}A_{11} & -M_{a22}A_{21} & -M_{a21} & 0 & -M_{a22} & 0 \\
0 & 0 & A_{12} & A_{22} & 0 & 0 & 0 & 1 & -M_{a21}A_{12} & -M_{a21}A_{22} & -M_{a22}A_{12} & -M_{a22}A_{22} & 0 & -M_{a21} & 0 & -M_{a22} \\
B_{11} & B_{21} & 0 & 0 & 1 & 0 & 0 & 0 & -M_{b11}B_{11} & -M_{b11}B_{21} & -M_{b12}B_{11} & -M_{b12}B_{21} & -M_{b11} & 0 & -M_{b12} & 0 \\
B_{12} & B_{22} & 0 & 0 & 0 & 1 & 0 & 0 & -M_{b11}B_{12} & -M_{b11}B_{22} & -M_{b12}B_{12} & -M_{b12}B_{22} & 0 & -M_{b11} & 0 & -M_{b12} \\
0 & 0 & B_{11} & B_{21} & 0 & 0 & 1 & 0 & -M_{b21}B_{11} & -M_{b21}B_{21} & -M_{b22}B_{11} & -M_{b22}B_{21} & -M_{b21} & 0 & -M_{b22} & 0 \\
0 & 0 & B_{12} & B_{22} & 0 & 0 & 0 & 1 & -M_{b21}B_{12} & -M_{b21}B_{22} & -M_{b22}B_{12} & -M_{b22}B_{22} & 0 & -M_{b21} & 0 & -M_{b22} \\
C_{11} & C_{21} & 0 & 0 & 1 & 0 & 0 & 0 & -M_{c11}C_{11} & -M_{c11}C_{21} & -M_{c12}C_{11} & -M_{c12}C_{21} & -M_{c11} & 0 & -M_{c12} & 0 \\
C_{12} & C_{22} & 0 & 0 & 0 & 1 & 0 & 0 & -M_{c11}C_{12} & -M_{c11}C_{22} & -M_{c12}C_{12} & -M_{c12}C_{22} & 0 & -M_{c11} & 0 & -M_{c12} \\
0 & 0 & C_{11} & C_{21} & 0 & 0 & 1 & 0 & -M_{c21}C_{11} & -M_{c21}C_{21} & -M_{c22}C_{11} & -M_{c22}C_{21} & -M_{c21} & 0 & -M_{c22} & 0 \\
0 & 0 & C_{12} & C_{22} & 0 & 0 & 0 & 1 & -M_{c21}C_{12} & -M_{c21}C_{22} & -M_{c22}C_{12} & -M_{c22}C_{22} & 0 & -M_{c21} & 0 & -M_{c22} \\
D_{11} & D_{21} & 0 & 0 & 1 & 0 & 0 & 0 & -M_{d11}D_{11} & -M_{d11}D_{21} & -M_{d12}D_{11} & -M_{d12}D_{21} & -M_{d11} & 0 & -M_{d12} & 0 \\
D_{12} & D_{22} & 0 & 0 & 0 & 1 & 0 & 0 & -M_{d11}D_{12} & -M_{d11}D_{22} & -M_{d12}D_{12} & -M_{d12}D_{22} & 0 & -M_{d11} & 0 & -M_{d12} \\
0 & 0 & D_{11} & D_{21} & 0 & 0 & 1 & 0 & -M_{d21}D_{11} & -M_{d21}D_{21} & -M_{d22}D_{11} & -M_{d22}D_{21} & -M_{d21} & 0 & -M_{d22} & 0 \\
0 & 0 & D_{12} & D_{22} & 0 & 0 & 0 & 1 & -M_{d21}D_{12} & -M_{d21}D_{22} & -M_{d22}D_{12} & -M_{d22}D_{22} & 0 & -M_{d21} & 0 & -M_{d22} \\
E_{11} & E_{21} & 0 & 0 & 1 & 0 & 0 & 0 & -M_{e11}E_{11} & -M_{e11}E_{21} & -M_{e12}E_{11} & -M_{e12}E_{21} & -M_{e11} & 0 & -M_{e12} & 0 \\
E_{12} & E_{22} & 0 & 0 & 0 & 1 & 0 & 0 & -M_{e11}E_{12} & -M_{e11}E_{22} & -M_{e12}E_{12} & -M_{e12}E_{22} & 0 & -M_{e11} & 0 & -M_{e12} \\
0 & 0 & E_{11} & E_{21} & 0 & 0 & 1 & 0 & -M_{e21}E_{11} & -M_{e21}E_{21} & -M_{e22}E_{11} & -M_{e22}E_{21} & -M_{e21} & 0 & -M_{e22} & 0 \\
0 & 0 & E_{12} & E_{22} & 0 & 0 & 0 & 1 & -M_{e21}E_{12} & -M_{e21}E_{22} & -M_{e22}E_{12} & -M_{e22}E_{22} & 0 & -M_{e21} & 0 & -M_{e22}
\end{pmatrix}
\begin{pmatrix} t_0 \\ t_1 \\ t_2 \\ t_3 \\ t_4 \\ t_5 \\ t_6 \\ t_7 \\ t_8 \\ t_9 \\ t_{10} \\ t_{11} \\ t_{12} \\ t_{13} \\ t_{14} \\ t_{15} \end{pmatrix} = \mathbf{0}$$

The matrix dimensions are

$$A_{(20,16)}\vec{T}_{(16,1)} = 0$$

meaning that the system is over-determined.

4.1.1 Calculating the terms T_i and the error terms e_{ij}

Solving for the T-parameters can be done in a variety of ways, and simplifies calculating the error terms [86]. Two common methods are normalizing by one of the unknown coefficients and solving directly or using a least-squares method, single value decomposition (SVD) is used often because of its ability to handle singularities [69, 86]. Because there are five total measurements this system is overdetermined, provided the system is consistent there is a solution, but, in either case, SVD provides a robust method of finding an approximate solution. Both of these methods were pursued. By using both of these common methods, their performance can be compared and contrasted. This comparison can then then be used to inform future decisions about which method is appropriate in a given situation.

The T-parameters can all be calculated analytically. A full algebraic solution is included in Appendix B. There is duplicate information in the matrix, by first removing this and then calculating either t_{15} or $\frac{\Gamma}{T}$ from a second-order equation the remaining t_n values can be calculated in a straightforward manner while t_{12} is assumed to be equal to 1 because it is used as a scaling parameter [69].

SVD (Single Value Decomposition) breaks down the matrix A into three parts, U, S, and V^T. A column orthogonal matrix, diagonal matrix, and row orthogonal matrix respectively. Substituting $A = USV^T$ into a normalized system yields

$$T = VS^{-1}U^T\vec{B}$$

where $\vec{B}$ is a column vector produced by the normalization of the set of equations that form the basis of calibration. There is a close relationship between the solutions to a linear system and the solutions to the corresponding homogeneous system:

$$A\vec{T} = \vec{B}$$

and

$$A\vec{T} = 0$$

Specifically, if p is any specific solution to the linear system $A\vec{T} = \vec{B}$, then the entire solution set can be described as

$$\{\vec{p} + \vec{v} : \vec{v} \text{ is any solution to } A\vec{T} = 0\}$$

Geometrically, this says that the solution set for $A\vec{T} = \vec{B}$ is a translation of the solution set for $A\vec{T} = 0$. Specifically, the flat for the first system can be obtained by translating the linear subspace for the homogeneous system by the vector $\vec{p}$.

This reasoning only applies if the system $A\vec{T} = \vec{B}$ has at least one solution. This occurs if and only if the vector $\vec{B}$ lies in the image of the linear

transformation A. When using SVD, the last column of V corresponds to the null space of A. Since W_{nm} is unambiguous for the nth row and mth column entry of W. Then let V_{*16} correspond to the 16 th column of V, V_{*16} is also a solution for T.

There are several algorithms used to implement SVD [87]:

- Golub-Reinsch SVD [88]
- Golub-Kahan SVD [89]
- High relative accuracy bidiagonal SVD
- Demmel-Kahan SVD
- Differential quotient-difference
- Bidiagonal Singular Values by Bisection
- Divide and conquer SVD
- Jacobi Rotation SVD
- Bi-orthogonalization SVD

MATLAB uses a method similar to [88, 89] in its computation of the SVD. The documentation for using the SVD implementation in MATLAB is available online [90].

4.2 Implementation

The 16-term error model is not solvable directly in the HP4395A receiver [91]. With its maximum operating frequency of 500MHz, the designers would not have anticipated a waveguide application, or that the SOLT (Short, Open, Load, Thru) calibration might not be possible[1]. The calibration method and

[1]The HP4395A was designed for measurements in coaxial systems and uses SOLT to solve for the 12-term error model.

solutions were therefore implemented on an external computer. The implementation on an external computer has some benefits such as the code can be migrated easily and maintained/updated with modern development tools like GIT. One significant drawback however is that checking measured data for issues before solving the error model is difficult. Issues in the data are difficult to automatically detect with software because it needs to detect legitimate system error (i.e the error terms) and error arising from the user or hardware issues.

The external computer first needs to connect to and control the receiver in order to specify the desired sweep parameters and then collect the measured "RAW" S-parameter data from the sweep. Python was selected as the main scripting language because of its extensive libraries, open-source licensing and overall flexibility. The Virtual Instrument Software Architecture (VISA) python libraries are used to retrieve Data from the HP4395A via the General Purpose Interface Bus (GPIB) either through a USB adapter or an Agilent E5810 network adapter. Data from the HP4395A can be retrieved in one of the following formats [91]:

1. ASCII
2. 32 and 64 bit IEEE 754 Floating point format
3. DOS PC format (32 bit IEEE with byte order reversed)

Currently, ASCII is used because it is human-readable, this allows for the inspection of the "RAW" data from the HP4395A receiver. The HP4395A receiver is controlled using commands listed in its programming manual [91], these commands allow the user to read and/or write a number of parameters including, device status, error status, sweep parameters, calibration data, measurement data, etc.

The main Python script controls the HP4395A receiver, prompting the user for the sweep parameters, and to perform each connection of the calibration

standards. The main python script defaults to a "run" behavior which is not verbose with warnings or other messages to the CLI (Command Line Interface), instead these are pushed to log files. Warnings and other messages to the CLI can be turned on for "debugging".

By using an application program interface (API) for MATLAB python is able to "parse" data and instructions with the MATLAB engine. This is advantageous because MATLAB is specifically designed for matrix algebra and has a GUI which enables quick development and data visualisation. All of main computation, matrix manipulation, SVD (Single value decomposition), circle fitting, etc was performed in MATLAB.

Starting with the Reflect, the user connects two Reflect standards, one to each port, using the prescribed bolt order and torque. Once a standard is connected to each port, the user then allows the script to perform a measurement. The next measurement is the Thru, the user now connects both of the ports directly together with the same bolt order and torque and allows the script to perform a measurement. The Next measurement is the Match which requires the sliding loads. Once the waveguide section is connected the script will prompt the user to slide the loads to a number of positions (> 3) for each port independently, i.e there is a minimum of six total measurements required. Although three is the minimum number of positions for the circle fitting method, a larger number is recommended to get better performance. The next two measurements are the Match-Reflect and Reflect-Match. These are performed by having a Match on one port and a Reflect on the other and then swapping them. Again the software will prompt the user to slide the load to at least three positions for the Match measurement. A graphic representation of this is shown in Figure 4.2.

The results of a calibration using numerical methods are shown in Figures 4.3–4.5. A simple test of any calibration method is to check it using one of the measured standards. This is not a verification of the calibration, rather it is a test of the implementation and a check for "bugs" in the codebase.

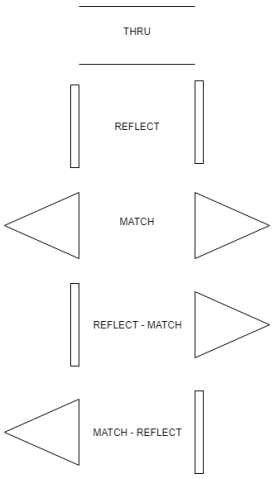

Figure 4.2: A graphic representation of the standards connected for the calibration process. From top to Bottom: Reflect, Match, Reflect-Match, Match-Reflect, Thru.

For example, using the Reflect standard if the calibrated S-parameters (S_a) resemble the ideal Reflect matrix C this indicates that the implementation of calibration has no "bugs" that affect this measurement. The closeness of the calibrated S-parameters (S_a) to the ideal Reflect matrix C also indicates the strength of the calibration to some degree.

i.e if the raw S-parameters (S_m) for the reflect standard are calibrated, and these calibrated parameters S_a are approximately equal to the ideal matrix C

$$S_a \approx C = \begin{bmatrix} \Gamma & 0 \\ 0 & \Gamma \end{bmatrix}$$

then the calibration has been successful for this standard.

Figure 4.3 shows the raw S-parameters S_m for the Reflect standard and Figure 4.4 shows the calibrated S-parameters for the Reflect S_a. The calibrated S-parameters S_{11a} and S_{22a} are shown to be very close to 0 dB, and the S-parameters S_{21a} and S_{12a} are approximately 40–50 dB. This shows that the reflection coefficients are indeed close to the ideal matrix. But, the transmission coefficients are not as close to ideal, and would ideally be much smaller. Because SVD uses the full over determined matrix these transmission coefficients give an indication of system noise, and performance.

Figure 4.5 shows the corrected data of the Thru (zero-length) standard

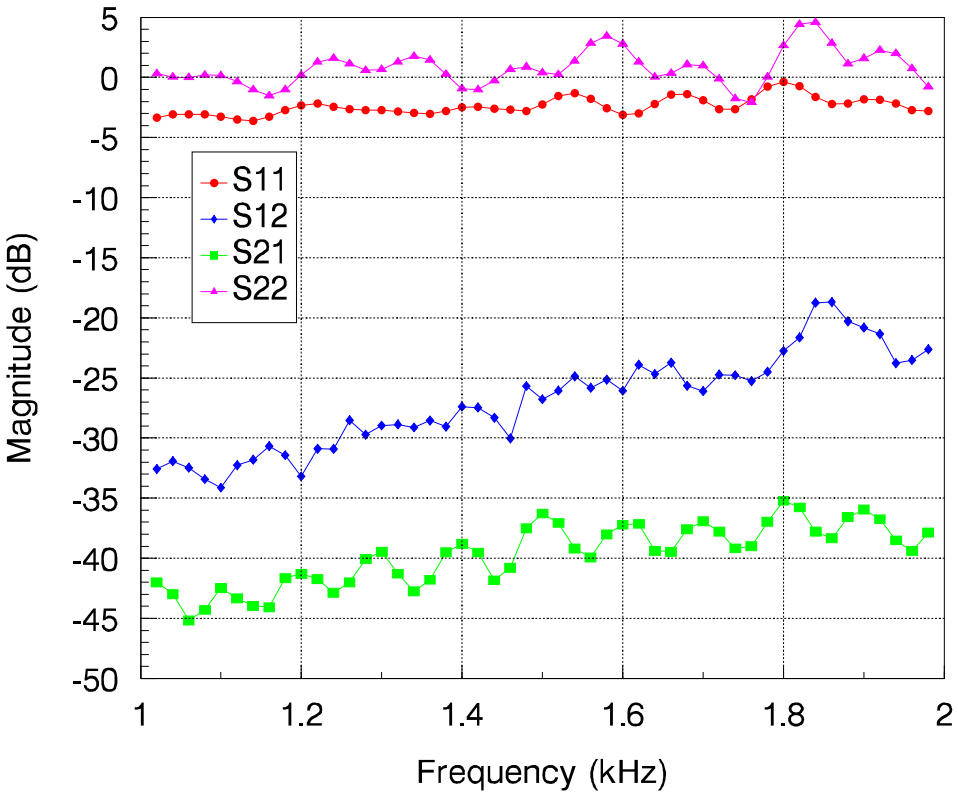

Figure 4.3: Raw S-parameters for the Reflect standard.

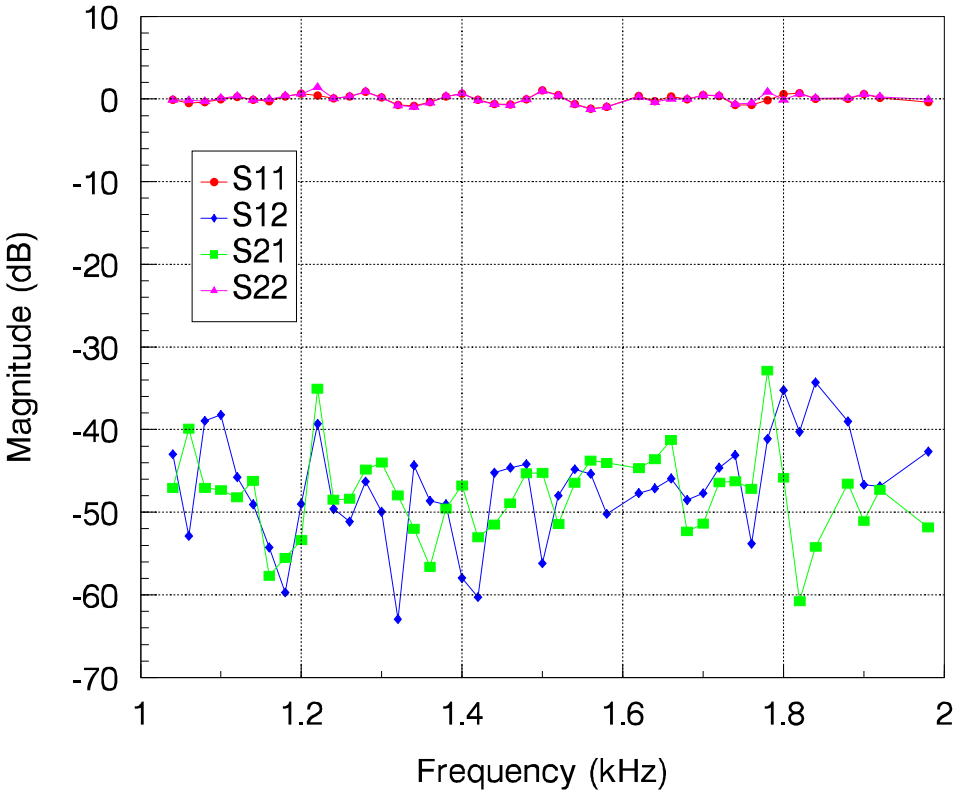

Figure 4.4: Result of measuring the Reflect calibration standard (a steel plate) using the numerical calibration method. The expected results are perfect reflection (0dB loss) as shown, and zero transmission (-∞ dB). The residual signal shows -40 dB to -50 dB, representing the noise floor of the system.

when using the error matrix produced by the numerical method. This shows that the transmission terms (S_{12} & S_{21}) very well calibrated to 0 dB (100% transmission) with reflections (S_{11} & S_{22}) sitting at least -40 dB down.

Figure 4.6 shows the corrected data of the Reflect standard when using the error matrix produced by the analytical method. This shows that the reflection terms (S_{11} & S_{22}) well calibrated to 0 dB (100% reflection). The transmission (S_{12} & S_{21}) is not shown but is approximately -350 dB. This is a result of error produced by the numerical computation with floats of an algebraic solution.

The performance of the Match standard which is implemented as a sliding load is limited by the performance of the load itself and the circle fit used. The circle fit used is the Taubin method. [72] In order for this method to work

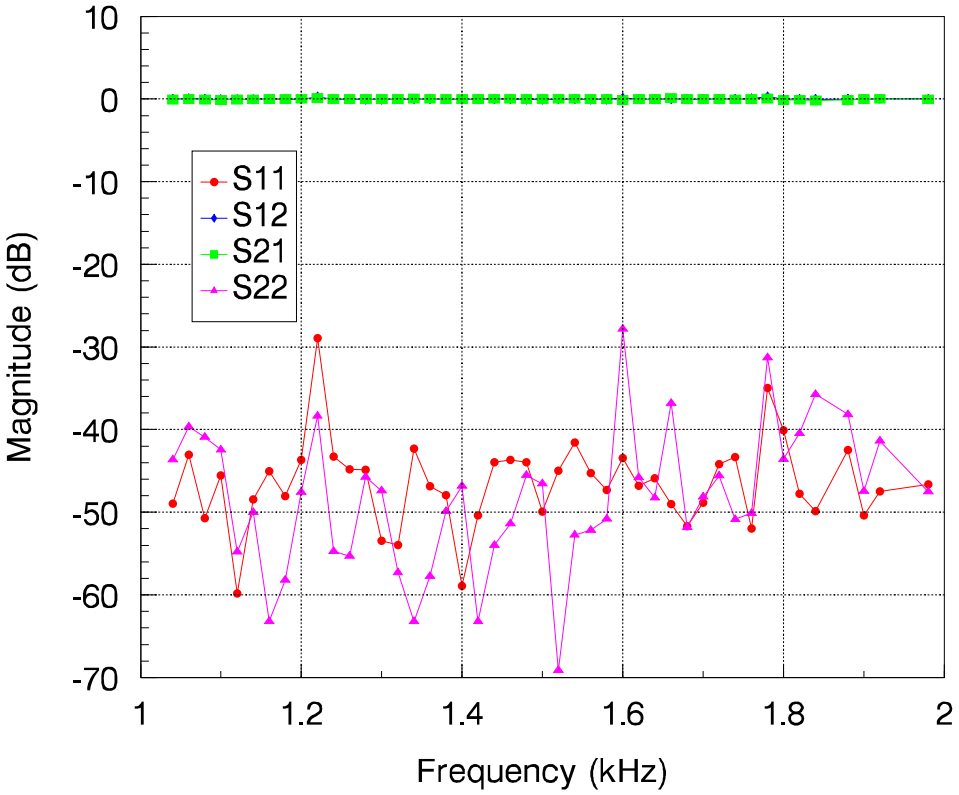

Figure 4.5: Result of measuring the Thru calibration standard (a tube of zero length) using the numerical calibration method. The expected results are perfect transmission (0dB loss) as shown, and zero reflection (-∞ dB). The residual signal shows -40 dB to -50 dB, representing the noise floor of the system.

effectively there need to be sufficient points for the method to fit a least-squares solution for all frequencies. Three points are theoretically sufficient, however, when implementing the sliding load practically there are frequencies where more points may be required for an accurate fit. Imperfections in the circle fit manifest themselves as an increase in the noise floor where the expected result is minute. The sliding load method could be optimized by collecting measurements of the load at as many positions as possible, over a distance that allows for the best circle fit without introducing a large variation in line loss.

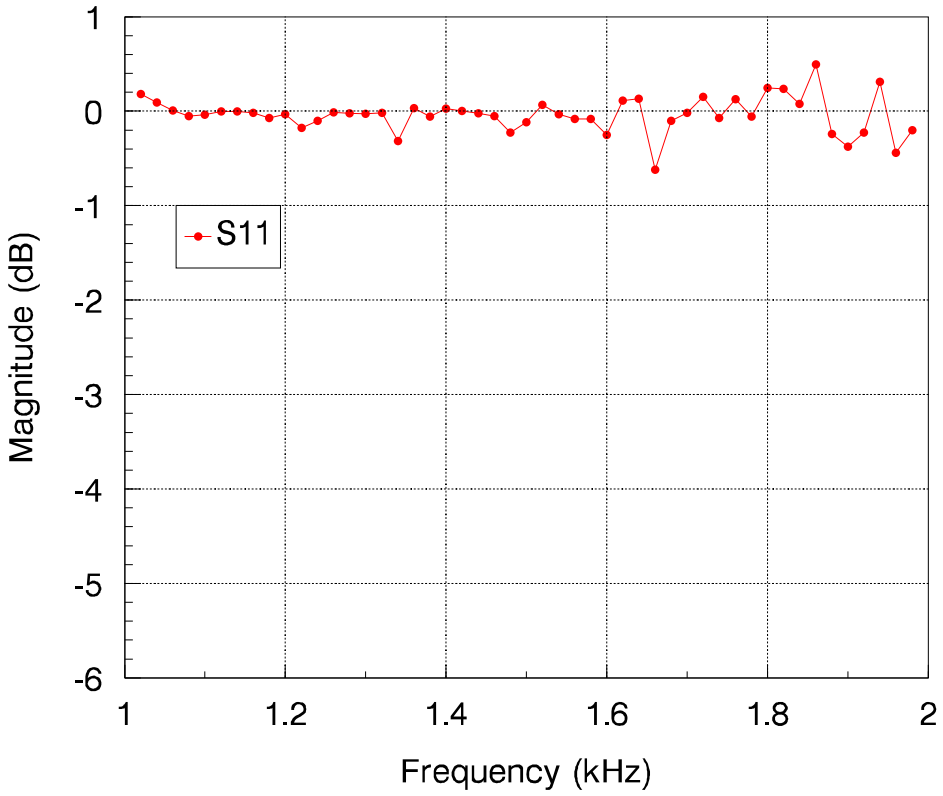

Figure 4.6: Result of measuring the Reflect calibration standard (a steel plate) using the analytical calibration method. The expected results are reflection of 0 dB, and zero transmission (-∞ dB). The reflection data is very close to 0 dB. The residual transmission (not shown) signal is ≈ -350 dB, which is approximately the limit of machine precision.

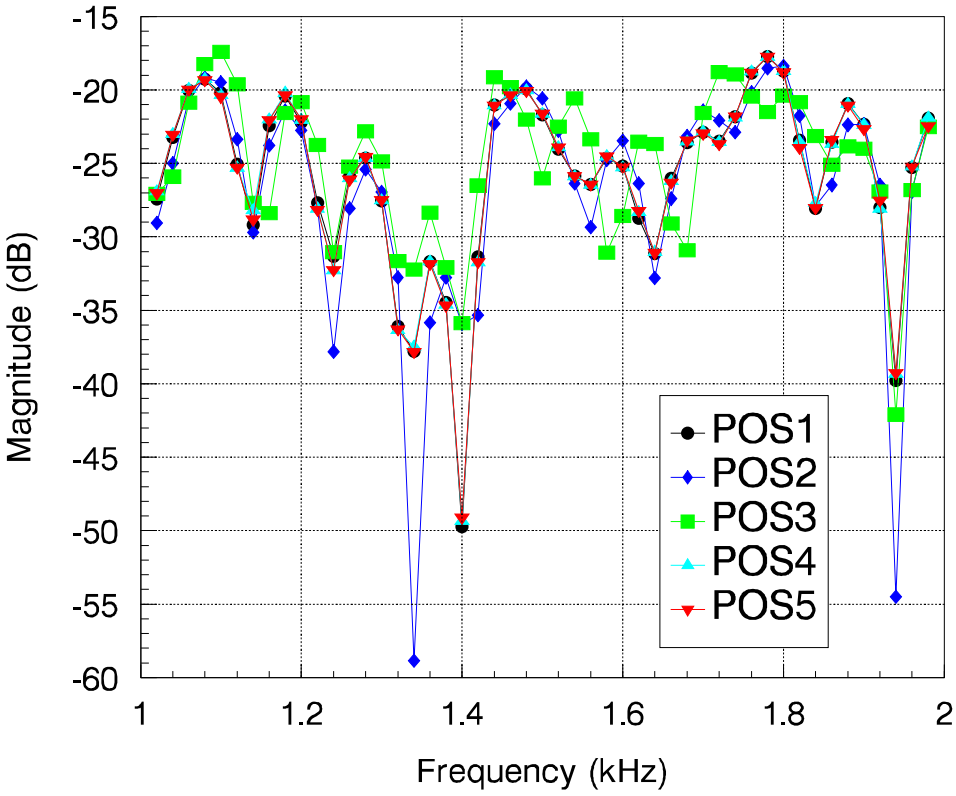

Figure 4.7: Raw S_{11} Match data for multiple load positions. The data varies with position as expected, with only small changes in magnitude.

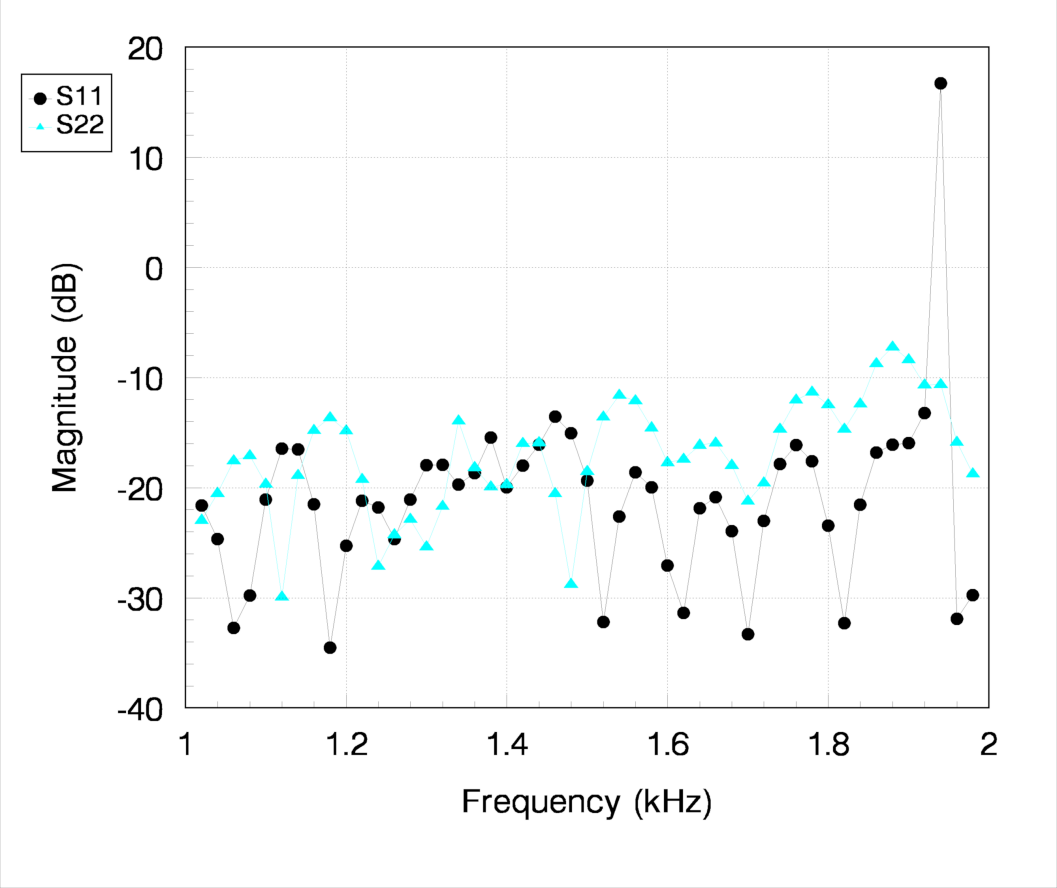

Figure 4.8: Raw Match data after the circle fit is performed for S_{11} and S_{22}. The data that is returned by the circle fit is an approximation for the raw data expected from an ideal load. The outliers from the circle fit are ignored since they are the product of a poor circle fit. The circle fit method can fail to produce a reasonable answer, due to point proximity or resonance in the system. There is a poor circle fit at 1940 Hz which can be identified by the large spike in magnitude.

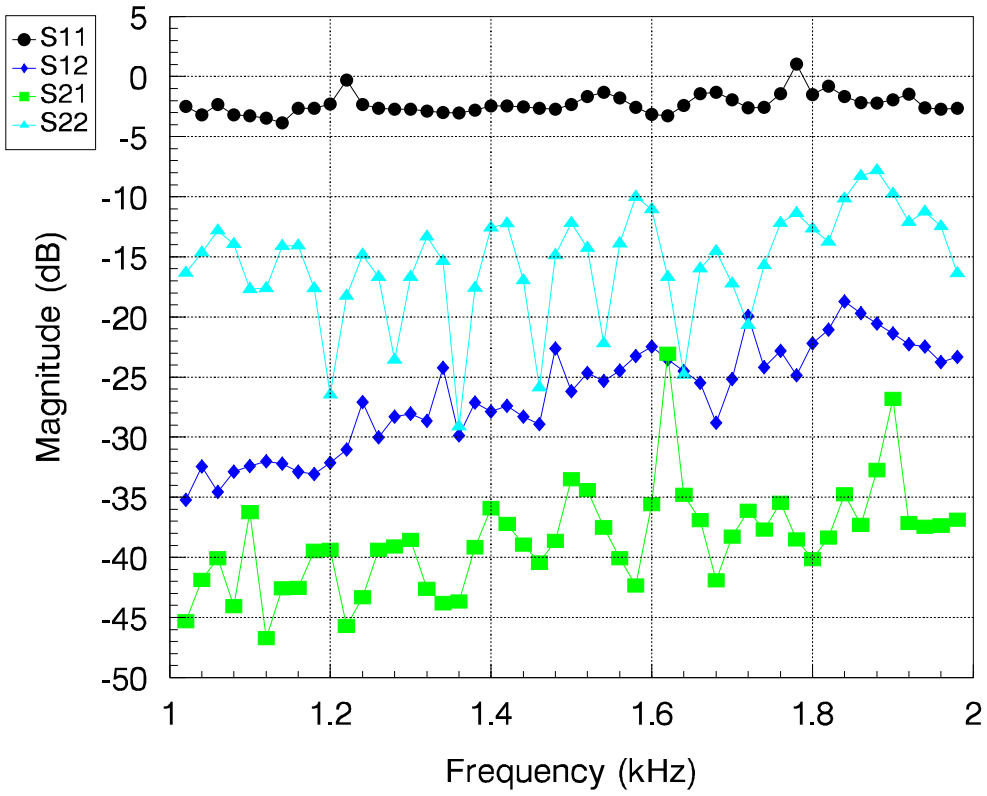

Figure 4.9: Reflect-Match after circle-fit, the circle fit failed for the Green trace at approximately 1620 Hz and 1900 Hz.

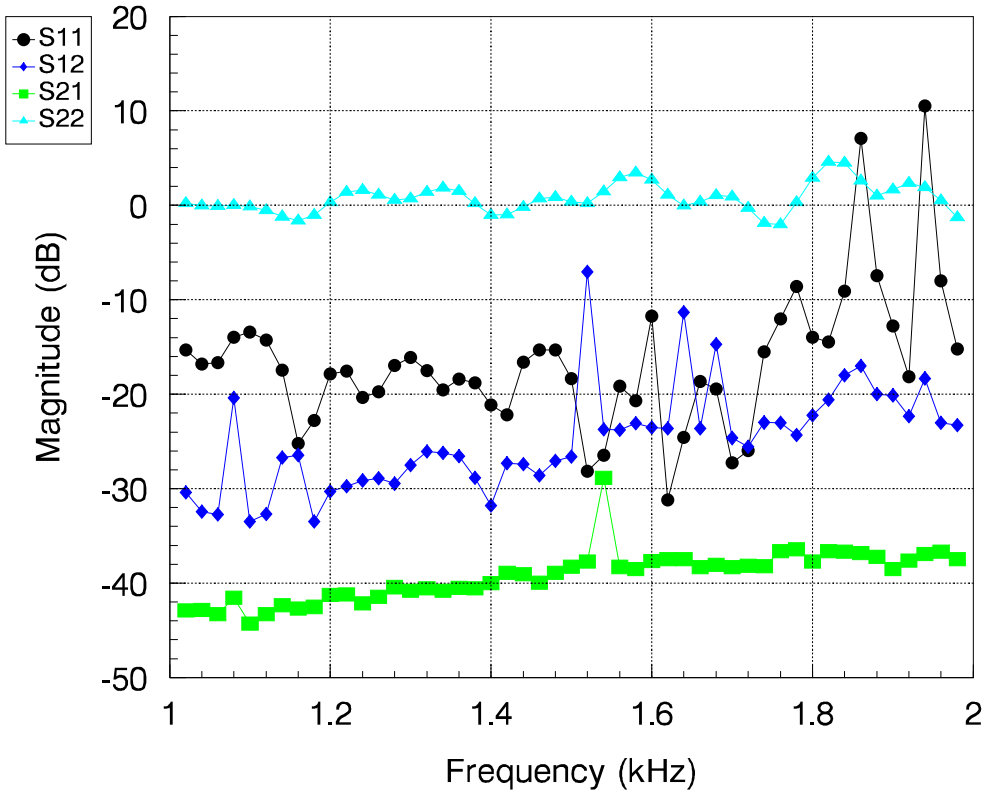

Figure 4.10: Match-Reflect after circle-fit, the circle fit failed for a number of points.

Chapter 5

Validation of the Acoustic Calibration

In this chapter the partial verification of the calibration with a PARD is presented. These PARD measurements were presented as part of an article published in the Journal of the Audio Engineering Society (JAES) [40].

5.1 Calibration Verification

5.1.1 PARD — Passive Asymmetrical Reciprocal Device

The PARD or Passive, Asymmetrical, Reciprocal Device was introduced in Chapter 2. A PARD has the characteristics: $S_{12} = S_{21}$ and $S_{11} \neq S_{22}$ [76]. If the PARD is then reversed and measured again, the S-parameters S'_{11}, S'_{12}, S'_{21}, and S'_{22} are obtained. If $S'_{11} = S_{22}$, $S'_{22} = S_{11}$, $S'_{12} = S_{21}$, and $S'_{21} = S_{12}$ the calibration has successfully accounted for the error adapters on both ports. This offers a partial verification of the calibration since there is no impedance standard to compare against. The acoustic PARD was constructed from sheet metal folded into a "V" shape that was filled with foam. Sides were added that enabled the PARD to be placed in the center of a section of waveguide. Figure 5.1 shows the 3D model for the device, and Figure 5.1.1 shows the

physical implementation. This device was constructed to fit a 60 mm by 60 mm waveguide, and inserted in a short length of suitable waveguide. This structure was created using a guess and check method and when placed in the waveguide provide the characteristics of a PARD since it is passive, asymmetrical due to the "V" structure and is reciprocal since it can be flipped and measured in both orientations.

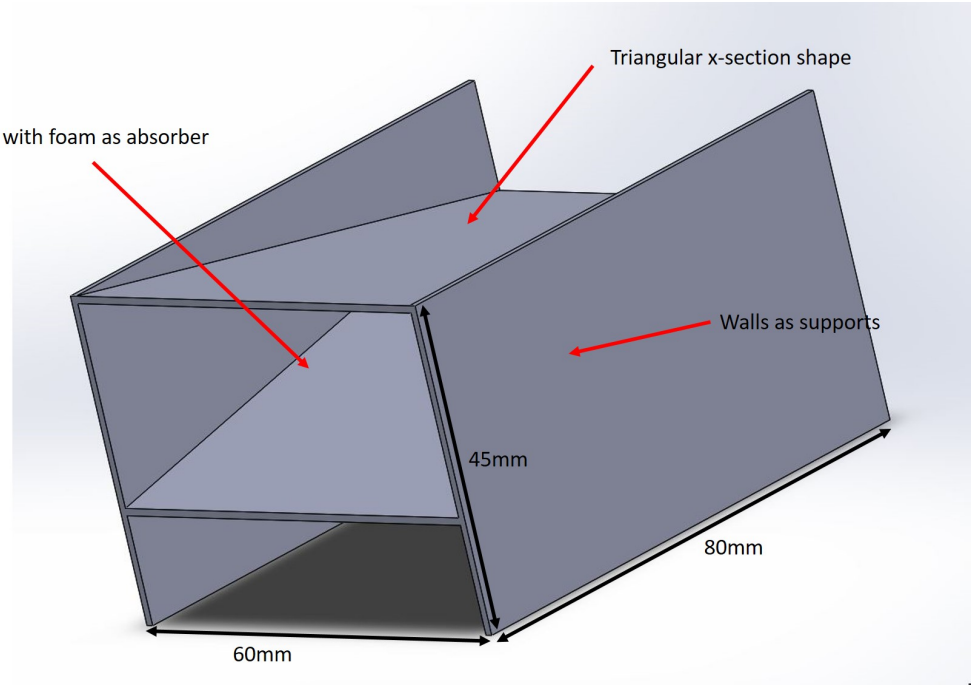

Figure 5.1: The passive, asymmetrical, reciprocal device (PARD) 3D CAD model. The model is labelled and dimensioned.

The PARD was measured in two orientations, forward and reverse. In the forward orientation, the nose of the triangular structure is pointed towards port one, and in the reverse orientation pointed towards port two. The forward and reverse response of S_{11} & S_{21} for the asymmetrical transmission line is shown in Figure 5.3. This response has typical transmission values of close to 0 dB while the magnitude of the reflection tends to increase with frequency from typical values below 40 dB to below 20 dB.

The reverse response mirrors the forward orientation and has typical transmission values of close to 0 dB while the magnitude of the reflection tends to increase with frequency from typical values below 40 dB to below 20 dB. The

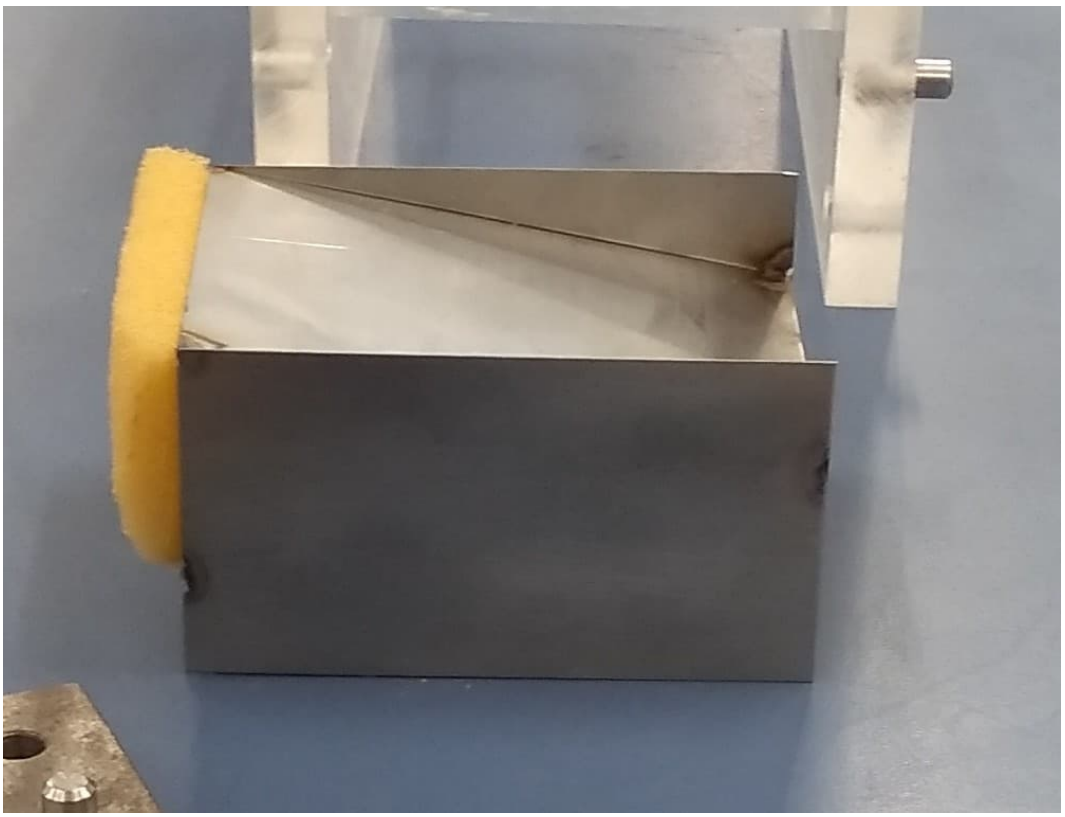

Figure 5.2: The PARD made from thin steel sheet (0.9 mm) and a foam wedge, this structure is then placed in a section of waveguide to complete the vitrifaction standard.

forward and reverse response of S_{22} & S_{12} for the asymmetrical transmission line is shown in Figure 5.4. This response has typical transmission values of -4 dB while the magnitude of the reflection tends to be small.

The repeatability of measurements using the acoustic network analyzer has been shown to have a worst case standard deviation of 0.4 dB [38]. The difference between the forward and reverse orientations for S_{11}, S'_{22}, S_{21}, and S'_{12} is less than 1 dB in most cases. The standard deviation for $S_{11} - S'_{22}$ is 0.506 dB and 0.694 dB for $S_{21} - S'_{12}$. The reflection coefficient is small, and we attribute the increased variance to random (thermal) noise [38, 39]. The variance is consistent with the repeatability of the instrument suggesting that the calibration is performing well.

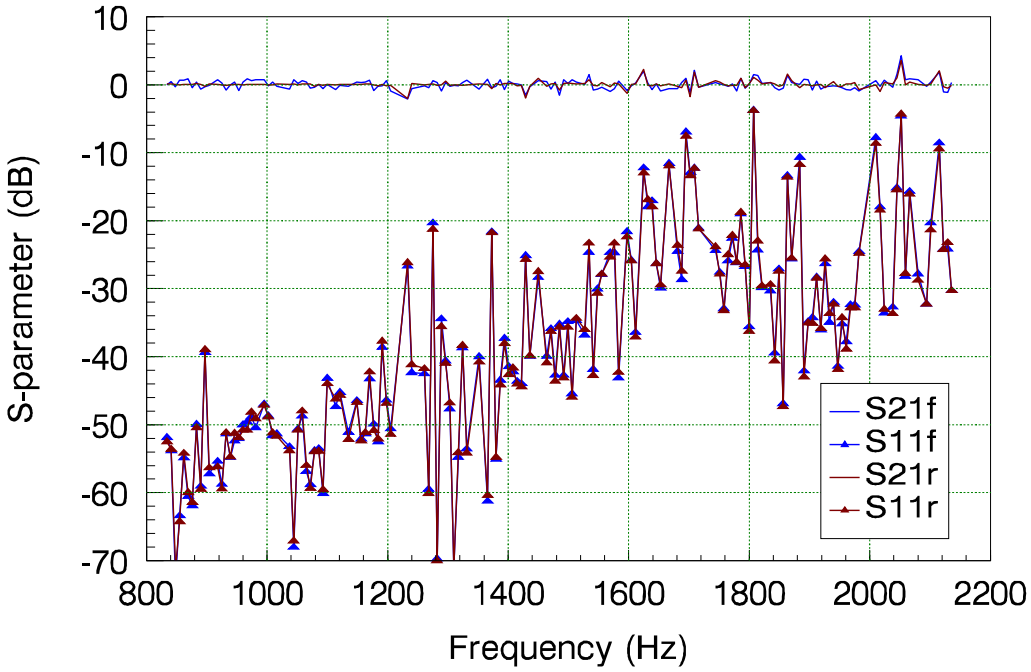

Figure 5.3: Comparison of S_{11} and S_{21} measured on the asymmetrical element inserted each way around. In the legend, S_{21} is labelled S_{21f} and S'_{21} is labelled S_{21r}, etc. Note that S_{21} measured in the first case is virtually indistinguishable from S'_{21} measured with the device physically inserted the other way around. Likewise the input side reflection coefficient S_{11} differs by only small values despite its enormous variability.

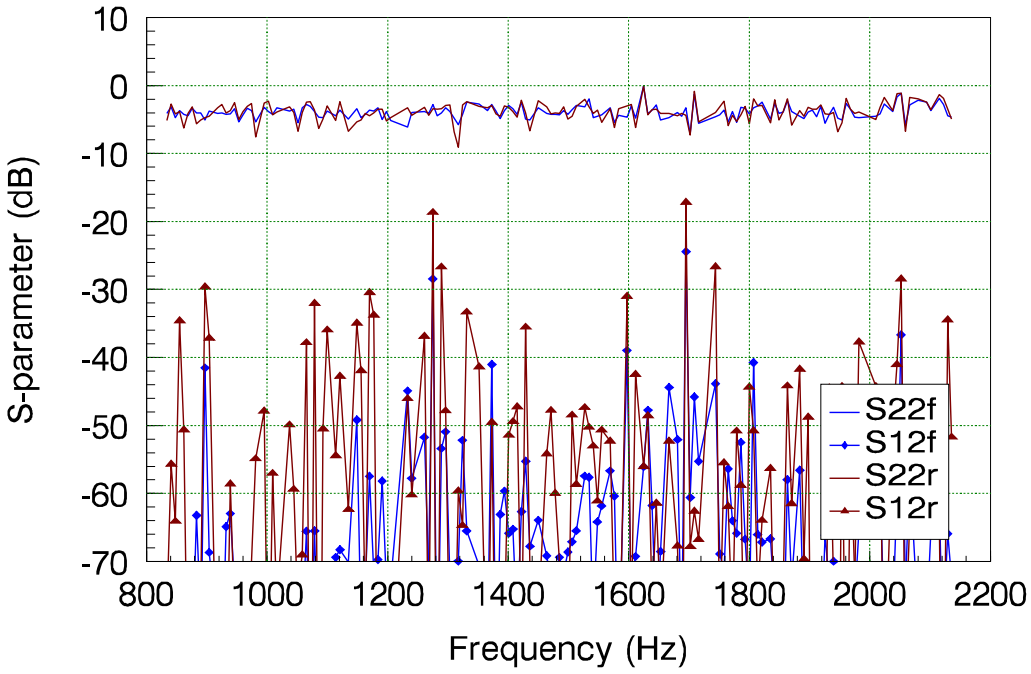

Figure 5.4: Comparison of S_{22} and S_{12} measured on the asymmetrical element inserted each way around. Again the legend has S'_{22} as S_{22r}, etc. The parameters measured in the forward orientation, S_{12f} and S_{22f} agree with the parameters measured in the reverse orientation S_{12r} and S_{22r}.

5.1.2 Comparison of Calibration Computation Methods

The same results should be expected when using either the analytical or numerical solutions to the error matrix. Figures 5.5 and 5.6 show the calibrated results using both methods. These results agree for the transmission coefficients S_{21} and S_{12} and for the reflection coefficients S_{11} and S_{22}. The numerical method on average returns slightly greater reflection coefficients and with greater variance, the transmission coefficients follow very closely with a slight increase in variance as well. The variation in the reflection coefficients can be attributed to the variation in measurements used for the numerical method that are excluded from the analytical one. This is because the five calibration measurements produce an over-determined system. In order to calibrate analytically, duplicate information is not used whereas in the numerical method it is left in leading to a slight increase in variance.

The numerical measurements of the PARD also show that the calibration has been successful. The forward and reverse measurements agree, with a slight increase in variance compared to the analytical method. There is a small variation increase for the results calibrated with the numerical solution of the error matrix.

Selection of a calibration method should be carefully considered for the measurement/application it is being used for. The analytical and the numerical solutions are used regularly in VNA literature. Based on the small amount of research on the acoustic application of both methods, it is perhaps wise to suggest both are viable options and that their trade-offs need to be more thoroughly explored.

5.1.3 Comparison of Corrected and Uncorrected Data

Figures 5.7 and 5.8 present uncorrected and corrected measurements of a zero-length thru re-connection. The data is presented in Smith Chart form, as is customary in the RF world. Traces run from 1220 to 1980 Hz. The plots are presented separately as the corrected data for a zero-length thru appears as

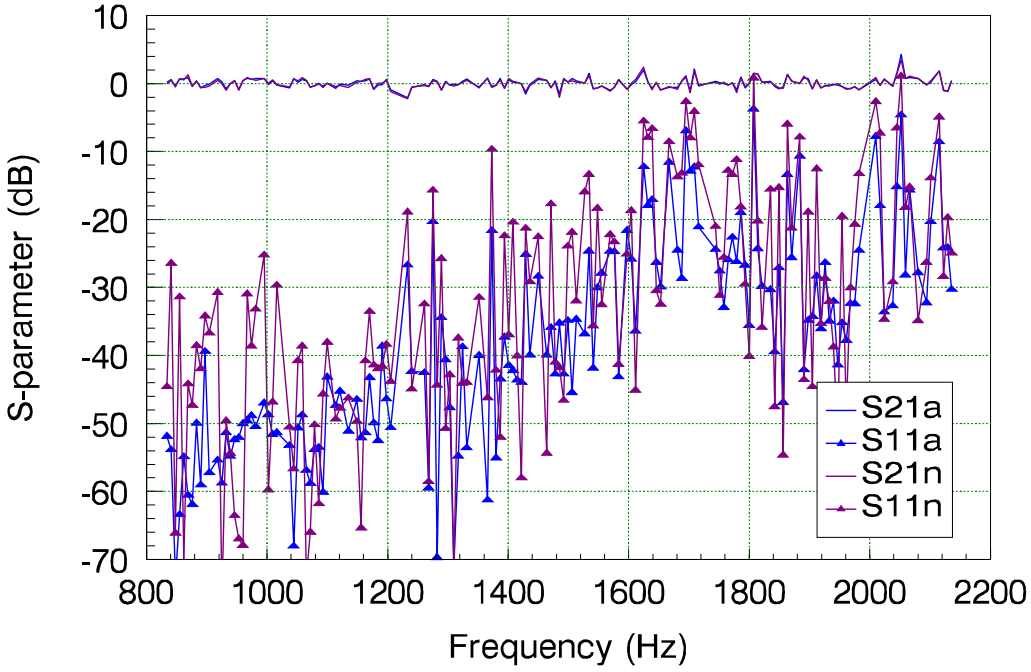

Figure 5.5: Comparison of parameters S_{21} and S_{11} obtained by numerical and analytic solution of the error matrix. The same raw measurements of standards are used in each case.

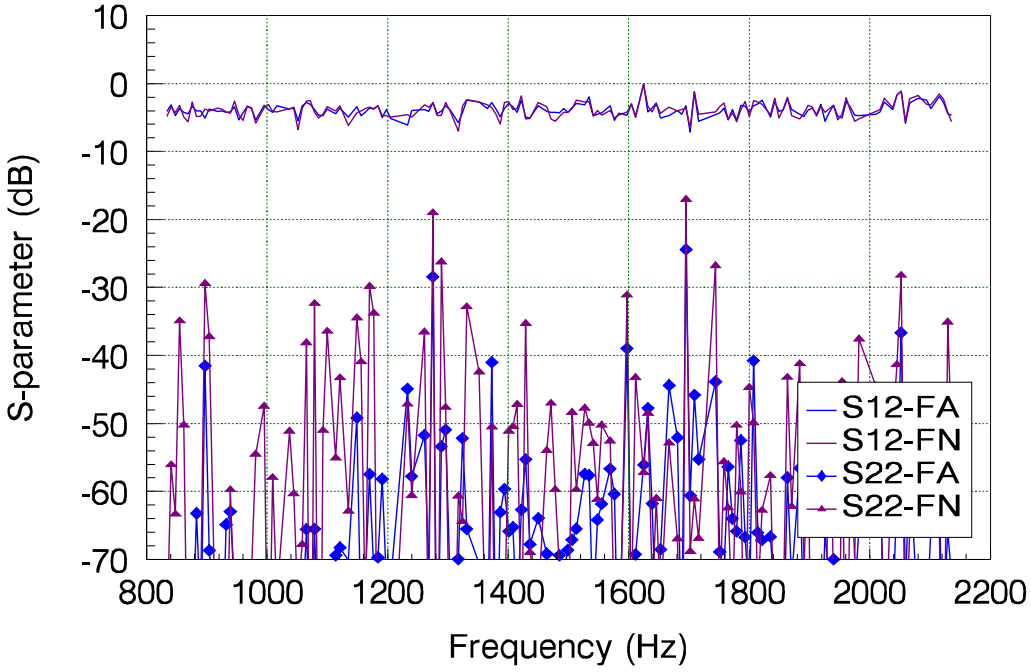

Figure 5.6: Comparison of parameters S_{12} and S_{22} obtained by numerical and analytic solution of the error matrix. The same raw measurements of standards are used in each case.

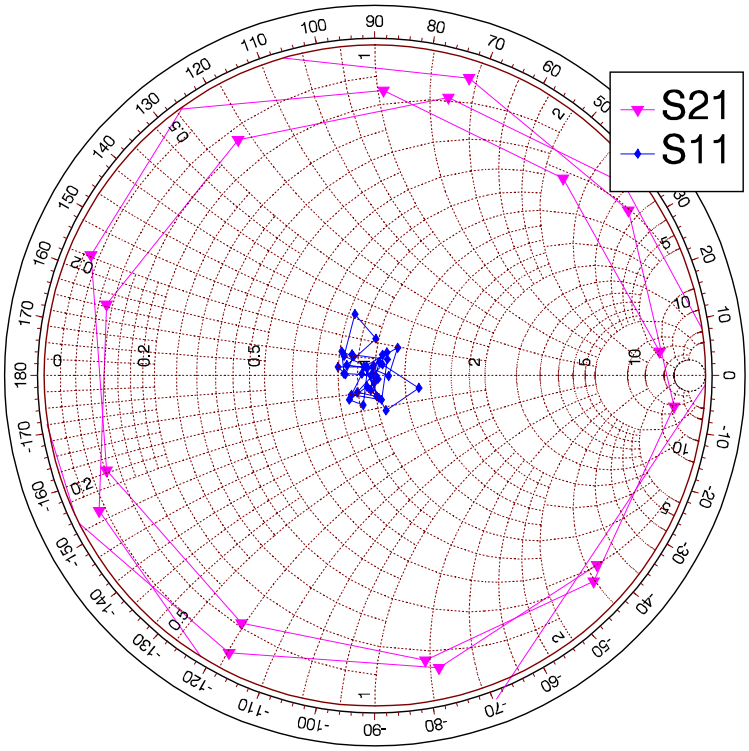

Figure 5.7: The S_{11} and S_{21} values of an uncorrected thru connection plotted on a Smith chart. Frequency runs from 1220 Hz to 1980 Hz.

a single point and can be hard to identify. The uncorrected data shows the wildly-varying magnitude and phase typical of raw data. In the case of Figure 5.8, the zero-length thru data is indicative of the repeatability error. Some data has been removed, especially between 1780 and 1820 Hz, owing to low confidence caused by the selection of sliding load positions. On our prototype it is not possible to check coverage gaps resulting from load position selections in real time, as might be the case on an integrated real-time instrument.

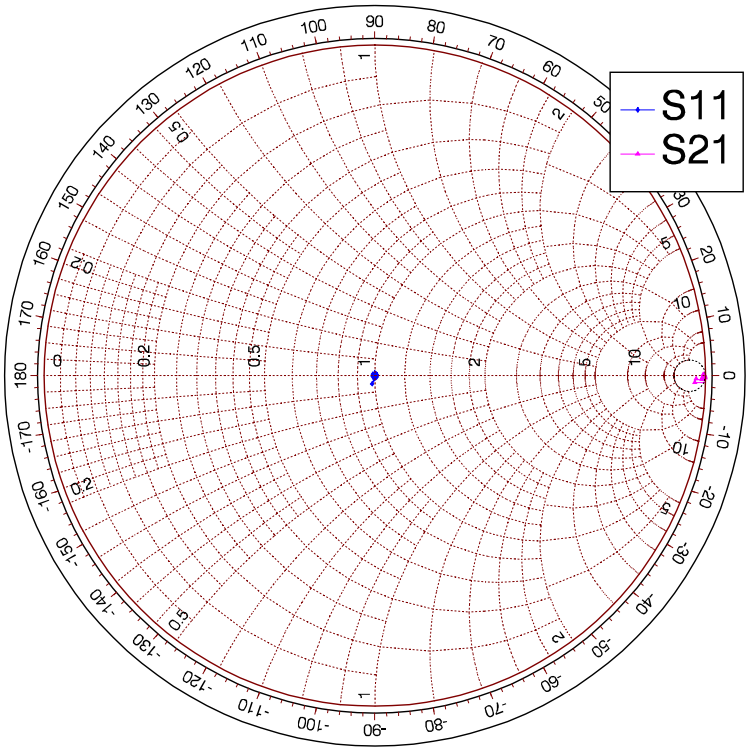

Figure 5.8: The S_{11} and S_{21} values of a zero-length thru after correction plotted on a Smith chart. The zero-length thru data are close to being points so appear as single symbols.

Chapter 6

Future Work

6.1 Limitations & Future Work

The PARD offers a good start to verifying a calibration for the AVNA. Further validation can be achieved with comparison of a measured impedance standard to some simulated results using computational fluid dynamics (CFD), this is beyond the scope of the present work and there are no existing physical standards that allow for the comparison of this measurement instrument to another. At the outset of this research, the intention was to compare the measured acoustic S-parameters of some physical device to simulated ones. The simulation was to be done using computational fluid dynamics (CFD). In any event, no meaningful simulation data was delivered in time. This simulation would have in effect been used as the verification standard in a cal-kit for the analyser. Any future work on acoustic vector network analysis needs to address this particular shortfall in this research.

If Acoustic VNAs become more common another measure of the instrument performance is a "round robin" measurement of standards between standards laboratories. This was common last century with radio frequency measurements [93]. These events involved the participation of different instruments, making good comparisons accross measurement technologies. In the acoustic case the goal should be a "round robin" comparison of acoustic VNAs with

current impedance tube instruments. To do this a DUT that can interface with both AVNA and impedance tubes is required. The calibration methods developed in this thesis could also be adapted to the impedance tube.

The Acoustic vector network analyser as built has some reliability issues that need to be resolved before a commercially viable instrument can be realised. In particular the flanges, directional couplers, and electronics had issues that reduced the instrument's reliability. As built, the low reliability means that calibrations need to be repeated often as parts are repaired or replaced. In addition to increased reliability, the flange system needs to be refined for easier use and higher repeatability.

The acoustic directional coupler may also benefit from the introduction of rubberised connections to loudspeakers and microphones. These rubberised connections could reduce the vibration introduced to the coupler structure by the loudspeaker, and from the coupler structure to the microphones. Furthermore by putting an enclosure on the back of the loudspeaker, leakage may also be reduced.

The reliability of the directional couplers and flanges can be increased in a number of ways. The addition of filleted corners to 3D prints will make them more reliable due to removing stress concentrations. Flanges can be re-enforced and/or be made from materials that improve flange strength. Measurements suggest titanium (Ti64) used in an additive process offers a good balance of directionality, reliability, repeatability, and usability for the 10–20 kHz band. Titanium is an expensive material for manufacturing(≈$1400 NZD for a pair of couplers) but in comparison a commercially available WR-22 12-inch long waveguide section is $505.22 USD at time of writing. The WR-22 is a good comparison because it is used for similar wavelengths and therefore has similar manufacturing constraints and tolerances. A process change could also be explored, it is not uncommon to machine channels into aluminium and the cap the blocks to ahieve lab grade waveguide hardware. The large couplers could also be refined by a material/process change. The acrylic sheet used to

manufacture the large couplers was glued together and typically failed at the glue joints between the main coupler structure and the flange. The repeated bending at these glue joins from bolts clamping them together possibly caused a fatigue like failure. The alignment pins also needed to be re-glued because they would tear out while separating the flanges. When separating the flanges they would need to be moved back and forth laterally which likely stressed the glue joins causing a fatigue like failure. Perspex® is manufactured in accordance with ISO 7823-1, which means for the thickness range of 2 to 25 mm, there is a production tolerance of $\pm 10\%$ plus 0.4 mm (e.g. 8 mm cast sheet could vary from 6.8 mm to 9.2 mm) [95].The tolerance of material stock and manufacturing tolerances will be important to consider when creating more reliable directional couplers and flanges.

The repeatability of the flanges might also be improved by changing the materials and manufacturing processes used. For instance, the 3D printed titanium couplers and flanges have a high reliability but the repeatability is reduced due to the surface finish and the dimensional accuracy of the additive 3D printing process. This could be improved by using both the additive manufacturing process and then using traditional subtractive manufacturing techniques. This would offer a good compromise between cost and performance because the additive manufacturing can reduce the cost of creating the bulk of the directional coupler. And the subtractive manufacturing will then create the high precision/quality features like flanges, alignment pins, holes, and surface finish. The large coupler and flange repeatability could be improved with increased flange rigidity and a new alignment pin system that does not require repeated back and forth movement. The flanges of both sizes would also benefit from having specified tolerances.

The flange system as it is requires a set bolt order and torque at each joint in the system. When carrying out a calibration, five measurements are required on two ports, meaning the flanges are disassembled and reassembled ten times. This process can take a significant amount of time, especially when working

as as an individual. This means that the usability of the flange system could be improved in future to allow for quicker apparatus/system changes. This usability cannot come at the cost of repeatability and needs to be carefully designed. This isn't an issue unique to the acoustic flanges, and there has been some work done by M. Horibe to show that clamps can be used for connections in radio frequency [96]. A cam mechanism might also be an option to apply a repeatable torque on a waveguide flange. The clamp or cam mechanisms could alleviate the large flange alignment pin issues.

Measurements in this research were performed using the inbuilt averaging functions of the HP4395A and the "IF bandwidth" option in particular. Averaging comes at the cost of speed, but improves measurements by reducing the random noise in the measurements [97]. It is not uncommon for RF analysers to average 32 or even 64 sweeps or points. Typically any measurements used for calibration are averaged 2–4 times more than the averaging used in measurement [98]. In future work an "IF Bandwidth"and averaging method could be purpose built for the acoustic analyser that optimizes sweep times and noise reduction for typical acoustic bandwidths and speeds in different propagation media.

The overall design meant the microphones needed an analog output. Finding an analog MEMS microphone was difficult because MEMS devices generally are used in market segments that are focused on miniaturizing their products, for instance the mobile device market. As a result MEMS devices now almost exclusively support a digital communications bus like I^2C or SPI. The electronics for an acoustic vector network analyser in the future should be mostly digital to avoid these problems, but also because the HP4395A analyser should be replaced with new purpose built analyser hardware. This hardware will need to handle data acquisition and calibration and should have a display or an available connection to a display and a some connection to a PC/Network.

The development of a vector-corrected two port acoustic network analyser

represents a compression of some 50 years of radio frequency measurement developments into the acoustic domain. Applications of this instrument will continue to be found in the future. As a starting point the following suggestions may be of interest.

- Rapid, precise measurement of the reflectivity of architectural and furnishing materials,
- Measurement of the sound transmissivity of building insulation materials and seals,
- Determination of the resonant properties of cabinets, tubes, and cavities such as speaker enclosures and engine exhaust structures,
- Characterisation of musical instrument components such as organ and brass pipes,
- Energy absorption provided by cavity filling materials,
- Sonar visibility of insects and other small items,
- Impact on sonar visibility of surface coatings,
- Indirect measurement of biological properties of flora correlated with sound absorption and reflection,
- Non-destructive testing of composite structures, and
- Plastic weld inspection.

As a test of the instruments capability and as a way to provide some meaningful demonstration the following measurements could be made:

- A measurement in a medium other than air, perhaps water or a hydraulic fluid.
- A tuned speaker enclosure.
- An acoustically long length of transmission line.

- A well understood acoustic material, perhaps a commercially available acoustic panel for room treatment.
- Transmission lines of varying geometry like those in shown in figure 6.1.
- Measurement of air humidity through line propagation delay and attenuation.

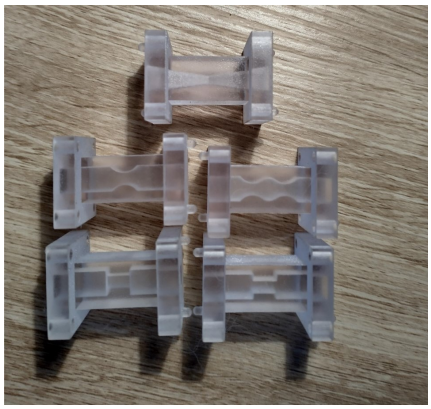

Figure 6.1: A selection of transmission lines, of varying geometry designed for the 10–20 kHz bandwidth.

The 3D printed directional couplers presently extend to the upper bound of the audible spectrum. The extension of the technology into ultrasound would allow the acoustic network analyser technology to find potential applications in:

- Non-contact sensing.
- Motion detection.
- Non-destructive testing.
- Ultrasonic range finding.
- Imaging and acoustic microscopy.
- Ultrasonic disintegration.
- Medical ultrasound applications.
- Ultrasonic SONAR.

Chapter 7

Conclusions

7.1 Summary And Conclusions

This thesis presents an investigation into a prototype measurement instrument. The prototype measurement instrument is an acoustic, vector-corrected, 2-port, network analyzer. This required several developments; a repeatable acoustic waveguide joint, a calibration method(s), calibration standards, and calibration verification.

Directional hardware was provided by the coupler design developed by Lagasse in the 1970s. A flange system was developed to ensure repeatable test fixtures and precise measurment. The flange system was built from acrylic for large waveguide and 3D-printed in plastics and Titanium for higher frequency smaller waveguide. The flange specification includes O-rings, bolt torque and fastening orders. The O-rings were added to prevent leakage but also to allow for the possible pressurisation of the measurement system as well as the use of other gasses or liquids. The flange system performance (repeatability) and reliability has been demostrated and presented. Calibration standards were developed to satisfy the requirements of the TRRM calibration procedure to solve for the sixteen error coefficients of the 16-term VNA error model. Signal leakage can be audable in the acoustic waveguide and using the 8-term or 12-term error model is innapropriatre for acoustic applications. These error terms

are often ignored in radio frequency, meaning that a 12-term or 8-term error model are used instead. The error coefficients are calculated with an analytical, algebraic approach and numerical methods. The performance differences of these approaches have been demonstrated. This is a significant contribution since previous acoustic measurement systems rely upon a calibration against a standard that is not well known. For example, [92] assumed a load, and [55] relied upon lossy lines. Here only an uncertain load and a reflection plate are required. The Acoustic VNA instrument achieves its aim of measurement of acoustic reflectivity and transmissivity and has a partial verification standard in a passive asymmetric, reciprocal device. The results of the analytical and numerical calibration are in a agreement and consistent with what would be expected of a PARD [76].

The acoustic directional coupler as described by Lagasse came at a time when developments in radio frequency vector network analysis were gaining momentum. The engineers of that time however neglected the acoustic equivalent technology. The next development was a calibrated one port analyser, or reflectometer. K. Pennington made considerable developments in creating acoustic standards to achieve this. In particular Pennington adapted the sliding load from the radio frequency domain to the acoustic one. One criticism of the acoustic VNA presented is that each set of couplers or "heads" spans just over an octave. Therefore, to perform measurements over the audio spectrum would require 8 to 10 test sets. An advantage of the acoustic impedance tube is that it can be made to span the human audio range [94].

7.2 Publications Arising From This Work

1. [37] MacDonell, M.S.G., Scott J.B. (2017) Development and Basic Calibration of an Acoustic Vector Network Analyser. Presented at the Electronics New Zealand Conference 2017 (ENZCon 2017), Christchurch, New Zealand, 4-6 December 2017.

2. [38] MacDonell, M. S. G., Scott, J. B., & Basnet, K. (2019). Waveguide joint design and validation for use in acoustic vector-corrected network analysers. Presented at the 2019 IEEE International Instrumentation and Measurement Technology Conference, Auckland, New Zealand.

3. [39] MacDonell, M.S.G., Scott J.B. (2019). Realizing an Acoustic Vector Network Analyser. In Proceedings of the 147th AES Convention (New York). New York, NY 10176.

4. [40] M.MacDonell, and J.Scott, "Full Two-Port Vector-Corrected Network Analyzer in the Acoustic Domain," J. Audio Eng. Soc., vol. 70, no. 3, pp. 185-198, (2022 March.). doi: https://doi.org/10.17743/jaes.2021.0058

Appendix A

Appendix A - Design Drawings

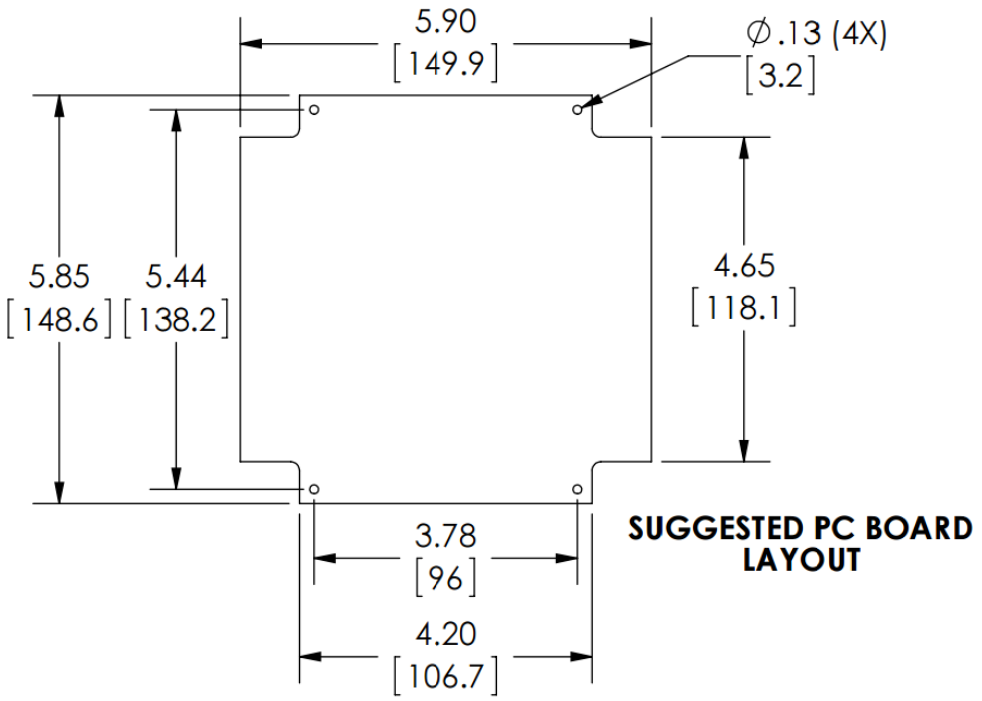

Figure A.1: The recommended Dimensions for a PCB in the head enclosure.

The Cables and pin allocations for the DB9 connections are found in Table A.1.

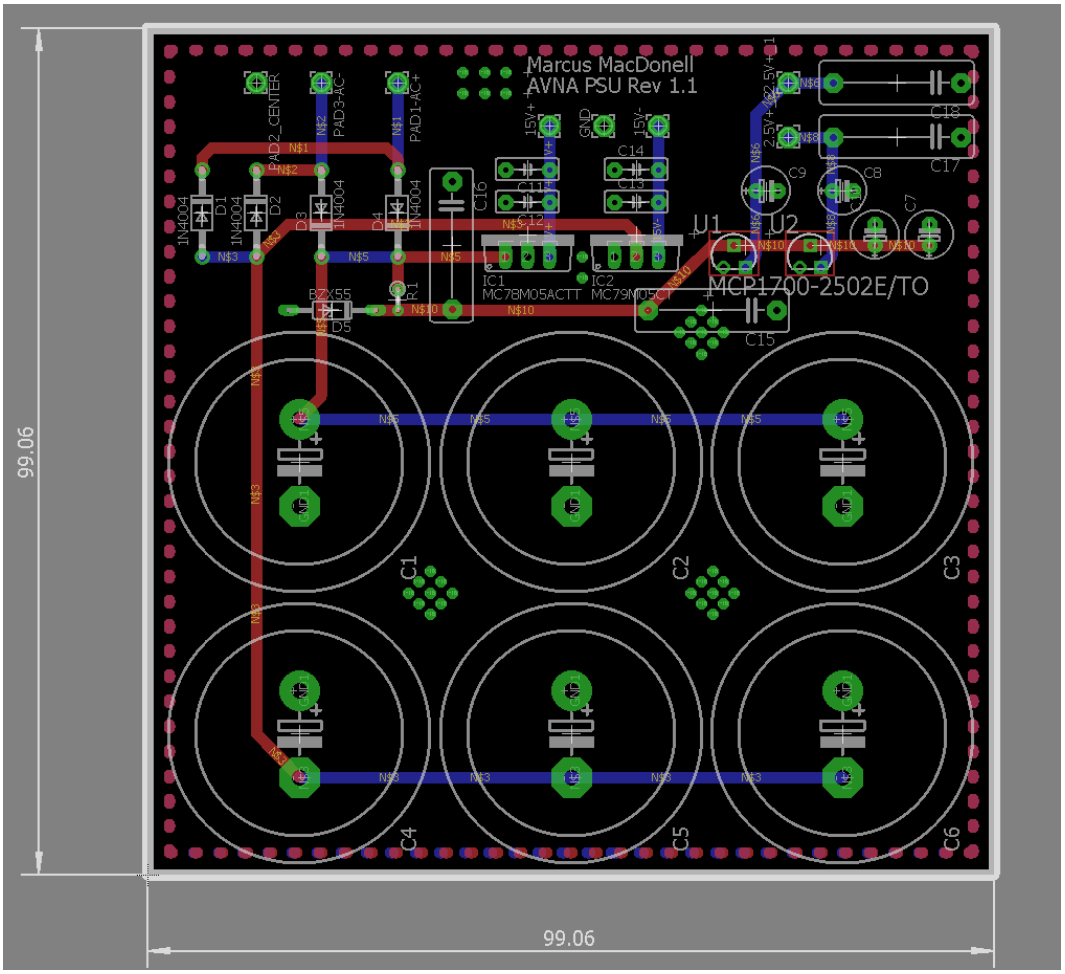

Figure A.2: PSU PCB layout.

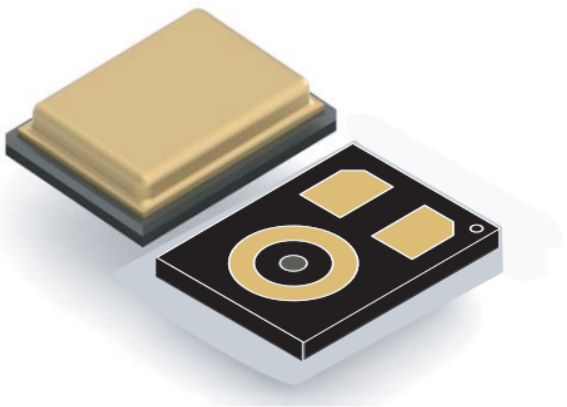

Figure A.3: A 3D model of the MEMS microphones used.

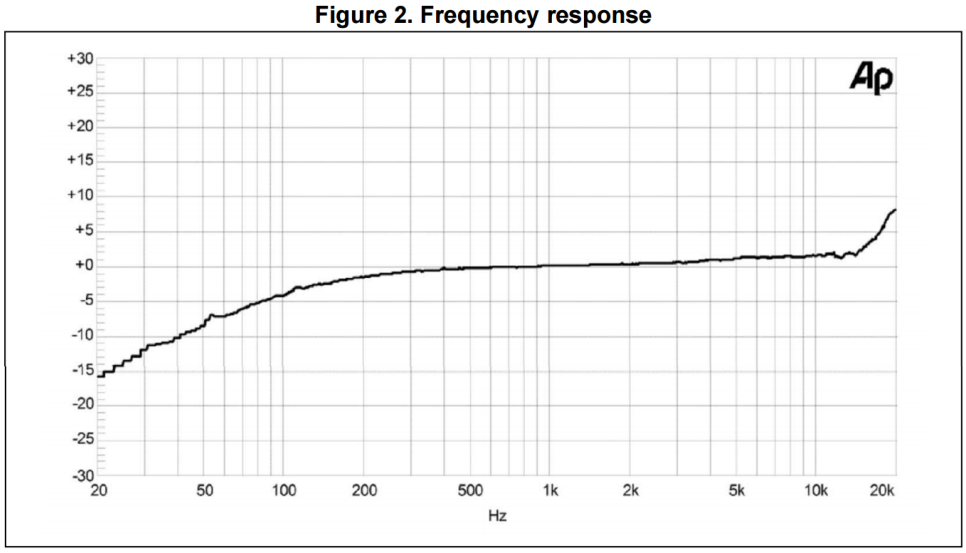

Figure A.4: Frequency response for the MEMS microphones used.

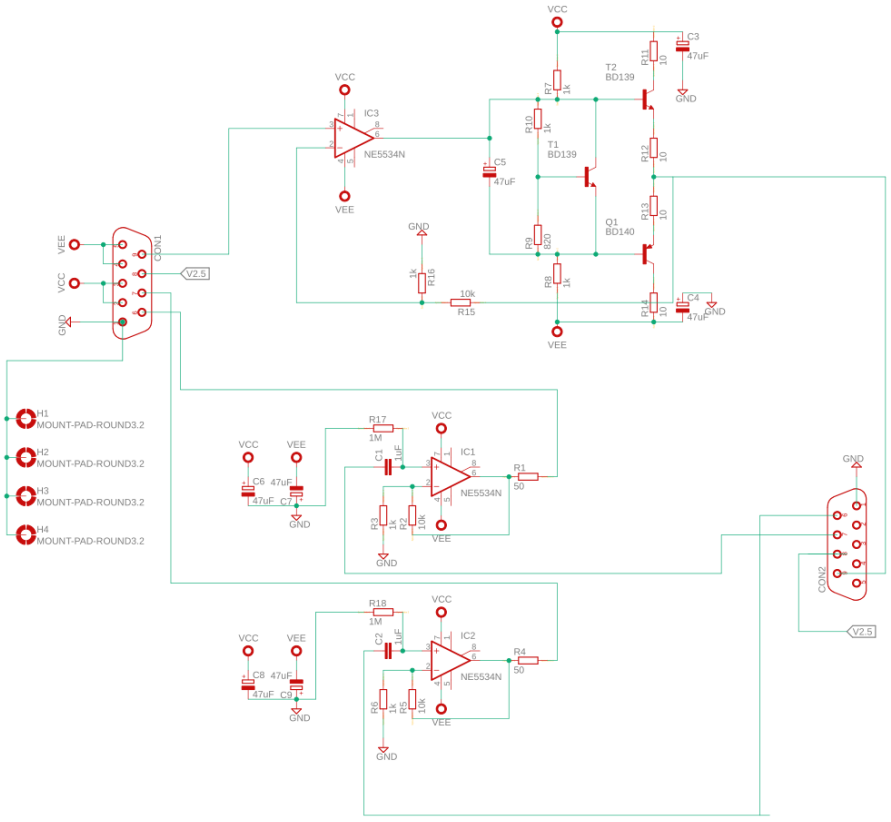

Figure A.5: Remote Head Schematic, contains three audio amplifiers designed to interface the HP3495A with the acoustic waveguide.

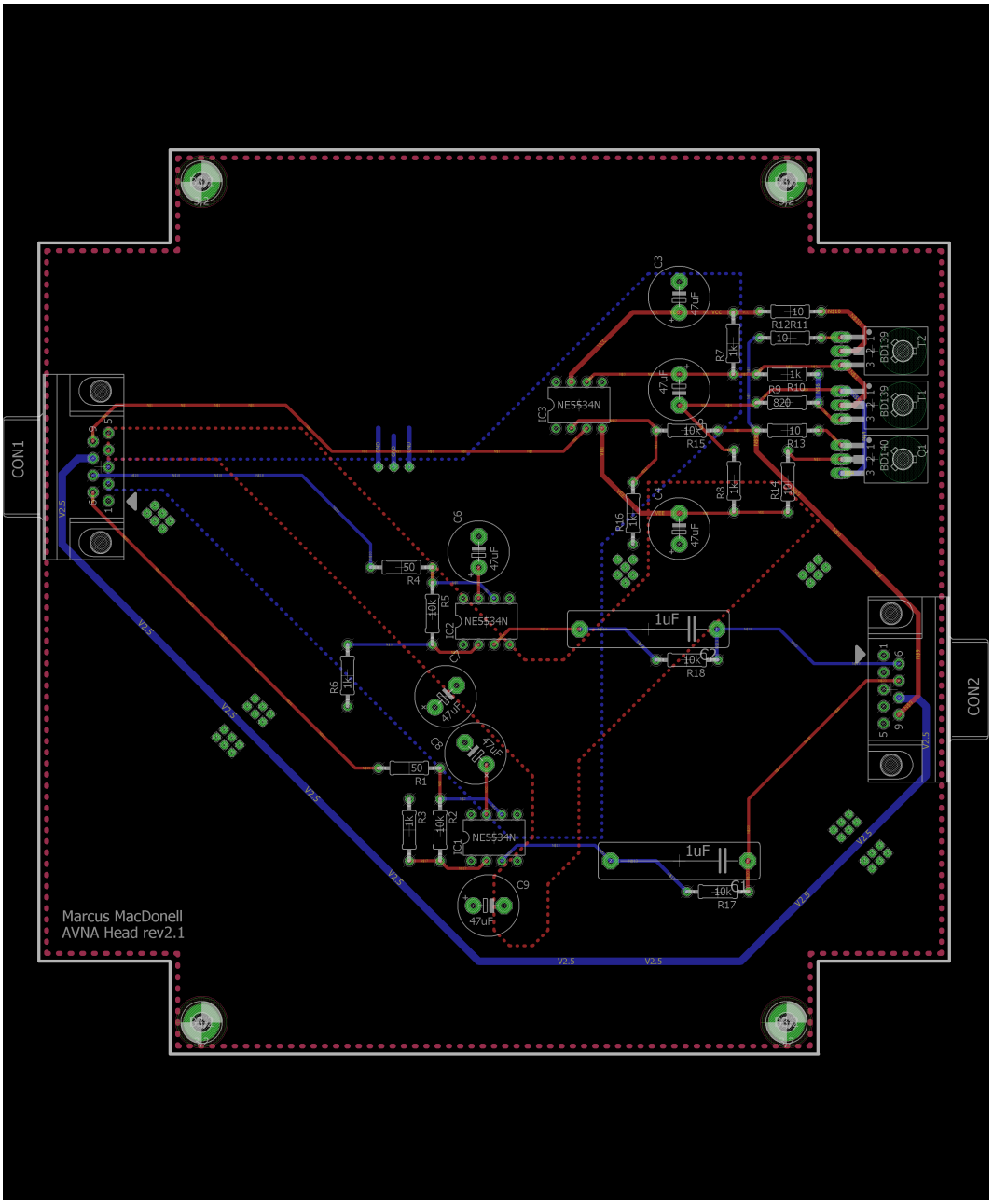

Figure A.6: Remote Head PCB layout, contains three audio amplifiers designed to interface the HP3495A with the acoustic waveguide.

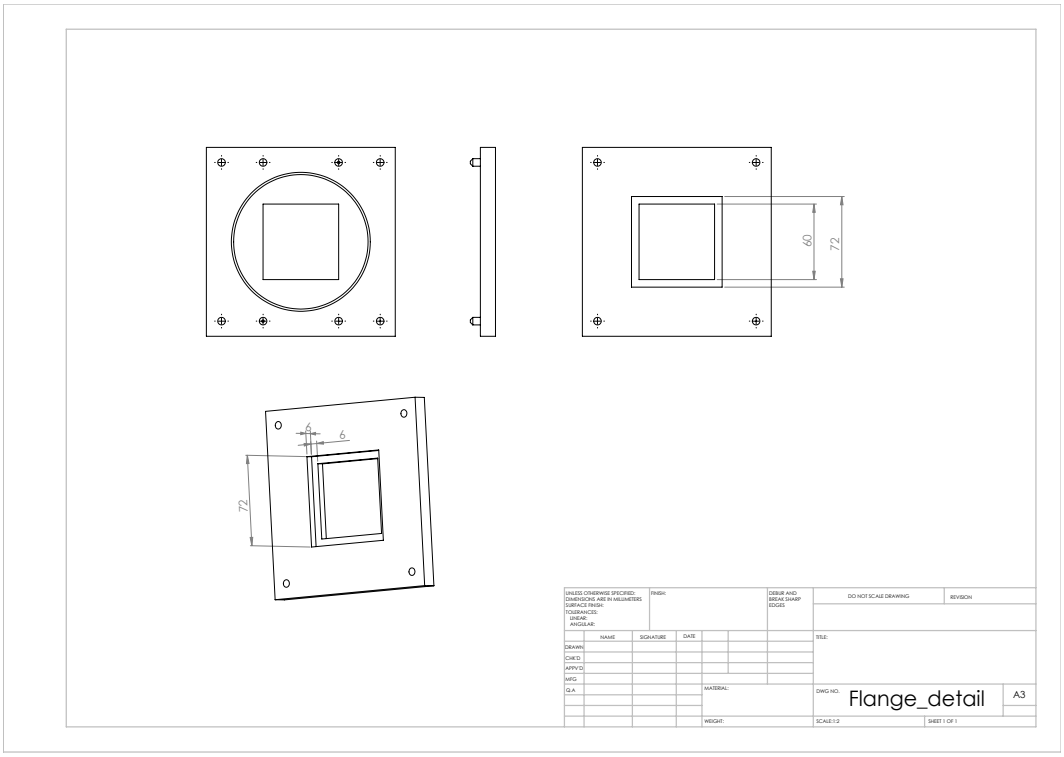

Figure A.7: The flange modification for the directional couplers as built by K. Pennington. These flanges are also used on the sliding load standards for the 1–2 kHz band.

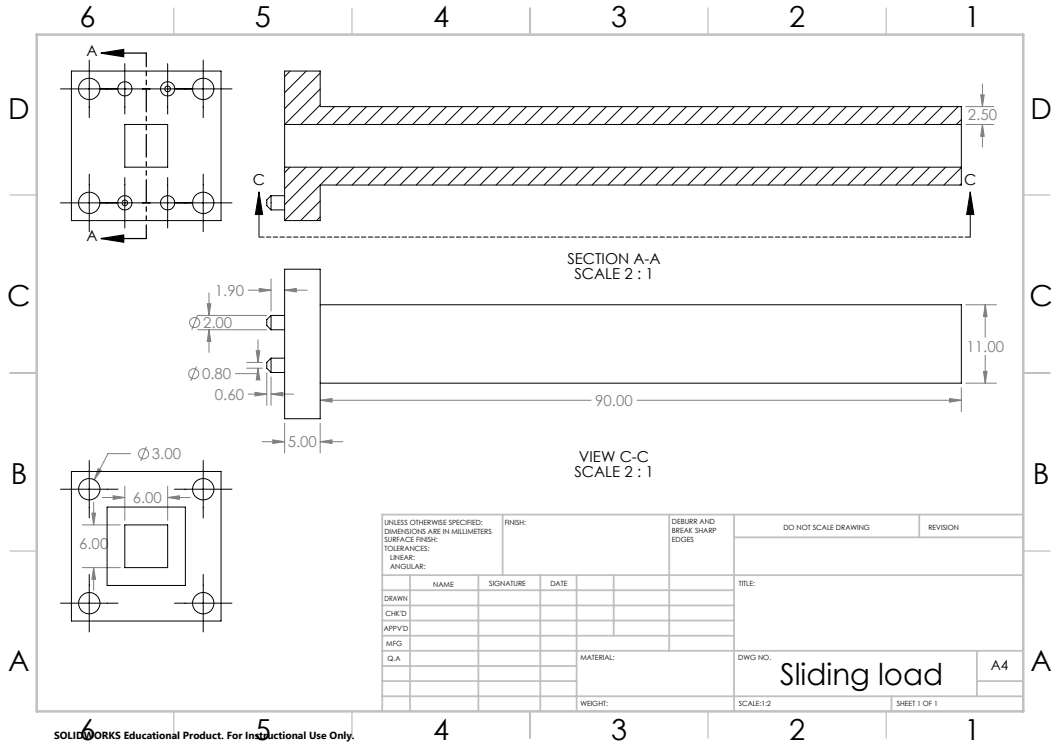

Figure A.8: Mechanical drawings for the 3D printed sliding load standards used for the 10–20 kHz band.

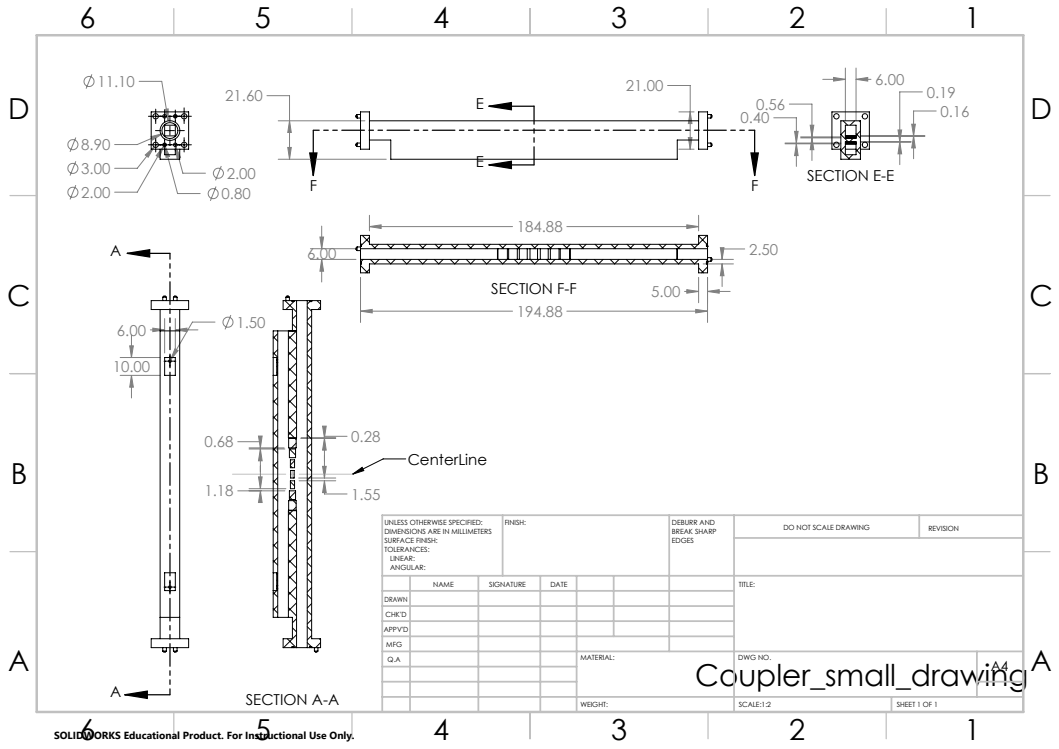

Figure A.9: Mechanical drawing for the directional couplers used in the 10–20 kHz band.

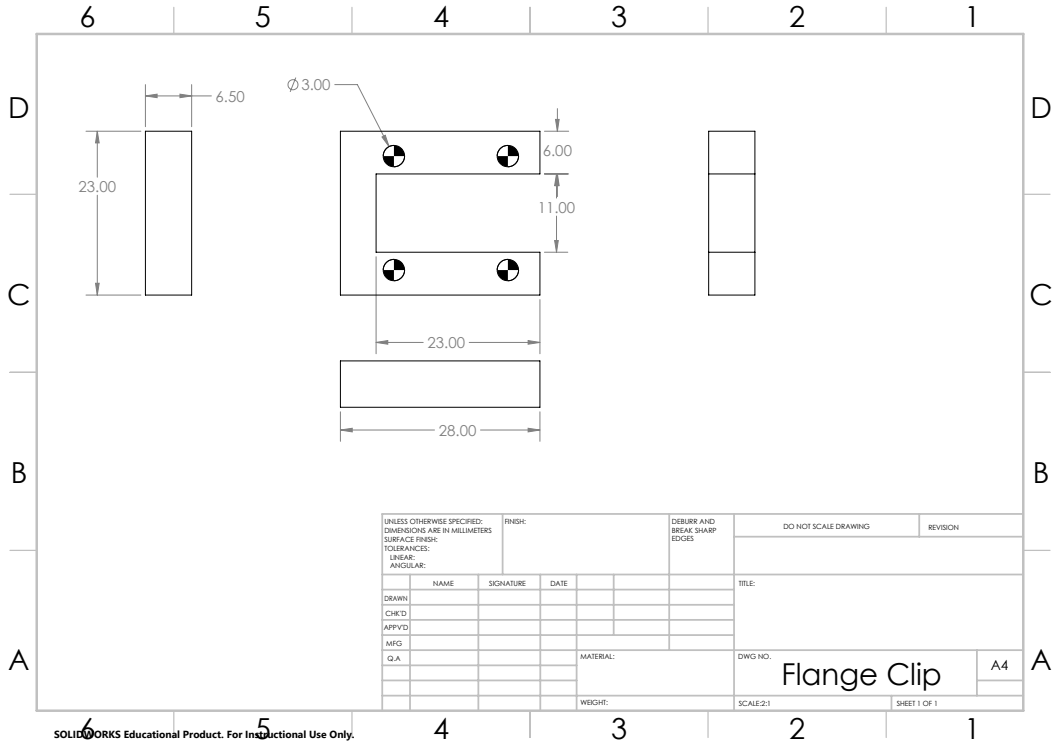

Figure A.10: Mechanical drawing for the U-shaped washer used in the assembly of the 10–20 kHz band flanges. Originally designed to be 3D printed it was eventually made from mild-steel as pictured in Chapter 3 (Hardware) of this thesis.

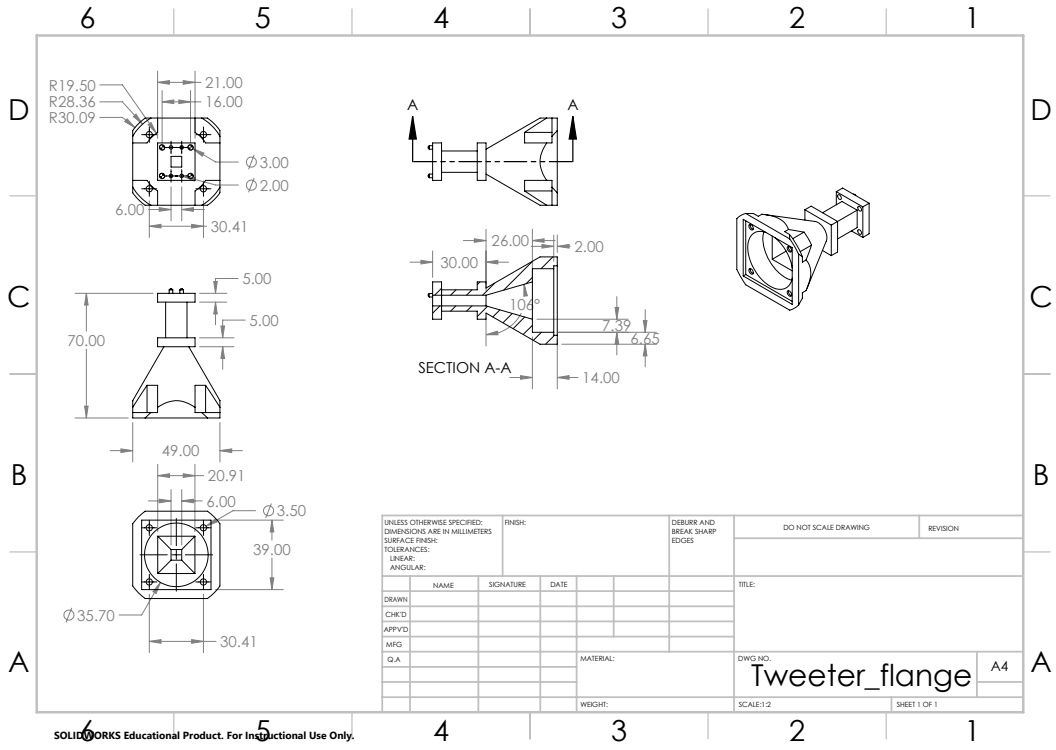

Figure A.11: Mechanical drawing for the horn waveguide section that connects the loudspeaker to the directional coupler for the 10–20 kHz band.

Table A.1: DB9 Pin Allocation

Pin	Colour	Connection
1	red	GND
2	blue	+15
3	orange	+15
4	purple	-15
5	brown	-15
6	green	mic
7	yellow	mic
8	black	+2.5
9	white	GEN
Chassis	N/A	GND(Shield)

Appendix B

Appendix B - Analytical solution

$$E \equiv \begin{bmatrix} E_1 & E_2 \\ E_3 & E_4 \end{bmatrix} = \left[\begin{array}{cc:cc} e_{00} & e_{03} & e_{01} & e_{02} \\ e_{30} & e_{33} & e_{31} & e_{32} \\ \hdashline e_{10} & e_{13} & e_{11} & e_{12} \\ e_{20} & e_{23} & e_{21} & e_{22} \end{array}\right] \tag{B.1}$$

$$\begin{bmatrix} b_0 \\ b_3 \end{bmatrix} = S_m \begin{bmatrix} a_0 \\ a_3 \end{bmatrix}, \; S_m = \begin{bmatrix} S_{11m} & S_{12m} \\ S_{21m} & S_{22m} \end{bmatrix} \tag{B.2}$$

$$\begin{bmatrix} a_1 \\ a_2 \end{bmatrix} = S_a \begin{bmatrix} b_1 \\ b_2 \end{bmatrix}, \; S_a = \begin{bmatrix} S_{11a} & S_{12a} \\ S_{21a} & S_{22a} \end{bmatrix} \tag{B.3}$$

$$S_m = E_1 + E_2 S_a (I - E_4 S_a)^{-1} E_3 \tag{B.4}$$

Where I is the unit matrix. Solving for S_a yields

$$S_a = [E_3 (S_m - E_1)^{-1} E_2 + E_4]^{-1} \tag{B.5}$$

$$\text{Thru:} \quad A = \begin{bmatrix} 0 & T \\ T & 0 \end{bmatrix}$$

$$\text{Match-Match:} \quad B = \begin{bmatrix} 0 & 0 \\ 0 & 0 \end{bmatrix}$$

$$\text{Reflect-Reflect:} \quad C = \begin{bmatrix} \Gamma & 0 \\ 0 & \Gamma \end{bmatrix}$$

$$\text{Reflect-Match:} \quad D = \begin{bmatrix} \Gamma & 0 \\ 0 & 0 \end{bmatrix}$$

$$\text{Match-Reflect:} \quad E = \begin{bmatrix} 0 & 0 \\ 0 & \Gamma \end{bmatrix}$$

$$E = \begin{bmatrix} T_2 T_4^{-1} & T_1 - T_2 T_4^{-1} T_3 \\ T_4^{-1} & -T_4^{-1} T_3 \end{bmatrix}$$

$$T = \begin{bmatrix} E_2 E_1 E_3^{-1} E_4 & E_1 E_3^{-1} \\ E_3^{-1} E_4 & E_3^{-1} \end{bmatrix}$$

$$\begin{bmatrix} b_0 \\ b_3 \\ a_0 \\ a_3 \end{bmatrix} = T \begin{bmatrix} a_1 \\ a_2 \\ b_1 \\ b_2 \end{bmatrix}$$

$$T \equiv \begin{bmatrix} T_1 & T_2 \\ T_3 & T_4 \end{bmatrix} = \left[\begin{array}{cc:cc} t_0 & t_1 & t_2 & t_3 \\ t_4 & t_5 & t_6 & t_7 \\ \hdashline t_8 & t_9 & t_{10} & t_{11} \\ t_{12} & t_{13} & t_{14} & t_{15} \end{array}\right]$$

$$S_m = (T_1 S_a + T_2)(T_3 S_a + T_4)^{-1} \tag{B.6}$$

$$T_1 S_a + T_2 - S_m T_3 S_a - S_m T_4 = 0 \tag{B.7}$$

$$S_a = (T_1 - S_m T_3)^{-1}(S_m T_4 - T_2) \tag{B.8}$$

$$\mathbf{Q} = \begin{bmatrix} 0 & 1 \\ 1 & 0 \end{bmatrix} \tag{B.9}$$

$$\mathbf{N_w} = \begin{bmatrix} 1 & 0 \\ 0 & 0 \end{bmatrix} \tag{B.10}$$

$$\mathbf{S_w} = \begin{bmatrix} 0 & 0 \\ 1 & 0 \end{bmatrix} \tag{B.11}$$

$$\mathbf{N_e} = \begin{bmatrix} 0 & 1 \\ 0 & 0 \end{bmatrix} \tag{B.12}$$

$$\mathbf{S_e} = \begin{bmatrix} 0 & 0 \\ 0 & 1 \end{bmatrix} \tag{B.13}$$

$$\mathbf{I} = \begin{bmatrix} 1 & 0 \\ 0 & 1 \end{bmatrix} \tag{B.14}$$

$$\mathbf{M} = (\mathbf{M_A} - \mathbf{M_C})\mathbf{N} \tag{B.15}$$

$$\mathbf{N} = (\mathbf{M_E} - \mathbf{M_A})^{-1}(\mathbf{M_B} - \mathbf{M_E}) \tag{B.16}$$

$$\mathbf{O} = \mathbf{M_B} - \mathbf{M_C} \tag{B.17}$$

$$\mathbf{P} = (\mathbf{M_A} - \mathbf{M_C})\mathbf{R} \tag{B.18}$$

$$\mathbf{R} = (\mathbf{M_D} - \mathbf{M_A})^{-1}(\mathbf{M_B} - \mathbf{M_D}) \tag{B.19}$$

From the de-embedding equation and the ideal matrices *A*–*E*:

$$\mathbf{M_A}(\mathbf{T_3A} + \mathbf{T_4}) - \mathbf{T_1A} = \mathbf{T_2} \tag{B.20}$$

$$\mathbf{M_B}(\mathbf{T_3B} + \mathbf{T_4}) - \mathbf{T_1B} = \mathbf{T_2} \tag{B.21}$$

$$\mathbf{M_C}(\mathbf{T_3C} + \mathbf{T_4}) - \mathbf{T_1C} = \mathbf{T_2} \tag{B.22}$$

$$\mathbf{M_D}(\mathbf{T_3D} + \mathbf{T_4}) - \mathbf{T_1D} = \mathbf{T_2} \tag{B.23}$$

$$\mathbf{M_E}(\mathbf{T_3E} + \mathbf{T_4}) - \mathbf{T_1E} = \mathbf{T_2} \tag{B.24}$$

By eliminating $\mathbf{T_2}$

$$\mathbf{M_BT_3B} - \mathbf{M_AT_3A} + (\mathbf{M_B} - \mathbf{M_A})\mathbf{T_4} = \mathbf{T_1}(\mathbf{B} - \mathbf{A})$$

$$\mathbf{M_BT_3B} - \mathbf{M_CT_3C} + (\mathbf{M_B} - \mathbf{M_C})\mathbf{T_4} = \mathbf{T_1}(\mathbf{B} - \mathbf{C})$$

$$\mathbf{M_BT_3A} - \mathbf{M_DT_3D} + (\mathbf{M_A} - \mathbf{M_D})\mathbf{T_4} = \mathbf{T_1}(\mathbf{A} - \mathbf{D})$$

$$\mathbf{M_BT_3A} - \mathbf{M_ET_3E} + (\mathbf{M_A} - \mathbf{M_E})\mathbf{T_4} = \mathbf{T_1}(\mathbf{A} - \mathbf{E})$$

$$[\mathbf{M_BT_3B} - \mathbf{M_AT_3A} + (\mathbf{M_B} - \mathbf{M_A})\mathbf{T_4}](\mathbf{B} - \mathbf{A})^{-1} = \mathbf{T_1}$$

$$[\mathbf{M_BT_3B} - \mathbf{M_CT_3C} + (\mathbf{M_B} - \mathbf{M_C})\mathbf{T_4}](\mathbf{B} - \mathbf{C})^{-1} = \mathbf{T_1}$$

$$[\mathbf{M_BT_3A} - \mathbf{M_DT_3D} + (\mathbf{M_A} - \mathbf{M_D})\mathbf{T_4}](\mathbf{A} - \mathbf{D})^{-1} = \mathbf{T_1}$$

$$[\mathbf{M_BT_3A} - \mathbf{M_ET_3E} + (\mathbf{M_A} - \mathbf{M_E})\mathbf{T_4}](\mathbf{A} - \mathbf{E})^{-1} = \mathbf{T_1}$$

$$[\mathbf{M_BT_3B} - \mathbf{M_AT_3A} + (\mathbf{M_B} - \mathbf{M_A})\mathbf{T_4}](\mathbf{B} - \mathbf{A})^{-1}$$
$$= [\mathbf{M_BT_3B} - \mathbf{M_CT_3C} + (\mathbf{M_B} - \mathbf{M_C})\mathbf{T_4}](\mathbf{B} - \mathbf{C})^{-1} \tag{B.25}$$

$$[\mathbf{M_BT_3B} - \mathbf{M_AT_3A} + (\mathbf{M_B} - \mathbf{M_A})\mathbf{T_4}](\mathbf{B} - \mathbf{A})^{-1}$$
$$= [\mathbf{M_BT_3A} - \mathbf{M_DT_3D} + (\mathbf{M_A} - \mathbf{M_D})\mathbf{T_4}](\mathbf{A} - \mathbf{D})^{-1} \tag{B.26}$$

$$[\mathbf{M_BT_3B} - \mathbf{M_AT_3A} + (\mathbf{M_B} - \mathbf{M_A})\mathbf{T_4}](\mathbf{B} - \mathbf{A})^{-1}$$
$$= [\mathbf{M_BT_3A} - \mathbf{M_ET_3E} + (\mathbf{M_A} - \mathbf{M_E})\mathbf{T_4}](\mathbf{A} - \mathbf{E})^{-1} \tag{B.27}$$

Substituting the S-parameters into the previous equations

$$\begin{aligned}&\mathbf{M_A T_3} - (\mathbf{M_B} - \mathbf{M_A})\mathbf{T_4 Q}\frac{\mathbf{1}}{\mathbf{T}}\\&= \mathbf{M_C T_3} - (\mathbf{M_B} - \mathbf{M_C})\mathbf{T_4 Q}\frac{\mathbf{1}}{\mathbf{\Gamma}}\end{aligned} \tag{B.28}$$

$$\begin{aligned}&\mathbf{M_A T_3} - (\mathbf{M_B} - \mathbf{M_A})\mathbf{T_4 Q}\frac{\mathbf{1}}{\mathbf{T}}\\&= \mathbf{M_A T_3}(\mathbf{I} + \mathbf{N_e}\frac{\mathbf{\Gamma}}{\mathbf{T}}) - \mathbf{M_D T_3 N_e}\frac{\mathbf{\Gamma}}{\mathbf{T}}\\&+(\mathbf{M_A} - \mathbf{M_D})\mathbf{T_4}(\mathbf{Q}\frac{\mathbf{1}}{\mathbf{T}} + \mathbf{S_e}\frac{\mathbf{\Gamma}}{\mathbf{T^2}})\end{aligned} \tag{B.29}$$

$$\begin{aligned}&\mathbf{M_A T_3} - (\mathbf{M_B} - \mathbf{M_A})\mathbf{T_4 Q}\frac{\mathbf{1}}{\mathbf{T}}\\&= \mathbf{M_A T_3}(\mathbf{I} + \mathbf{S_w}\frac{\mathbf{\Gamma}}{\mathbf{T}}) - \mathbf{M_E T_3 S_w}\frac{\mathbf{\Gamma}}{\mathbf{T}}\\&+(\mathbf{M_A} - \mathbf{M_E})\mathbf{T_4}(\mathbf{Q}\frac{\mathbf{1}}{\mathbf{T}} + \mathbf{N_w}\frac{\mathbf{\Gamma}}{\mathbf{T^2}})\end{aligned} \tag{B.30}$$

Multiplying by $\frac{T}{\Gamma}$ yields

$$\begin{aligned}&(\mathbf{M_A} - \mathbf{M_C})\mathbf{T_3}\\&= (\mathbf{M_B} - \mathbf{M_A})\mathbf{T_4 Q}\frac{\mathbf{1}}{\mathbf{T}} - (\mathbf{M_B} - \mathbf{M_C})\mathbf{T_4}\frac{\mathbf{1}}{\mathbf{\Gamma}}\end{aligned} \tag{B.31}$$

$$\begin{aligned}&(\mathbf{M_D} - \mathbf{M_A})\mathbf{T_3 N_e}\\&= (\mathbf{M_B} - \mathbf{M_D})\mathbf{T_4 Q}\frac{\mathbf{1}}{\mathbf{\Gamma}} + (\mathbf{M_A} - \mathbf{M_D})\mathbf{T_4 S_e}\frac{\mathbf{1}}{\mathbf{T}}\end{aligned} \tag{B.32}$$

$$\begin{aligned}&(\mathbf{M_E} - \mathbf{M_A})\mathbf{T_3 S_w}\\&= (\mathbf{M_B} - \mathbf{M_E})\mathbf{T_4 Q}\frac{\mathbf{1}}{\mathbf{\Gamma}} + (\mathbf{M_A} - \mathbf{M_E})\mathbf{T_4 N_w}\frac{\mathbf{1}}{\mathbf{T}}\end{aligned} \tag{B.33}$$

$(\mathbf{M_A} - \mathbf{M_C})$ is not guaranteed to exist, by multiplying by $\mathbf{N_e}$ and then by $\mathbf{S_w}$, noting that $\mathbf{QN_e} = \mathbf{S_e}$ and $\mathbf{QS_w} = \mathbf{N_w}$

$$\begin{aligned}&(\mathbf{M_A} - \mathbf{M_C})\mathbf{T_3 N_e}\\&= (\mathbf{M_B} - \mathbf{M_A})\mathbf{T_4 S_e}\frac{\mathbf{1}}{\mathbf{T}} - (\mathbf{M_B} - \mathbf{M_C})\mathbf{T_4 N_e}\frac{\mathbf{1}}{\mathbf{\Gamma}}\end{aligned} \tag{B.34}$$

$$\begin{aligned}&(\mathbf{M_A} - \mathbf{M_C})\mathbf{T_3 N_e}\\&= (\mathbf{M_B} - \mathbf{M_A})\mathbf{T_4 S N_w}\frac{\mathbf{1}}{\mathbf{T}} - (\mathbf{M_B} - \mathbf{M_C})\mathbf{T_4 S_w}\frac{\mathbf{1}}{\mathbf{\Gamma}}\end{aligned} \tag{B.35}$$

$$\mathbf{T_3 N_e} = (\mathbf{M_D} - \mathbf{M_A})^{-1} \Bigg[(\mathbf{M_B} - \mathbf{M_D}) \mathbf{T_4 Q} \frac{\mathbf{1}}{\mathbf{\Gamma}} + (\mathbf{M_A} - \mathbf{M_D}) \mathbf{T_4 S_e} \frac{\mathbf{1}}{\mathbf{T}} \Bigg] \tag{B.36}$$

$$\mathbf{T_3 S_w} = (\mathbf{M_E} - \mathbf{M_A})^{-1} \Bigg[(\mathbf{M_B} - \mathbf{M_E}) \mathbf{T_4 Q} \frac{\mathbf{1}}{\mathbf{\Gamma}} + (\mathbf{M_A} - \mathbf{M_E}) \mathbf{T_4 N_w} \frac{\mathbf{1}}{\mathbf{T}} \Bigg] \tag{B.37}$$

$$(\mathbf{M_A} - \mathbf{M_C})(\mathbf{M_D} - \mathbf{M_A})^{-1}(\mathbf{M_B} - \mathbf{M_D}) \mathbf{T_4 Q} + (\mathbf{M_B} - \mathbf{M_C}) \mathbf{T_4 N_e} + (\mathbf{M_C} - \mathbf{M_B}) \mathbf{T_4 S_e} \frac{\Gamma}{T} = 0 \tag{B.38}$$

$$(\mathbf{M_A} - \mathbf{M_C})(\mathbf{M_E} - \mathbf{M_A})^{-1}(\mathbf{M_B} - \mathbf{M_E}) \mathbf{T_4 Q} + (\mathbf{M_B} - \mathbf{M_C}) \mathbf{T_4 S_w} + (\mathbf{M_C} - \mathbf{M_B}) \mathbf{T_4 N_w} \frac{\Gamma}{T} = 0 \tag{B.39}$$

Using the defined matrices **M**–**R** a more compact representation is

$$\mathbf{P T_4 Q} + \mathbf{O T_4 N_e} - \mathbf{O T_4 S_e} \frac{\Gamma}{T} = 0 \tag{B.40}$$

$$\mathbf{M T_4 Q} + \mathbf{O T_4 S_w} - \mathbf{O T_4 N_w} \frac{\Gamma}{T} = 0 \tag{B.41}$$

$$m = (P_{21} + O_{21}) M_{22} - (P_{22} + O_{22}) M_{21} \tag{B.42}$$

$$n = O_{21} P_{12} - O_{22} P_{11} \tag{B.43}$$

$$o = (M_{12} + O_{12}) P_{11} - (M_{11} + O_{11}) P_{12} \tag{B.44}$$

$$p = O_{12} M_{21} - O_{11} M_{22} \tag{B.45}$$

As t_{12} is set to 1 and

$$\mathbf{T_4} = \begin{bmatrix} t_{12} & t_{13} \\ t_{14} & t_{15} \end{bmatrix}$$

the remaining t_n values can be found, t_{15} or $\frac{\Gamma}{T}$ must first be calculated from a second-order equation

$$\left(\frac{\Gamma}{T}\right)^2 = \frac{mo}{np}(t_{15})^2 = \frac{mp}{no}\frac{P_{12}^2}{M_{22}^2}t_{12}^2 \tag{B.46}$$

$$\frac{\Gamma}{T} = -\frac{o}{p}\frac{M_{22}^2}{P_{11}^2}\frac{t_{15}}{t_{12}} \tag{B.47}$$

$$t_{15} = -\frac{p}{o}\frac{P_{11}^2}{M_{22}^2}\frac{\Gamma}{T}t_{12} \tag{B.48}$$

$$t_{14} = -\frac{M_{21}}{M_{22}}t_{12} \tag{B.49}$$

$$t_{13} = -\frac{P_{12}}{P_{11}}t_{15} \tag{B.50}$$

$$t_{11} = (N_{21}t_{13} + N_{22}t_{15})\frac{1}{\Gamma} - t_{14}\frac{1}{T} \tag{B.51}$$

$$t_{10} = (R_{21}t_{12} + R_{22}t_{14})\frac{1}{\Gamma} - t_{15}\frac{1}{T} \tag{B.52}$$

$$t_9 = (N_{11}t_{13} + N_{12}t_{15})\frac{1}{\Gamma} - t_{12}\frac{1}{T} \tag{B.53}$$

$$t_8 = (R_{11}t_{12} + R_{12}t_{14})\frac{1}{\Gamma} - t_{13}\frac{1}{T} \tag{B.54}$$

$$t_7 = M_{B21}t_{13} + M_{B22}t_{15} \tag{B.55}$$

$$t_6 = M_{B21}t_{12} + M_{B22}t_{14} \tag{B.56}$$

$$t_5 = M_{B11}t_{13} + M_{B12}t_{15} \tag{B.57}$$

$$t_4 = M_{B11}t_{12} + M_{B12}t_{14} \tag{B.58}$$

$$t_3 = MC21t_9 + MC22t_{11} - \frac{1}{T}(O_{21}t_{13} + O_{22}t_{15}) \tag{B.59}$$

$$t_2 = MC21t_8 + MC22t_{10} - \frac{1}{T}(O_{21}t_{12} + O_{22}t_{14}) \tag{B.60}$$

$$t_1 = MC11t_9 + MC12t_{11} - \frac{1}{T}(O_{11}t_{13} + O_{12}t_{15}) \tag{B.61}$$

$$t_0 = MC11t_8 + MC12t_{10} - \frac{1}{T}(O_{11}t_{12} + O_{12}t_{14}) \tag{B.62}$$

Appendix C

Publications

C.1 EnzCon 2017 Conference Paper

Reference: MacDonell, M., & Scott, J. B. (2017). Development and Basic Calibration of an Acoustic Vector Network Analyser. Presented at the Electronics New Zealand Conference 2017 (ENZCon 2017), Christchurch, New Zealand, 4-6 December 2017.

Development and Basic Calibration of an Acoustic Vector Network Analyser

Marcus MacDonell
Department of Engineering
University of Waikato
Hamilton, NZ

Jonathan Scott
Department of Engineering
University of Waikato
Hamilton, NZ

***Abstract*—This project aims to develop a method that drastically improves measurement of the acoustic properties of objects. Previous research at the University of Waikato has made progress with acoustic technologies as a precursor to a dual port vector network analyser. These technologies have been furthered to this end by 3D printing a modified coupler that now includes a flange with alignment pins, and a groove to house an O-ring as well as a number of other "custom" components for the coupler assembly. This assembly has been interfaced successfully with a VNA and collected data, this process is not straightforward and requires carefully thought-out adjustment to produce sensible data. Complicating this process is the vast difference in propagation speeds for acoustic and electromagnetic signals. The swept measurements performed show promising results that further prove the hardware and indicate that particular calibration terms namely those for isolation that are normally ignored in the electromagnetic domain are potentially crucial in the acoustic domain.**

***Index Terms*—Vector Network Analysis, Waveguide, Acoustic.**

I. Introduction

This project aims to develop a method that drastically improves measurement of the acoustic properties of objects. These objects can be measured using manual techniques, but these techniques are often impractical or too uncertain [1]. We aim to achieve fast, easy, traceable measurements by applying the lessons from six decades of highly successful research into fast, traceable microwave electromagnetic (EM) network measurements to the acoustic domain to develop an Acoustic Vector-corrected Network Analyser (AVNA). The instrument will take the form of a test set that integrates with a commercial electromagnetic Vector-corrected Network Analyser, and a set of carefully modeled standards. A key step in the development of this measurement system is the construction of an acoustic test set, remote heads and calibration standards, this paper discusses the development of these crucial elements.

This concatenation of techniques is possible because the wavelengths of sound waves in air and water are comparable to the wavelengths of radio waves in free space. There are many modern applications of acoustic measurement. These include, but are not limited to the following: Characterising the absorption of sound by furnishings or architectural materials, estimating dry matter yield of pasture via its acoustic permeability, tuning the impedance presented by wind or brass instruments, establishing the safety margin of ear plugs by traceable measurement of their transmission of sound as a function of frequency, finding the frequency response of various ear canal shapes, measuring the sonar cross section of an insect you wish to detect or the reflection from a torpedo that you might wish to conceal, the reflectivity of a tumour you seek with ultrasound, optimising energy loss in a muffler, or the undesirable transmission of sound through an air duct. All of these measurement challenges are approached crudely, looking as did their electromagnetic equivalents in the 1950s and early 1960s.

Technical advances in electromagnetic measurement spanning the last 60 years have led to the VNA that can be purchased today [2]. VNAs are manufactured by a number of global companies, for example Keysight Technologies in the USA, Rhode & Schwarz in Germany, Anritsu based out of Japan, and Copper Mountain sourced from Russia. Although the VNA is accepted as the most precise and versatile measurement instrument available to radio-frequency and microwave designers, clever advances continue to appear, especially in the arena of calibration and traceability. These improvements are spurred on by the advance to millimeter-wave and terahertz domains.

Low-cost, single-box commercial VNAs are available with operating bandwidths from low frequency up to 500 MHz; more expensive units reach 67 GHz. This implies free space wavelengths from many meters down to 600 mm in the case of the low-cost units, or down to about 5 mm for the 67 GHz flagship machines. When higher frequencies are required, or waveguide ports are needed, it is customary for the instrument to be extended from the single box by means of remote measurement heads, providing an outboard test set. Provision is made on many VNAs for the attachment of such remote heads. These may be manufactured in house, or supplied to the manufacturer by a third party. In the case of Keysight Technologies, suppliers such as OML Microwave or Virginia

The Authors would like to thank SFTI for funding this research.

Diodes provide the remote head components.

Acoustic measurement of network properties for sound and vibration application, in contrast, is an underdeveloped but very important technology. Equipment supplied by the likes of Brüel & Kjær, a leader in the field, is not vector corrected, and is rarely traceable to national standards. Measurements are often laborious, mechanical, and expensive. An Acoustic VNA provides a solution to these problems.

Two standards outline current methods for measuring acoustic impedance: ISO 10534-1:1996 and ISO 10534-2:1998. These standards rely on 'Impedance tubes' and use the 'standing wave ratio' or 'transfer function' methods respectively [10] [11]. The AVNA addresses the issues of applying laborious methods by being able to perform swept measurements of the parameter of interest directly. To do this the AVNA will require some known standards. Although these standards do not yet exist, it is expected that they will be analogous to those required for a TRL or TRM calibration.

Acoustic impedance is the effective resistance of a material to vibration. In the case of solids impedance is therefore related to many familiar material properties like stiffness (Young's modulus) and hardness but also it's geometry and structure. These properties in combination contribute to the amount of energy transmitted through the material via vibration and the amount of energy reflected from the interface. S-parameters of a VNA describe the transfer of energy in terms of source and sink. In a dual port system the subscripts of the S-parameter describe the port the energy originated from and the port the energy was received. For example energy transmitted is S_{21} and energy reflected is S_{11}.

The following sections detail the development of the hardware for the AVNA as well as indicative measurements of materials whose acoustic properties are somewhat known such as stiff metals, foam and earplugs to show that the hardware is functional.

II. Hardware

Previous work at the University of Waikato has made progress with acoustic waveguide showing that 3D printing enables effective scaling to mm waveguide [3] and that a sliding load enables the approximation of an ideal acoustic load [4]. This body of research led to the desire to calibrate a reflectometer, i.e a single port measuring S_{11} [4]. Calibrating a single port is difficult to do because there does not exist an analogous acoustic standard for the 'open' in the standard '12 term' calibration process. The inability of most existing VNAs of appropriate bandwidth to perform calibrations intended for waveguide (8 term model etc) further complicates the problem. Following a single port calibration the logical next step is the calibration of a dual port system. The dual port system is envisaged to look much like a modern VNA system with remote heads. An example of such a system is shown in figure 1.

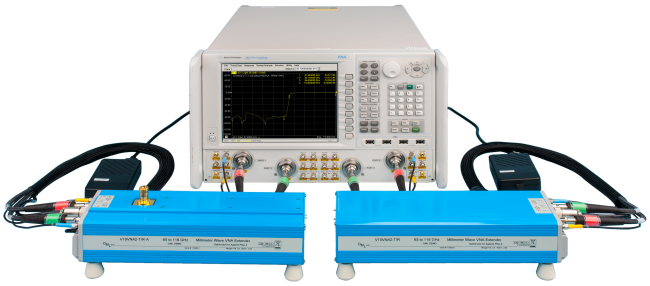

Fig. 1. A Keysight Performance Network Analyser system with remote heads containing all the mm-Wave components. [12]–[14]

The indicative measurements presented in this manuscript aim to verify the operation of acoustic remote heads constructed in-house, and to be used in conjunction with an early generation HP/Agilent 4395A vector network analyser. We essentially show uncalibrated Smith charts that indicate the system as a whole is functioning as expected, i.e., demonstrating directional separation.

A. Flange Design

This project continues work done with the acoustic directional coupler design of Lagasse [5]. The design, scaled to work in the upper half of the audible spectrum (10–20 kHz), is realised using 3D printing. A second set of heads, scaled for 1–2 kHz, is being constructed using conventional workshop facilities out of transparent acrylic.[1]

A major historical issue in the advance of microwave components was the development of a satisfactory standard for connecting waveguides, i.e., the flange design. We have, likewise, had to design a mechanical arrangement for connection of components. The larger heads destined for use from 1–2 kHz are less demanding, just as high-power waveguide for L-band (frequency 1–2 GHz, wavelength 150–300 mm) is straightforward. Nevertheless, mechanical stresses have demanded that the flanges in this system be made stronger. The directional coupler from [3] has been modified to include a flange with alignment pins, and a groove to house an O-ring. This is required to obtain good alignment and an air-tight seal. An example of the new flange design can be seen in figure 2. This figure presents the design of a short through length that is intended to be used in the 2-port calibration procedure.[2]

[1]The use of two coupler sets, and the chosen frequency ranges, exercises the two fabrication technologies. The physically larger set, and the use of transparent acrylic, makes for a system whose inner form is plainly visible and easier to explain.

[2]Although beyond the scope of this manuscript, we feel the need to point out that one of the challenges in the design is determining the "electrical length" of a piece of guide in the acoustic world. In the case of EM radiation, air is virtually indistinguishable from space, but in the acoustic world the air is the medium of energy transfer, and temperature, humidity, and the like affect the speed of propagation.

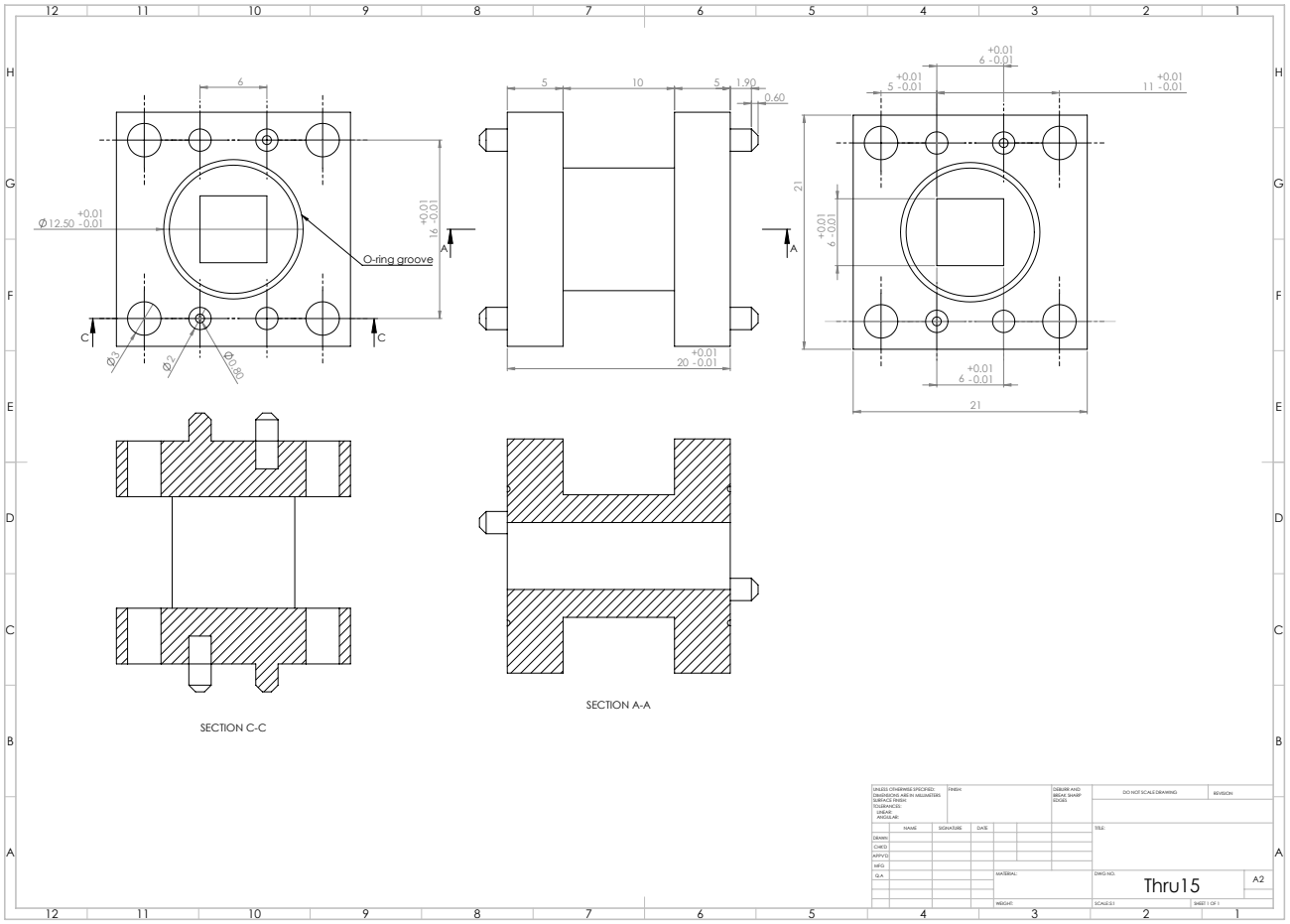

Fig. 2. Solidworks technical drawing of a proposed Thru to be 3D printed for calibrating the dual port system.

A number of other "custom" components are needed. For example, a waveguide horn for the attachment of the driver and mounting holes for MEMS microphones. These are the acoustic equivalent of the electromagnetic structures that introduce waves to the guide or collect and rectify waves in detectors, etc.

It will only be after calibration that the repeatability of guide junctions can be assessed. Nevertheless, we have some confidence. This kind of "bootstrapping" occurred a lot in the early development of microwave systems, which explains why it took 50 years to get from a few GHz to a few hundred GHz. We hope to short-circuit much of this in the acoustic domain by learning from the EM mm-Wave domain.

B. VNA Interface

A block diagram of the required hardware for an AVNA is shown in Figure 3. A large portion of the required hardware can be found in the 4395A, but the rest must be custom built to interface with the 4395A. An 87511A test-set has been retrofitted with the remaining hardware and capacity to connect the acoustic waveguide heads.

Figure 4 is a block diagram of the Agilent 87511A test-set as configured to measure the reflection coefficient S_{11}. This block diagram shows the switching and coupler layout of the test-set in the electromagnetic domain that must be replicated in the acoustic domain.

It should be noted that the 4395A does not support TRL (Thru, Reflect, Line) or TRM (Thru, Reflect, Match) calibration methods, nor any waveguide calibration standards. [7] This is because, with a maximum operating frequency of 500 MHz, the designers did not imagine it would ever have waveguide application, or be used in situations where SOLT (Short, Open, Load, Thru) calibration might not be able to achieve more than enough accuracy. All of these will be implemented in a controlling computer, treating the VNA as a simple synthesiser with three channels of phase-resolving receivers.

The test setup to measure S_{11} has been realised with the hardware seen in Figures 5 & 6. The hardware is comprised of a block of amplifiers, loudspeaker, microphones and cabling. The amplifiers on the PCB are to drive the loudspeaker and to amplify the microphone signals specifically to interface with the 50 Ω input ports on the HP4395A.

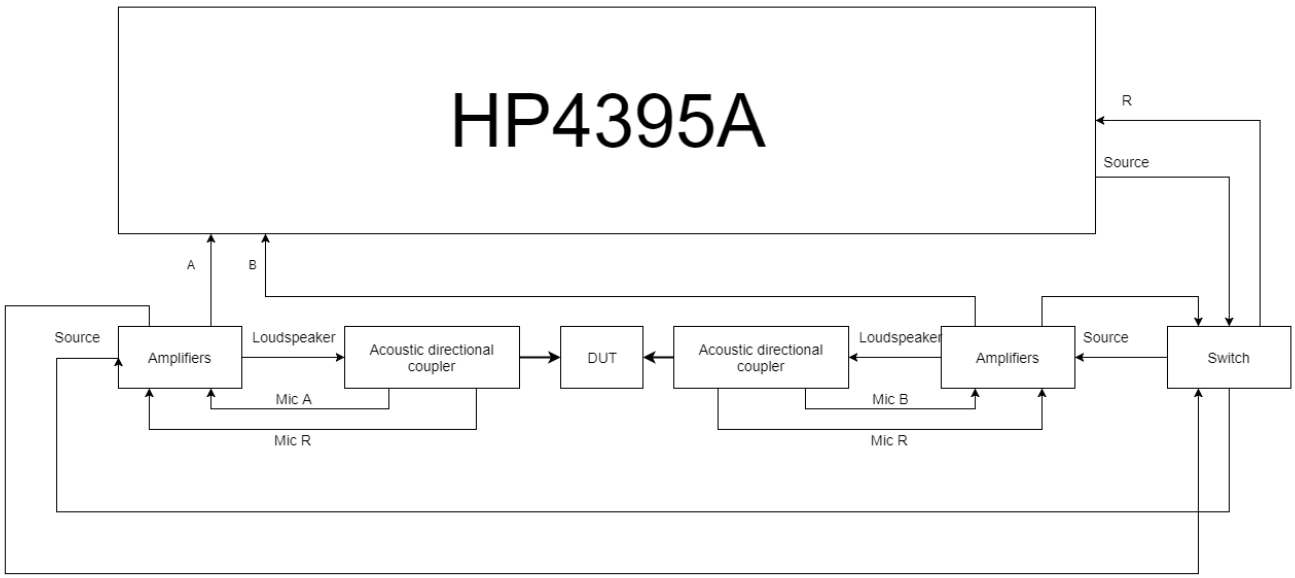

Fig. 3. A block diagram of the hardware required for the acoustic VNA. The R, A and B signals refer to microphone signals, where R is the 'reference' microphone or FWD coupled signal and A and B are the REV coupled signals of either port. So S_{11} is the ratio of A/R and S_{21} is the ratio of B/A. DUT stands for 'Device under test'.

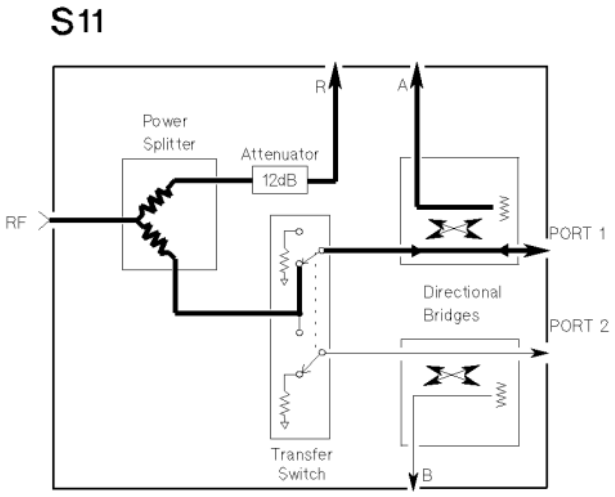

Fig. 4. Block diagram of the 87511A test-set configured to measure S_{11}. [6]

The Dayton audio ND20FB-4 is a 4 Ω tweeter with a usable frequency range of 3.5–25 kHz, making it suitable for the 10–20 kHz coupler set. Its rear mount design makes it ideal for mounting to the coupler via a horn waveguide.

The microphones used are the MP23AB02B, a high-performance analog bottom-port MEMS (Micro-electromechanical systems) device. The MP23AB02B covers the full audible frequency range but becomes more responsive at frequencies above 15 Hz. Its characteristics above 20 kHz

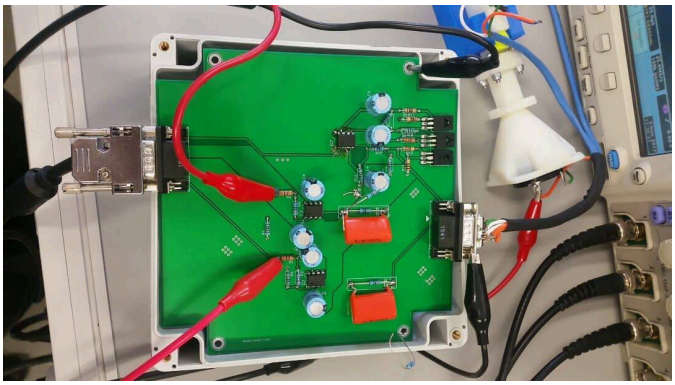

Fig. 5. Remote head PCB assembly.

are not specified.

The frequency response of the speaker and microphones will have some effect on the overall response of the system but these can ultimately be corrected via calibration.

In figure 8 the MEMS microphone can be seen mounted to a PCB that is turn mounted to the coupler, the assembled flange for the horn-coupler interface can also be seen.

C. Acoustic Gotchas

In a conventional network analyser, the generator and receiver are phase locked and sweep simultaneously through the desired frequency span. The speed of acoustic signals ($\approx$ 340 ms^{-1}) is much slower than the speed of light ($\approx 300 * 10^6$ ms^{-1}), therefore in the acoustic domain the signal being measured would not be the same frequency as the signal at the source. This is due to the energy taking milliseconds

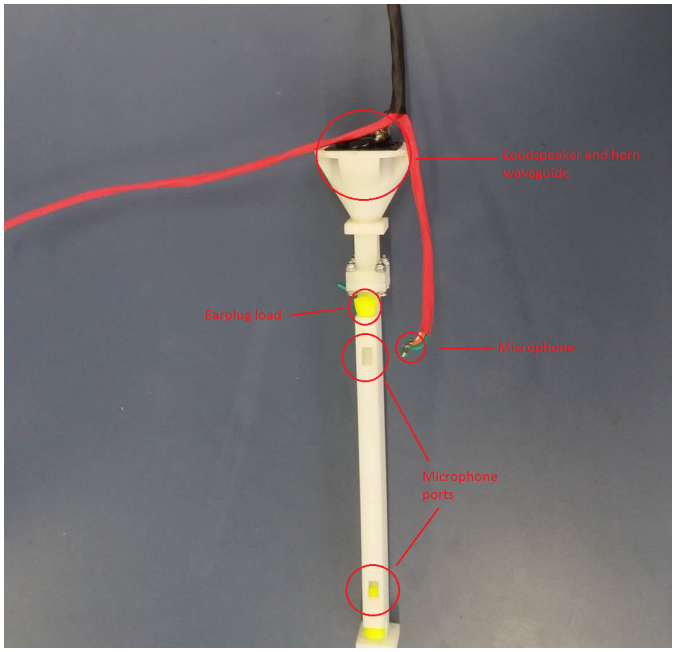

Fig. 6. Coupler assembly for the remote head.

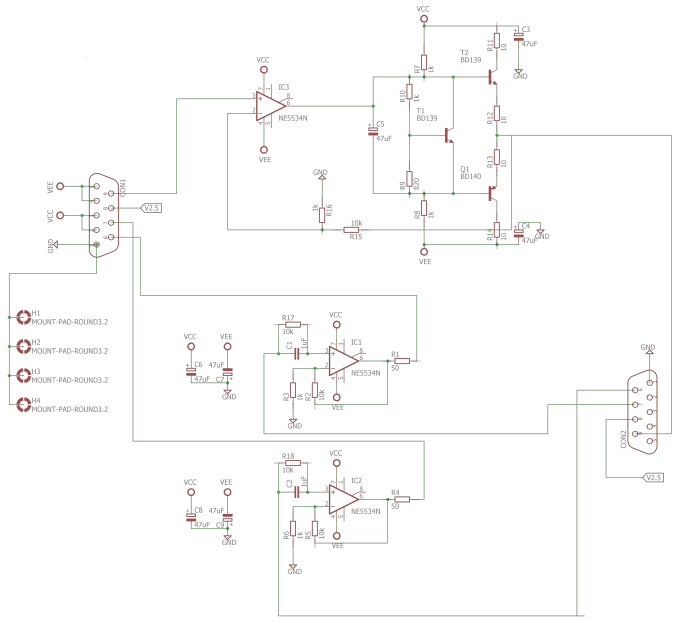

Fig. 7. Remote Head PCB Schematic, contains three audio amplifiers designed to interface the HP3495A with the acoustic waveguide.

to propagate through the hardware. Without allowing for this huge difference in propagation speed, results will make very little sense. The dwell time specifies the time the generator stays at each frequency step in the sweep before the analyser takes the measurement. The sweep speed must be considerably reduced so that the energy has time to bounce back and forth a few times through the test setup before data is captured.

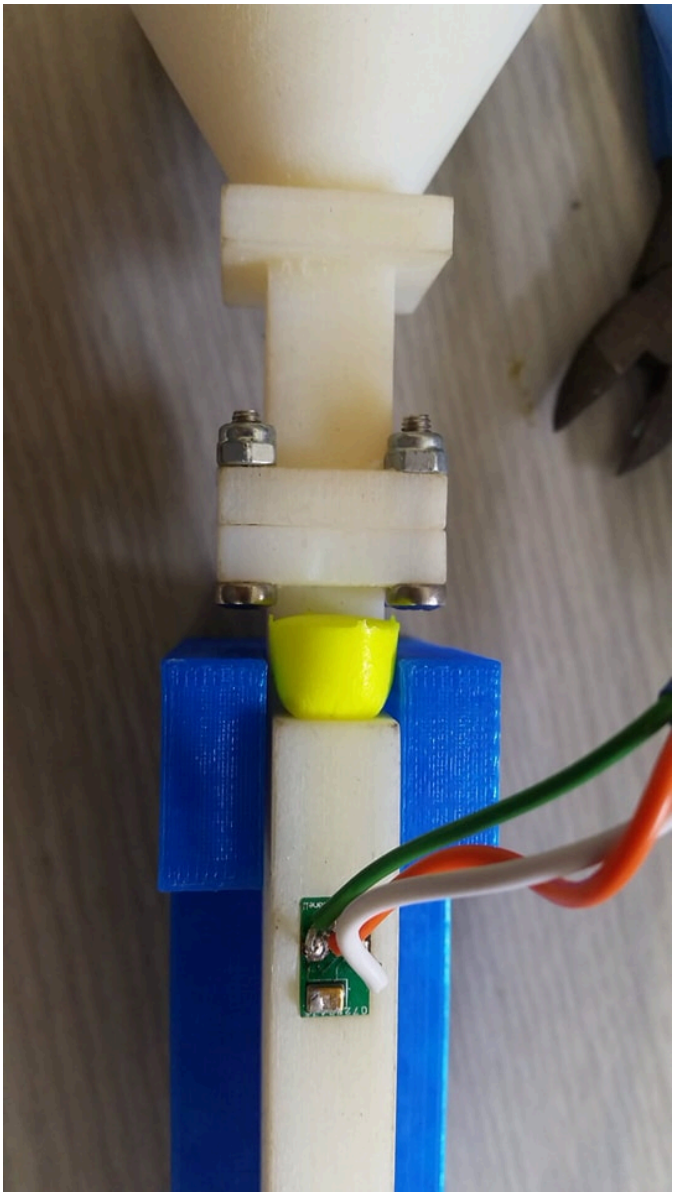

Fig. 8. Coupler assembly with mounted microphones and loudspeaker.

Next, the phase delay through the setup is relatively huge. This means that a small change in frequency causes a huge change in phase. Any practical number of points in a sweep give random-looking results on a Smith chart. Port extension compensates for the phase shift of an extended measurement reference plane due to cables, adapters, and fixtures. Port extension is used predominantly when a calibration is unable to be performed directly at the device or at a convenient place. In this case we are as yet unable to calibrate, but we need to compensate for the (electrical) length of waveguide in the system. This is done by estimating the length of time waves will take to propagate within the waveguide system, and adjusting the port extension so as to “unravel” the data points on the display.

III. Results

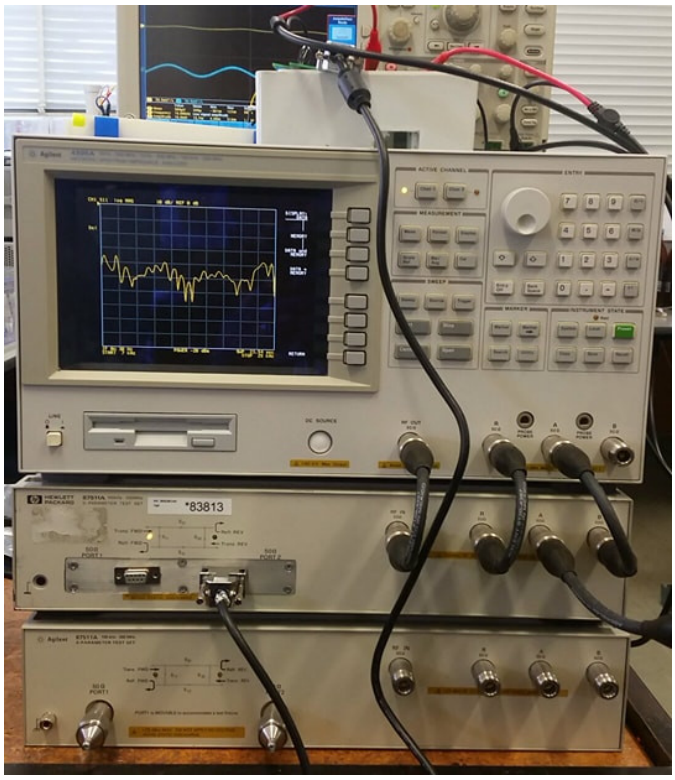

Fig. 9. AVNA set-up.

Figure 9 shows the AVNA set-up. The amplifier PCB is connected to the test-set and coupler assembly via DB9 connectors, the microphones are powered by an internal power supply, as is the amplifier PCB. A Tektronix MSO 4054 oscilloscope was used to check levels, monitor operation, and ensure there was no system failure during measurement. (Setup is still fragile at this stage.)

By using the data-to-memory and math functions, traces can be shown for multiple S_{11} measurements on the instrument display. Figure 10 captures key results for the 10–20 kHz coupler.

The blue trace shows uncalibrated S_{11} with the port terminated with a titanium plate that is assumed to be very reflective with negligible transmission. The assumption that the titaniums is very reflective is made because of the thickness and stiffness of the titanium plate. The plate was laser sintered and can be seen in figure 11.

The yellow trace has the port terminated with a load in the form of an ear plug. With appropriate dwell time and port extension the Smith chart has been made to display sensible uncalibrated results.

In this case the coupler is nearly 200 mm in total length so a port extension was made to approximately 200–300 μs, corresponding to approximately 70–100 mm. For our larger couplers the port extensions will need to be in the order of milliseconds.

Fig. 10. Both S_{11} traces for the metal reflect and the load as displayed on the HP4395A screen. The smith chart shows amplitude information as a ratio of the source power (therefore always ≤ 1) as the distance from the center, position indicates phase, the arcs from the outside of the circle to the far right are lines of constant phase.

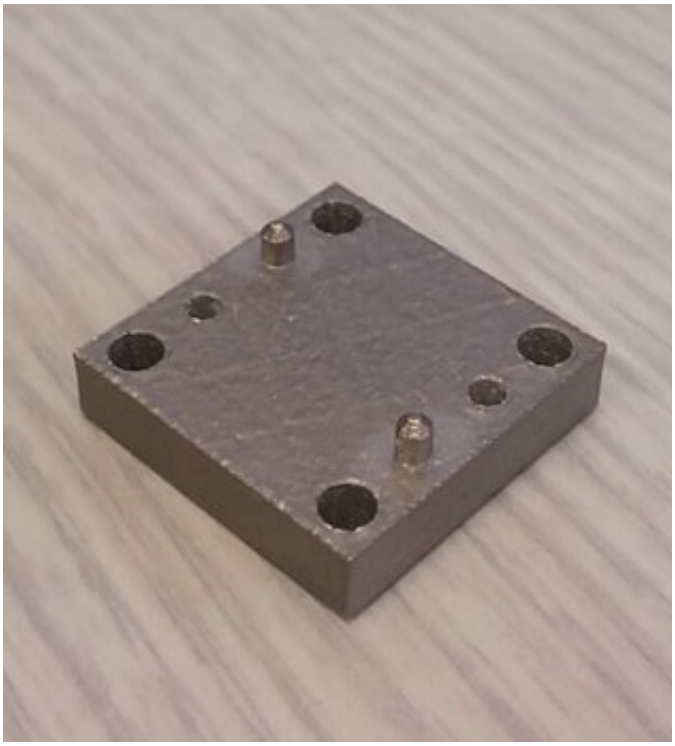

Fig. 11. The laser sintered (3D printed) titanium 'reflect' standard. It's unclear what effect if any the surface finish may have on the 'reflect' standard.

These S_{11} measurements on the Smith chart show the trace collapses closer to the center of the chart when a load is placed on the port, and conversely expands with a reflect, consistent with theory.

The loops in the traces indicate that there may be some resonances in the system. These can be accounted for in the

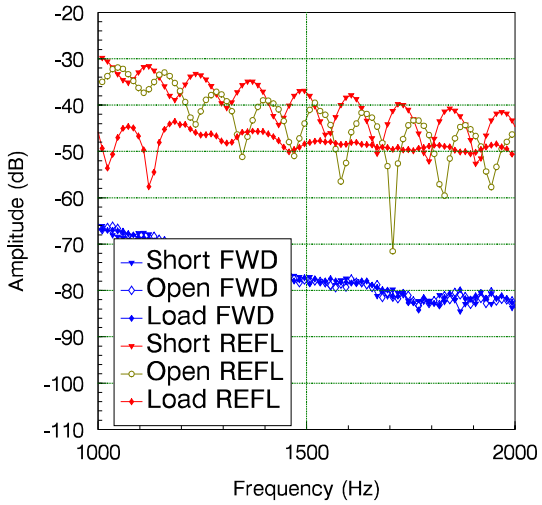

Fig. 12. Measurements for a Short, Open and Load with the 1–2 kHz coupler system.

future with calibration. The port extension function can also effect the number of loops in the trace. It is common to see these loops 'unravel' with more extension and then reappear as the extension goes too far, this can be used to tune the port extension where minimising the number of loops optimise's the extension. These loops are related to the phase of the wave which can be be impacted by the combination of dwell time, port extension, standing waves in the waveguide and vibration of the waveguide itself transmitting energy. Vibration of the waveguide could introduce difficulties in performing two port measurements which can be compensated for with calibration.

Figure 12 shows similar data captured using the 1–2 kHz coupler, this log-mag plot (no phase information) shows similar results to the 10–20 kHz coupler for a reflect and load. This plot shows the individual signals seen by the HP4395A for the 'R' and 'A' signals, as expected the forward coupled signal 'R' changes very little in each case and the 'A' signal changes in each case, with measured magnitude increasing generally with the reflect and decreasing generally with a load.

IV. Conclusion

These S_{11} measurements show that the system works as expected. The load and reflect measurements show that the hardware is functional by demonstrating directionality and producing data that aligns with expectations of acoustically absorbent and reflective materials. These measurements also attest to the ability of the waveguide hardware to be interfaced with the HP4395A.

Some aspects of the calibration are going to be challenging in achieving a dual port system. All calibration code will have to be developed, and it will need to include the oft-omitted isolation terms, irrelevant in many EM scenarios, but suspected to be inescapable in the acoustic situation, as sound travels through all matter. [8] [9]

References

[1] ASTM Standard C384, 2004, "Standard test method for impedance and absorption of acoustical materials by impedance tube method".

[2] Doug Rytting ARFTG 50 Year Network Analyser History Rytting Consulting, Santa Rosa, California, 95405, USA

[3] M. MacDonell, 'Scaling acoustic directional couplers using 3D printing', Thesis, Master of Engineering (ME), University of Waikato, 2015.

[4] Scott, J. and K. E. Pennington, "Acoustic Vector-Corrected Impedance Meter", *IEEE Transactions on Instrumentation and Measurement, 2014. DOI: 10.1109/TIM.2014.2327474*

[5] Lagasse, P., "Realisation of an acoustical directional coupler", Journal of sound and vibration*, 15(3), April 1971, pp367–372.*

[6] HP87511A User manual.

[7] HP4395A User Manual

[8] Network Analyser Error Models and Calibration Methods by Doug Rytting

[9] Agilent AN 1287-3 Applying Error Correction to Network Analyser Measurements

[10] ISO 10534-1:1996 Acoustics – Determination of sound absorption coefficient and impedance in impedance tubes – Part 1: Method using standing wave ratio

[11] ISO 10534-2:1998 - Acoustics – Determination of sound absorption coefficient and impedance in impedance tubes – Part 2: Transfer-function method

[12] http://www.keysight.com/en/pdx-x202277-pn-N5242A/pna-x-microwave-network-analyzer-265-ghz?cc=NZ&lc=eng

[13] https://www.nsi-mi.com/products/system-solutions/near-field-systems

[14] http://www.mwrf.com/sites/mwrf.com/files/styles/article_featured_standard/public/uploads/2012/12/25aoml_0.jpg?itok=DeRbx8FU

C.2 I^{2}MTC 2019 Conference Paper

Reference: M. MacDonell, K. Basnet and J. Scott, "Waveguide Joint Design and Validation for use in Acoustic Vector-corrected Network Analysers", 2019 IEEE International Instrumentation and Measurement Technology Conference (I2MTC), 2019, 1-5, 10.1109/I2MTC.2019.8826926

Waveguide Joint Design and Validation for use in Acoustic Vector-corrected Network Analysers

1st Marcus MacDonell, Student Member IEEE
Department of Engineering
University of Waikato
Hamilton, NZ

2nd Keshav Basnet
Department of Engineering
University of Waikato
Hamilton, NZ

3rd Jonathan Scott, Senior Member IEEE
Department of Engineering
University of Waikato
Hamilton, NZ

***Abstract*—The Vector-corrected Network Analyser (VNA) has been an indispensable tool for many decades in the field of RF and microwave engineering where the availability of calibrated and traceable results is taken for granted. However, calibrated and traceable measurements are not so easily available in the acoustic domain. In an effort to allow such measurements, a dual-port acoustic vector network analyser (AVNA) has been designed and built. The calibration of this test and measurement system hinges on the repeatability of the uncalibrated system and its acoustic waveguide joints. The first generation of acoustic waveguide joints have been 3D printed with a high precision printer and designed to include alignment pins, O-rings, and a reinforcing 'clip' system to allow for a consistent bolt torque without damaging the plastic waveguide. We show that the resulting variation in measurements between cycles of disassembly and reassembly is acceptably small and will allow for calibration of the system. Three-dimensional printed titanium joints show increased rigidity and ease of use but similar repeatability.**

***Index Terms*—Vector Network Analysis, Waveguide, Acoustic.**

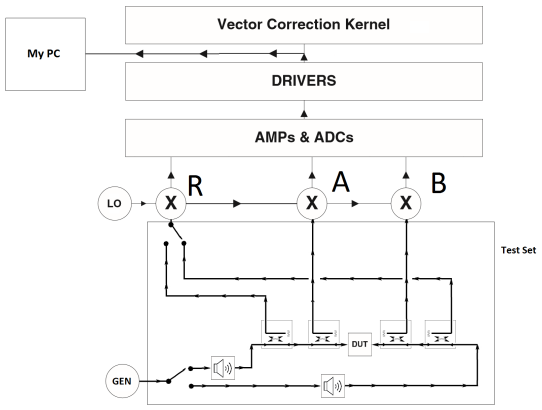

Fig. 1. A block diagram of the AVNA including signal paths, the test set, HP4395A analyser, and the PC, ultimately used for correction of the data.

I. Introduction

A Vector Network Analyzer (VNA) is an instrument that measures the scattering parameters, or S-parameters, of an electrical network. S-parameters are the most commonly measured parameters because the reflection and transmission of waves from and through electrical networks are easy to measure at high frequencies. The VNA is indispensable in the fields of RF and microwave engineering. Its calibrated and traceable data is taken for granted. The authors are investigating the production of an acoustic equivalent of the microwave VNA. The project intends to build upon the decades-long investment in the technology in the microwave arena [1] to shorten the development cycle of the acoustic version. In the field of audio calibrated and traceable measurements are not so readily available. In an effort to allow such measurements a full 2-port Acoustic VNA (AVNA) has been designed and built. The calibration now hinges on the repeatability of the uncalibrated system and its waveguide joints.

Acoustic measurements to characterize materials are currently done with one of two industry standard techniques [2], [3]. Both of these methods are crudely calibrated, have not been implemented with a traceable standard, and require the operator to carry out measurement manually, frequency by frequency, in a laborious manner. Various alternative schemes have been reported in the literature to measure acoustic reflection coefficient, see for example [4], and a summary of the literature is available in [5]. In an effort to improve on these methods an Acoustic Vector Impedance Meter has been created. [5]. It was shown to measure uncalibrated acoustic S_{11}, the acoustic reflection coefficient. To further improve this system we are working towards using two ports, and calibrating the measurement system to permit traceable standards [6].

The accuracy of AVNA will be determined by the calibration and in turn on the system repeatibility and reliability. Once the repeatibility and reliability are estabilised the resulting accuracy of the calibrated AVNA is dependant on the calibration standards themselves [7]. The repeatibility of flanges is the subject of many papers in microwave engineering and many of the designs and developments to improve repeatibility have been adapted for our work in acoustics [8] [9] [10].

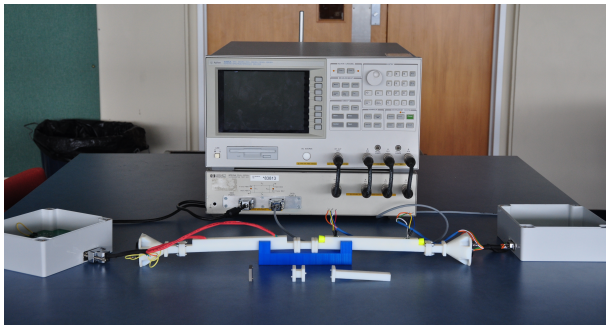

Fig. 2. The AVNA photographed with the remote heads for the 10 kHz–20 kHz range. The waveguide joints are either pressed together, or bolted without washers. (Photograph taken before the necessity for washers was understood)

II. AVNA Hardware

Figure 1 shows the block diagram of the analyser. The test set including directional couplers has been custom built with acoustic components, while the remainder of the system is provided by an Agilent 4395A Network/Spectrum Analyzer interfaced to a generic Windows-based PC. Figure 2 presents a picture of the system with remote heads having a frequency range of 10–20kHz. The waveguide components in this case were fabricated by a resin-based Objet 3D printer.

Before addressing the development of calibration standards and algorithms it is prudent to ensure that waveguide joints are repeatable and reliable. This manuscript reports on the joint design and performance.

III. Joint Design

The design of the directional couplers permits a working bandwidth of a little more than one octave. For example, in in [5], [11] a range of 750Hz–2.2kHz, or just over 1.5 octaves, was demonstrated for the coupler design taken from [12]. Anticipating that an instrument covering the whole acoustic bandwidth will require several test sets, we have fabricated two examples covering nominal frequency ranges of 1–2kHz and 10–20kHz. The lower-frequency couplers have been made in a conventional workshop using transparent acrylic. The waveguide is square with a dimension of 60.0 mm. The higher-frequency set was initially fabricated using an Objet30 resin printer. [13] The waveguide is square with a dimension of 6.00 mm.

Figure 3 shows the ends of two resin-printed couplers whose flanges have failed. The picture serves to show the alignment pins and the square flanges with 4 holes for bolts to secure the joint. When the bolts were torqued up, the plastic initially bulged. Investigations to select an appropriate torque setting showed that the flanges were unable to cope with any reasonable torque, and only small amounts of over-torque could do permanent damage. In order to address this problem a U-shaped washer was designed to distribute the force across the flange.

Figure 4 shows the cross section through a joint between two flanges (waveguide itself is not shown). Figure 5 makes it easier to visualise by showing the outside lateral view of two couplers joined directly (a "zero-length thru"). Figure 6 shows photographs of the zero-length thru connection between two couplers fabricated in a translucent resin plastic. Also visible in the photograph are orange ear plugs used as loads in the off-axis arms of the couplers. Support legs have been added behind the washers to support the guide above the table.

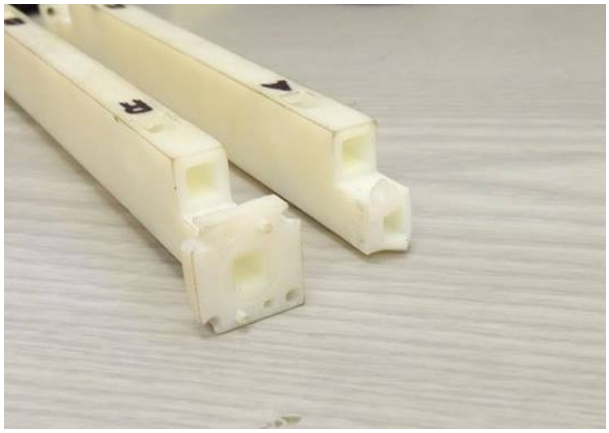

Fig. 3. Examples of broken flanges from repeated use without U-shaped washers.

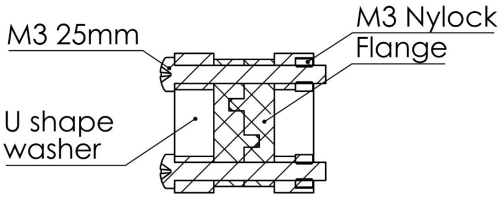

Fig. 4. Cross section diagram of two mated flanges held by bolts passing through mild steel washers. Nylon locking nuts are used with stainless steel M3 bolts.

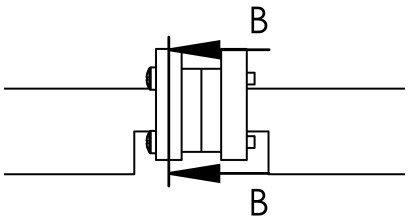

Fig. 5. Lateral view diagram where two directional couplers are joined flange-to-flange using U-shaped washers and threaded bolts and nylon locking (nylock) nuts. The line B–B marks a cross section through one of the U-washers. See figure 7 for the directional couplers without washers.

The joints are designed to a high precision, and include alignment pins and a slot for O-rings. In response to the difficulty of plastic flanges, we printed some components in titanium (Ti). The titanium set does not require the reinforcing washers but is a significantly more expensive waveguide material. Figure 7 shows a pair of couplers in Ti. One is presented

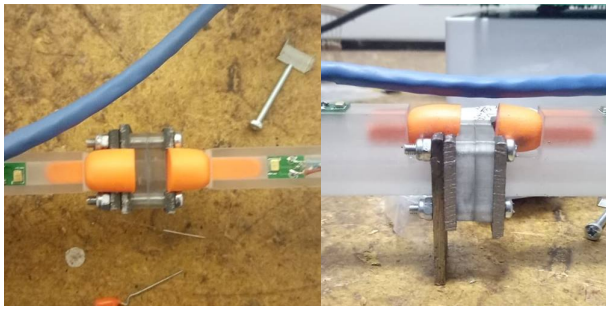

Fig. 6. Actual flange assembly. Left: Top down view, Right: Profile view. NB: mild steel U shape clips.

with an O-ring, the other without, showing the groove. In all of the small joints, a bolt torque of 0.5 Nm is specified.

In the case of the low-frequency acrylic test set, joints are bolted together by M6 bolts and nylon locking nuts at a torque of 1.5 Nm. Generally, the flanges are sufficiently strong at this scale that full U-shaped washers are not necessary. We normally fit simple metallic washers appropriate for M6 bolts. Figure 8 shows an example waveguide component in the low-frequency acrylic system.

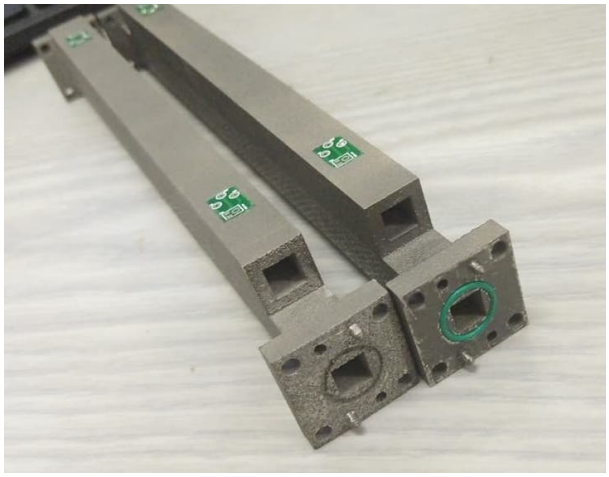

Fig. 7. The Titanium coupler set with an as sintered surface finish. The right hand coupler has an O-ring in its O-ring groove.

IV. Validation

A sample of ten measurements at each of 50 frequencies were taken in the high-frequency system without an O-ring, and another 10 sets with an O-ring. The presence of an O-ring significantly altered the measurements, so all measurements reported in this manuscript involve joints with O-rings fitted. We infer from this that the O-rings are working as intended. O-rings are specified for use in all joints.

Figure 9 exemplifies the kind of repeatability that was obtained with the printed resin guide. The figure suggests that a final accuracy of about 0.2dB or just over 2% is to be expected.

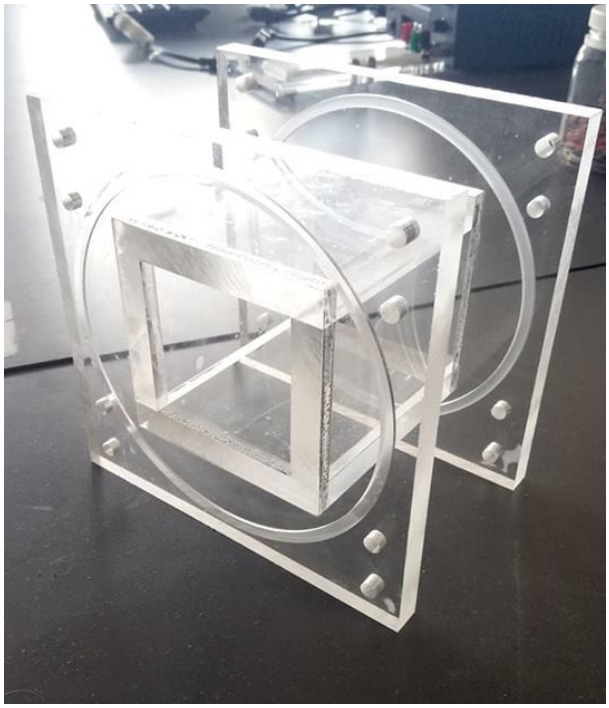

Fig. 8. Photograph of a short thru in the low-frequency, acrylic waveguide.

Surprisingly, we observe that the order in which the bolts are torqued up makes a significant difference to the repeatability. Figure 10 shows the variation in measured raw S_{21} with a variety of assembly sequences. It is not worth plotting standard deviation—the gross discrepancies are visible in the raw data. It is clear that the assembly procedure matters a great deal; we suggest the bolt order depicted in figure 11.

Figure 12 shows the same type of data for a titanium (Ti) joint as figure 9 shows for the printed resin version. It is clear that the deviation is slightly worse than the softer, resin-based joints. Figure 13 shows the Standard deviation in the large couplers for Raw S21 for three different bolt orders. Bolt orders were clockwise, or 3-2-4-1 as in Figure 10, recommended, and thirdly a Z or N shape, or 2-3-4-1 as in Figure 10. All other bolt orders are rotations or mirrors of these.

V. Conclusion

The repeatability of the joints in the AVNA is an a limiting factor in the overall performance of the system, including the chosen calibration algorithm. A modest torque of 0.5 Nm is enough to cause permanent damage or total failure without washers to evenly distribute pressure over the flange, the washers also create a hard surface for the bolt/nut to press against without localized deformation of the flange. The presented plastic joint design performs relatively well, although they are sensitive to bolt order which could be due to the softness and flex of the flange material. Laser sintered Titanium versions have so far proven robust but no more repeatable than the

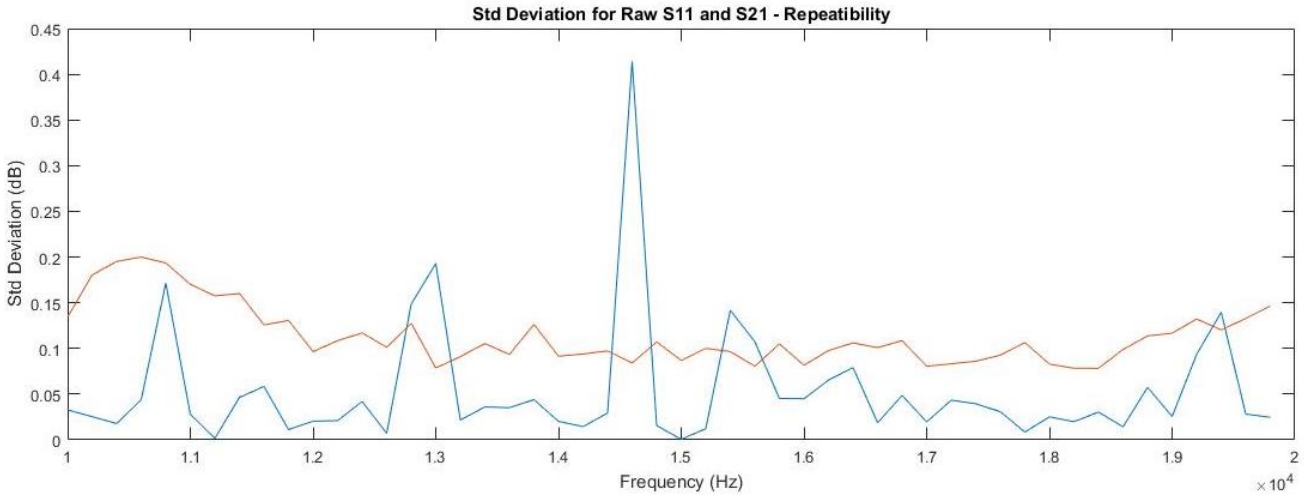

Fig. 9. Standard Deviation of raw S_{11} and S_{21} obtained at each measurement frequency when the joint was disassembled and reassembled ten times. The flanges were resin, the joints fitted with O-rings and U-shaped washers to distribute the torque. Bolt torque was 0.5 Nm.

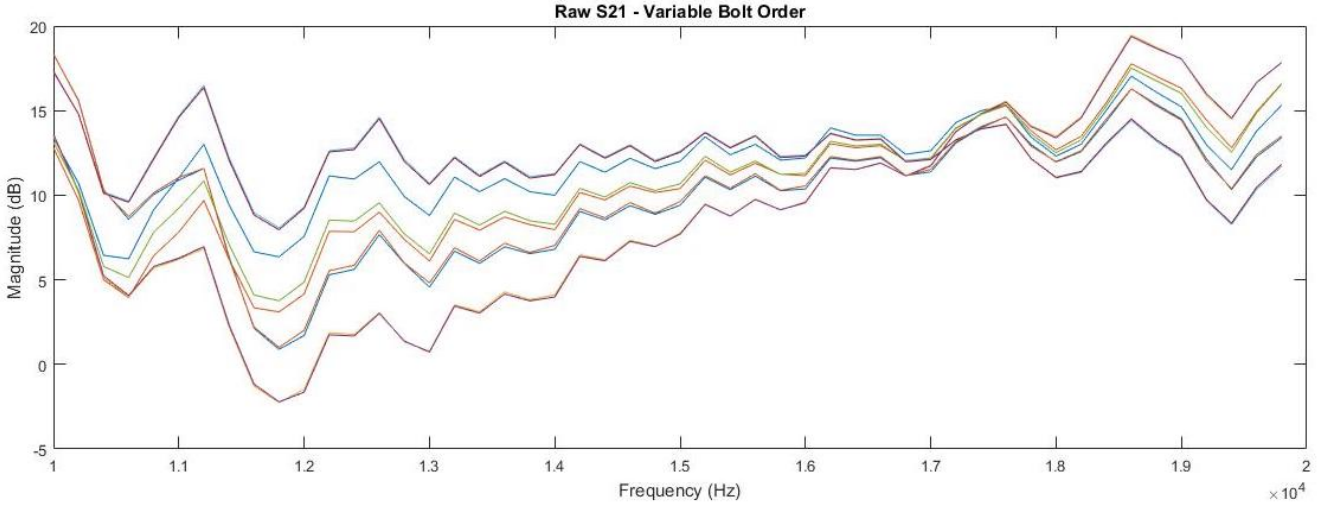

Fig. 10. Magnitude of raw S_{21} measured on multiple instances of disassembly and reassembly with variable bolt order in the resin flanges.

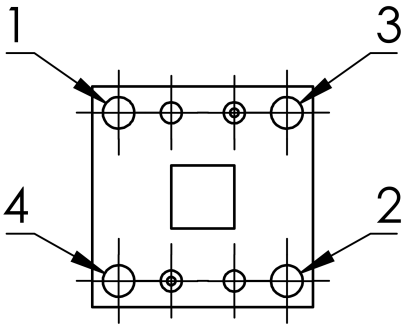

Fig. 11. Suggested bolt order for assembly of flange joints.

sintered plastic type. They do eliminate the need for washers by increasing the hardness and rigidity of the flange.

VI. Acknowledgment

The authors would like to thank the MBIE for funding this research as part of the Smart Ideas Fund. Thanks to Peter Higgins for workshop assistance.

References

[1] Doug Rytting, "ARFTG 50 year network analyzer history", *71st ARFTG Microwave Measurement Conference*, 20 June 2008, Atlanta, GA, USA.
[2] ISO 10534-1:1996 Acoustics – Determination of sound absorption coefficient and impedance in impedance tubes – Part 1: Method using standing wave ratio
[3] ISO 10534-2:1998 - Acoustics – Determination of sound absorption coefficient and impedance in impedance tubes – Part 2: Transfer-function method

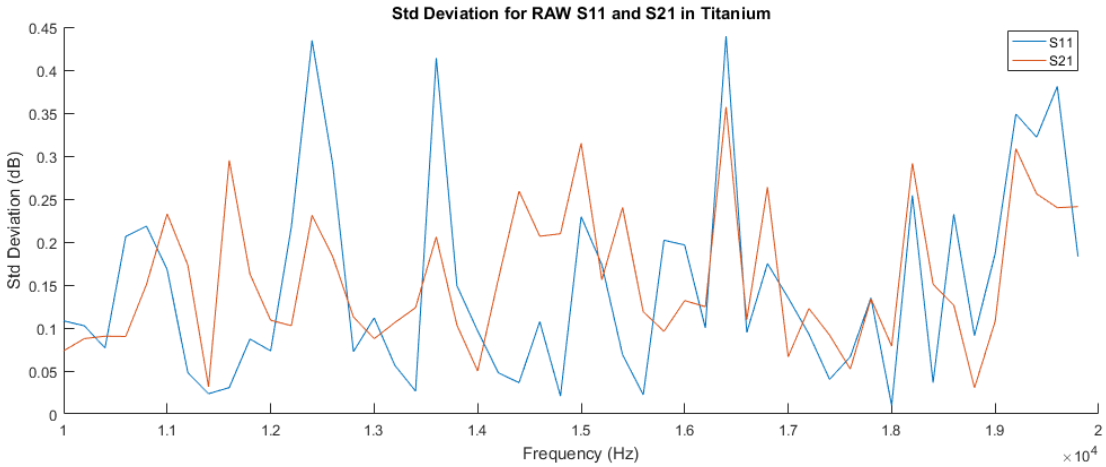

Fig. 12. Standard Deviation of raw S_{11} and S_{21} obtained at each measurement frequency when the joint was disassembled and reassembled ten times. The flanges were Ti, the joints fitted with O-rings. Bolt torque was 0.5 Nm, and the bolt order was random.

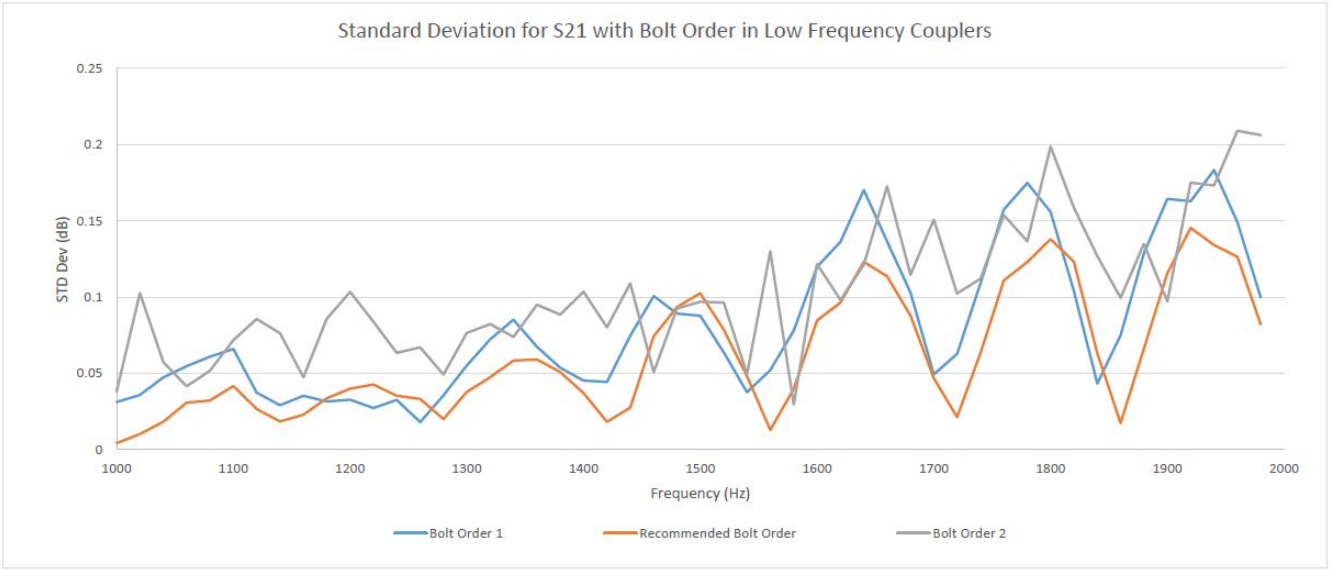

Fig. 13. Standard Deviation of raw S_{21} obtained at each measurement frequency when the joint was disassembled and reassembled thirty times, with three different bolt orders (ten measurements for each bolt order).

[4] C. M. de Blok and R. F. M. van den Brink, "Direct-reading one-port acoustic network analyzer," J. Audio Eng. Soc., vol. 41, no. 4, pp. 231–238, 1993.

[5] Pennington, K. (2017). Acoustic Vector Network Analyser (Thesis, Doctor of Philosophy (PhD)). The University of Waikato, Hamilton, New Zealand. Retrieved from https://hdl.handle.net/10289/11530

[6] Marcus, M., & Scott, J. B. (2017). Development and Basic Calibration of an Acoustic Vector Network Analyser. Presented at the Electronics New Zealand Conference 2017 (ENZCon 2017), christchurch, New Zealand, 4-6 December 2017.

[7] D. Rytting, "Network Analyzer Accuracy Overview", 58th ARFTG Conference Digest, 2001. Available: 10.1109/arftg.2001.327486 [Accessed 16 January 2019].

[8] H. Li, A. Kerr, J. Hesler and R. Weikle, "Repeatability of waveguide flanges with worst-case tolerances in the 500–750 GHz band", 79th ARFTG Microwave Measurement Conference, 2012. Available: 10.1109/arftg79.2012.6291185.

[9] M. Horibe and R. Kishikawa, "Performance of new design of waveguide flange for measurements at frequencies from 800 GHz to 1.05 THz", 79th ARFTG Microwave Measurement Conference, 2012. Available: 10.1109/arftg79.2012.6291186.

[10] S. Rahiminejad, E. Pucci, V. Vassilev, S. Haasl, P. Kildal and P. Enoksson, "AMC pin waveguide flange for screw redundant millimeter and submillimeter measurements", 2016 87th ARFTG Microwave Measurement Conference (ARFTG), 2016. Available: 10.1109/arftg.2016.7501946

[11] Scott, J. and K. E. Pennington, "Acoustic Vector-Corrected Impedance Meter", *IEEE Transactions on Instrumentation and Measurement*, 2014. DOI: 10.1109/TIM.2014.2327474

[12] Lagasse, P., "Realisation of an acoustical directional coupler", *Journal of sound and vibration*, 15(3), April 1971, pp367–372.

[13] M. MacDonell, 'Scaling acoustic directional couplers using 3D printing', Thesis, Master of Engineering (ME), University of Waikato, 2015.

C.3 AES 2019 Conference Paper

M. MacDonell and J. Scott, “Realizing an Acoustic Vector Network Analyzer”, Proc. 147th Audio Engineering Society Convention, 2019.

Audio Engineering Society

Convention Paper

Presented at the 147th Convention
2019 October 16 – 19, New York

Realizing An Acoustic Vector Network Analyser

Marcus MacDonell[1] and Jonathan Scott[1]

[1] *University of Waikato*

Correspondence should be addressed to Marcus MacDonell (msgm1@students.waikato.ac.nz)

ABSTRACT

Acoustic absorption, reflection, and transmission is typically measured using an impedance tube. We present the design and initial measurements of a radically different measurement system. The instrument builds on the rich history and deep mathematics developed in pursuit of electromagnetic Vector-corrected Network Analyzers (VNAs). Using acoustic directional couplers and a traditional VNA mainframe we assembled an "Acoustic Vector Network Analyzer" (AVNA). The instrument measures acoustic scattering parameters, the complex reflection and transmission coefficients, of materials, transmission lines, ported structures, ducts, etc. After the fashion of electromagnetic VNAs we have constructed millimeter-wave measurement heads that span the 800 Hz–2200 Hz (420–150 mm) and 10 kHz–22 kHz (35–15 mm) bands, demonstrating scalability. We present initial measurement results.

1 Introduction

Absorbing materials play an important role in architectural acoustics, the design of recording studios, listening rooms, and automobile interiors. The growth and decay of the reverberant sound field in a room depends on the absorbing properties of the materials used [1–3]. The sound transmission properties of components are also of interest to acoustic engineers. For example, attenuation in ducts impacts the delivery of fan noise, and the loss in pipe-shaped components of musical instruments affects their performance. The acoustic attenuation of material samples placed in a waveguide reflects subtle properties of the material. In this manuscript we describe a new instrument that offers the potential to deliver acoustic reflection and transmission measurements with traceable accuracy and unprecedented measurement speed. The design is inspired by an instrument developed and refined over many decades since the second world war and now ubiquitous in radio and microwave laboratories all over the world: the Vector-corrected Network Analyzer or "VNA".

A Vector Network Analyzer (VNA) is an instrument that measures the parameters of an electrical network. There is a rich history of their design spanning over 50 years [4]. Vector network analyzers are mostly 'two-port' analyzers that measure two port systems like amplifiers and filters, but single-port and higher order systems with an arbitrary number of ports are possible. Key to the operation of VNAs is the ability to separate waves traveling in opposite directions along a transmission line [5]. This allows the instrument to report reflection coefficient, the ratio of incident to reflected signal. It also enables a mathematically-sophisticated calibration procedure that can negate the effects of imperfections in the instrument itself.

VNAs measure so-called "scattering parameters" or S-parameters [5]. S-parameters are the most commonly

measured parameters because the reflection and transmission coefficients of electrical networks are easy to measure at high frequencies compared with ordinary complex impedance [6].

At present, acoustic measurements to characterize materials are typically done with two industry standard techniques [7, 8]. Neither of these methods is traceable to an external standard. Both are performed frequency by frequency in a laborious manner. The multiple-microphone method can be unreliable especially when phase is important [9]. Other methods in the acoustic domain essentially use an impedance divider in a waveguide [10–13]. None of these methods is particularly precise, and none have become common.

In the early years of radio frequency (RF) test and measurement there were a few techniques available to measure magnitude and phase traveling waves. The slotted line was one of the first techniques that was developed by what is now the company Rohde & Schwarz. The "slotted-line" is the radio frequency equivalent of the moving-microphone method for separation of two acoustic traveling waves propagating in opposite directions. Rantec and Wiltron introduced various Phase/-Gain/amplitude meters/receivers in the 1950s that covered the microwave frequency range. In the 1960s simple Network Analyzers were assembled by mating directional couplers with vector meters. At that time, s-parameters were proposed as a design tool for microwave circuit design and engineering, requiring measurement of the parameters. In the late 1960s the Hewlett-Packard company released the HP 8410, a Network Analyzer without inbuilt error calibration, and began work on vector correction. By the middle of the 1980s the so-called SOLT (Short, Open, Load, Thru) and TRL (Thru, Reflect, Line) calibrations had been proven as mathematically-sound ways of achieving precise calibration; the HP 8510 was introduced to the market as the first instrument with in-built error correction. By the 1990s VNA capability had been extended into the world of optics [14, 15] and on wafer measurement [16, 17] with the added development of LR(R)M calibration techniques [18, 19]. The development of the TRL and TR(R)M calibration methods required fewer standards than SOLT, greatly improved calibration accuracy by allowing weaker standards to be discarded, and extended the number of error terms corrected up to the full 16. Machines were now being sold that spanned the frequency range from below 50MHz (wavelength of 6m) to over 110GHz (wavelength of 3mm). A wavelength of 6m in the case of sound in air represents a frequency of just over 50Hz, while 3mm corresponds to 110kHz, a very wide range indeed.

The VNA was instrumental in the development of every new generation of radar. It enabled most of the high-frequency electronic systems we enjoy today, including cellular phones, global positioning, WiFi, and ethernet. In all of the VNAs sold, directional couplers are the fundamental building block. Directional couplers in their waveguide form are not dissimilar from one another, and this proves to be true even in the acoustic case. As such it may be surprising to note that the development in 1971 of the acoustic directional coupler [21] was never followed by the serious adoption of VNA techniques in acoustics.

2 Hardware

In an effort to improve on the available acoustic methods, we have constructed a dual-port Acoustic Vector Network Analyser (AVNA) [20]. This is based around Lagasse's coupler design [21]. Figure 1 shows our prototype system consisting of an old HP4395A VNA mainframe fitted with two 3D-printed measurement heads. Figure 2 presents the block diagram of the system; interested readers will find it similar to those of millimetre-wave commercial electro-magnetic VNAs. The physical design also mimics the remote-head, waveguide-based VNA designs offered by companies such as Keysight and Anritsu. Each head incorporates a directional coupler for 10–20 kHz operation [22], within which is a matching pad & sound source [20], and electronics to interface sensing microphones to the VNA receivers. This system will be used here to measure acoustic S-parameters.

Figure 3 depicts an early version of the coupler-pad-source component, conveniently constructed for the 1–2 kHz band, in transparent acrylic to show the internal geometry. In front of that is shown a sliding load and other waveguide components. To the rear of the image a 1-foot (300mm) ruler gives scale.

To further improve this system we report here a system for calibrating our AVNA, and we discuss standards that we anticipate can be made traceable. The reliability and repeatability of the flange system is crucial to the physical performance of the acoustic VNA as well as the performance of any potential calibration

technique, and we have explored this design in some detail elsewhere [23], and incorporated it into all of our hardware.

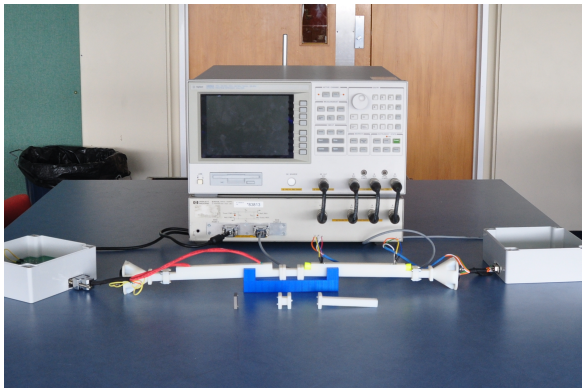

Fig. 1: The physical hardware for the acoustic vector network analyser. The commercial VNA (rear top) sits atop of a retrofitted 'test-set' which connects the waveguide (front center) via external amplifiers (white boxes on the far left and right).

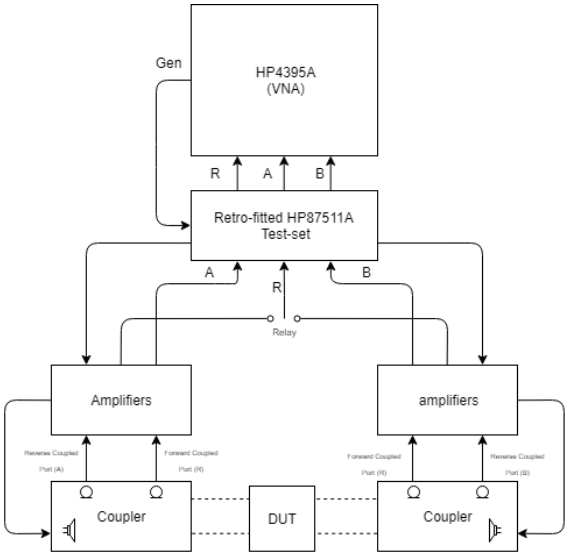

Fig. 2: A block diagram of the hardware presented in Figure 1. The presented configuration is using two ports to measure a "Device Under Test" (DUT).

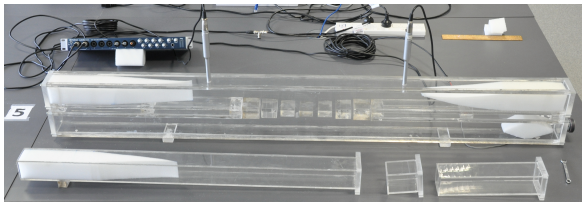

Fig. 3: An example of an acoustic directional coupler for 1–2 kHz, the branch waveguide structure responsible for it's directional behavior is clearly visible thanks to being constructed of colourless polycarbonate. Microphones left and right are the forward and reverse coupled "ports" respectively.

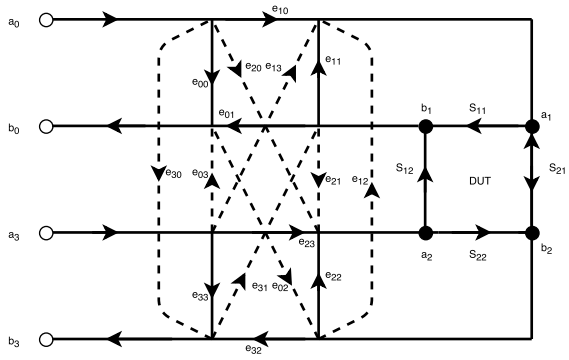

Fig. 4: A flow-graph of the 16 term error model. This flow-graph represents the physical paths for systematic error in the system, these are numerically represented in the error matrix 'E'

3 Calibration Methods

Owing to the imperfections of acoustic directional couplers, the advance of the AVNA depends upon the development of a calibration method. The calibration method is a process for determining the systematic error of the measurement device. A correction algorithm is then applied to convert raw measurements into corrected ones.

The analysis of a VNA is traditionally carried out using traveling-wave flow graphs [24, 25]. The complete 16-term error model represented in flow-graph form is shown in figure 4. Based on the model, a system of equations relating raw to corrected measurements is found. This system of linear equations that relate the measured acoustic properties of a device under test

(DUT) to the actual acoustic properties of the DUT, present a considerable algebraic problem. The act of calibration takes measurements made on known devices, and solves for the 16 error terms. The 16 term error model was chosen because of the inclusion of leakage paths that are expected to be an issue in the acoustic VNA, but that may often be ignored in the electromagnetic case by virtue of Faraday shielding.

We face finding 16 complex error terms. Unfortunately, very few known acoustic standards exist. The most obvious standard is a perfect reflection, consisting of a guide closed with a solid panel. In previous work, it was shown that the so-called "sliding load" method, adapted from a scheme popular in the electromagnetic domain in the 1980s, could provide the equivalent of a perfect absorber [26, 29]. The sliding load works by utilizing the phase change of the reflected signal from an imperfect absorber whose reflection magnitude is invariant at different positions in a guide. The result that would have been obtained from a perfect absorber can be calculated from the value of a imperfect absorber. This is normally done with a numerical circle fit, or possibly a spiral fit. These two standards (Reflect, [sliding] Load) are insufficient by themselves, even for a single port VNA [9].

As we have two ports, it is possible to connect them directly, measuring a so-called "zero-length Thru". With the available 'Thru', 'Match', and 'Reflect' standards we can adapt the LRM or TRRM electromagnetic calibration methods proposed by Silvonen [27] to solve the system. This method utilizes five measurements of combinations of the standards to produce a set of twenty equations. This overdetermined system can be solved with a numerical method like Single Value Decomposition (SVD), or with the analytical results from [27].

3.1 Calibration

The five required measurements have the ideal matrices:

$$\text{Thru:} \quad A = \begin{bmatrix} 0 & T \\ T & 0 \end{bmatrix} \tag{1}$$

$$\text{Match-Match:} \quad B = \begin{bmatrix} 0 & 0 \\ 0 & 0 \end{bmatrix} \tag{2}$$

$$\text{Reflect-Reflect:} \quad C = \begin{bmatrix} \Gamma & 0 \\ 0 & \Gamma \end{bmatrix} \tag{3}$$

$$\text{Reflect-Match:} \quad D = \begin{bmatrix} \Gamma & 0 \\ 0 & 0 \end{bmatrix} \tag{4}$$

$$\text{Match-Reflect:} \quad E = \begin{bmatrix} 0 & 0 \\ 0 & \Gamma \end{bmatrix} \tag{5}$$

For a zero-length Thru $T = 1$, and our method uses a zero-length Thru since it is the simplest option. T is otherwise calculated from its length l and propagation constant γ, where $T = e^{-\gamma l}$, but the (time) length of a thru in the acoustic domain is subject to many uncertainties, not least concerning the variable properties of air. The 16-term error model shown in figure 4 yields the matrix representation in equation (6), expanded in 7. E represents the 16-term error matrix while e represents and individual error term. e_{00} for example represents the error as a result of signal following the path shown in Figure 4 from port a_0 to b_0.

$$\begin{bmatrix} b_0 \\ b_3 \\ b_1 \\ b_2 \end{bmatrix} = E \begin{bmatrix} a_0 \\ a_3 \\ a_1 \\ a_2 \end{bmatrix} \tag{6}$$

$$E \equiv \begin{bmatrix} E_1 & E_2 \\ E_3 & E_4 \end{bmatrix} = \left[\begin{array}{cc:cc} e_{00} & e_{03} & e_{01} & e_{02} \\ e_{30} & e_{33} & e_{31} & e_{32} \\ \hdashline e_{10} & e_{13} & e_{11} & e_{12} \\ e_{20} & e_{23} & e_{21} & e_{22} \end{array}\right] \tag{7}$$

S_m, the "measured" S-parameters and S_a, the "actual" S-parameters are defined as

$$\begin{bmatrix} b_0 \\ b_3 \end{bmatrix} = S_m \begin{bmatrix} a_0 \\ a_3 \end{bmatrix}, \; S_m = \begin{bmatrix} S_{11m} & S_{12m} \\ S_{21m} & S_{22m} \end{bmatrix} \tag{8}$$

$$\begin{bmatrix} a_1 \\ a_2 \end{bmatrix} = S_a \begin{bmatrix} b_1 \\ b_2 \end{bmatrix}, \; S_a = \begin{bmatrix} S_{11a} & S_{12a} \\ S_{21a} & S_{22a} \end{bmatrix} \tag{9}$$

$$S_m = E_1 + E_2 S_a (I - E_4 S_a)^{-1} E_3 \tag{10}$$

Where I is the unit matrix. Solving for S_a yields

$$S_a = [E_3(S_m - E_1)^{-1}E_2 + E_4]^{-1} \tag{11}$$

This equation is very non-linear and difficult to solve directly. Cascading T-parameters are used to linearize the problem. Solving for the T-parameters can be done in a variety of ways. Two common methods are normalizing by one of the unknown coefficients and solving directly or using a least squares method, single value decomposition (SVD) is used often because of its ability to handle singularities [28].

The E and T matrices are related by the following:

$$E = \begin{bmatrix} T_2T_4^{-1} & T_1 - T_2T_4^{-1}T_3 \\ T_4^{-1} & -T_4^{-1}T_3 \end{bmatrix} \tag{12}$$

$$T = \begin{bmatrix} E_2E_1E_3^{-1}E_4 & E_1T_3^{-1} \\ E_3^{-1}E_4 & E_3^{-1} \end{bmatrix} \tag{13}$$

Substituting the T matrix into the system yields:

$$\begin{bmatrix} b_0 \\ b_3 \\ a_0 \\ a_3 \end{bmatrix} = T \begin{bmatrix} a_1 \\ a_2 \\ b_1 \\ b_2 \end{bmatrix} \tag{14}$$

$$T \equiv \begin{bmatrix} T_1 & T_2 \\ T_3 & T_4 \end{bmatrix} = \left[\begin{array}{cc:cc} t_0 & t_1 & t_2 & t_3 \\ t_4 & t_5 & t_6 & t_7 \\ \hdashline t_8 & t_9 & t_{10} & t_{11} \\ t_{12} & t_{13} & t_{14} & t_{15} \end{array}\right] \tag{15}$$

Using the T-parameters and the definitions of S_m and S_a the following can be derived

$$S_m = (T_1S_a + T_2)(T_3S_a + T_4)^{-1} \tag{16}$$

$$T_1S_a + T_2 - S_mT_3S_a - S_mT_4 = 0 \tag{17}$$

$$S_a = (T_1 - S_mT_3)^{-1}(S_mT_4 - T_2) \tag{18}$$

Equation 17 forms the basis of calibration and can be arranged into the form of $\mathbf{A} \cdot T = 0$ and produces a set of twenty linear equations in terms of the 16 T-parameters t_n. Equation 18 allows for de-embedding of the DUT.

The full system of equations generated by the five measurements is presented for the interested reader in Figure 9 towards the end of this manuscript.

4 Results

Figure 5 shows the corrected data of the 'Thru' (zero-length) standard when using the error matrix produced by the numerical method. This shows that the transmission terms (S_{12} & S_{21}) very well calibrated to 0 dB (100% transmission) with reflections (S_{11} & S_{22}) sitting at least -40 dB down.

Figure 6 shows the the corrected data of the 'reflect' standard when using the error matrix produced by the analytical method. This shows that the reflection terms (S_{11} & S_{22}) very well calibrated to 0 dB (100% reflection) with transmission (S_{12} & S_{21}) down around -350 dB. This is the numerical computation noise, as expected because the calibration is algebraic, rather than numerical.

The performance of the 'Match' standard which is implemented as a sliding load is limited by the performance of the circle fit used. The circle fit used is the Taubin method [30]. In order for this method to work effectively there needs to be sufficient points for the method to fit a least squares solution for all frequencies. Three points are theoretically sufficient, however when implementing the sliding load practically there are frequencies where more points may be required for an accurate fit. Imperfections in the circle fit manifest themselves as an increase in the noise floor, especailly where the result is small.

5 Discussion

Once the error matrix has been generated using the analytical and numerical methods, the error matrix can be checked. To check the error matrix is valid mathematically it is multiplied by any set of measured S-parameters for a standard. If the result of this multiplication is the same as the ideal matrix for that standard then the calibration has been successful.

When the SVD and analytic solutions proved results that are in agreement, we may be reasonably sure that there are no errors or bugs in the calibration algorithms.

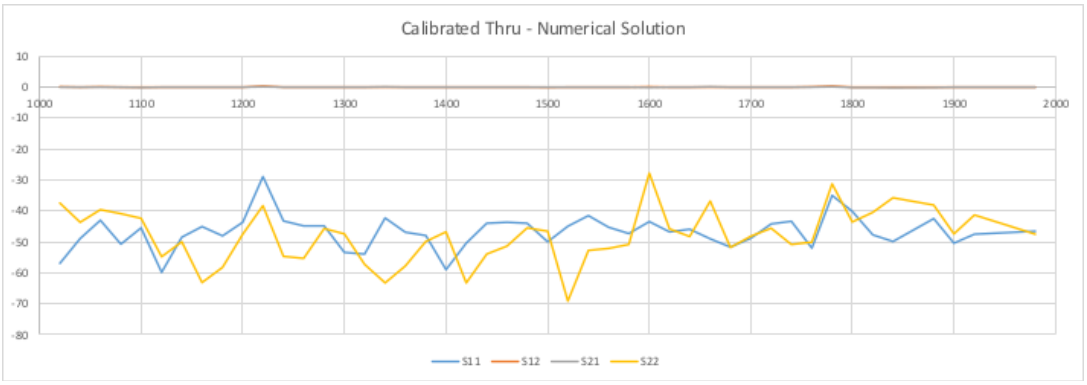

Fig. 5: Result of measuring the 'Thru' calibration standard (a tube of zero-length) using the numerical calibration method. The expected results are perfect transmission (0dB loss) as shown, and zero reflection (-∞ dB). The residual signal shows -40–50dB, representing the noise floor of the system.

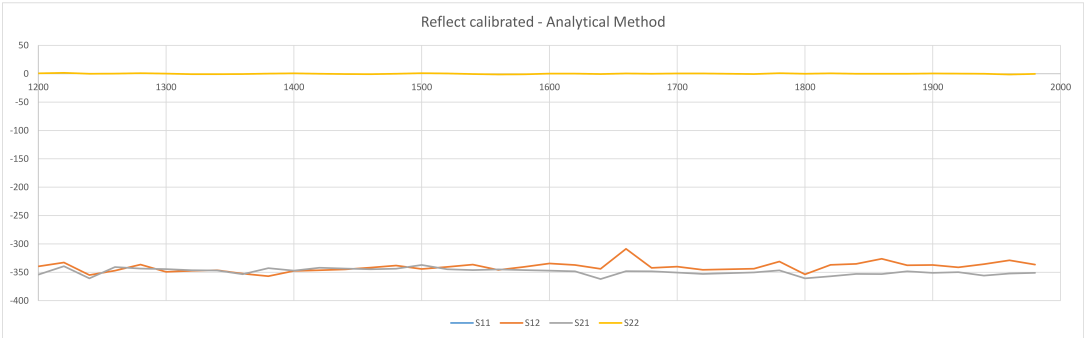

Fig. 6: Result of measuring the 'reflect' calibration standard (a steel plate) using the analytical calibration method. The expected results are perfect perfect reflection (0dB loss) as shown, and zero transmission (-∞ dB). The residual signal is ≈ -350 dB.

In favour of the numerical approach, we may observe that the noise floor gives an indication for the noise in the measurements including those used in the calibration. Further, it can be used in principle with any set of standards or permutations of standards that produces enough information to solve the equations. Against this approach, it tends to give a weaker calibration. While the analytical method is weaker in it's indication of noise, and requires a specific set of standards it does give strong calibrations.

6 Summary

We have built a dual-port acoustic vector network analyser and we have shown an initial calibration. These two steps are crucial to the realization of the vector network analyser as a traceable acoustic measurement system. Further comparison of calibrated results with with a simulation, using Computational Fluid Dynamics (CFD) is required. This characterisation will be of a complicated acoustic waveguide structure, and if our instrument agrees with simulations of that structure, We will pronounce our instrument fully functional. Colleagues at another university are working on simulations currently.

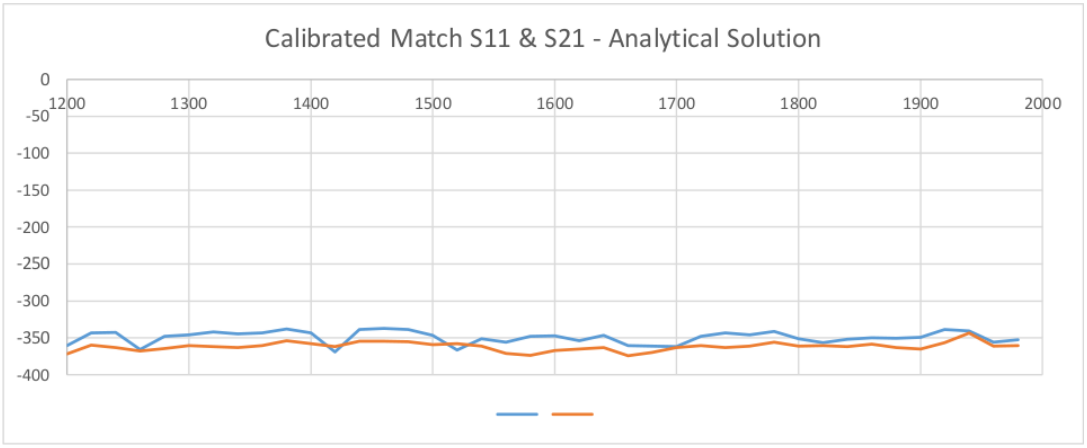

Fig. 7: Result of measuring S_{11} & S_{21} for the 'Match' calibration standard (a sliding load made of open cell foam [29]) using the analytical calibration method. The expected results are zero transmission (-∞ dB), and zero reflection (-∞ dB). The residual signal is ≈ -350 dB.

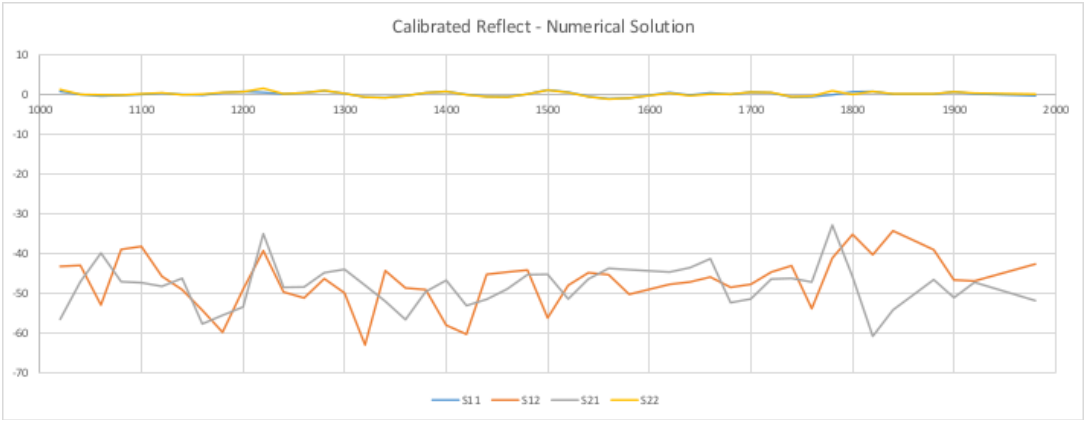

Fig. 8: Result of measuring the 'reflect' calibration standard (a steel plate) using the numerical calibration method. The expected results are perfect reflection (0dB loss) as shown, and zero transmission (-∞ dB). The residual signal shows -40–50dB, representing the noise floor of the system.

$$
\begin{pmatrix}
A_{11} & A_{21} & 0 & 0 & 1 & 0 & 0 & 0 & -M_{a11}A_{11} & -M_{a11}A_{21} & -M_{a12}A_{11} & -M_{a12}A_{21} & -M_{a11} & 0 & -M_{a12} & 0 \\
A_{12} & A_{22} & 0 & 0 & 0 & 1 & 0 & 0 & -M_{a11}A_{12} & -M_{a11}A_{22} & -M_{a12}A_{12} & -M_{a12}A_{22} & 0 & -M_{a11} & 0 & -M_{a12} \\
0 & 0 & A_{11} & A_{21} & 0 & 0 & 1 & 0 & -M_{a21}A_{11} & -M_{a21}A_{21} & -M_{a22}A_{11} & -M_{a22}A_{21} & -M_{a21} & 0 & -M_{a22} & 0 \\
0 & 0 & A_{12} & A_{22} & 0 & 0 & 0 & 1 & -M_{a21}A_{12} & -M_{a21}A_{22} & -M_{a22}A_{12} & -M_{a22}A_{22} & 0 & -M_{a21} & 0 & M_{a22} \\
B_{11} & B_{21} & 0 & 0 & 1 & 0 & 0 & 0 & -M_{b11}B_{11} & -M_{b11}B_{21} & -M_{b12}B_{11} & -M_{b12}B_{21} & -M_{b11} & 0 & -M_{b12} & 0 \\
B_{12} & B_{22} & 0 & 0 & 0 & 1 & 0 & 0 & -M_{b11}B_{12} & -M_{b11}B_{22} & -M_{b12}B_{12} & -M_{b12}B_{22} & 0 & -M_{b11} & 0 & -M_{b12} \\
0 & 0 & B_{11} & B_{21} & 0 & 0 & 1 & 0 & -M_{b21}B_{11} & -M_{b21}B_{21} & -M_{b22}B_{11} & -M_{b22}B_{21} & -M_{b21} & 0 & -M_{b22} & 0 \\
0 & 0 & B_{12} & B_{22} & 0 & 0 & 0 & 1 & -M_{b21}B_{12} & -M_{b21}B_{22} & -M_{b22}B_{12} & -M_{b22}B_{22} & 0 & -M_{b21} & 0 & -M_{b22} \\
C_{11} & C_{21} & 0 & 0 & 1 & 0 & 0 & 0 & -M_{c11}C_{11} & -M_{c11}C_{21} & -M_{c12}C_{11} & -M_{c12}C_{21} & -M_{c11} & 0 & -M_{c12} & 0 \\
C_{12} & C_{22} & 0 & 0 & 0 & 1 & 0 & 0 & -M_{c11}C_{12} & -M_{c11}C_{22} & -M_{c12}C_{12} & -M_{c12}C_{22} & 0 & -M_{c11} & 0 & -M_{c12} \\
0 & 0 & C_{11} & C_{21} & 0 & 0 & 1 & 0 & -M_{c21}C_{11} & -M_{c21}C_{21} & -M_{c22}C_{11} & -M_{c22}C_{21} & -M_{c21} & 0 & -M_{c22} & 0 \\
0 & 0 & C_{12} & C_{22} & 0 & 0 & 0 & 1 & -M_{c21}C_{12} & -M_{c21}C_{22} & -M_{c22}C_{12} & -M_{c22}C_{22} & 0 & -M_{c21} & 0 & -M_{c22} \\
D_{11} & D_{21} & 0 & 0 & 1 & 0 & 0 & 0 & -M_{d11}D_{11} & -M_{d11}D_{21} & -M_{d12}D_{11} & -M_{d12}D_{21} & -M_{d11} & 0 & -M_{d12} & 0 \\
D_{12} & D_{22} & 0 & 0 & 0 & 1 & 0 & 0 & -M_{d11}D_{12} & -M_{d11}D_{22} & -M_{d12}D_{12} & -M_{d12}D_{22} & 0 & -M_{d11} & 0 & -M_{d12} \\
0 & 0 & D_{11} & D_{21} & 0 & 0 & 1 & 0 & -M_{d21}D_{11} & -M_{d21}D_{21} & -M_{d22}D_{11} & -M_{d22}D_{21} & -M_{d21} & 0 & -M_{d22} & 0 \\
0 & 0 & D_{12} & D_{22} & 0 & 0 & 0 & 1 & -M_{d21}D_{12} & -M_{d21}D_{22} & -M_{d22}D_{12} & -M_{d22}D_{22} & 0 & -M_{d21} & 0 & -M_{d22} \\
E_{11} & E_{21} & 0 & 0 & 1 & 0 & 0 & 0 & -M_{e11}E_{11} & -M_{e11}E_{21} & -M_{e12}E_{11} & -M_{e12}E_{21} & -M_{e11} & 0 & -M_{e12} & 0 \\
E_{12} & E_{22} & 0 & 0 & 0 & 1 & 0 & 0 & -M_{e11}E_{12} & -M_{e11}E_{22} & -M_{e12}E_{12} & -M_{e12}E_{22} & 0 & -M_{e11} & 0 & -M_{e12} \\
0 & 0 & E_{11} & E_{21} & 0 & 0 & 1 & 0 & -M_{e21}E_{11} & -M_{e21}E_{21} & -M_{e22}E_{11} & -M_{e22}E_{21} & -M_{e21} & 0 & -M_{e22} & 0 \\
0 & 0 & E_{12} & E_{22} & 0 & 0 & 0 & 1 & -M_{e21}E_{12} & -M_{e21}E_{22} & -M_{e22}E_{12} & -M_{e22}E_{22} & 0 & -M_{e21} & 0 & -M_{e22}
\end{pmatrix}
\begin{pmatrix} t_0 \\ t_1 \\ t_2 \\ t_3 \\ t_4 \\ t_5 \\ t_6 \\ t_7 \\ t_8 \\ t_9 \\ t_{10} \\ t_{11} \\ t_{12} \\ t_{13} \\ t_{14} \\ t_{15} \end{pmatrix} = 0
$$

Fig. 9: Full system of equations. A corresponds to the ideal 'Thru' and M_a corresponds to the measured 'Thru', and so on for all standards.

Acknowledgment

The Authors would like to acknowledge Science for Technological Innovation (SfTI) one of the New Zealand Ministry of Business, Innovation, and Employment (MBIE) science challenges for funding this research.

References

[1] J. Vieira, "Automatic Estimation of Reverberation Time", in Audio Engineering Society Convention 116, 2004.

[2] J. Vieira, "Estimation of Reverberation Time without Test Signals", in Audio Engineering Society Convention 118, 2005.

[3] P. D'Antonio, T. Cox, "Characterization of Acoustical Materials", Audio Engineering Society Conference: UK 12th Conference: The Measure of Audio (MOA), 1997.

[4] Doug Rytting, "ARFTG 50 year network analyzer history", *71st ARFTG Microwave Measurement Conference*, 20 June 2008, Atlanta, GA, USA.

[5] M. Hiebel, Fundamentals of vector network analysis, 4th ed. Munchen: Rohde & Schwarz, 2008, pp. 15,16.

[6] K. Kurokawa, "Power Waves and the Scattering Matrix", IEEE Transactions on Microwave Theory and Techniques, vol. 13, no. 2, pp. 194-202, 1965. Available: 10.1109/tmtt.1965.1125964 [Accessed 18 July 2019].

[7] ISO 10534-1:1996 Acoustics – Determination of sound absorption coefficient and impedance in impedance tubes – Part 1: Method using standing wave ratio

[8] ISO 10534-2:1998 - Acoustics – Determination of sound absorption coefficient and impedance in impedance tubes – Part 2: Transfer-function method

[9] Pennington, K. (2017). Acoustic Vector Network Analyser (Thesis, Doctor of Philosophy (PhD)). The University of Waikato, Hamilton, New Zealand. Retrieved from `https://hdl.handle.net/10289/11530`

[10] Smith, J., Fritz, C. and Wolfe, J. 'A new technique for the rapid measurement of the acoustic impedance of wind instruments', Proc. Seventh International Congress on Sound and Vibration, July 2000, Garmisch-Partenkirchen, Germany, Vol III, pp.1833?1840.

[11] De Blok, C. M., and R. F. M. Van den Brink, 'Direct-Reading One-Port Acoustic Network Analyzer', Journal of the Audio Engineering Society, vol. 41, no. 4, April 1993, pp231-238.

[12] D. H. Keefe, R. Ling, and J. C. Bulen, 'Method to measure acoustic impedance and reflection coefficient', J. Acoust. Soc. Am., vol. 91, pp. 470?485, January 1992.

[13] Kausel, W., 'Bore reconstruction of tubular ducts from its acoustic input impedance curve', IEEE Transactions on Instrumentation and Measurement, vol. 53, no. 4, August 2004, pp. 1097-1105.

[14] A. Freundorfer, "A coherent optical network analyzer", IEEE Photonics Technology Letters, vol. 3, no. 12, pp. 1139-1142, 1991.

[15] A. P. Freundorfer, "Optical vector network analyzer as a reflectometer," Appl. Opt. 33, 3559-3561 (1994)

[16] V. Adamian, "2-26.5 GHZ On-Wafer Noise and S-Parameter Measurements Using a Solid State Tuner", 34th ARFTG Conference Digest, 1989.

[17] L. Dunleavy, "A Ka-Band On-Wafer S-Parameter and Noise Figure Measurement System", 34th ARFTG Conference Digest, 1989.

[18] A. Davidson, E. Strid and K. Jones, "Achieving greater on-wafer S-parameter accuracy with the LRM calibration technique", 34th ARFTG Conference Digest, 1989.

[19] A. Davidson, K. Jones and E. Strid, "LRM and LRRM Calibrations with Automatic Determination of Load Inductance", 36th ARFTG Conference Digest, 1990.

[20] M. Macdonell, & J. Scott, (2017). Development and Basic Calibration of an Acoustic Vector Network Analyser. Presented at the Electronics New Zealand Conference 2017 (ENZCon 2017), Christchurch, New Zealand, 4-6 December 2017.

[21] Lagasse, P., “Realisation of an acoustical directional coupler”, *Journal of sound and vibration*, 15(3), April 1971, pp367–372.

[22] M. MacDonell, ’Scaling acoustic directional couplers using 3D printing’, Thesis, Master of Engineering (ME), University of Waikato, 2015.

[23] M. MacDonell, K. Basnet and J. Scott, "Waveguide Joint Design and Validation for use in Acoustic Vector-corrected Network Analysers", 2019 IEEE International Instrumentation and Measurement Technology Conference (I2MTC), Auckland, New Zealand, 2019, pp. 879-883.

[24] Mason and Zimmerman, Electronic Circuits, Signals & Systems, Wiley, 1960.

[25] Kuhn, ’Signal Flow Graphs’, Microwave Journal, November 1963, pp 59+.

[26] H. C. Heyker, ’The Choice of Sliding Load Positions to Improve Network Analyzer Calibration’, 12th European Microwave Conference, Helsinki, September 1982, pp429-434.

[27] K. Silvonen, "LMR 16-a self-calibration procedure for a leaky network analyzer", IEEE Transactions on Microwave Theory and Techniques, vol. 45, no. 7, pp. 1041-1049, 1997.

[28] J. Butler, D. Rytting, M. Iskander, R. Pollard and M. Vanden Bossche, "16-term error model and calibration procedure for on-wafer network analysis measurements", IEEE Transactions on Microwave Theory and Techniques, vol. 39, no. 12, pp. 2211-2217, 1991.

[29] Scott, J. and K. E. Pennington, “Acoustic Vector-Corrected Impedance Meter”, *IEEE Transactions on Instrumentation and Measurement*, 2014. DOI: 10.1109/TIM.2014.2327474

[30] G. Taubin, “Estimation of planar curves, surfaces, and nonplanar space curves defined by implicit equations with applications to edge and range image segmentation,” IEEE Trans. Pattern Anal. Mach. Intell., vol. 13, no. 11, pp. 1115–1138, Nov. 1991.

C.4 JAES 2022 Journal Article

M. Macdonell and J. Scott, "Full Two-Port Vector-Corrected Network Analyzer in the Acoustic Domain", Journal of the Audio Engineering Society, vol. 70, no. 3, pp. 185-198, 2022. doi: 10.17743/jaes.2021.0058

Full 2-port Vector-corrected Network Analyzer in the Acoustic Domain *

MARCUS MACDONELL, *AES Student Member* **AND JONATHAN SCOTT,** *AES Member*
(coraxaudiolabs@gmail.com) (scottj@waikato.ac.nz)

University of Waikato, Hamilton New Zealand
Corax Audio Labs, Cambridge, New Zealand

This manuscript presents the theory and design of a Vector-corrected Network Analyzer (VNA) realized in the acoustic domain. This is a novel measurement instrument based on the established microwave vector network analyzer. It employs directional couplers to separate forward and reverse traveling waves in acoustic waveguide. This instrument is intended to supersede the acoustic impedance tube. Advantages include greatly increased measurement speed and potential for traceability to external standards. Traceability is achieved by means of a calibration through an analytical solution of the error matrix produced from the measurement of a limited number of available acoustic standards. Operation is verified through analysis of the acoustic S-parameters of a passive, asymmetrical, reciprocal acoustic device constructed inside the acoustic waveguide. To the best of our knowledge this Acoustic Vector-corrected Network Analyzer (AVNA) is the first of its kind.

0 INTRODUCTION

An impedance-tube instrument like Brüel and Kjær "Standing Wave Apparatus Type 4002" was first introduced in 1955; the 4002 is still widely used today [1]. An impedance tube is typically used to measure the acoustic reflection and transmission coefficients of materials. Other methods of measuring these parameters have been reported (see for example [2, 3, 4, 5, 6]) but industry has settled on a set of standards based on the impedance tube [7, 8, 2]. These methods have no external traceability, meaning there is no physical standard, only a methodology.

An acoustic vector network analyzer (AVNA) is a device for measuring traveling waves, much like an impedance tube, but it has speed and accuracy advantages over the impedance tube [9, 10, 11]. An AVNA is capable of swept measurements at ≈200 points per minute. It offers the potential for traceability to a set of physical standards. [12] This relative speed and point density represents a huge step up in acoustic measurement. Our prototype AVNA is made using the receiver system from an HP4395A analyzer, a modified HP87511A test-set, and sets of heads based around acoustic directional couplers. Directional couplers are the key waveguide structure capable of separating forward and reverse traveling waves enabling vector network analysis. Acoustic directional couplers were first described by Lagasse [13], and used as a reflectometer by Pennington [10].

1 The Electromagnetic VNA

In the early years of Radio Frequency (RF) test and measurement there were very few techniques available to measure impedance. Such a measurement requires determining, or at least inferring, the relative or absolute magnitude and phase of the forward and reverse traveling waves present on an interconnection.

The slotted line was one of the first techniques that was developed by what is now Rohde & Schwarz. It was in world-wide commercial use by the end of the second world war. [14, 15] A slotted line permits the measurement of a Standing Wave Ratio (SWR) pattern present along a uniform transmission line. [16] The SWR pattern appears in the scalar magnitude of signal as a function of distance along the line. It is possible to infer the relative magnitudes and phases of the forward and reverse waves from the position and depth of minima in the scalloped-magnitude SWR function. [17] The slotted line is analogous to the impedance tube. The first impedance tube instrument was introduced in 1955 by Brüel and Kjær. Finding acoustic impedance using an impedance tube is still the basis of such measurements in the acoustic world today. [7, 8]

In 1965 the Wiltron 310 Vector Network Analyzer (VNA) was introduced. It was the first instrument to re-

*Correspondence should be addressed to Marcus Macdonell, coraxaudiolabs@gmail.com

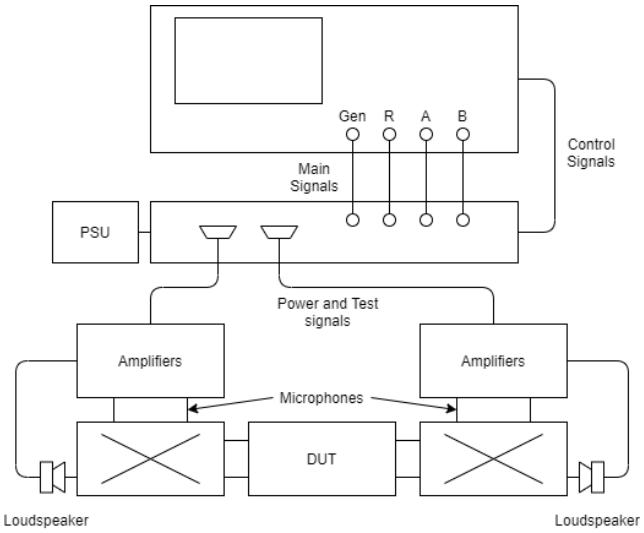

Fig. 1. Block diagram of the acoustic vector network analyzer, including power supply and modified test set, external microphone and loudspeaker amplifiers and directional couplers in the heads. The couplers are marked with the "X" crossover symbol common in microwave parlance. Shown with a device under test (DUT).

semble modern VNAs. [18] Soon after, in 1969, Hewlett-Packard brought out the model 8410A. Neither of these instruments had inbuilt vector calibration to automatically correct for errors; rather they offered the RF & microwave equivalent of the same calibration procedures employed with acoustic impedance tubes and slotted lines.

Nevertheless, both instruments were commercially successful for several reasons. There were large savings of time and effort owing to the increased speed arising from the use of directional couplers instead of slotted lines, eliminating moving parts and dispensing with any mechanical adjustment during measurement. The frequency of measurement could thus be swept automatically, and a continuous trace viewed in real time on a screen if desired. Both machines offered two ports, so that both impedance (in the form of reflection coefficient) and gain (in the form of transmission coefficient) in forward and reverse configuration (to accomodate asymmetrical devices) could be measured without complicated reconnection of the device under test (DUT). Finally, directional couplers proved to be cheaper to manufacture, since slotted lines required precision parts. [19]

All VNAs possess the same basic hardware architecture. It is the same architecture that we use in the AVNA, depicted in Figure 1, except that the electromagnetic version requires no microphones or loudspeakers to transduce between acoustic and electrical signals. The two coupled ports from each directional coupler are fed into amplifiers and then into circuits that measure the amplitude and relative phase of the four signals. These signals are usually termed a_1^M for the measured wave incident on port 1, b_1^M for the measured wave reflected from port 1, and so on. These four complex measurements are then manipulated to display whatever parameter the user desires, for example measured reflection coefficient at port 1 is

$$\Gamma_1^M = \frac{b_1^M}{a_1^M} \tag{1}$$

Calibration to remove magnitude and phase errors was achieved by placing a known short circuit in place of the DUT, and applying a fixed correction factor to gain and phase to read the known result.

The first generation of vector correction was developed in the following few years. By 1960 signal flow graphs were routinely applied to analysis of circuits composed of transmission-line interconnects. [20] Early in the 1970s, a number of researchers realised that these might be applied to VNAs. [21, 22, 23, 24] Although potentially tedious, the equations required to return the corrected parameters given the measured ones and a series of "error terms" could be found by pure algebra or through application of simple geometric rules that anyone could follow [25], although the arithmetic is sufficiently involved that it is all but impractical without a computer. The technique represented a significant theoretical advance for the VNA. By the 1980s the capacity to perform the complicated, frequency-by-frequency correction of errors was built into instruments and performed with relative ease. [18] The Hewlett-Packard 8510A "Vector-corrected Network Analyzer" incorporated the computing capability and came to dominate the industry for over a decade.

The difficult part of implementing a fully-corrected instrument lies in finding the error terms. This requires measurement of some known standards and solution of a system of equations through matrix algebra. Even in the electromagnetic domain, there are very few objects whose true impedance or transmission characteristics can be determined independently. For example, a single-port calibration to find the error coefficients demands measurement of three known, different loads, which can be especially demanding in the acoustic domain. [10]

Readers interested in the mathematical approach and solution flow can find an initial tutorial in the appendix of reference [10].

New calibration procedures, especially ones that require less knowledge about the standards, have been appearing over many years, leading to simpler and cheaper calibration methods in various general and special circumstances, see for example [26, 27, 28, 29, 30]. An excellent summary is given in [31]. A major contribution of this manuscript is the development of a calibration procedure that overcomes the difficulties enumerated in [10], enabled by the presence of two, rather than only one port.

Our prototype AVNA hardware is built around an old HP4395A Vector Network Analyzer. This instrument was designed with a separate "test set", which is to say that the parts of the instrument that involve RF, or in this case audio, components are in a separate enclosure. This arrangement is common in waveguide-based VNA designs. Thus only the test set changes in moving to the acoustic domain. Use of an existing receiver-mainframe also means that we

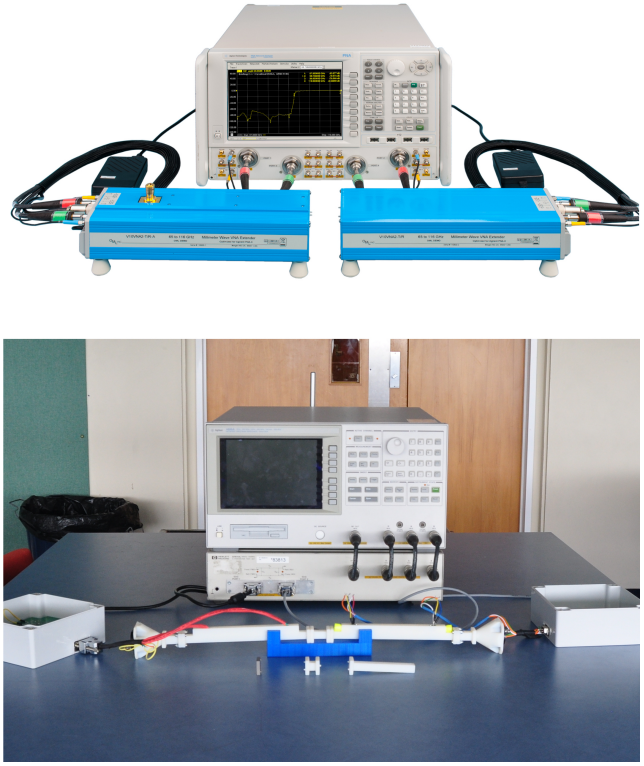

Fig. 2. A visual comparison of an Agilent (now Keysight) Technologies' Performance Network Analyzer (PNA) in the electromagnetic domain (top) and the Acoustic Vector Network Analyzer (AVNA) built for this research, fitted with 10–20 kHz heads (lower photo).

have not had to construct the phase-measurement circuits, analog-to-digital circuits, and data communications system.

2 HARDWARE

The instrument consists of two separate boxes, a so-called "test set" that contains high-frequency components including directional couplers, and a so-called "receiver" that provides data acquisition, control of the test set, signal generation from a few Hz to hundreds of megahertz, data processing, displays, and computer connectivity. We have replaced the HP87511A test set with a test set modified for acoustic, rather than electromagnetic, operation. This new test set attaches by umbilical cables to "heads" that carry the ports to which the device under test (DUT) can be connected, after the fashion of millimeter-wave and waveguide-port electromagnetic VNAs, see Figure 2. The test set will be described in more detail below. The block diagram of the measurement system is shown in Figure 1. The prototype version with low-frequency heads is shown in Figure 3.

The HP4395A instrument does not intrinsically support any waveguide or wafer calibration methods [32]. Given the receiver maximum operating frequency of 500MHz, the designers would not have anticipated a waveguide application, or that the conventional radio-frequency (RF) "Short, Open, Load, Thru" (SOLT) calibration might not be possible. Here it is used simply for data acquisition and control. The acoustic calibration methods are quite different as will be described in section 3, so these limitations are not important. The wavelengths of sound in air between a few hundred Hertz and 50kHz are the same as those of electromagnetic waves running up to almost 50GHz, as the speed of sound is a little more than one-millionth of the speed of light, so the similarity with microwave and millimeter-wave instruments is not surprising.

2.1 DIRECTIONAL COUPLERS

A Directional Coupler is a 4-port network conducting travelling waves. Figure 4 shows a symbolic directional coupler. Forward travelling waves are conducted, typically with small loss, from the input or first port P1, to the transmitted or second port, P2. Reverse travelling waves behave similarly moving from P2 to P1. Portions of the forward and reverse traveling waves are separately coupled to the two side ports. [33] It is often assumed that a directional coupler is inherently an electromagnetic device, since the majority of commercial examples have either coaxial or electromagnetic waveguide ports. In this work the directional couplers are acoustic.

The coupled port, P3, receives a portion (typically in the order of 1 %) of the forward wave power which arrives at the input port, P1, and substantially exits the transmitted port, P2. The isolated port receives the same portion of the reverse wave power that travels the other way, into P2 and out of P1. Ideally, none of the forward power appears at the isolated port, P4. The directionality of a directional coupler is a measure of the isolation between the coupled and isolated ports, i.e., how much unwanted forward power arrives at the isolated reverse side port and vice versa. Directional couplers are all imperfect; if 1% of the forward power is desirably diverted to the coupled port, one tenth or one-hundredth as much will reach the isolated port. The coupling and isolation typically both vary with frequency. Calibrations are used to measure and remove the error introduced by the directional coupler. Although the calculations can be arduous, modern computers make this practicable. Nevertheless, calibration demands some minimum directionality in order to work correctly. We believe the full two-port calibration presented in this manuscript is the first such calibration in the acoustic domain, and successfully corrects for all losses and imperfections in the directional couplers and all other hardware in the instrument.

The AVNA instrument uses a design of directional couplers presented by Lagasse in 1971. [13] The Lagasse coupler is built using a synthesis method for microwave waveguide [34] with experiment to determine the general form of a branch-line acoustic directional coupler. The key part of the structure can be seen in Figure 5, and a photograph of an example constructed in transparent acrylic in Figure 6. It may also be possible to make out the structure in Figure 3. The reader may imagine sound waves traversing from left to right above the "blocks" shown

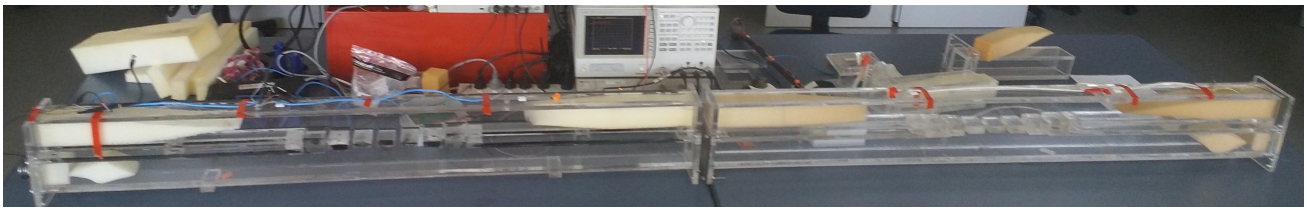

Fig. 3. The AVNA prototype setup with the much larger 1000–2000 Hz heads constructed in transparent acryllic. A DUT would be inserted between the two couplers, at bench level, where the two tables meet. Steel flange screws are just visible in the image.

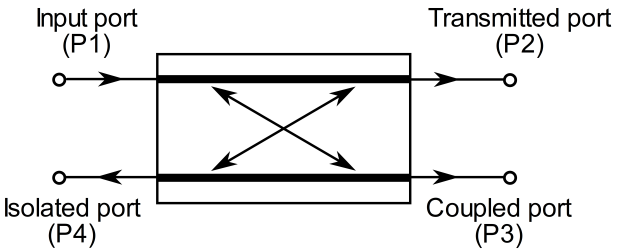

Fig. 4. A symbolic representation of a Directional Coupler with labeled ports. In spite of the naming of ports, a coupler is typically symmetrical so that it could be flipped around vertical or horizontal axes.

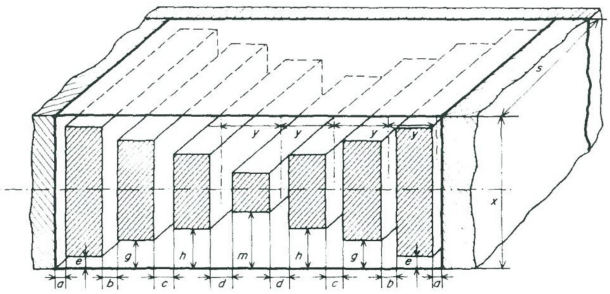

Fig. 5. The general form of the acoustic branch-line directional coupler as described by Lagasse, image taken from [13]. The reader must imagine the spaces above and below the array of gaps to be waveguides traversing left and right to form the four ports of the coupler.

in the figure. Gaps between the blocks periodically permit sound to travel downwards from the waveguide above the array of blocks to the waveguide below the array of blocks. The gaps between the blocks are the branch lines, with the width of the gaps and their spacing selected so that waves in the guide below the string of blocks interfere constructively and destructively moving left and right in the guide. This is similar to the radio frequency Butterworth and Chebyshev synthesised couplers that use the same method [34].

A version of the Lagasse design was built by Pennington and used in an acoustic impedance meter [10]. Pennington's coupler used a 60 mm square waveguide with a designed frequency range of 1–2 kHz and a usable range of 800–2,200 Hz. It had a crude flange connection system. In this work we include a 3D-printed set of couplers scaled up a decade in frequency, and improved flanges.

Fig. 6. A Lagasse coupler constructed in transparent acrylic with black tape marking the divide between parallel waveguides and the branch-line section.

2.1.1 COUPLER FLANGES AND REPEATABILITY

The directional couplers need to be connected to both the rest of the analyzer and to the DUT to function as part of the analyzer. Connections in electronics at low frequency are often paid little attention, but at high frequency and in waveguide systems in particular these connections are critical to the repeatability, precision and reliability of equipment. Microwave waveguide is typically machined from brass for reasons of precision. It usually features a rectangular cross-section and similar mounting flanges for each port. There are a number of standards for microwave flange construction and testing [35, 36]. A mechanical drawing for a commercially available WR-22 waveguide flange can be seen in Figure 7.

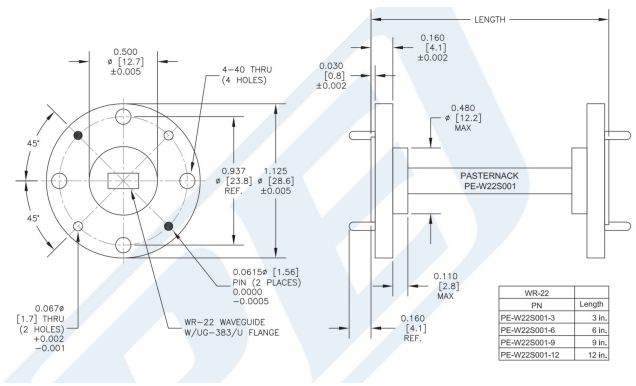

Fig. 7. WR-22 mechanical specifications taken from the datasheet for a pasternack PE-W22S001-12.

Microwave waveguide is sometimes pressurized to stop the ingress of dust and moisture. When the waveguide needs to seal O-rings can feature in microwave waveguide flange [37]. Another feature of microwave waveguide is the use of alignment pins that allow for precision mating of two flanges. Most flanges feature a bolt pattern with specific torque requirements for proper connection [38, 39, 40, 41, 42].

By borrowing from these standard microwave waveguide features, improved flanges for the acoustic coupler were developed in consultation with our university workshop. The O-ring feature was adapted to the acoustic waveguide because it is important that the waveguide seals to prevent signal leakage. The addition of alignment pins increases the ease of assembly, ensures minimum discontinuity at the junctions, and reduces sliding of the waveguide sections past one another during assembly that may scratch the mating surfaces. Figures 8 and 9 show the final designs for acoustic couplers for two bandwidths. The smaller size couplers operate over 10–20 kHz, have a guide dimension of 6 mm by 6 mm and the larger set over 1–2 kHz with the same dimensions used by Pennington.

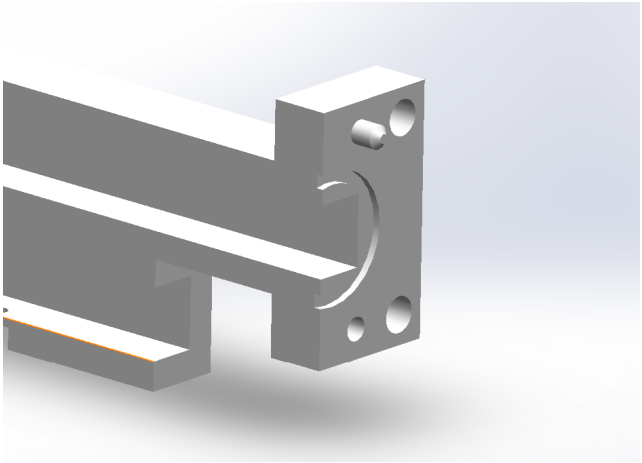

Fig. 8. A cross-section of the flange designed for the scaled and 3D printed directional couplers. This flange features an O-ring groove and alignment pins.

The performance of the acoustic waveguide flanges has been carefully studied using statistical methods. [11] This is done by taking a number of measurements of the same DUT, disconnecting it in between each measurement. It is then possible to determine the standard deviation in these measurements and then use this value as an indicator of the repeatability of the joint [11]. We concluded that even the order of tightening the flange bolts affects how repeatable is a connection. Tightening in a star pattern with a torque wrench was specified.

3 CALIBRATION

Before we can discuss calibration, we should introduce S-Parameters and the error model upon which the calibration is built.

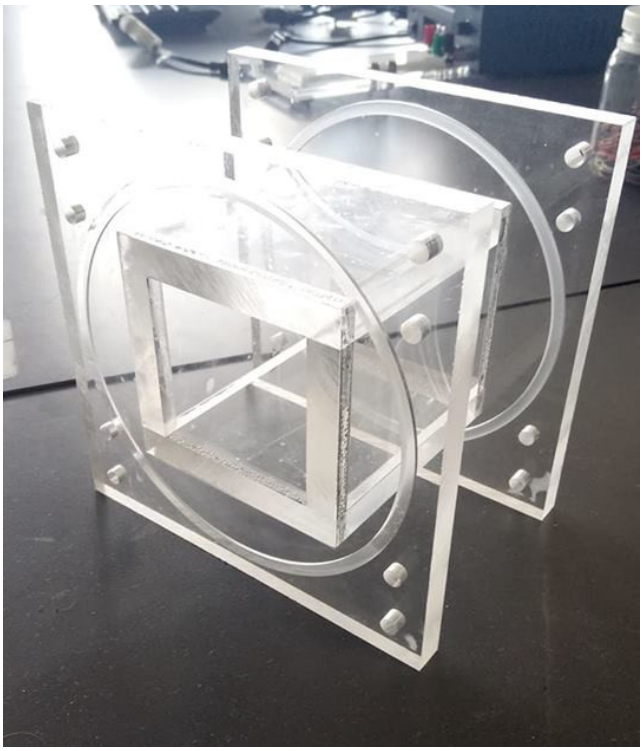

Fig. 9. An example of the larger acoustic waveguide with flanges and alignment pins visible. The component is a short length of plain waveguide, again constructed in transparent acrylic.

3.1 ACOUSTIC S-PARAMETERS

Scattering or S-parameters are used to measure the reflection and transmission coefficients of a device in the world of travelling waves, see [43] for theory and applications the RF domain, wikipedia [44] for a complete introduction & history, and [45] for a tutorial of their application in the acoustic domain. When displayed on a Smith chart, S-parameters offer an easy-to-interpret visualisation of a Device Under Test (DUT). They are routinely used in the RF world. S-parameters are equally applicable in the acoustic domain. [4, 45]

Measurement of the S-parameters for a 2-port DUT yields a set of four complex numbers. These represent of the change in signal magnitude and phase from input to output (S_{21}), output to input (S_{12}), and the input (S_{11}) and output (S_{22}) reflection coefficients. This means that the S-parameters convey impedance and gains. S_{11} is sometimes called the reflection coefficient Γ_1 for port 1, and S_{22}, Γ_2 for port 2. The complex impedance of the load is related to the reflection coefficient by the familiar formula

$$\Gamma_x = \frac{Z_x - Z_0}{Z_x + Z_0} \tag{2}$$

where Z_x is the port impedance and Z_0 is the characteristic impedance of the transmission line.

3.2 ERROR MODEL

The acoustic vector network analyzer is described with an error model that contains all sixteen terms associated with a two-port error box as has been done in the microwave domain [46, 9]. Nevertheless, it is usual in the mi-

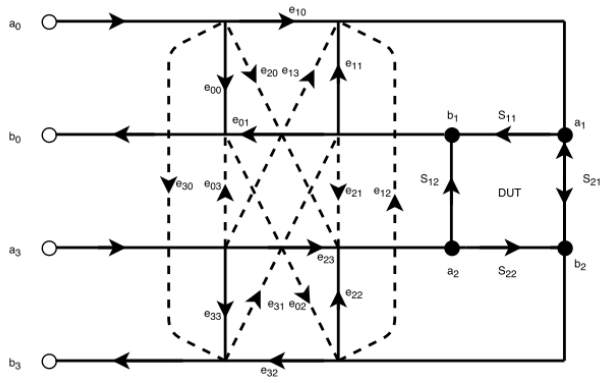

Fig. 10. A flow graph of the 16 term error model

crowave domain to truncate the 16-term model to either 12 terms in the case of planar measurements on wafer, or to 8-terms in the case of coaxial RF systems. These simplifications are possible because the physics of those situations allow a number of terms to be discarded, or more precisely to be assumed to have values that will have negligible effect. For example, one error term describes the amount of energy radiated from one port past the DUT in free space to the second port. In a coaxial system this can safely be assumed to be zero. We have observed that these simplifications lead to calibration failure in the acoustic domain. We attribute this to the imperfect guiding properties of acoustic waveguide; consider that sound energy may propagate in the walls of an acoustic waveguide, but the equivalent cannot practically occur in the electromagnetic world.

The 16-term error model can be visualized as a flow graph as shown in Figure 10 from which the equations relating measured to true S-parameters may be derived. Expressing the error model as a matrix, the equations can be solved for the unknown coefficients by means of a series of measurements for which the correct answer is known [9]. Let the error model matrix be E, then

$$E \equiv \begin{bmatrix} E_1 & E_2 \\ E_3 & E_4 \end{bmatrix} = \begin{bmatrix} e_{00} & e_{03} & e_{01} & e_{02} \\ e_{30} & e_{33} & e_{31} & e_{32} \\ e_{10} & e_{13} & e_{11} & e_{12} \\ e_{20} & e_{23} & e_{21} & e_{22} \end{bmatrix} \tag{3}$$

The relationship between the measured S-parameters S_m and the actual calibrated S-parameters S_a is by definition:

$$\begin{bmatrix} b_0 \\ b_3 \end{bmatrix} = S_m \begin{bmatrix} a_0 \\ a_3 \end{bmatrix}, \; S_m = \begin{bmatrix} S_{11m} & S_{12m} \\ S_{21m} & S_{22m} \end{bmatrix} \tag{4}$$

$$\begin{bmatrix} a_1 \\ a_2 \end{bmatrix} = S_a \begin{bmatrix} b_1 \\ b_2 \end{bmatrix}, \; S_a = \begin{bmatrix} S_{11a} & S_{12a} \\ S_{21a} & S_{22a} \end{bmatrix} \tag{5}$$

and we can then show that

$$S_m = E_1 + E_2 S_a (I - E_4 S_a)^{-1} E_3 \tag{6}$$

Where I is the unit matrix. Solving for S_a yields

$$S_a = [E_3 (S_m - E_1)^{-1} E_2 + E_4]^{-1} \tag{7}$$

Equation 7 is the result that is used to de-embed the actual S-parameters from the measured S-parameters.

In order to utilise/create a calibration method there needs to be some known standards or measurements that can be used to satisfy the equations and yield values for the error terms within the error matrix. In other words, we need to measure some devices whose S-parameters are known, in order to solve for the E matrix. In the acoustic domain we have knowledge of only a few possible standards.

- Zero length "Thru"
  A Zero length "Thru" is provided by directly coupling the two ports of the analyzer by their flanges and provides no attenuation or phase change.
- Line
  A line is less accurately known but its attenuation and phase change are related to its length. The attenuation is due to the lossy nature of air.
- Reflect
  An almost ideal reflect is provided by terminating the waveguide port with a very hard and stiff material.
- Match
  A match is provided by the sliding load method. The sliding load produces a number of points on the Smith chart; circles are then fitted to these results by the Taubin method [47, 2] and the circle center reveals the position of an ideal load. The sliding load will be discussed in detail below.

By knowing what standards we have available in the acoustic domain the number of possible methods is reduced to only a few. Most of the remaining methods are for an 8 term calibration method, which can be extended to 12 with an extra measurement. Crucially TRRM also remains, which is a method for a full 2 port 16-term calibration. The abbreviation TRRM stands for "Thru-Reflect-Reflect-Match", meaning that only a through connection of some sort, two reflection scenarios, and a match are required. [48] TRRM was selected because it is achievable with the available standards. Using TRRM in order to solve for the 16-term model, five measurements are required. A Thru, Match-Match, Reflect-Reflect, Match-Reflect and Reflect-Match. These measurements produce five sets of measured S-parameter matrices that have a corresponding known "actual" S-parameter matrix.

The ideal matrices are:

$$\text{Thru:} \quad A = \begin{bmatrix} 0 & T \\ T & 0 \end{bmatrix} \tag{8}$$

$$\text{Match-Match:} \quad B = \begin{bmatrix} 0 & 0 \\ 0 & 0 \end{bmatrix} \tag{9}$$

$$\text{Reflect-Reflect:} \quad C = \begin{bmatrix} \Gamma & 0 \\ 0 & \Gamma \end{bmatrix} \tag{10}$$

$$\text{Reflect-Match:} \quad D = \begin{bmatrix} \Gamma & 0 \\ 0 & 0 \end{bmatrix} \tag{11}$$

$$\text{Match-Reflect:} \quad E = \begin{bmatrix} 0 & 0 \\ 0 & \Gamma \end{bmatrix} \tag{12}$$

(13)

T is known from the length l and propagation constant γ, where $T = e^{-\gamma l}$, for a zero length Thru, $T = 1$.

Equation 7 is very non-linear and difficult to solve directly. Cascading T-parameters can be used to linearize the problem. Solving for the T parameters can be done in a variety of ways. Two common methods are normalizing by one of the unknown coefficients and solving directly or using a least squares method. Single value decomposition (SVD) is used often because of its ability to handle singularities [49, 48].

The E and T matrices are related by the following:

$$E = \begin{bmatrix} T_2 T_4^{-1}, & T_1 - T_2 T_4^{-1} T_3 \\ T_4^{-1}, & -T_4^{-1} T_3 \end{bmatrix} \tag{14}$$

$$T = \begin{bmatrix} E_2 E_1 E_3^{-1} E_4, & E_1 E_3^{-1} \\ E_3^{-1} E_4, & E_3^{-1} \end{bmatrix} \tag{15}$$

Substituting the T matrix into the system yields:

$$\begin{bmatrix} b_0 \\ b_3 \\ a_0 \\ a_3 \end{bmatrix} = T \begin{bmatrix} a_1 \\ a_2 \\ b_1 \\ b_2 \end{bmatrix} \tag{16}$$

Using the T parameters and the definitions of S_m and S_a the following can be derived

$$S_m = (T_1 S_a + T_2)(T_3 S_a + T_4)^{-1} \tag{17}$$

$$T_1 S_a + T_2 - S_m T_3 S_a - S_m T_4 = 0 \tag{18}$$

$$S_a = (T_1 - S_m T_3)^{-1}(S_m T_4 - T_2) \tag{19}$$

Equation 19 is the new de-embedding equation and allows for a solution of the error model. The results of both the analytical and numerical methods are presented in this manuscript.

3.3 PHYSICAL STANDARDS

In order to utilise the calibration method there needs to be actual physical known standards that can be used to satisfy the equations and yield an error matrix. The standards required in this case are:

- Zero length "Thru"
  A Zero length "Thru" is provided by directly coupling the two ports of the analyzer by their flanges and provides no attenuation or phase change.
- Reflect
  An virtually ideal reflect is provided using a 5 mm mild steel plate to close the guide.
- Match
  A match is provided by the sliding load method where the load is a foam wedge free to move within a length of open waveguide. In this work we used 5 points per frequency, suitably selected [50, 51]. Circles were then fitted to these results by the Taubin method [47, 2] and the circle center taken as the result that would have been measured had an ideal load been used.

Commercial vector network analyzers often have an optional (often expensive) calibration kit such as the one pictured in Figure 11. These production standards must be produced with very high precision and tolerances so that any customer can be confident that their results are reproducible in other laboratories around the world.

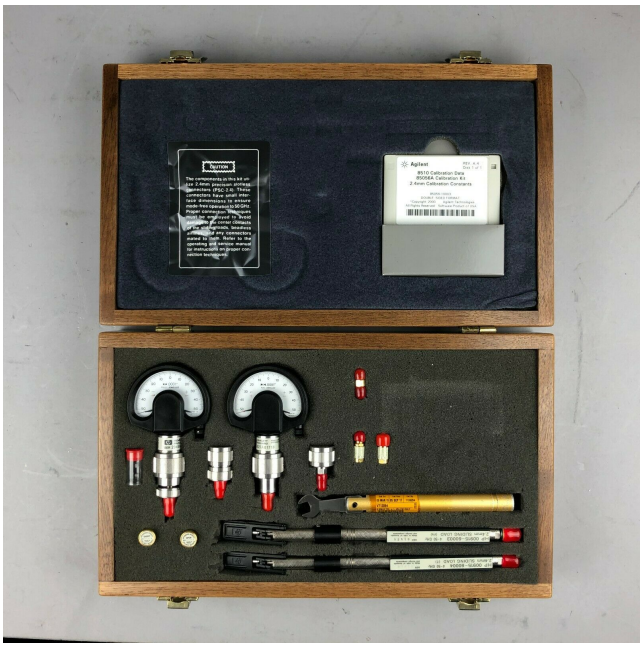

Fig. 11. An Agilent 85056A 2.4 mm VNA calibration kit including sliding loads and calibration data.

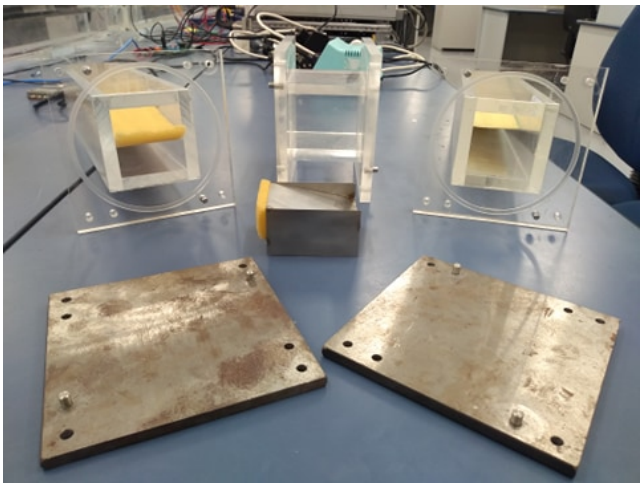

Fig. 12. A full set of acoustic standards. Large Reflect standards made from 5 mm mild steel plate, front left and right. Large Match standards made from open cell foam in a section waveguide, rear left and right. In the middle is a finite-lenghth "thru", in front of which is an inclusion after the fashion of that to be described around Figure 14.

A full set of standards that make up the 1-2 kHz acoustic calibration kit can be seen in Figure 12. A Line, or "Thru" of non-zero length was also built, since it is of known length it is possible to know the phase change through its length for each frequency making it a potential acoustic standard. The zero-length Thru is achieved by connecting both ports together repeatably by using a specific bolt pattern and bolt torque [11]. The "Reflect" is achieved by closing off the port with a 5 mm mild steel plate, us-

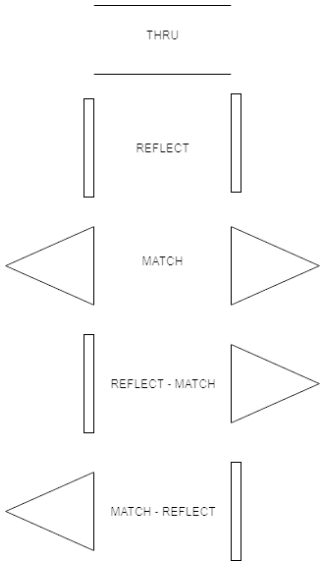

Fig. 13. A symbolic representation of the standards as connected to the analyzer for each of the five total measurements. The left hand column is the port one standards in order, port two is the right hand column

ing the same bolt pattern and torque. The idea is that a sufficiently-massive end-plate completely reflects incident sound. The Match (a load with negligible reflecion) is provided by a section of waveguide that contains a wedge section of foam, again using the same bolt pattern and torque. This section of foam is used as an acoustic analogue of the "Sliding load" that was used in radio-frequency (RF) VNA calibrations and Pennington's acoustic impedance meter. [50, 10].

The standards are connected in order and their four S-parameters are measured. The sliding loads for each of the "Match" measurements are slid to several positions and measured as discussed in some detail in section 3.3.1. The standards are represented symbolically in Figure 13. The figure shows the connections required for each of five measurements. The standards in order that are connected to port one are shown in the left hand column while those that are connected to port two are on the right.

3.3.1 THE SLIDING LOAD

A sliding load is used to separate the magnitude of any residual reflection due to the imperfections of a practical load. The magnitude of any fixed reflection from the actual load is assumed not to change with position of the absorber. The reflection from the load can be separated from other reflections in the system by sliding the load and using the resulting phase change. In the electromagnetic case, magnitude of the reflection from the load does not change with position, but the phase does. In the acoustic case the change in length means that the reflection magnitude may be reduced with increased distance from the source. This means in the acoustic case any lossy line or waveguide will result in a spiral locus on a Smith chart [10]. We discovered in practice the loss is often small enough that the spiral may be assumed to be a circle, as in the electromagnetic case.

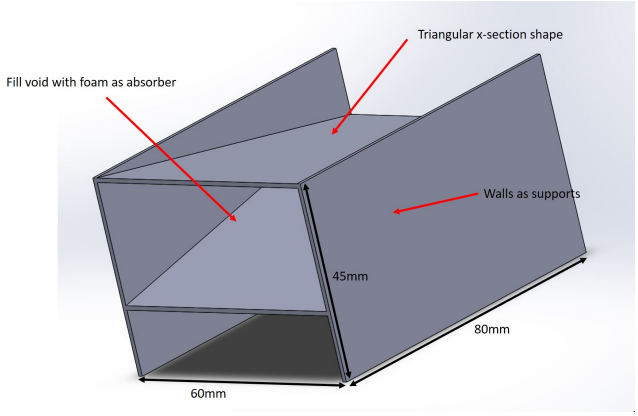

Fig. 14. A 3D CAD model for the Asymmetrical element to be inserted into a section of waveguide, creating the Asymmetrical "Thru"/transmission line verification standard. This CAD model can be 3D printed to implement the Asymmetrical element.

The circle or spiral fit is realised with a numerical method. On occasion that method can return unsatisfactory results, most commonly when the combination of frequency and load positions leads to measurements clustered rather than distributed alround the circle. These points are readily detected in the processing phase and can be automatically removed.

4 VERIFICATION

4.1 ASYMMETRICAL TRANSMISSION LINE STRUCTURE

An asymmetrical, reciprocal device embedded in a transmission line has the following characteristics: $S_{12} = S_{21}$ and $S_{11} \neq S_{22}$ [52]. If such an asymmetrical device's orientation is reversed and it is then measured again, swapped-around S-parameters S'_{11}, S'_{12}, S'_{21}, and S'_{22} are obtained. Then if $S'_{11} = S_{22}$, $S'_{22} = S_{11}$, $S'_{12} = S_{21}$, and $S'_{21} = S_{12}$ the calibration has successfully accounted for the error adapters on both ports.

An asymmetrical device was made by folding some light gauge steel sheet into a 'V' shape and filling the space between with foam. Sides were added that extend past the 'V' so that it can be placed in the waveguide and rest on the bottom surface. This structure, when placed in a length of waveguide will provide the characteristics of an asymmetrical transmission line. Figure 14 shows the 3D model for the device, and Figure 15 shows the physical implementation. This device was constructed to fit a 60 mm by 60 mm waveguide, and inserted in a short length of suitable guide.

The asymmetrical transmission line was measured in two orientations, forward and reverse. In the forward orientation, the nose of the triangular structure is pointed towards port one, and in the reverse orientation pointed towards port two. The forward and reverse response of S_{11} & S_{21} for the asymmetrical transmission line is shown in Figure 16. This response has typical transmission values of close to 0 dB while the magnitude of the reflection tends to increase with frequency from typical values below 40 dB to below 20 dB.

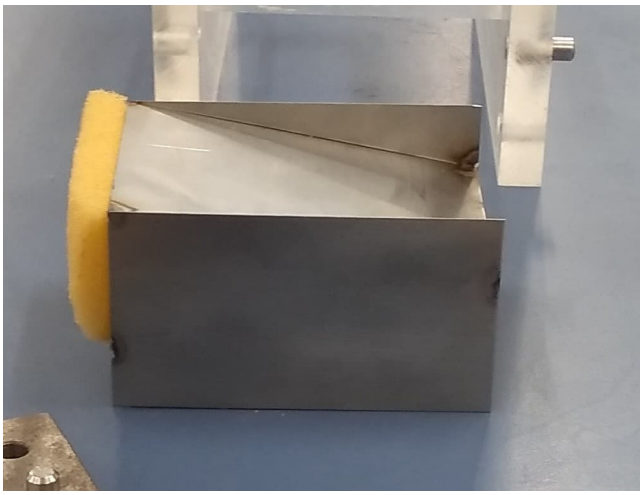

Fig. 15. The Asymmetrical element made from thin steel sheet (0.9 mm) and a foam wedge, this structure is then placed in a section of waveguide to complete the vitrifaction standard.

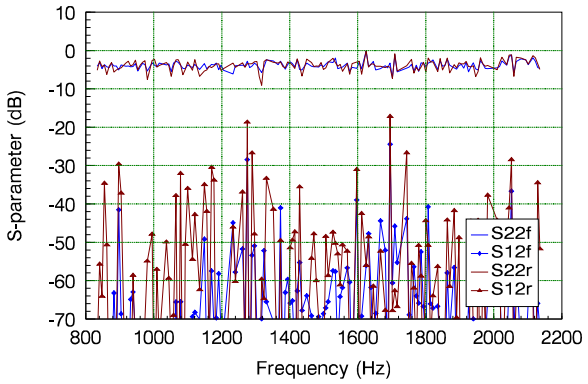

Fig. 17. Comparison of S_{22} and S_{12} measured on the asymmetrical element inserted each way around. Again the legend has S'_{22} as S_{22r}, etc. The parameters measured in the forward orientation, S_{12f} and S_{22f} agree strongly with the parameters measured in the reverse orientation S_{12r} and S_{22r}.

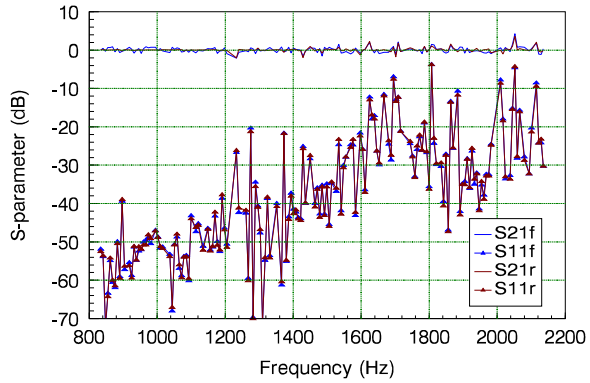

Fig. 16. Comparison of S_{11} and S_{21} measured on the asymmetrical element inserted each way around. In the legend, S_{21} is labelled S_{21f} and S'_{21} is labelled S_{21r}, etc. Note that S_{21} measured in the first case is virtually indistinguishable from S'_{21} measured with the device physically inserted the other way around. Likewise the input side reflection coefficient S_{11} differs by only small values despite its enormous variability.

The reverse response mirrors the forward orientation and has typical transmission values of close to 0 dB while the magnitude of the reflection tends to increase with frequency from typical values below 40 dB to below 20 dB.

The forward and reverse response of S_{22} & S_{12} for the asymmetrical transmission line is shown in Figure 17. This response has typical transmission values of -4 dB while the magnitude of the reflection tends to be small.

The repeatability of measurements using the acoustic network analyzer has been shown to have a worst case standard deviation of 0.4 dB [11]. The difference between the forward and reverse orientations for S_{11}, S'_{22}, S_{21}, and S'_{12} is less than 1 dB in most cases. The standard deviation for $S_{11} - S'_{22}$ is 0.506 dB and 0.694 dB for $S_{21} - S'_{12}$. The reflection coefficient is small, and we attribute the increased variance to random noise [9, 11]. The variance is consistent with the repeatability of the instrument suggesting that the calibration is performing well.

4.2 Comparison of Calibration Computation Methods

The same results should be expected when using either the analytical or numerical solutions to the error matrix. Figures 18 and 19 show the calibrated results using both methods. These results agree strongly for the transmission coefficients S_{21} and S_{12} and less strongly for the reflection coefficients S_{11} and S_{22}. The numerical method on average returns slightly greater reflection coefficients and with greater variance, the transmission coefficients follow very closely with a slight increase in variance as well. The variation in the reflection coefficients can be attributed to the variation in measurements used for the numerical method that are excluded from the analytical one. This is because the five calibration measurements produce an overdetermined system. In order to calibrate analytically, duplicate information is not used whereas in the numerical method it is left in leading to a slight increase in variance.

The numerical measurements of the asymmetrical transmission line also show that the calibration has been successful. The forward and reverse measurements agree, with a slight increase in variance compared to the analytical method. There is a small variation increase for the results calibrated with the numerical solution of the error matrix.

Because the results of the analytical and numerical calibration are in a agreement and consistent with what would be expected of an asymmetrical, reciprocal device [52] we are confident that the AVNA is now complete and validated. Further validation can be achieved with comparison to results simulated by means of CFD, but this is beyond the scope of the present work. It should also be noted that there are no physical standards that exist to allow for

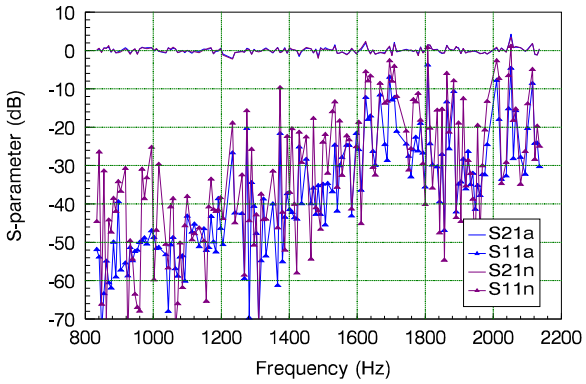

Fig. 18. Comparison of parameters S_{21} and S_{11} obtained by numerical and analytic solution of the error matrix. The same raw measurements of standards are used in each case.

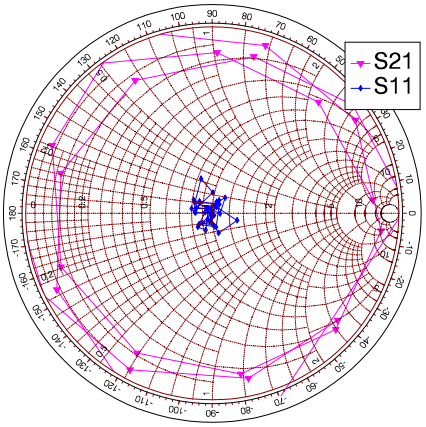

Fig. 20. The S_{11} and S_{21} values of an uncorrected thru connection plotted on a Smith chart. Frequency runs from 1220 Hz to 1980 Hz.

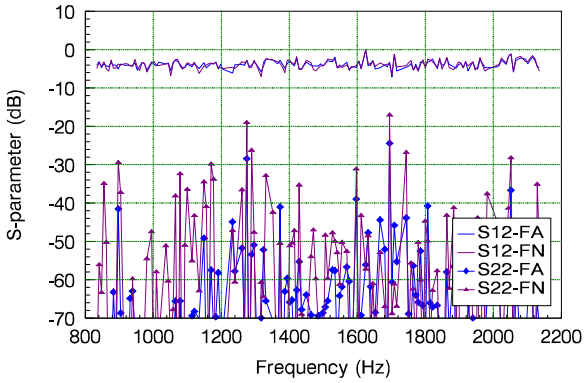

Fig. 19. Comparison of parameters S_{12} and S_{22} obtained by numerical and analytic solution of the error matrix. The same raw measurements of standards are used in each case.

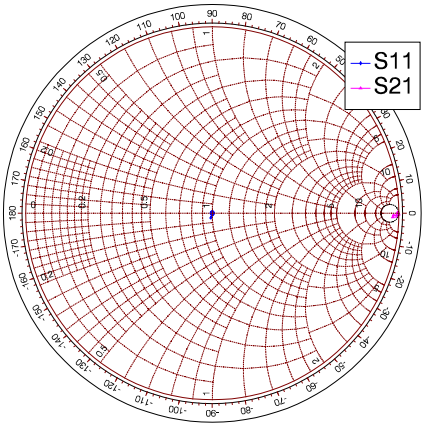

Fig. 21. The S_{11} and S_{21} values of a zero-length thru after correction plotted on a Smith chart. The zero-length thru data are close to being points so appear as single symbols.

the comparison of this measurement instrument to another. Alas, this is one of the problems the authors wish to address with the development of the AVNA.

4.3 Comparison of Corrected and Uncorrected Data

Figures 20 and 21 present uncorrected and corrected measurements of a zero-length thru re-connection. The data is presented in Smith Chart form, as is customary in the RF world. Smith charts present magnitude and phase, but sacrifice the visibility of frequency. Data runs from 1220 to 1980 Hz. The plots are presented separately as the corrected data for a zero-length thru appears as a single point and can be hard to identify. The uncorrected data shows the wildly-varying magnitude and phase typical of raw data. In the case of Figure 21, the zero-length thru data is indicative of the repeatability error. Some data has been removed, especially between 1780 and 1820 Hz, owing to low confidence caused by the selection of sliding load positions. On our prototype it is not possible to check coverage gaps resulting from load position selections in real time, as might be the case on an integrated real-time instrument.

5 SUMMARY AND CONCLUSIONS

This manuscript presents the first acoustic, vector-corrected, 2-port, network analyzer. Like any new high-performance measurement instrument, there are several separate advances required to realise the final instrument. There must be hardware that achieves directionality, for which we have relied upon a decades-old design by Lagasse, elegant but neglected. There must be calibration and verification standards. For these, we have mined the rich history of electromagnetic VNAs, adapting technologies such as the sliding load and (passive) asymmetric, reciprocal devices to the acoustic domain. There must be an

interconnection mechanism for the acoustic waveguides that is highly repeatable, for which we designed a flanged system with inbuilt O-ring seals, 3D-printed in titanium in the case of higher frequencies and smaller parts. Finally and most importantly, a series of measurements of known standards must be devised that permits solution for all the error coefficients in the system. This manuscript presents a pathway to find the 16 complex error coefficients of a general 2-port travelling-wave system that correct out the imperfections of the couplers and measurement electronics. This is the calibration procedure. We investigated both an analytical and a numerical approach to solving the error matrix, identifying the performance differences between these two approaches. We have shown that the AVNA instrument achieves its aim of measurement of acoustic reflectivity and transmissivity.

A notable advance of this work lies in the standards required for calibration. All previous acoustic measurement systems have relied to some extent upon calibration against a standard that is not well known. For example, [4] assumed a load, and [10] relied upon lossy lines. Here only an uncertain load and a reflection plate are required.

This manuscript reports the culmination of several years of work. Following in the footsteps of early electromagnetic vector network analyzer development, we have successfully built a prototype instrument capable of fast, swept, acoustic measurements. We have verified its operation. We have demonstrated operation in two frequency bands; extension to cover the audio spectrum is now possible. We consider that this represents a compression of some 5-plus decades of radio-frequency measurement experience into the acoustic domain.

One criticism of this design is that each set of heads spans just over an octave. Covering a reasonable audio spectrum would require 8 to 10 test sets. This same criticism was directed at EM VNAs as they moved from a few GHz bandwidth, past 100 GHz to the present terahertz range, each waveguide step adding less than one octave of bandwidth. As time passed, directional sensing structures with ever-increasing bandwidth were developed, and multiple couplers were incorporated into single head structures. By the end of the last century couplers whose highest operational frequency was 1000 times their lowest operational frequency became available. We believe the same will occur when sufficient need appears in the acoustic domain. An advantage of the acoustic impedance tube is that it can be made to span the human audio range. [6] With fixed-position microphones, the method relies upon a numerical fit to separate the forward and reverse waves. Each scheme has its advantages and disadvantages.

Applications of this instrument will continue to be found in the future. For now we suggest

- rapid, precise measurement of the reflectivity of architectural and furnishing materials,
- measurement of the sound transmissivity of building insulation materials and seals,
- determination of the resonant properties of cabinets, tubes, and cavities such as speaker enclosures and engine exhaust structures,
- characterisation of musical instrument components such as organ and brass pipes,
- energy absorption provided by cavity filling materials,
- sonar visibility of insects and other small items,
- impact on sonar visibility of surface coatings,
- indirect measurement of biological properties of flora correlated with sound absorption and reflection,
- non-destructive testing of composite structures, and
- plastic weld inspection.

Finally, we see no reason that a test set could not be constructed with water in place of air as the conducting medium. This would allow testing in an aquatic sonar scenario.

6 ACKNOWLEDGMENT

This research was partially funded by the "science for technological innovation" (SfTI) science challenge, one of the New Zealand national science challenges. (http://www.sftichallenge.govt.nz/) The authors wish to acknowledge the assistance of Peter Higgins in the Waikato University workshop.

7 REFERENCES

[1] "Technical review 1955-1 standing wave apparatus_1955," Tech. rep., Bruel and Kjaer (1955 Jan).

[2] K. Pennington, *Acoustic Vector Network Analyser*, Ph.D. thesis, The University of Waikato, Hamilton, New Zealand. (2017).

[3] J. Smith, C. Fritz, J. Wolfe, "A new technique for the rapid measurement of the acoustic impedance of wind instruments," *Proc. Seventh International Congress on Sound and Vibration* (2000 July).

[4] C. M. De Blok, R. F. M. Van den Brink, "Direct-Reading One-Port Acoustic Network Analyzer," *Journal of The Audio Engineering Society*, vol. 41, no. 4, pp. 231–238 (1993 April).

[5] J. Price, "Acoustic VNA User's Guide," (2008 January), URL `https://spot.colorado.edu/~pricej/downloads/AVNAUsersGuide.pdf`.

[6] R. Schlieper, S. Li, J. Peissig, "Development and validation of a full audio range acoustic impedance tube," presented at the *144th Convention of the AES, Milan, Italy*, pp. 1–4 (2018 May).

[7] "Acoustics – Determination of sound absorption coefficient and impedance in impedance tubes – Part 1: Method using standing wave ratio," Standard, International Organization for Standardization, ISO Central Secretariat, Chemin de Blandonnet 8, CP 401 - 1214 Vernier, Geneva, Switzerland (1996).

[8] "Acoustics – Determination of sound absorption coefficient and impedance in impedance tubes – Part 2: Transfer-function method," Standard, International Organization for Standardization, ISO Central Secretariat,

Chemin de Blandonnet 8, CP 401 - 1214 Vernier, Geneva, Switzerland (1996).

[9] M. MacDonell, J. Scott, "Realizing an Acoustic Vector Network Analyzer," *Proc. 147th Audio Engineering Society Convention* (2019).

[10] J. Scott, K. E. Pennington, "Acoustic Vector-Corrected Impedance Meter," *IEEE Transactions on Instrumentation and Measurement*, vol. 63, no. 12, pp. 2726–2732 (2014), [Online]. Available: 10.1109/TIM.2014.2327474.

[11] M. MacDonell, K. Basnet, J. Scott, "Waveguide Joint Design and Validation for use in Acoustic Vector-corrected Network Analysers," presented at the *2019 IEEE International Instrumentation and Measurement Technology Conference (I2MTC)*, pp. 1–5 (2019), [Online]. Available: 10.1109/I2MTC.2019.8826926.

[12] K. Wong, "Traceability of vector network analyzer measurements," doi:10.1109/ARFTG.2008.4804283, pp. 157–167 (2008).

[13] P. Lagasse, "The realization of an acoustical directional coupler," *Journal of Sound and Vibration*, vol. 15, no. 3, pp. 367 – 372 (1971), [Online]. Available: https://doi.org/10.1016/0022-460X(71)90430-5.

[14] F. E. Terman, *Radio Engineering* (McGraw-Hill Book Co.), 3rd ed. (1947).

[15] W. B. Wholey, "Greater Reliability in UHF Impedance Measurements," *HP Journal Vol. 1*, vol. 53, no. 5 (1950), URL `http://www.hparchive.com/`.

[16] M. Golio, *The RF and Microwave Handbook* (CRC Press) (2001).

[17] S. Y. Liao, *Microwave Devices and Circuits* (Prentice-Hall), 3rd ed. (1990).

[18] D. Rytting, "ARFTG 50 year network analyzer history," presented at the *2008 71st ARFTG Microwave Measurement Conference*, pp. 1–8 (2008), [Online]. Available: 10.1109/ARFTG.2008.4633319.

[19] "Slotted Line," *Wikipedia* (retrieved March 2021), URL `https://en.wikipedia.org/wiki/Slotted_line`.

[20] Mason, Zimmerman, *Electronic Circuits, Signals & Systems* (Wiley) (1960).

[21] S. Rehnmark, "On the Calibration Process of Automatic Network Analyzer Systems," *IEEE Transactions on Microwave Theory and Techniques*, vol. 22, pp. 457–458 (1974).

[22] B. P. Hand, "Developing accuracy specifications for automatic network analyzer systems," *Hewlett-Packard Journal*, pp. 16–19 (1970 February).

[23] W. Kruppa, K. Sodomsly, "An explicit solution for the scattering parameters of a linear two-port measured with an imperfect test set," *IEEE Transactions on Microwave Theory and Techniques*, vol. 19, pp. 122–123 (1971 January).

[24] H. V. Shurmer, "Calibration procedure for computer-corrected parameter characterisation of devices mounted in microstrip," *Electronics Letters*, pp. 323–324 (1973 July).

[25] Kuhn, "Signal Flow Graphs," *Microwave Journal*, p. 59 (1963 November).

[26] G. Engen, C. Hoer, "Thru-reflect-line: An improved technique for calibrating the dual six-port automatic network analyzer," *IEEE Trans. Microwave Theory Tech.*, vol. 27, no. 12, pp. 987–993 (1979).

[27] K. J. A. Davidson, E. Strid, "LRM and LRRM calibrations with automatic determination of load inductance," *36th ARFTG Conference digest*, pp. 57–63 (1990).

[28] A. Ferrero, U. Pisani, "Two-Port Network Analyzer Calibration Using an Unknown Thru," *IEEE Microwave and Guided Wave Letters*, vol. 2, no. 12, pp. 505–507 (1992 December).

[29] L. Hayden, "An Enhanced Line-Reflect-Reflect-Match Calibration," *Proceedings of the 67th IEEE ARFTG Conference*, pp. 143–149 (2006).

[30] C. Huang, H. Lin, "A Novel Calibration Algorithm With Unknown Line-Series-Shunt Standards for Broadband S-Parameter Measurements," *IEEE TRANSACTIONS ON INSTRUMENTATION AND MEASUREMENT*, vol. 57, no. 5 (2008 may).

[31] A. Rumiantsev, N. Ridler, "VNA Calibration," *IEEE Microwave Magazine*, pp. 86–99 (2008 June).

[32] Agilent, "Agilent 4395A Network/ Spectrum/ Impedance Analyzer Operation Manual," (2007 May), URL `https://literature.cdn.keysight.com/litweb/pdf/04395-90040.pdf`.

[33] P. Rizzi, *Microwave Engineering - Passive Circuits* (Prentice-Hall Inc, Englewood Cliffs NJ) (1988).

[34] R. Levy, L. F. Lind, "Synthesis of Symmetrical Branch-Guide Directional Couplers," *IEEE Transactions on Microwave Theory Techniques*, vol. 19, no. 2, pp. 80–89 (1968 feb), [Online]. Available: 10.1109/TMTT.1968.1126612.

[35] "Flanges for waveguides - Part 1: General requirements," Standard, International Electrotechnical Commission, Geneva (2016).

[36] "Flanges for waveguides - Part 2: Relevant specifications for flanges for ordinary rectangular waveguides," Standard, International Electrotechnical Commission, Geneva (2016).

[37] "Sealing test for pressurized waveguide tubing and assemblies," Standard, International Electrotechnical Commission, Geneva (2016).

[38] T. N. Anderson, "Rectangular and Ridge Waveguide," *IRE Transactions on Microwave Theory and Techniques*, vol. 4, no. 4, pp. 201–209 (1956), [Online]. Available: 10.1109/TMTT.1956.1125063.

[39] M. Horibe, K. Noda, "Modification of waveguide flange design for millimeter and submillimeter-wave measurements," *77th ARFTG Microwave Measurement Conference*, pp. 1–7 (2011).

[40] M. Horibe, R. Kishikawa, "Performance of new design of waveguide flange for measurements at frequencies from 800 GHz to 1.05 THz," *79th ARFTG Microwave Measurement Conference*, pp. 1–6 (2012).

[41] M. Horibe, "Measurement Uncertainty in Terahertz VNAs: Using Terahertz Vector Network Analyzers for Stable, Accurate Measurement and to Evaluate Uncertainty," *IEEE Microwave Magazine*,

vol. 19, no. 2, pp. 24–34 (2018), [Online]. Available: 10.1109/MMM.2017.2779678.

[42] "IEEE Standard for Rectangular Metallic Waveguides and Their Interfaces for Frequencies of 110 GHz and Above–Part 2: Waveguide Interfaces," *IEEE Std 1785.2-2016*, pp. 1–22 (2016), [Online]. Available: 10.1109/IEEESTD.2016.7564020.

[43] R. E. Collin, *Foundations for Microwave Engineering* (Wiley-IEEE Press) (2001).

[44] Wikipedia, "Scattering parameters," .

[45] W. Koontz, "Multiport Acoustic Models with Applications in Audio Signal Processing," *Journal of the Audio Engineering Society*, vol. 61, no. 10, pp. 727–736 (2013 October).

[46] H. Van Hamme, M. Vanden Bossche, "Flexible vector network analyzer calibration with accuracy bounds using an 8-term or a 16-term error correction model," *IEEE Transactions on Microwave Theory and Techniques*, vol. 42, no. 6, pp. 976–987 (1994), [Online]. Available: 10.1109/22.293566.

[47] G. Taubin, "Estimation of planar curves, surfaces, and nonplanar space curves defined by implicit equations with applications to edge and range image segmentation," *IEEE Transactions on Pattern Analysis and Machine Intelligence*, vol. 13, no. 11, pp. 1115–1138 (1991).

[48] K. Silvonen, "LMR 16-a self-calibration procedure for a leaky network analyzer," *IEEE Transactions on Microwave Theory and Techniques*, vol. 45, no. 7, pp. 1041–1049 (1997).

[49] J. V. Butler, D. K. Rytting, M. F. Iskander, R. D. Pollard, M. Vanden Bossche, "16-term error model and calibration procedure for on-wafer network analysis measurements," *IEEE Transactions on Microwave Theory and Techniques*, vol. 39, no. 12, pp. 2211–2217 (1991), [Online]. Available: 10.1109/22.106567.

[50] H. C. Heyker, "The Choice of Sliding Load Positions to Improve Network Analyser Calibration," presented at the *1982 12th European Microwave Conference*, pp. 429–434 (1982), [Online]. Available: 10.1109/EUMA.1982.333099.

[51] G. Vandersteen, Y. Rolain, J. Schoukens, A. Verschueren, "An improved sliding-load calibration procedure using a semiparametric circle-fitting procedure," *IEEE Transactions on Microwave Theory and Techniques*, vol. 45, no. 7, pp. 1027–1033 (1997), [Online]. Available: 10.1109/22.598437.

[52] J. B. Scott, "Investigation of a method to improve VNA calibration in planar dispersive media through adding an asymmetrical reciprocal device," *IEEE Transactions on Microwave Theory and Techniques*, vol. 53, no. 9, pp. 3007–3013 (2005), [Online]. Available: 10.1109/TMTT.2005.854225.

THE AUTHORS

Marcus MacDonell

Jonathan Scott

Marcus attended The university of Waikato in Hamilton, New Zealand from 2010 to 2020, and was awarded a BE(hons) in 2014, and a Master of Engineering in 2015. Marcus founded Corax Audio labs in 2016 with seed money awarded by the Summer Start-Up Program at the University of Waikato. His PhD research marries the fields of vector network analysis and acoustic measurement.

●

Jonathan has worked as an EE for universities and private industry in Australia, California and for the last 15 years as a professor of electronics engineering at the University of Waikato in New Zealand. His research focuses on characterization, measurement, modeling and simulation, especially at RF & microwave frequencies. Recent work has strong biomedical context revolving around modeling electrodes for human implantation, and techniques for making implant leads safe in MRI scanners. Other research includes acoustic measurement, fractional-order equivalent-circuit modeling and characterization of lithium batteries, and engineering education especially in the context of threshold concepts.

C.5 Co-authorship

THE UNIVERSITY OF WAIKATO
Te Whare Wānanga o Waikato

Co-Authorship Form

Postgraduate Studies Office
Student and Academic Services Division
Wahanga Ratonga Matauranga Akonga
The University of Waikato
Private Bag 3105
Hamilton 3240, New Zealand
Phone +64 7 838 4439
Website: http://www.waikato.ac.nz/sasd/postgraduate/

This form is to accompany the submission of any PhD that contains research reported in published or unpublished co-authored work. **Please include one copy of this form for each co-authored work.** Completed forms should be included in your appendices for all the copies of your thesis submitted for examination and library deposit (including digital deposit).

Please indicate the chapter/section/pages of this thesis that are extracted from a co-authored work and give the title and publication details or details of submission of the co-authored work. Hardware chapter. Theory chapter.

"Development and Basic Calibration of an Acoustic vector network analy

Nature of contribution by PhD candidate	LEAD AUTHOR, LIT REVIEW, LAB WORK
Extent of contribution by PhD candidate (%)	60

CO-AUTHORS

Name	Nature of Contribution
J. B. Scott	management, theory, editing

Certification by Co-Authors

The undersigned hereby certify that:

- the above statement correctly reflects the nature and extent of the PhD candidate's contribution to this work, and the nature of the contribution of each of the co-authors; and

Name	Signature	Date
J. B. Scott	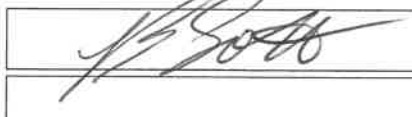	22 FEB 2024

THE UNIVERSITY OF WAIKATO
Te Whare Wānanga o Waikato

Co-Authorship Form

Postgraduate Studies Office
Student and Academic Services Division
Waharanga Ratonga Matauranga Akonga
The University of Waikato
Private Bag 3105
Hamilton 3240, New Zealand
Phone +64 7 838 4439
Website: http://www.waikato.ac.nz/sasd/postgraduate/

This form is to accompany the submission of any PhD that contains research reported in published or unpublished co-authored work. **Please include one copy of this form for each co-authored work.** Completed forms should be included in your appendices for all the copies of your thesis submitted for examination and library deposit (including digital deposit).

Please indicate the chapter/section/pages of this thesis that are extracted from a co-authored work and give the title and publication details or details of submission of the co-authored work.
IEEE I²MTC (may 2019) chapter 4: "Hardware design and implementation"
"Waveguide joint design and validation for use in an acoustic vector corrected Network analyser"

Nature of contribution by PhD candidate	Lab work, main author
Extent of contribution by PhD candidate (%)	80%

CO-AUTHORS

Name	Nature of Contribution
Jonathan Scott	Second author, editing
Keshav Basnet	Lab work

Certification by Co-Authors

The undersigned hereby certify that:

- the above statement correctly reflects the nature and extent of the PhD candidate's contribution to this work, and the nature of the contribution of each of the co-authors; and

Name	Signature	Date
Keshav Basnet		19/02/2021
J. B Scott		22 FEB 2021

THE UNIVERSITY OF WAIKATO
Te Whare Wānanga o Waikato

Co-Authorship Form

Postgraduate Studies Office
Student and Academic Services Division
Wahanga Ratonga Mataurang Akonga
The University of Waikato
Private Bag 3105
Hamilton 3240, New Zealand
Phone +64 7 838 4439
Website: http://www.waikato.ac.nz/sasd/postgraduate/

This form is to accompany the submission of any PhD that contains research reported in published or unpublished co-authored work. **Please include one copy of this form for each co-authored work.** Completed forms should be included in your appendices for all the copies of your thesis submitted for examination and library deposit (including digital deposit).

Please indicate the chapter/section/pages of this thesis that are extracted from a co-authored work and give the title and publication details or details of submission of the co-authored work. Chapters 3,5
AES NY 147 (OCT 2019)
" Realizing an acoustic vector network analyser"

Nature of contribution by PhD candidate	Lab work, main author
Extent of contribution by PhD candidate (%)	90%

CO-AUTHORS

Name	Nature of Contribution
Jonathan Scott	Second author, editing

Certification by Co-Authors

The undersigned hereby certify that:

- the above statement correctly reflects the nature and extent of the PhD candidate's contribution to this work, and the nature of the contribution of each of the co-authors; and

Name	Signature	Date
	J. B. Scott	22 FEB 2021

THE UNIVERSITY OF WAIKATO
Te Whare Wānanga o Waikato

Co-Authorship Form

Postgraduate Studies Office
Student and Academic Services Division
Wahanga Ratonga Mataurange Akonga
The University of Waikato
Private Bag 3105
Hamilton 3240, New Zealand
Phone +64 7 838 4439
Website: http://www.waikato.ac.nz/sasd/postgraduate/

This form is to accompany the submission of any PhD that contains research reported in published or unpublished co-authored work. **Please include one copy of this form for each co-authored work.** Completed forms should be included in your appendices for all the copies of your thesis submitted for examination and library deposit (including digital deposit).

Please indicate the chapter/section/pages of this thesis that are extracted from a co-authored work and give the title and publication details or details of submission of the co-authored work. Chapter 5, Journal of The Audio Engineering Society (submitted Feb 12 2021) "Full 2-port vector-corrected Network analyser in acoustic domain"

Nature of contribution by PhD candidate	Lab work, main author
Extent of contribution by PhD candidate (%)	80%

CO-AUTHORS

Name	Nature of Contribution
Jonathan Scott	second author, editing

Certification by Co-Authors

The undersigned hereby certify that:

- the above statement correctly reflects the nature and extent of the PhD candidate's contribution to this work, and the nature of the contribution of each of the co-authors; and

Name	Signature	Date
J. B. Scott		22 FEB 2021

Bibliography

[1] D. Rytting, "ARFTG 50 year network analyzer history," 2008 71st ARFTG Microwave Measurement Conference, Atlanta, GA, USA, 2008, pp. 1-8.

[2] G. Simpson, "Vector Network Analysis and ARFTG: A Historical Perspective," 50th ARFTG Conference Digest, 1997, pp. 41-41, doi: 10.1109/ARFTG.1997.327255.

[3] V. Gibiat and F. Laloë, "Acoustical impedance measurements by the two-microphone-three-calibration (TMTC) method," J. Acoust. Soc. Am., vol. 88, no. 6, pp. 2533–2545, Dec. 1990.

[4] T. Y. Lung and Doige, "A time-averaging transient testing method for acoustic properties of piping systems and mufflers with flow," J. Acoust. Soc. Am., vol. 73, no. 3, pp. 867–876, Mar. 1983.

[5] R. Boonen and P. Sas, "Determination of the acoustical impedance of an internal combustion engine exhaust," in Proceedings of ISMA2002, vol. 5, 2002, pp. 1939–1946.

[6] Z. Tao and A. Seybert, "A review of current techniques for measuring muffler transmission loss," in SAE 2003 Noise & Vibration Conference and Exhibition, May 2003.

[7] AS/NZS 2107:2016 Acoustics – Recommended design sound levels and reverberation times for building interiors.

[8] J. González Suárez, M. Machimbarrena Gutiérrez, A. Tarrero Fernández, T. Lorenzana Lorenzana, and A. Moreno, "Comparative analysis of several acoustic impedance measurements," in Forum Acusticum Sevilla 2002. Sociedad Española de Acústica, 2002. [Online]. Available: http://hdl.handle.net/10261/7995

[9] Standard Test Method for Sound Absorption and Sound Absorption Coefficients by the Reverberation Room Method, ASTM C 423, Rev. A, 2009.

[10] T. G. H. Basten and H.-E. de Bree, "Full bandwidth calibration procedure for acoustic probes containing a pressure and particle velocity sensor," J. Acoust. Soc. Am., vol. 127, no. 1, pp. 264–270, Jan. 2010.

[11] Pennington, K. (2017). Acoustic Vector Network Analyser (Thesis, Doctor of Philosophy (PhD)). The University of Waikato, Hamilton, New Zealand. Retrieved from https://hdl.handle.net/10289/11530

[12] A. F. Seybert and D. F. Ross, "Experimental determination of acoustic properties using a two-microphone random-excitation technique," J. Acoust. Soc. Am., vol. 61, no. 5, pp. 1362–1370, May 1977.

[13] J. C. Webster, "An electrical method of measuring the intonation of cup-mouthpiece instruments," J. Acoust. Soc. Am., vol. 19, no. 5, pp. 902–906, Sep. 1947.

[14] O. K. Mawardi, "Measurement of acoustic impedance," J. Acoust. Soc. Am.,vol. 21, no. 2, pp. 84–91, Mar. 1949.

[15] C. M. de Blok and R. F. M. van den Brink, "Full characterization of linear acoustic networks based on n-ports and S parameters," J. Audio Eng. Soc., vol. 40, no. 6, pp. 517–523, Jun. 1992.

[16] Acoustics—Determination of sound absorption coefficient and impedance in impedance tubes— Part 1: Method using standing wave ratio, ISO Std. 10 534-1, 1996.

[17] Standard Test Method for Impedance and Absorption of Acoustical Materials by Impedance Tube Method, ASTM C 384, 2004.

[18] H.-E. de Bree, P. Leussink, T. Korthorst, H. Jansen, T. S. Lammerink, and M. Elwenspoek, "The microflown: a novel device for measuring acoustic flows," Sensors and Actuators A: Physical, vol. 54, no. 1-3, pp. 552–557, Jun. 1996.

[19] R. L. Pratt, S. J. Elliott, and J. M. Bowsher, "The measurement of the acoustic impedance of brass instruments," Acustica, vol. 38, no. 4, pp. 236–246, Oct. 1977.

[20] Y. Liu and F. Jacobsen, "Measurement of absorption with a p-u sound intensity probe in an impedance tube (l)," J. Acoust. Soc. Am., vol. 118, no. 4, pp. 2117–2120, Oct. 2005.

[21] J. D. Mcintosh, M. T. Zuroski, and R. F. Lambert, "Standing wave apparatus for measuring fundamental properties of acoustic materials in air," J. Acoust. Soc. Am., vol. 88, no. 4, pp. 1929–1938, Oct. 1990.

[22] J.-P. Dalmont, "Acoustic impedance measurement, Part II: A new calibration method," Journal of Sound and Vibration, vol. 243, no. 3, pp. 441–459, 2001.

[23] R. T. Muehleisen andW. I. C. Beamer, "Comparison of errors in the three- and four-microphone methods used in the measurement of the acoustic properties of porous materials," Acoustics Research Letters Online, vol. 3, no. 4, pp. 112–117, Jun. 2002.

[24] O. Doutres, Y. Salissou, N. Atalla, and R. Panneton, "Evaluation of the acoustic and non-acoustic properties of sound absorbing materials using a three-microphone impedance tube," Applied Acoustics, vol. 71, no. 6, pp. 506 – 509, 2010. [Online]. Available: http://www.sciencedirect.com/science/article/ B6V1S-4YC8RH8-2/2/5b17adc5a4ac91db5ed5d10760f5750a

[25] B. H. Song and J. S. Bolton, "A transfer-matrix approach for estimating the characteristic impedance and wave numbers of limp and rigid porous materials," J. Acoust. Soc. Am., vol. 107, no. 3, pp. 1131–1152, Mar. 2000.

[26] K. M. Ho, Z. Yang, X. Zhang, and P. Sheng, "Measurements of sound transmission through panels of locally resonant materials between impedance tubes," Appl. Acoust., vol. 66, no. 7, pp. 751–765, Jul. 2005.

[27] Y. Salissou and R. Panneton, "A general wave decomposition formula for the measurement of normal incidence sound transmission loss in impedance tube," J. Acoust. Soc. Am., vol. 125, no. 4, pp. 2083–2090, Apr. 2009.

[28] J. Y. Chung and D. A. Blaser, "Transfer function method of measuring in-duct acoustic properties. i. theory," J. Acoust. Soc. Am., vol. 68, no. 3, pp. 907–913, Sep. 1980.

[29] J. Y. Chung and D. A. Blaser, "Transfer function method of measuring in-duct acoustic properties. ii. experiment," J. Acoust. Soc. Am., vol. 68, no. 3, pp. 914– 921, Sep. 1980.

[30] W. T. Chu, "Extension of the two-microphone transfer function method for impedance tube measurements," J. Acoust. Soc. Am., vol. 80, no. 1, pp. 347–348, Jul. 1986

[31] M. G. Jones and T. L. Parrott, "Evaluation of a multi-point method for determining acoustic impedance," Mechanical Systems and Signal Processing, vol. 3, no. 1, pp. 15–35, Jan. 1989.

[32] H. Bodén and M. Åbom, “Influence of errors on the two-microphone method for measuring acoustic properties in ducts,” J. Acoust. Soc. Am., vol. 79, no. 2, pp. 541–549, Feb. 1986

[33] Bell Telephone Laboratories Inc, 1952. Directional coupler for all-dielectric waveguide. US2794959A.

[34] Sperry Corp, 1949. Directional coupler. US2641648A.

[35] N. M. Ridler and R. G. Clarke, ”Establishing Traceability to the International System of Units for Scattering Parameter Measurements From 750 GHz to 1.1 THz,” in IEEE Transactions on Terahertz Science and Technology, vol. 6, no. 1, pp. 2-11, Jan. 2016, doi: 10.1109/TTHZ.2015.2502068.

[36] Fahd Rushd Faridi and Sascha Preu, ”Pulsed free space two-port photonic vector network analyzer with up to 2 THz bandwidth,” Opt. Express 29, 12278-12291 (2021)

[37] MacDonell, M., & Scott, J. B. (2017). Development and Basic Calibration of an Acoustic Vector Network Analyser. Presented at the Electronics New Zealand Conference 2017 (ENZCon 2017), Christchurch, New Zealand, 4-6 December 2017.

[38] M. MacDonell, K. Basnet and J. Scott, “Waveguide Joint Design and Validation for use in Acoustic Vector-corrected Network Analysers”, 2019 IEEE International Instrumentation and Measurement Technology Conference (I2MTC), 2019, 1-5, 10.1109/I2MTC.2019.8826926

[39] M. MacDonell and J. Scott, “Realizing an Acoustic Vector Network Analyzer”, Proc. 147th Audio Engineering Society Convention, 2019.

[40] M. Macdonell and J. Scott, ”Full Two-Port Vector-Corrected Network Analyzer in the Acoustic Domain”, Journal of the Audio Engineering Society, vol. 70, no. 3, pp. 185-198, 2022. doi: 10.17743/jaes.2021.0058

[41] “Standing Wave Apparatus Type 4002” manual `https://pearl-hifi.com/06_Lit_Archive/15_Mfrs_Publications/10_Bruel_Kjaer/02_Product_Data/4002_Standing_Wave_Apparatus.pdf`

[42] https://dl.cdn-anritsu.com/en-us/test-measurement/files/Brochures-Datasheets-Catalogs/Brochure/11410-00905J.pdf

[43] A. Freundorfer, ”A coherent optical network analyzer”, IEEE Photonics Technology Letters, vol. 3, no. 12, pp. 1139-1142, 1991.

[44] A. P. Freundorfer, "Optical vector network analyzer as a reflectometer," Appl. Opt. 33, 3559-3561 (1994)

[45] V. Adamian, "2-26.5 GHZ On-Wafer Noise and S-Parameter Measurements Using a Solid State Tuner", 34th ARFTG Conference Digest, 1989.

[46] L. Dunleavy, "A Ka-Band On-Wafer S-Parameter and Noise Figure Measurement System", 34th ARFTG Conference Digest, 1989.

[47] A. Davidson, E. Strid and K. Jones, "Achieving greater on-wafer S-parameter accuracy with the LRM calibration technique", 34th ARFTG Conference Digest, 1989.

[48] A. Davidson, K. Jones and E. Strid, "LRM and LRRM Calibrations with Automatic Determination of Load Inductance", 36th ARFTG Conference Digest, 1990.

[49] P.A Rizzi, "Directional Couplers" in *Microwave Engineering - Passive Circuits.* Englewood Cliffs NJ: Prentice-Hall Inc, 1988, 8, 3, pp 367 - 369.

[50] HP Journal Vol. 1, No. 5, January 1950, "Greater Reliability in UHF Impedance Measurements". http://hparchive.com/Journals/HPJ-1950-01.pdf

[51] HP805C Slotted Line Operating & Service Manual; https://literature.cdn.keysight.com/litweb/pdf/00805-90011.pdf?id=1870833

[52] LAVERGHETTA, T. S. (1988). "Modern microwave measurements and techniques". Norwood, MA, Artech House.

[53] R. Levy and L. Lind, "Synthesis of Symmetrical Branch-Guide Directional Couplers", IEEE Transactions on Microwave Theory and Techniques, vol. 16, no. 2, pp. 80-89, 1968. Available: 10.1109/tmtt.1968.1126612 [Accessed 18 July 2020].

[54] Lagasse, P., "Realisation of an acoustical directional coupler", *Journal of sound and vibration*, 15(3), April 1971, pp367–372.

[55] Scott, J. and K. E. Pennington, "Acoustic Vector-Corrected Impedance Meter", *IEEE Transactions on Instrumentation and Measurement*, 2014. DOI: 10.1109/TIM.2014.2327474

[56] M. MacDonell, 'Scaling acoustic directional couplers using 3D printing', Thesis, Master of Engineering (ME), University of Waikato, 2015.

[57] K. Kurokawa, "Power Waves and the Scattering Matrix", IEEE Transactions on Microwave Theory and Techniques, vol. 13, no. 2, pp. 194-202, 1965. Available: 10.1109/tmtt.1965.1125964 [Accessed 3 February 2019].

[58] R. Nelson. "How does a Smith chart work?" Test & Measurement World, July 2001. http://www.sss-mag.com/pdf/smith_chart_basics.pdf

[59] P. Smith, "Electronic applications of the Smith Chart". Raleigh, NC. Scitech, June 30, 1995. ISBN-10 : 1884932398

[60] Agilent Application Note 1287-3 "Applying Error Correction to Network Analyzer Measurements" http://anlage.umd.edu/Microwave%20Measurements%20for%20Personal%20Web%20Site/5965-7709E.pdf

[61] K. Goser, "Tunneling and thermal noise as limiting factors in microelectronics", Microelectronics Reliability, vol. 28, no. 4, pp. 605-611, 1988. Available: 10.1016/0026-2714(88)90146-1.

[62] K. Lundberg, "Noise Sources in Bulk CMOS", Web.mit.edu, 2022. Available: http://web.mit.edu/klund/www/papers/UNP_noise.pdf.

[63] S. Mason, "Feedback Theory-Some Properties of Signal Flow Graphs", Proceedings of the IRE, vol. 41, no. 9, pp. 1144-1156, 1953. Available: 10.1109/jrproc.1953.274449 [Accessed 19 May 2022].

[64] Kuhn, 'Signal Flow Graphs', Microwave Journal, November 1963, pp 59+.

[65] D. Rytting, "Network Analyzer Error Models and Calibration Methods". https://www.rfmentor.com/sites/default/files/NA_Error_Models_and_Cal_Methods.pdf

[66] Douglas K. Rytting, "Network Analyzer Error Models and Calibration Methods," 62nd ARFTG Conference Short Course Notes, December 2-5, 2003, Boulder, CO.

[67] J. Butler, D. Rytting, M. Iskander, R. Pollard and M. Vanden Bossche, "16-term error model and calibration procedure for on-wafer network analysis measurements", IEEE Transactions on Microwave Theory and Techniques, vol. 39, no. 12, pp. 2211-2217, 1991. Available: 10.1109/22.106567.

[68] Jonathan B. Scott, Personal communication, May 17, 2020

[69] K. Silvonen, "LMR 16-a self-calibration procedure for a leaky network analyzer", IEEE Transactions on Microwave Theory and Techniques, vol. 45, no. 7, pp. 1041-1049, 1997.

[70] K. Dahlberg and K. Silvonen, "A Method to Determine LRRM Calibration Standards in Measurement Configurations Affected by Leakage", IEEE Transactions on Microwave Theory and Techniques, vol. 62, no. 9, pp. 2132-2139, 2014.

[71] 911D/E Sliding Load Operating and Service Manual - Agilent Technologies

[72] G. Taubin, "Estimation of planar curves, surfaces, and nonplanar space curves defined by implicit equations with applications to edge and range image segmentation," IEEE Trans. Pattern Anal. Mach. Intell., vol. 13, no. 11, pp. 1115–1138, Nov. 1991.

[73] A. Al-Sharadqah and N. Chernov, "Error analysis for circle fitting algorithms", Electronic Journal of Statistics, vol. 3, no. 0, pp. 886-911, 2009. Available: 10.1214/09-ejs419 [Accessed 11 March 2019].

[74] R. A. Ginley, "Confidence in VNA Measurements," IEEE Microwave Magazine, vol. 8, no. 4, pp. 54-58, Aug. 2007.

[75] D. F. Williams, A. Lewandowski, D. LeGolvan, and R. Ginley, "Electronic vector-network-analyzer verification," IEEE Microwave Mag., vol. 10, no. 6 Oct. 2009.

[76] J. Scott, "Investigation of a method to improve VNA calibration in planar dispersive media through adding an asymmetrical reciprocal device", IEEE Transactions on Microwave Theory and Techniques, 2005, Vol.53, pp 3007-3013, 10.1109/TMTT.2005.854225.

[77] IEC 60154-1:2016 Flanges for waveguides - Part 1: General requirements

[78] IEC 60154-2:2016 Flanges for waveguides - Part 2: Relevant specifications for flanges for ordinary rectangular waveguides

[79] IEC 60261:1989 Sealing test for pressurized waveguide tubing and assemblies

[80] T. Anderson, "Rectangular and Ridge Waveguide", IEEE Transactions on Microwave Theory and Techniques, vol. 4, no. 4, pp. 201-209, 1956. Available: 10.1109/tmtt.1956.1125063 [Accessed 20 July 2020].

[81] M. Horibe and K. Noda, "Modification of waveguide flange design for millimeter and submillimeter-wave measurements", 77th ARFTG Microwave Measurement Conference, 2011. Available: 10.1109/arftg77.2011.6034557 [Accessed 18 July 2020].

[82] M. Horibe and R. Kishikawa, "Performance of new design of waveguide flange for measurements at frequencies from 800 GHz to 1.05 THz", 79th ARFTG Microwave Measurement Conference, 2012. Available: 10.1109/arftg79.2012.6291186 [Accessed 18 July 2020].

[83] M. Horibe, "Measurement Uncertainty in Terahertz VNAs: Using Terahertz Vector Network Analyzers for Stable, Accurate Measurement and to Evaluate Uncertainty," in IEEE Microwave Magazine, vol. 19, no. 2, pp. 24-34, March-April 2018. doi: 10.1109/MMM.2017.2779678

[84] IEEE Standard for Rectangular Metallic Waveguides and Their Interfaces for Frequencies of 110 GHz and Above–Part 2: Waveguide Interfaces," in IEEE Std 1785.2-2016 , vol., no., pp.1-22, 9 Sept. 2016, doi: 10.1109/IEEESTD.2016.7564020.

[85] PreSonus Audiobox1818 manual.

[86] J. Butler, D. Rytting, M. Iskander, R. Pollard and M. Vanden Bossche, "16-term error model and calibration procedure for on-wafer network analysis measurements", IEEE Transactions on Microwave Theory and Techniques, vol. 39, no. 12, pp. 2211-2217, 1991.

[87] A. Cline, I. Dhillon, Handbook of Linear Algebra, pp. 45-1–45-13, January 2006.

[88] G. Golub and C. Reinsch, "Singular value decomposition and least squares solutions", Numerische Mathematik, vol. 14, no. 5, pp. 403-420, 1970.

[89] G. Golub and W. Kahan, "Calculating the Singular Values and Pseudo-Inverse of a Matrix", Journal of the Society for Industrial and Applied Mathematics Series B Numerical Analysis, vol. 2, no. 2, pp. 205-224, 1965.

[90] "svd", MathWorks, 2022. [Online]. Available: https://www.mathworks.com/help/matlab/ref/double.svd.html.

[91] HP4395A Manual

[92] T. Watanabe and S. Yamada, "Sound attenuation through absorption by vegetation," J. Acoust. Soc. Jpn., vol. 17, no. 4, pp. 175–182, 1996.

[93] J. Raggio, "Results of a Multi-Site Round-Robin to Examine Probed Measurements of an Impedance Standard Substrate," 34th ARFTG Conference Digest, 1989, pp. 41-50, doi: 10.1109/ARFTG.1989.323955.

[94] R. Schlieper, S. Li, J. Peissig, "Development and validation of a full audio range acoustic impedance tube," presented at the 144th Convention of the AES, Milan, Italy, pp. 1–4 (2018 May).

[95] `https://perspex.com/images/uploads/info_centre/Perspex_PRODUCT_GUIDE_Sweet_Pastels.pdf`

[96] Horibe, M.. "Connection torque consideration for waveguide flange at millimeter-wave and terahertz frequencies." 2016 87th ARFTG Microwave Measurement Conference (ARFTG) (2016): 1-4.

[97] https://www.keysight.com/main/editorial.jspx?cc=NZ&lc=eng&ckey=606542&nid=-11143.0.00&id=606542

[98] Jonathan B. Scott, Personal communication, Feb 11, 2021

[99] D. H. Keefe, R. Ling, and J. C. Bulen, "Method to measure acoustic impedance and reflection coefficient," J. Acoust. Soc. Am., vol. 91, no. 1, pp. 470–485, Jan. 1992.

[100] ISO 10534-2:1998 - Acoustics – Determination of sound absorption coefficient and impedance in impedance tubes – Part 2: Transfer-function method

[101] J. Vieira, "Automatic Estimation of Reverberation Time", in Audio Engineering Society Convention 116, 2004.

[102] J. Vieira, "Estimation of Reverberation Time without Test Signals", in Audio Engineering Society Convention 118, 2005.

[103] P. D'Antonio, T. Cox, "Characterization of Acoustical Materials", Audio Engineering Society Conference: UK 12th Conference: The Measure of Audio (MOA), 1997.

[104] Smith, J., Fritz, C. and Wolfe, J. "A new technique for the rapid measurement of the acoustic impedance of wind instruments", Proc. Seventh International Congress on Sound and Vibration, July 2000, Garmisch-Partenkirchen, Germany, Vol III, pp.1833?1840.

[105] Kausel, W., "Bore reconstruction of tubular ducts from its acoustic input impedance curve", IEEE Transactions on Instrumentation and Measurement, vol. 53, no. 4, August 2004, pp. 1097-1105.

[106] Mason and Zimmerman, Electronic Circuits, Signals & Systems, Wiley, 1960.